

# **How bacteria conquer, compete, and cooperate**

**A study on spatial dynamics and self-organisation of  
*Escherichia coli* communities**



**Mireia Cordero**

Supervisor: Liselotte Jauffred  
Co-supervisor: Namiko Mitarai

This thesis has been submitted to the PhD School of The Faculty of Science,  
University of Copenhagen

July 31, 2024



*"Science is a liar sometimes"*

Ronald McDonald



## Acknowledgements

First, I want to acknowledge my supervisor, Liselotte Jauffred, for giving me the opportunity to work with her. Her guidance over the last years has been invaluable, from our writing sessions and scientific discussions to her deep knowledge of Danish flora and fauna. Likewise, I would like to extend my gratitude to my co-supervisor, Namiko Mitarai, who was always available to discuss and offer sharp insights. I hope this thesis reflects some of what I've learned from both of you.

I'd like to give special thanks to Stanley Brown, who has taught me countless life and scientific lessons. I greatly appreciate his patience and his recommendations of mid-20th-century microbiology papers (which I'm still trying to understand) and mandatory high school books. Most importantly, he has shown me that in order to build character, one must experience many inconveniences.

I would also like to acknowledge all the scientific collaborators I've worked with over the past years. Starting from the co-authors of the paper "Emergent collective alignment gives competitive advantage to longer cells during range expansion," particularly the first authors, Nathan van den Berg, Dr. Kristian Thijssen, and Trang Nguyen. I am also grateful to Sine Lo Svenningsen for supplying strains and feedback for the chloramphenicol study and to Brage Haldor Thomsen for his simulations, which provided additional information about the system. I would like to express my gratitude to Dr. Martin Ackermann and Dr. Olga Schubert for sharing their strain collection with me and to Kim Schlegel for arranging the shipment of the strains I needed to Denmark. Thanks to Marianne Lund and Inger Jensen for their work keeping the lab running during my years here, a task that is no easy feat.

I cannot fit all the reasons why I am grateful to Dr. Sarlet in one (and only one) sentence. Thank you for your support throughout the whole writing process; your incisive and constructive feedback has truly made a difference. You've also expanded my knowledge of imaging techniques and have always been available to have stimulating scientific discussions. For the weekly beers, daily eggs, and hourly laughs, I couldn't have asked for a better office mate to share the experience—well, maybe one who shuts up from time to time.

I would like to thank Artemis for a plethora of reasons, particularly for giving me the opportunity to supervise her in the lab and learn how to do it along the way. It has been a pleasure to share discussions and frustrations with you.

A big thank you to the Biocomplexity and Experimental Biophysics group, past, present, and future members. You've created an inspiring environment where I've not only found colleagues but also built friendships. Thanks to Alessandra, Irene, Lars Erik, Yoshi, and Anja for countless enjoyable game nights and social events. I'd especially like to thank Victoria, whose vitality and advice have been essential in keeping me grounded over the past years. I admire you greatly and am thankful for the many experiences we've had together.

Special thanks to the coffee club, which wouldn't be possible without Malthe. You made going to work enjoyable rather than a chore. I'll always cherish our discussions about the most random topics that Lukas (annoyingly) knew every detail about while Tuan almost single-handedly finished a 1.5L French press. I'd love to include Miguel as part of the cc, but since you had to bike all the way from Amager, you were always late. Regardless of your passion for Vest-Amager, you have been an invaluable source of encouragement and a wonderful friend.

Thank you, Bente. Not only are you the best academic officer anyone could wish for, but you're also an incredible friend. You have no idea how much brighter my days have been when I started them with a conversation with you. I can't imagine my time at Biocomplexity without your unconditional warmth and support.

I'd also like to extend my gratitude to everyone in the UMIK department at Eawag, where I had the pleasure of spending three months of my PhD. Particularly everyone in the MCA group, including Lea, Miao, Agustina, and, of course, Laika. Thank you, Dave, for being the best group leader and cheerleader and for making me feel welcome from day one. You've taught me that some challenges don't need to be tackled one day at a time but one hour at a time instead. Thank you, Chujin, for the coffee breaks and engaging discussions. I have learned a lot about what it means to be a scientist from you. Deepthi, getting to know you was the highlight of my stay. While I could write pages about it, I'll simply say thank you for letting me be a part of your life. I will always treasure the moments we shared together.

I want to thank my friends and family for driving me to the airport without charging me for gas and doing so with hardly any complaints. A special thanks to my mother for her unwavering support throughout my life. Thanks, Jose, for keeping me challenged with your basic chemistry questions. And thanks, Maria, for making the best diagrams ever and sharing so many traumatic experiences with me; I truly appreciate it.

I want to extend my gratitude to those who are no longer with us. While you may not fully understand what this journey has been about, I am certain you would be proud. I miss you deeply.

Finally, if you made it to this point and I have not written your name explicitly, I am extremely sorry. This acknowledgement section is for you as well.

And thanks to Albert.



## Abstract

This thesis explores the emergence of spatial self-organisation within bacterial communities and its impact on their spreading dynamics. By combining novel experimental setups with stochastic numerical simulations, I quantify the influence of specific bacterial interactions and environmental conditions on their community formation. I do so by studying three distinct experimental systems of *Escherichia coli* with increasing complexity between interactions of their constituents.

The first study examines the three-dimensional organisation of isogenic colonies within semi-solid media. In this setting, environmental factors are the main driver of self-organisation. This study reveals the formation of satellite colonies due to flagellar motility, an enhancing mechanism for bacterial invasion that allows cells to **conquer** new territories while maintaining the protection benefits of the main colony.

The second study addresses the effect of cell morphology on spreading **competition**, revealing a competitive advantage of slender cells in two-dimensional settings. Those cells align due to mechanical interactions, which promote their takeover of the colony edge. Likewise, this thesis proves that cell morphology is a key factor in the efficiency of processes that require cell-to-cell contact within subpopulations of cells.

The third study investigates the origin of indirect antibiotic resistance as a consequence of the spatial arrangement of cells. When the detoxification of the environment occurs locally, cells require close contact to gain protection against the antibiotic. Here, three-dimensional configurations are shown to increase the tolerance of the sensitive cells to an antibiotic compared to their two-dimensional counterparts. The significance of cell contacts is further highlighted as the environment shifts from promoting competition at low antibiotic levels to enhancing **cooperation** via indirect resistance at high ones. This transition leads to the rearrangement of subpopulations in space, resulting in increased cell interactions.

Overall, this thesis emphasises the importance of spatial factors in studies of bacterial communities and reveals how physical interactions and environmental conditions shape their behaviour. The results presented aim to offer new insights into bacterial self-organisation and resistance mechanisms that may have been previously overlooked.



## Resumé på Dansk

Denne afhandling undersøger fremkomsten af rumlig selvorganisering i bakteriesamfund og dens indvirkning på deres spredningsdynamik. Ved at kombinere nye forsøgsopstillinger med stokastiske numeriske simuleringer, kvantificerer jeg indflydelsen af specifikke bakterielle interaktioner og miljøforhold på deres samfundsdannelse. Det gør jeg ved at studere tre forskellige eksperimentelle systemer af *Escherichia coli*, hvor interaktionerne mellem bestanddelene er af stigende kompleksitet.

Det første studie undersøger den tredimensionelle rumlige organisering af isogene kolonier i halvfast medier. I denne sammenhæng er miljøfaktorer den vigtigste drivkraft for selvorganisering. Denne undersøgelse afslører dannelsen af satellitkolonier på grund af flagellær motilitet, en mekanisme, der forbedrer bakteriel invasion ved at gøre det muligt for celler at sprede sig til nye territorier, samtidig med at hovedkoloniens beskyttelsesfordele opretholdes.

Den anden undersøgelse omhandler effekten af cellemorfologi på konkurrence i spredning og afslører en konkurrencefordel for slanke celler i todimensionelle omgivelser. Disse celler tilpasser sig på grund af mekaniske interaktioner, som fremmer deres overtagelse af kanten af kolonien. På samme måde viser denne afhandling, at cellemorfologi er en nøgelfaktor i effektiviteten af processer, der kræver celle-til-celle-kontakt inden for delpopulationer af celler.

Det tredje studie undersøger oprindelsen af indirekte antibiotikaresistens som en konsekvens af cellernes rumlige placering. Når afgiftningen af miljøet sker lokalt, kræver det direkte kontakt mellem cellerne for at opnå beskyttelse mod antibiotikummet. Her viser det sig, at tredimensionelle konfigurationer øger de følsomme cellers tolerance over for et antibiotikum sammenlignet med todimensionelle konfigurationer. Betydningen af cellekontakt fremhæves yderligere, når miljøet skifter fra at fremme konkurrence ved lave antibiotikaniveauer til at forbedre samarbejdet via indirekte resistens ved høje niveauer.

Denne overgang fører til omorganisering af delpopulationer i rummet, hvilket resulterer i flere celleinteraktioner.

Samlet set understreger denne afhandling betydningen af rumlige faktorer i studier af bakteriesamfund og afslører, hvordan fysiske interaktioner og miljøforhold former samfundets adfærd. De præsenterede resultater har til formål at give ny indsigt i bakteriel selvorganisering og resistensmekanismer, som måske tidligere er blevet overset.

## Resumen en castellano

Esta tesis explora la aparición de la autoorganización espacial dentro de las comunidades bacterianas y su impacto en su dinámica de propagación. Mediante la combinación de nuevas configuraciones experimentales con simulaciones numéricas estocásticas, cuantifico la influencia de las interacciones bacterianas específicas y las condiciones ambientales en la formación de su comunidad. Lo hago mediante el estudio de tres sistemas experimentales distintos de *Escherichia coli* con una complejidad creciente entre las interacciones de sus constituyentes.

El primer estudio examina la organización espacial tridimensional de las colonias isogénicas dentro de medios semisólidos. En este contexto, los factores ambientales son el principal motor de la autoorganización. Este estudio revela la formación de colonias satélite debido a la motilidad flagelar, un mecanismo potenciador de la invasión bacteriana que permite que las células **conquisten** nuevos territorios manteniendo los beneficios de protección de la colonia principal.

El segundo estudio aborda el efecto de la morfología celular, revelando una ventaja **competitiva** de las células esbeltas en entornos bidimensionales. Esas células se alinean debido a interacciones mecánicas, que promueven su toma de control del extremo de la colonia. Asimismo, esta tesis demuestra que la morfología celular es un factor clave en la eficiencia de los procesos que requieren contacto célula a célula entre subpoblaciones.

El tercer estudio investiga el origen de la resistencia indirecta a los antibióticos como consecuencia de la disposición espacial de las bacterias. Cuando la desintoxicación del medio ambiente se produce localmente, las células requieren un contacto directo para obtener protección contra el antibiótico. Aquí, se muestra que las configuraciones tridimensionales aumentan la tolerancia de las células sensibles a un antibiótico en comparación con las bidimensionales. La importancia de los contactos celulares se destaca aún más a medida que el entorno pasa de promover la competencia a niveles bajos de antibióticos a propiciar la

**cooperación** a través de la resistencia indirecta a niveles altos. Esta transición conduce a la reorganización de las subpoblaciones en el espacio, lo que resulta en un aumento de las interacciones celulares.

En general, esta tesis enfatiza la importancia de los factores espaciales en los estudios de las comunidades bacterianas y revela cómo las interacciones físicas y las condiciones ambientales moldean su comportamiento. Los resultados presentados pretenden ofrecer nuevos conocimientos sobre la autoorganización bacteriana y los mecanismos de resistencia que pueden haberse pasado por alto anteriormente.

## Resum en català

Aquesta tesi explora l'emergència de l'autoorganització espacial dins de les comunitats bacterianes i el seu impacte en la seva dinàmica de propagació. Combinant experiments amb simulacions numèriques estocàstiques, quantifico la influència d'interaccions bacterianes específiques i condicions ambientals en la formació de la seva comunitat. Ho faig estudiant tres sistemes experimentals diferents d'*Escherichia coli* amb una complexitat creixent entre les interaccions dels seus components.

El primer estudi examina l'organització espacial tridimensional de colònies isogèniques en medis semisòlids. En aquest entorn, els factors ambientals són el principal motor de l'autoorganització. Aquest estudi revela la formació de colònies satèl·lit a causa de la motilitat flagel·lar, un mecanisme de millora de la invasió bacteriana que permet que les cèl·lules **conquistin** nous territoris mantenint els beneficis de protecció de la colònia principal.

El segon estudi aborda l'efecte de la morfologia cel·lular revelant un avantatge **competitiu** de les cèl·lules esveltes en entorns bidimensionals. Aquestes cèl·lules s'alineen a causa d'interaccions mecàniques, que promouen la seva presa de control de la vora de la colònia. Així mateix, aquesta tesi demostra que la morfologia cel·lular és un factor clau en l'eficiència de processos que requereixen contacte cèl·lula a cèl·lula dins de subpoblacions de bacteries.

El tercer estudi investiga l'origen de la resistència indirecta als antibiòtics com a conseqüència de la disposició espacial. Quan la desintoxicació del medi es produeix localment, les cèl·lules requereixen contacte directe per obtenir protecció contra l'antibiòtic. Aquí, es demostra que les configuracions tridimensionals augmenten la tolerància de les cèl·lules sensibles a un antibiòtic en comparació amb les bidimensionals. La importància dels contactes cel·lulars es posa de manifest a mesura que l'entorn passa de promoure la competència a nivells baixos d'antibiòtics a induir la **cooperació** a través de la resistència indirecta als alts. Aquesta transició condueix a la reordenació de les subpoblacions a l'espai, donant lloc a un augment de les interaccions cel·lulars.

En general, aquesta tesi emfatitza la importància dels factors espacials en els estudis de les comunitats bacterianes i revela com les interaccions físiques i les condicions ambientals configuren el seu comportament. Els resultats presentats tenen com a objectiu oferir nous coneixements sobre els mecanismes d'autoorganització i resistència bacteriana que abans podien haver-se passat per alt.





# Table of contents

<b>List of figures</b>	<b>xxi</b>
<b>List of tables</b>	<b>xxiii</b>
<b>Nomenclature</b>	<b>xxv</b>
<b>1 Introduction</b>	<b>1</b>
1.1 Background . . . . .	1
1.2 Thesis motivation and outline . . . . .	6
<b>2 Motility mediates satellite formation in confined biofilms</b>	<b>9</b>
2.1 Introduction . . . . .	9
2.1.1 Objectives . . . . .	12
2.2 Materials and Methods . . . . .	13
2.2.1 Experimental Methods . . . . .	13
2.2.2 Computational methods . . . . .	17
2.3 Results . . . . .	19
2.3.1 Satellite colonies form around three-dimensional colonies . . . . .	19
2.3.2 Deletion of extracellular structures causes loss of satellite morphology	22
2.3.3 Motility is reduced when extracellular structures are deleted . . . . .	24
2.3.4 Density of the substrate matrix controls satellite emergence . . . . .	25
2.3.5 Satellite formation speeds up colonisation . . . . .	27
2.4 Discussion . . . . .	30
<b>3 Cell morphology shapes the self-organisation of bacterial communities</b>	<b>35</b>
3.1 Introduction . . . . .	35
3.1.1 Objectives . . . . .	37
3.2 Materials and Methods . . . . .	38
3.2.1 Experimental Methods . . . . .	38

3.2.2	Computational methods . . . . .	42
3.3	Results . . . . .	46
3.3.1	Batch cultures favour rounder cells . . . . .	46
3.3.2	Two-dimensional range expansions favour slender cells . . . . .	47
3.3.3	Mechanical interactions control edge takeover . . . . .	49
3.3.4	Cell shape controls segregation patterns in isogenic two-dimensional colonies . . . . .	51
3.3.5	Patterning of communities affects conjugation events . . . . .	56
3.4	Discussion . . . . .	58
<b>4</b>	<b>Indirect antibiotic resistance arises from local interactions</b>	<b>63</b>
4.1	Introduction . . . . .	63
4.1.1	Objectives . . . . .	66
4.2	Materials and Methods . . . . .	67
4.2.1	Experimental methods . . . . .	67
4.2.2	Computational methods . . . . .	72
4.3	Results . . . . .	74
4.3.1	Spatial organisation affects the outcome of indirect resistance . . . . .	74
4.3.2	Indirect resistance emerges in liquid cultures . . . . .	78
4.3.3	Resistant cells dominate two-dimensional range expansions . . . . .	80
4.3.4	Indirect resistance arises in lower competitive settings . . . . .	83
4.3.5	Intermixing between populations is induced by indirect resistance . . . . .	85
4.4	Discussion . . . . .	87
<b>5</b>	<b>Discussion</b>	<b>93</b>
5.1	Closing remarks . . . . .	96
	<b>References</b>	<b>99</b>
	<b>Appendix A Manuscripts</b>	<b>115</b>
A.1	Motility mediates satellite formation in confined biofilms . . . . .	115
A.2	Emergent collective alignment gives competitive advantage to longer cells during range expansion . . . . .	130
A.3	Indirect antibiotic resistance enhances colony tolerance in mixed bacterial communities . . . . .	160

# List of figures

2.1	5-step biofilm model diagram . . . . .	10
2.2	Motility mechanisms diagram . . . . .	12
2.3	Growth curves of the parental strain (wt) . . . . .	15
2.4	Mature 3D colonies in different polysaccharide matrices . . . . .	16
2.5	Thresholded experimental 3D colony . . . . .	17
2.6	Radial expansion of experimental 3D colony . . . . .	19
2.7	Morphologies of 3D colonies of the parental strain (wt) in 0.3% agarose . . . . .	20
2.8	Morphologies of 3D colonies of the parental strain (wt) in 0.5% agar . . . . .	20
2.9	Quantification of 3D wt+ colonies . . . . .	21
2.10	Maximum intensity projections of zoom-in wt+ colony . . . . .	22
2.11	Diagram of an <i>E. coli</i> cell with the depleted structures in the mutants . . . . .	23
2.12	Maximum intensity projection of the 3D mutant colonies . . . . .	24
2.13	Motility assays in minimal and rich media . . . . .	25
2.14	Effect of agarose concentration on 3D colony morphology . . . . .	26
2.15	Effect of matrix elasticity on 3D colony morphology . . . . .	26
2.16	<i>In silico</i> 3D colonies . . . . .	28
2.17	Quantification of <i>in silico</i> colonies . . . . .	29
2.18	Time-evolution of <i>in silico</i> colonies . . . . .	30
2.19	Cryo-SEM micrograph of 0.3% agarose hydrogel . . . . .	31
2.20	Comparison <i>in vitro</i> vs <i>in silico</i> 3D colony . . . . .	33
3.1	Sketch of different cell shapes . . . . .	35
3.2	Growth curve of WT and MreB mutants . . . . .	39
3.3	Sketch of parameters used for CellModeller simulations . . . . .	44
3.4	Data analysis parameters used to quantify isogenic colonies . . . . .	45
3.5	Experimental liquid competitions . . . . .	47
3.6	Experimental 2D range expansion competitions . . . . .	48

---

3.7	Occupied fraction of longer cells along the radial direction and expansion rates of 2D isogenic colonies . . . . .	49
3.8	Single-cell time evolution of range expansion front . . . . .	50
3.9	Quantification of 2D range expansion of isogenic colonies . . . . .	52
3.10	Quantification of simulated colonies for cells with fixed aspect ratio . . . . .	54
3.11	Quantification of simulated colonies for cells with fixed volume . . . . .	55
3.12	Number of transconjugant regions for <i>in silico</i> colonies . . . . .	57
3.13	Transconjugant sectors under phage predation . . . . .	59
4.1	Diagram with antibiotic targets and resistance mechanisms . . . . .	64
4.2	Growth rate and relative fitness in well-mixed conditions for simulated populations . . . . .	75
4.3	Relative fitness in 2D colonies for simulated populations . . . . .	76
4.4	Relative fitness in 3D colonies for simulated populations . . . . .	77
4.5	Experimental cell divisions in liquid cultures at different chloramphenicol concentrations . . . . .	79
4.6	Relative fitness of the sensitive strain in liquid co-cultures . . . . .	80
4.7	Strain occupation at the centre and at the edge of 2D range expansions . . . . .	81
4.8	Relative fitness of the sensitive strain in 2D colonies . . . . .	82
4.9	Growth rate of RES and SEN in liquid cultures at different chloramphenicol concentrations . . . . .	83
4.10	Colony collision in blue-white screening media . . . . .	84
4.11	Colony collision in blue-white screening media after 24 and 72 hours of incubation . . . . .	85
4.12	Colony collision of fluorescent strains after 24 hours of incubation . . . . .	86
4.13	Tortuosity of the collision front . . . . .	87

# List of tables

2.1	<i>E. coli</i> strains used in the study . . . . .	13
3.1	<i>E. coli</i> strains used in the study . . . . .	39
3.2	Quantification of isogenic 2D experimental colonies . . . . .	52
3.3	Cell shapes used for CellModeller simulations . . . . .	53
3.4	Quantification of <i>in silico</i> 2D colonies for cells with the same aspect ratio . . . . .	54
3.5	Quantification of <i>in silico</i> 2D colonies for cells with the same volume . . . . .	55
3.6	Fraction of transconjugants for <i>in silico</i> colonies . . . . .	57
4.1	<i>E. coli</i> strains used in the study . . . . .	68
4.2	MIC values of the sensitive strains used in the study . . . . .	69



# Nomenclature

## Abbreviations

2D Two-dimensional

3D Three-dimensional

*E. coli* *Escherichia coli*

amp Ampicillin

CAT Choramphenicol acetyltransferase

CFUs Colony Forming Units

Cm Chloramphenicol

DNA Deoxyribonucleic acid

FACS Fluorescence-Activated Cell Sorting

GFP Green Fluorescent Protein

HGT Horizontal Gene Transfer

IBM Individual-based model

IPTG Isopropyl  $\beta$ -d-1-thiogalactopyranoside

IR Indirect Resistance

kan Kanamycin

lac Lactose

LB Luria-Bertani

LSCM Laser-scanning confocal microscope

M63+glu M63 minimal medium supplemented with glucose

MIC Minimum Inhibitory Concentration

OD<sub>600</sub> Optical density at 600 nm

RFP Red Fluorescent Protein

RPM Revolutions per minute

sfGFP Superfolder GFP

w/v Weight in volume

X-gal 5-bromo-4-chloro-3-indolyl- $\beta$ -D-galactopyranoside

YFP Yellow fluorescent protein

### **Bacterial Strains**

$\Delta$ cps *E. coli* K-12 EPS colanic acid mutant

$\Delta$ csgAB *E. coli* K-12 curli fimbriae mutant

$\Delta$ fim *E. coli* K-12 Type I pili mutant

$\Delta$ fliC *E. coli* K-12 Flagella mutant

$\Delta$ flu *E. coli* K-12 Antigen 43 mutant

AK *E. coli* REL606*mreB*<sup>A53K</sup>

AS *E. coli* REL606*mreB*<sup>A53S</sup>

RES *E. coli* K-12 TSS290

RES-G *E. coli* K-12 TB193

RES-R *E. coli* K-12 TB194

SEN *E. coli* K-12 SLS4223

SEN-G *E. coli* K-12 TB204

SEN-R *E. coli* K-12 TB205

wt *E. coli* K-12 MG1655

WT-REL *E. coli* REL606



# Chapter 1

## Introduction

This thesis investigates the complex world of self-organised bacterial communities from a biophysical point of view. Experiments in previously unexplored settings were conducted and coupled with numerical simulations to uncover the key mechanisms driving the observed phenomena.

### 1.1 Background

**Bacteria** Bacteria are prokaryotic cells and the most abundant organism on Earth [1]. They can be found in almost every environment, including extreme ones. Within the human body, bacteria predominantly participate in harmless or beneficial processes, though some pathogenic strains can cause serious infections [2]. Additionally, these prokaryotic cells play a leading role in countless natural processes and are also important in numerous industrial processes [3].

**Bacterial growth** Bacteria reproduce mostly by binary fission [4]. When growing in optimal environments, they can divide within minutes. However, in heterogeneous and poor nutritional media, the division time increases, and in extremely harsh environments, it is suggested to occur as slowly as years [5]. When bacteria grow in controlled liquid environments, their growth dynamics can be differentiated into four distinct phases [6]. The first phase corresponds to the lag phase, during which the cells do not grow. This phase usually corresponds to the time needed by the cells to get used to the environment before initiating division. The lag phase finishes once the initial amount of cells has been doubled. The second phase corresponds to the exponential or log phase, where bacteria divide continuously at a constant rate. The growing rate of a bacterial population,  $\lambda$  ( $\text{h}^{-1}$ ), can be estimated from the growth curve during the log phase. The doubling time (or generation

time) of a bacterial population is the time required for the number of cells to double. The doubling time ( $\tau$ ) can be calculated from the growth rate ( $\lambda$ ) using the equation:

$$\tau = \frac{\ln(2)}{\lambda} \quad (1.1)$$

As cells grow exponentially, the nutrient level of the environment decreases until it can no longer sustain the growth of the entire population. When this occurs, the cells enter the stationary phase, during which there is no net growth of the population. In this phase, the number of dividing cells equals the number of dying ones. When the nutrient level declines further, the cells enter the death phase, where the population decreases in size. The four-phase growth does not always apply to real systems, where cells may face limited access to nutrients for multiple reasons, such as competition with other organisms and spatial constraints.

**Bacterial classification** Bacteria can be divided into two main groups, Gram-positive or Gram-negative, based on the structural characteristics of their cell walls [7]. Bacterial cell walls are primarily constituted by peptidoglycan, large macromolecules that form a mesh-like scaffold around the cells and are targeted by some antibiotics [8]. Gram-positive bacteria present a thick peptidoglycan wall and lack a protective outer membrane. Gram-negative bacteria have two membranes surrounding a thin peptidoglycan wall. The name derives from the distinct reactions of each cell group to a Gram staining assay [9]. Bacteria in each group respond differently to the same inputs, such as surface stiffness [10, 11] or antimicrobial agents [12, 13]. Therefore, studies performed with one group of bacteria cannot always be generalised to the other. Different model organisms are used for each group to understand bacterial behaviour. In Gram-positive bacteria, most of the studies are performed with *Bacillus subtilis* [14], while *Escherichia coli* (*E. coli*) is the preferred organism for Gram-negative bacteria,

***Escherichia coli*** *E. coli* is a Gram-negative, non-sporulating, rod-shaped bacterium predominantly found in the digestive tract of mammals [15]. Some pathogenic strains can produce infections of different severity [16]. The first *E. coli* strain used for *in vitro* studies was *E. coli* K-12, which was initially isolated from the stool of a convalescent diphtheria patient in California in 1922 [17]. *E. coli* K-12 is a non-pathogenic strain with a short generation time and low nutritional requirements, which makes its growth robust in various media. It grows optimally at 37°C and can live in a Petri dish for several weeks. Its genome was sequenced in 1997 [18], and since then, multiple laboratory strains have been derived from it, such as *E. coli* B-strains [19].

**Bacterial communities** Bacteria are typically not found isolated in nature but rather as communities [20]. Natural communities are highly complex, making it challenging to understand all their properties. *In vitro* assays with artificial bacterial communities have been designed to comprehend such systems. The assays are often conducted in batch cultures, but their results may not fully reflect properties from natural settings. In nature, bacterial communities grow in environments with spatial heterogeneities that cannot be reproduced in well-mixed liquid cultures. Furthermore, these communities develop as spatial structures, forming aggregates or biofilms. Sessile bacterial communities vary widely in size and function and often provide protection to cells against environmental stresses compared to their planktonic counterparts [21]. Bacterial communities expand across the environment as the cells grow, divide and disperse, a process referred to as range expansion. To study spatially distributed communities, surface-associated systems are among the most common for *in vitro* experiments.

**Surface-attached bacterial communities** Cells attached to a surface are often non-motile. Therefore, range expansions in surface-associated communities primarily occur as a consequence of cell division. As bacteria divide, daughter cells appear adjacent to their mother cells, increasing the local density of the community. The increase in density generates mechanical interactions among bacteria, leading to a passive expansion of the community as cells shove with each other [22, 23]. Bacterial range expansion in surface-attached communities has been extensively investigated *in vitro* over the last years, as these systems provide a powerful setup for studying multiple ecological processes within bacterial communities, such as horizontal gene transfer [24, 25]. Additionally, they are also used to explore applications of microbial communities in biotechnological processes [26, 27] and to examine the impact of these communities on infections and diseases [28]. The experimental setup usually involves inoculating a bacterial population onto solid media and allowing its growth. This growth results in the formation of pseudo-two-dimensional communities with sectors that segregate subpopulations of cells. During a surface-attached range expansion, the communities exhibit some growth in the third dimension [29], primarily due to cell shoving, but the effective growth of the community occurs at the edge of the colony. When communities expand on surfaces, only the outer regions have access to the nutrients and space necessary for growth [30]. Since the population at the edge constitutes a small fraction of the total community, minor fluctuations in it can significantly impact the overall population [31]. Genetic drift, which refers to changes in the frequency of existing genes, is a direct consequence of such fluctuations [32], and can lead to the extinction of subpopulations within the community, reducing the overall genetic diversity of the system [24].

**Spatial self-organisation** *In vitro* surface-attached bacterial communities spatially self-organise into sectors with distinct subpopulations as they grow [33]. This spatial self-organisation is often quantified using the spatial intermixing parameter, which measures the number of transitions between different subpopulations of cells within the colony. High spatial intermixing indicates a high level of diversity within the community and reflects a high number of cell-to-cell interactions between subpopulations [34]. Although genetic drift impacts the self-organisation process, it is not the only influencing factor. Multiple processes counteract its stochastic effects and contribute to the spatial self-organisation of the system. For *in vitro* systems, the initial properties of the community, such as cell density and cell arrangement [35], significantly affect the intermixing patterns of the colony. Environmental factors like metabolite toxicity and resource supply also play an important role in shaping those patterns [36, 37]. However, the most important process that will counterbalance genetic drift and maintain diversity is social interactions between constituents of the community [38–40].

**Bacterial social interactions** The social interactions between bacteria can be positive, negative, or neutral. Six different synergies can be identified between two types of cells from these interactions. Mutualism is a bidirectional positive interaction where cells benefit from growing in close proximity to one another. This type of interaction has been investigated in range expansions using cross-feeding systems, where different strains or species exchange essential metabolites for growth [41, 42]. In mutualistic systems, the number of cell interactions increases, leading to a higher intermixing in spatially organised communities [43]. At the opposite end of interactions is competition, where cells experience detrimental effects from proximity to other strains or species. In range expansions, competition is prevalent as cells strive to reach the edge of the colony in order to proliferate. During this type of interaction, one subpopulation will eventually displace the others over time, reducing the spatial intermixing of the community [44, 45]. The final type of bidirectional interaction is parasitism, where one type of cell benefits from growing alongside another while the latter experiences negative effects. The resulting intermixing in parasitic interactions arises from two opposite trends: *host* cells aim to reduce their interactions, while *parasite* cells seek to increase them [46]. There are also unidirectional interactions, such as commensalism and amensalism. In commensalism, only one type of cell benefits from the presence of another without harming the latter. In amensalism, one type of cell harms the other without itself being affected. Unidirectional and neutral interactions are challenging to study during range expansions because, given the limited space and resources, cells are always in competition. As long as there is any degree of nutrient limitation, competition will occur [37].

**Experimental setups** Two-dimensional range expansions remain the most commonly used experimental setup to study the spatial arrangement of microbial communities. Research in this area has explored navigated movement by investigating chemotactic and swarming systems [47–49]. New experiments are pushing the boundaries of surface-attached range expansions, with advances enabling precise control of initial conditions through the printing of cells into droplets [50]. Current research also explores how surface-attached bacteria interact with environmental defects [51] or with other microorganisms, such as fungi [52, 53] and phages [54, 55].

**Modelling of bacterial communities** Recent studies on bacterial communities have gained insights from hypotheses generated through mathematical modelling. By simplifying the complexity of the communities sufficiently to enable computational modelling, the fundamental mechanisms driving the dynamics of the populations can be pinpointed [56]. There are multiple theoretical approaches to describe synthetic bacterial communities, which can be modelled using either continuum or individual-based models [57]. On continuum models, the community is described as a density that grows following deterministic functions, typically formulated by partial differential equations. These are best suited to describe large populations of cells where the continuum approximation is valid. Although these models are computationally efficient, they often fail to capture finer-scale phenomena, even when accounting for the stochasticity of the system. On the other hand, individual-based models describe communities by simulating the individual agents that compose them. These agents follow growth rules that describe environmental changes applied at each system update. While agent-based simulations are computationally expensive, they are well-suited to describe stochastic systems. The simulation space of the agents can be either continuum or discrete, with lattice models being a commonly used setup for the latter. In a lattice model, each site of the system has a discretised state and corresponds to either a single cell or an aggregate of cells. Furthermore, agent-based models can be coupled with continuum quantities that evolve according to partial differential equations, such as nutrient or antibiotic fields.

**Modelling applications** On many occasions, computational models are used to explain *in vitro* data. For experimental studies conducted with *E. coli*, models have successfully reproduced genetic drift observed during range expansion using both lattice models [58] and continuum models [59]. Individual-based models have also been used to describe the colonisation abilities of *E. coli* as their aspect ratio [60] or resistance to antibiotics [61] changes. When individual-based models are coupled with partial differential equations, syntrophic

interactions that maintain diverse communities have also been characterised [62]. As the key mechanisms that describe experimental data are identified, mathematical modelling allows further insight into the system by testing conditions that would be challenging to explore in an *in vitro* setup. For instance, the various social interactions between bacteria previously described can be simulated with the same agent-based model [40]. However, it would be extremely difficult to identify strains that allow for conducting all the experimental conditions analogous to those simulated.

## 1.2 Thesis motivation and outline

In this thesis, I aim to investigate unexplored systems within spatially organised bacterial communities.

The first studied system explores spatial organisation in three-dimensional conformations as *E. coli* cells grow embedded in a semi-solid matrix. Few studies focus on the morphology of self-contained microcolonies. In this research, I perform an experimental investigation complemented by simulations of simple three-dimensional isogenic colonies. Despite its apparent simplicity, the system provides relevant insights into new navigation mechanisms of cells in complex environments. By changing the environmental conditions, I investigate the direct consequences of motility on the spatial organisation of the communities.

The second system delves into social interactions between two types of cells as their spatial configuration changes. It is a collaborative project focused on competition between cells with different morphologies, here characterised by their aspect ratio. While some studies have explored the effect of cell shape in bacterial communities, none have reported the competitive advantage of slender cells as the communities transition from a batch culture to a two-dimensional community, nor have they explored the physical mechanisms underlying these phenomena. I conducted simulations that offered additional insights into the effect of cell shape in processes that require direct cell-to-cell contact when cells grow as surface-attached communities.

The third system continues to examine the effect of space on social interactions within bacterial communities. In this case, the interactions extend beyond competition to cooperation, potentially increasing the tolerance of the community to antibiotics. While higher antibiotic tolerance in spatially organised communities compared to planktonic cells has been reported, such structures have never been coupled with the study of indirect antibiotic resistance. Indirect resistance occurs when resistant cells protect sensitive cells from antibiotic stress. While this phenomenon is typically studied in batch systems, its nature depends

on the architectural arrangement of cells. I designed experiments and models to investigate indirect resistance as the cells transition to different geometries.

Overall, the thesis offers a comprehensive description of newly observed phenomena as cells interact and develop in spatial configurations, highlighting the importance of considering the self-organisation of bacterial communities when performing *in vitro* experiments.



# Chapter 2

## Motility mediates satellite formation in confined biofilms

### 2.1 Introduction

Bacteria tend to grow as dense communities in confined spaces or when adhered to surfaces [63]. These dense communities are often referred to as biofilms, a biomaterial associated with an interface. Biofilms differ from other aggregates when the aggregate of cells is held together by a self-produced extracellular matrix[64].

When bacteria form dense communities, they gain protection from local threats compared to their planktonic counterparts. For instance, the inner cells of a biofilm are shielded against environmental stresses such as toxins or bacteriophages [65, 66]. Thus, understanding biofilms is crucial from a medical perspective, as they are present in both acute and chronic infections [67]. For that reason, many biofilm studies are performed with *Pseudomonas aeruginosa* [68, 69], a rod-shaped gram-negative bacterium commonly found in infections difficult to treat [70]. *Pseudomonas aeruginosa* is not the only gram-negative bacteria that forms biofilms; *Escherichia coli* is also known to do so [71]. Biofilm studies are also conducted with gram-positive organisms such as *Bacillus subtilis* [72], and *Staphylococcus aureus* [73].

When growing attached to surfaces, biofilms follow a well-established 5-step model (represented in Fig.2.1) that applies to both gram-positive and gram-negative bacteria [74, 75]. The first step is the initial attachment to the surface, where bacteria adhere due to interactions between adhesive proteins, or fibres, and the abiotic surface. The initial attachment is unstable and, most of the time, reversible. Active motility is an important mechanism for adhering to surfaces; however, non-motile bacteria can also adhere to the surface if they exhibit strong

expression of adhesion factors. If initial adhesion persists, a signal transduction pathway will respond to the physical forces and shift gene expression towards biofilm formation. During the irreversible attachment phase, there is a reduction of flagellar expression and an increase in the expression of adhesive structures. Once the cells are irreversibly attached, the biofilm will mature. The first maturation step involves the production of an extracellular matrix while the cells form clusters. The cell clusters merge in the second maturation step to form micro-colonies with complex three-dimensional structures. The biofilm cells will eventually return to a planktonic form following dispersion. Biofilm dispersion can occur due to nutrient limitation or degradation of the extracellular matrix [76, 77].

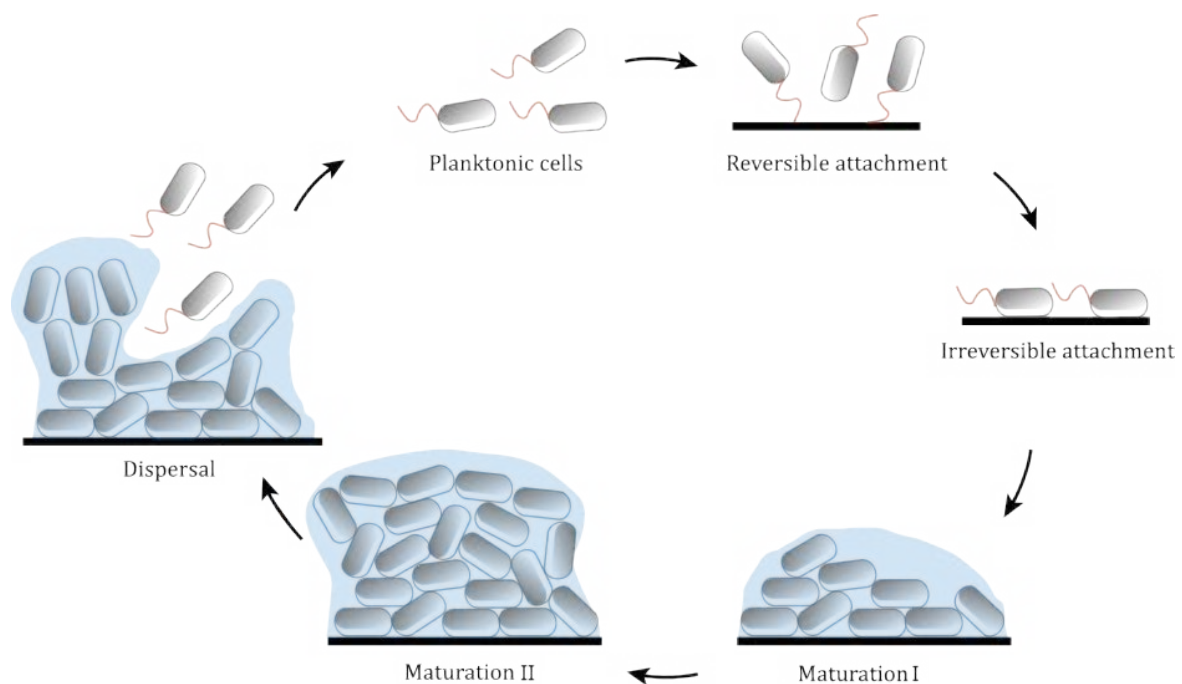


Fig. 2.1 Diagram of the 5-step biofilm model. It shows how planktonic cells attach to a surface, first irreversibly and then reversely. Once the cells adhere to the surface, the biofilm starts forming (maturation I and II) until it is fully mature and its components disperse into the environment.

Recently, there has been an expansion in the conceptual model of biofilm formation [78]. The classical 5-step model does not account for non-surface attached aggregates observed in clinical and environmental settings. In this new approach, the dispersed cells from the biofilm are still considered a part of it, leading to the concept of non-attached biofilms. These dispersed cells form aggregates that can re-enter the biofilm formation at any point. An increasing amount of interest has been placed on non-attached biofilms, and several experimental systems have been designed to study them [28].

Despite the widespread occurrence of non-attached biofilms in nature, there is a significant lack of understanding about them. This is especially true considering that these biofilms exist as three-dimensional aggregates and are anticipated to exhibit highly dynamic morphologies. Therefore, the study of three-dimensional bacterial colonies serves as a starting point to gain insight into such systems.

In *in vitro* studies where bacteria grow as dense colonies, only the cells on the outer part of the system proliferate with a doubling time similar to that in well-mixed systems. Therefore, the population increases linearly with the active surface area of the colony. Behind this leading edge, cell growth is significantly reduced due to nutrient availability and space constraints [79–81]. These limitations make cellular motility a critical mechanism to enhance the growth and invasion into the surrounding environment [82].

Motility enables bacteria to migrate towards favourable environments, such as regions with higher nutrients or lower toxins levels. Bacteria direct their motion towards favourable environments and away from harsh ones via chemotaxis[83]. Chemotactic cells present chemical pathways that detect the gradient of molecules in the environment and direct their motion according to them [84]. Bacteria can move through liquid or over moist surfaces by various mechanisms [85, 86], shown in Fig.2.2. During swimming, individual planktonic cells rotate their helical flagella to create a thrust force that propels them forward [87]. Also powered by flagella, the collective motion, referred to as swarming, leads to bacterial migration in groups of tightly bound cells across solid or semisolid surfaces. This motility requires bacteria to undergo a phenotypic transition to adopt swarming behaviour [88]. Bacteria can additionally move over surfaces via twitching, where the cells crawl by extending and retracting Type IV pili [89]. Cell movement can also occur without propulsive structures. During gliding, focal adhesion complexes enable bacteria to move over surfaces and aqueous films [90]. Lastly, passive movement can happen due to the force generated by dividing cells. Sliding of cells can be facilitated by a surfactant [23].

In low-density hydrogels ( $\approx 0.2\%$  agar) and in liquid media, swimming is the preferred motility mode for bacteria to navigate their surroundings, while chemotaxis is enhanced by nutrient shortage or attractant gradients [91–93]. However, the mechanism by which cells move in confined environments remains less understood. In medium-density hydrogels (0.2-0.6 % agar), bacteria find their movement restricted due to the decreasing pore size of the material [94]. Additionally, the chemotactic ability of the cells is impaired, leading to reduced sensing capabilities as the stiffness of the environment increases [92]. In high-density hydrogels ( $\geq 0.6\%$  agar), cells encounter a threshold that completely diminishes their motility, and chemotaxis is unlikely to play a role [95].

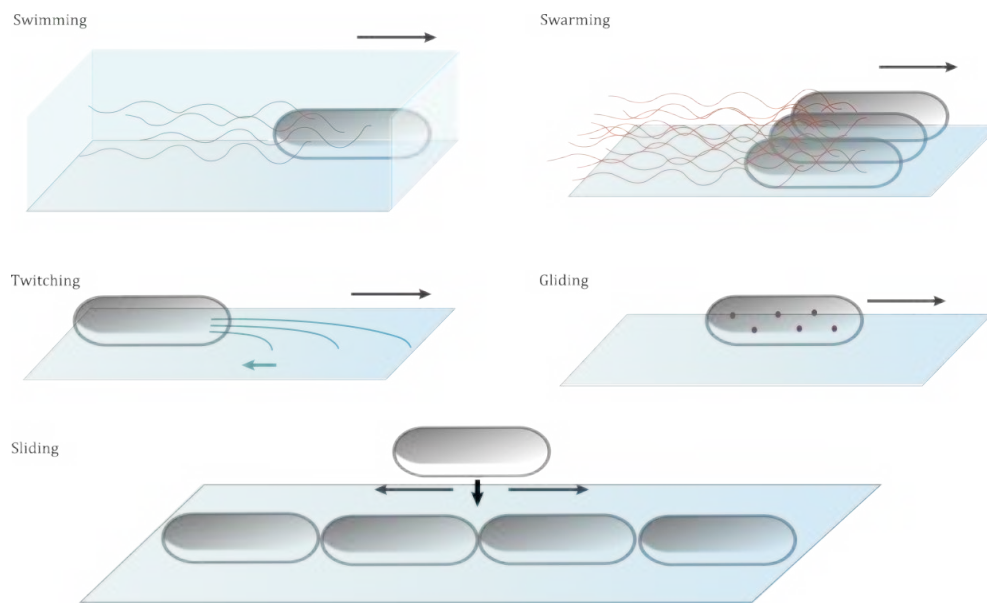


Fig. 2.2 Diagram with the five motility mechanisms described in the main text. Bacteria use flagella (orange) to propel themselves during swimming and swarming. Twitching is powered by the retraction of type IV pili (dark green). Local adhesion complexes (red) allow gliding motility. The movement of cells due to cell shoving is referred to as sliding.

### 2.1.1 Objectives

This chapter explores three-dimensional bacterial colonies formed as single motile *E. coli* (K-12) cells grow embedded within an agarose matrix. The stiffness of the environment promotes the growth of cells as dense bacterial communities, mimicking some of the characteristics of non-aggregated biofilms [96].

The 3D bacterial colonies were investigated using both experiments and agent-based simulations. The experiments were designed to explore how the stiffness of the medium influences the self-organisation and spread of the communities in the environment. Specifically, the focus was on studying the colonies at medium-density hydrogels, which reproduce the conditions found in tissues where infections caused by biofilms are prevalent. It is under said conditions that cell motility was expected to play a more important role in comparison to low and high-density hydrogels, where the cells can move freely or are completely restrained, respectively.

Seven *E. coli* K-12 mutants were studied to understand which extracellular structures control the morphology and spread of three-dimensional colonies. The mutants presented deletions in structures known to be important to biofilm formation, like flagella and type I pili.

I performed all the experiments and simulations presented in the chapter. The results led to the manuscript "Motility mediates satellite formation in confined biofilms" [97], published in The ISME Journal (Appendix: A.1).

## 2.2 Materials and Methods

### 2.2.1 Experimental Methods

**Bacterial Strains** To perform the experimental study, derivatives of the *Escherichia coli* (*E. coli*) wild-type MG1655 (K-12 F-lambda-ilvG-rfb-50 rph-1) [17] strain were used. Six mutants with deletions in structures affecting cell motility and biofilm development were selected. Detailed information about the strains can be found in Table 2.1 and references therein [98].

The non-flagellated mutant,  $\Delta fliC$  (NM109), was constructed for this study through P1 transduction by moving  $\Delta fliC::kan$  from JW1908-1 (Keio collection [99]) to MS613 and selecting on kanamycin [100]. All strains contained the plasmid pV132 [30], which carried an Isopropyl  $\beta$ -D-1-thiogalactopyranoside (IPTG) induced yellow fluorescent protein (YFP) and ampicillin (amp) resistance for selection. The plasmid [30] was transferred to the cells following a well-established transformation protocol [101–103].

Name	Strain	Relevant characteristics	Reference
wt	MS613	MG1655 K-12 (F-lambda- ilvG- rfb-50 rph-1)	[17]
$\Delta flu$	MS427	MG1655 $\Delta flu$	[102]
$\Delta fim$	MS428	MG1655 $\Delta fim$	[104]
$\Delta flu\Delta fim$	MS528	MG1655 $\Delta flu,\Delta fim$	[104]
$\Delta cps$	RMV340	MG1655 $cps::tet$	[103]
$\Delta csgAB$	RMV612	MG1655 $csgAB::kan$	[98]
$\Delta fliC$	NM109	MG1655 $fliC::kan$	This study

Table 2.1 *E. coli* strains used in the study

**Culture media** Experiments were performed with either rich or minimal medium. Luria-Bertani (LB) was the medium chosen for the high-nutrient experiments [105]. The LB medium was composed of 10 g/l tryptone (16279751, Fisher Scientific), 5 g/l yeast extract (16279781, Fisher Scientific) and 5 g/l NaCl ( $\geq 99\%$ , S9888, Sigma-Aldrich) dissolved in Millipore water.

For the low-nutrient experiments, M63 minimal medium supplemented with glucose (M63+glu) was used. M63+glu was composed of 20% 5X M63 salt, 1  $\mu\text{g/ml}$  thiamine hydrochloride ( $\geq 99\%$ , T4625, Sigma-Aldrich), 2 mM  $\text{MgSO}_4$  (63138, Sigma-Aldrich), and 2 mg/ml glucose ( $\geq 99.5\%$ , G7528, Sigma-Aldrich) dissolved in Millipore water. The 5X M63 salt solution was prepared with 15 g/l anhydrous  $\text{KH}_2\text{PO}_4$  ( $\geq 98.0\%$ , P9791, Sigma-Aldrich), 35 g/l 24 anhydrous  $\text{K}_2\text{HPO}_4$  ( $\geq 99.0\%$ , 60353, Sigma-Aldrich), 10 g/l  $(\text{NH}_4)_2\text{SO}_4$  ( $\geq 99.0\%$ , 09978, Sigma-Aldrich), 2.5 ml 20 mM  $\text{FeSO}_4$  ( $\geq 99.5\%$ , 44970, Sigma-Aldrich), 20mM Na-Citrate ( $\geq 99.5\%$ , 71402, Sigma-Aldrich).

**Growth rate measurements** *E. coli* strains were grown overnight at  $37^\circ\text{C}$  while shaking in either LB or M63+glu medium supplemented with ampicillin (100  $\mu\text{g/ml}$ ). In the next morning, the samples were 1000x diluted in fresh medium without antibiotics. The initial optical density at 600 nm ( $\text{OD}_{600}$ ) of the diluted sample was measured. Once the incubation started (at  $37^\circ\text{C}$ ), the  $\text{OD}_{600}$  was measured every hour for 6 hours in total. All the  $\text{OD}_{600}$  measurements were performed using an IMPLLEN Nanophotometer C40.

**Swimming Assay** Prior to experimentation, 96 mm Petri dishes with 25 ml of either LB or M63+glu were prepared at multiple agarose (11404, SERVA) concentrations: 0.2 %, 0.3 % and 0.4 % (w/v), without antibiotics. In parallel, strains were grown overnight with shaking ( $37^\circ\text{C}$ ) in LB supplemented with ampicillin (100  $\mu\text{g/ml}$ ). The dishes were left to dry for 18h at room temperature before inoculating 1  $\mu\text{l}$  of saturated cultures at the centre of each dish. The culture droplet was placed on top of the agarose substrate. After 24h of incubation ( $37^\circ\text{C}$ ), the diameter of the range expansions was measured.

**3D bacterial colonies** *E. coli* strains were grown overnight ( $37^\circ\text{C}$ ) while shaking in LB medium supplemented with antibiotic (amp, 100  $\mu\text{g/ml}$ ) until saturation, reaching an  $\text{OD}_{600}$  of approximately 4. Then, three consecutive thousand-fold dilutions were performed to obtain a solution with a concentration of  $\approx 10^3$  cells/ml. The cells were embedded in a transparent, semi-dense matrix using the following procedure. First, the medium with 0.2-0.4% (w/v) agarose (11404, SERVA) was melted using a microwave, taking care to prevent evaporation. It was then shaken rigorously to ensure a homogeneous mixture. To minimise heat-induced ageing [106] and evaporation of water, a new 25 ml bottle of media was used for each experiment. Secondly, the melted media with different agarose concentrations were aliquoted into 1 ml Eppendorf tubes and placed in a block heater pre-warmed at  $55^\circ\text{C}$  [107]. After 20 min, once the Eppendorf tubes containing the media had reached a stable temperature of  $55^\circ\text{C}$ , they were supplemented with ampicillin (100  $\mu\text{g/ml}$ ) and IPTG (0.5mM) for induction

of the fluorophore. Then, 10  $\mu\text{l}$  of the solution of  $\approx 10^3$  cells/ml was added to the media, and the content of the Eppendorf tube was quickly poured out into a glass-bottomed Petri dish (WillCo HBST-5040). It was important to pour the content as fast as possible to prevent cells from receiving a heat shock and avoid gelification of the media. After a few minutes, the media solidified, and each Petri dish presented  $\approx 10$  embedded cells ( $\approx 10$  cells/ml). To have colonies of comparable size, the incubation time at 37°C changed depending on the media used since the growth rates of the cells are dependent on it (Fig: 2.3). For LB, the plates were imaged after 13h, while for M63+glu, the incubation time was increased to 15h.

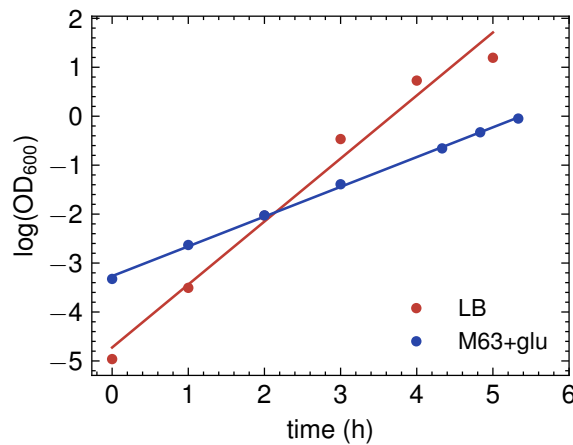


Fig. 2.3 Growth curves for the parental strain (wt). The plot shows the experimental data (circles) and the exponential fit (full lines). The doubling time is found with equation 1.1 where  $\lambda$  is the slope of the growth curve (full lines). The resulting doubling times are 27.8 min in rich medium (LB) and 68.4 min in minimal medium (M63+glu).

When 1 ml was poured into the Petri dish, the resulting gel had a thickness of less than 400  $\mu\text{m}$ . Such a thin layer limited the radius of the colonies to sizes smaller than 200  $\mu\text{m}$  in radius, but it also ensured that there was not any oxygen depletion [108] or different growing conditions between cells at different points of the matrix. It was checked that no correlation existed between the number of satellites and the z-position of the centre of the colony.

If some of the colonies grew too much, they started spreading on top of the dish (as two-dimensional communities), and as the gels presented low agarose concentrations, the colonies occupied a great surface area of the plates. Therefore, the plates where these events happened were discarded to ensure that the other colonies were not growing under depletion of nutrients.

To determine if the observed results were only exclusive to agarose, the gelling material was swapped to agar (10455513, Fisher Scientific). Using the same concentrations of agar and agarose led to environments of different stiffness, as agar gels were less stiff than agarose

ones [109]. The protocol to grow colonies with agar was similar to the one for agarose, with the exception of the range of concentrations (w/v) explored. For agarose, the range used was 0.2-0.4 % (w/v), and for agar was 0.4-0.6 % (w/v). The main results observed at 0.3 % agarose were reproduced at 0.5 % agar (Fig. 2.4).

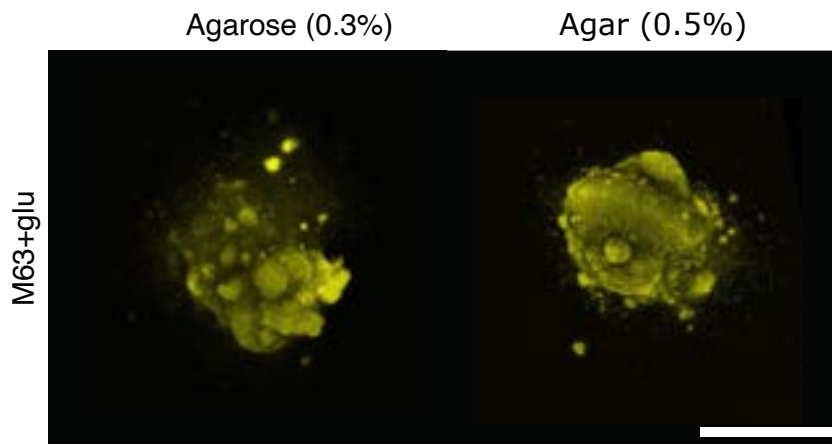


Fig. 2.4 Mature 3D colonies of the (wt) strain in agarose (0.3%) and agar (0.5%). The colonies were incubated under the same conditions in M63+glu for 15 hours at 37°C. The difference in polysaccharide concentration ensured that the cells grew under approximately the same environmental stiffness. The scale bar corresponds to 200  $\mu\text{m}$ .

**Image acquisition** Mature 3D colonies were imaged with a laser-scanning confocal microscope (LSCM, Leica, SP5) using a 20x air objective (Nplan, L20x, 0.40corr  $\infty$ ). The objective provides a (x,y)-resolution of 1.52  $\mu\text{m}$ . The yellow fluorescent protein (YFP) was excited with an argon laser at 514 nm, and its emission was collected around  $550 \pm 30$  nm. To reconstruct the 3D structures, z-stacks that captured the whole colony with a z-resolution of 1.33  $\mu\text{m}$  were collected. Each colony presented the order of 100 z-stacks, and its imaging time was measured in minutes.

An inverted microscope (Nikon Eclipse Ti fluorescent) was used to image the time evolution of the colonies. The microscope was paired with a camera (Andor, Belfast, UK), and for consistency, a 20x air immersion objective (Span fluor, L20x, 0.45-corr  $\infty$ ) was chosen. In this setup, the YFP was excited with a mercury-vapour lamp,  $500 \pm 20$  nm, and the emission was collected at  $535 \pm 30$  nm. The inverted microscope was chosen for the time-lapse movies to reduce the bleaching of the samples and phototoxicity. To estimate the change of colony radius over time, the frequency of imaging was set to 40 minutes. For the time-lapse movies, an image was taken every 50 minutes.

**Image processing** The 3D colonies had a diameter of approximately  $200\ \mu\text{m}$ . Since LSCM has a penetration depth of around  $100\ \mu\text{m}$  [110], the half of the colony farthest from the z-imaging direction experienced significant distortions. Consequently, the image analysis was limited to half of the colony. To choose the area of interest, a custom-made Fiji [111] routine was developed to crop the z-stacks once the colony began to look distorted. The following points of the image analysis were performed using BiofilmQ [112]. First, the colony was thresholded following the Otsu method [113]. Then, outlier voxels of clusters smaller than  $11\ \mu\text{m}^3$  were removed to reduce background noise (Fig.2.5). Lastly, the following parameters provided by BiofilmQ were exported for analysis: convexity, number of colonies, volumes, and distances. Two different distances were chosen: between a satellite and the centre of mass of the colony and between a satellite and its nearest neighbour.

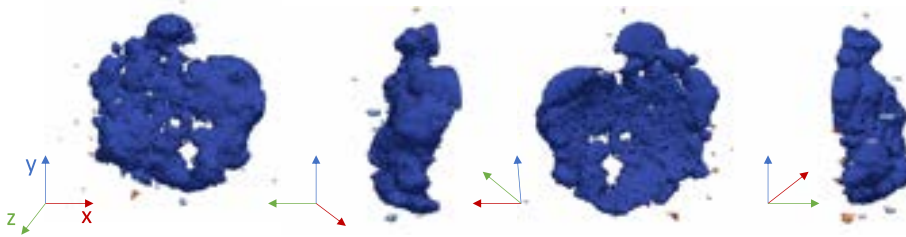


Fig. 2.5 Thresholded experimental half-colony. After thresholding and removing the noise from the experimental stacks using BiofilmQ, the colony was saved as a .vtk file and visualised using the software ParaView.

### 2.2.2 Computational methods

A modified Eden growth model [114] was developed in order to reproduce the key features of the experimental colonies. A 3D cubic lattice (of size  $L$ ) was defined where each of the sites could be, at most, occupied for one cell. Each cell had then six neighbouring sites; if at least one of them were available, the bacteria would grow at rate  $k$ . If a cell presented three or more neighbouring sites available, it would mean that it was located in the outer part of the community. Therefore, in addition to the growth, the cell could move to a different lattice site. This movement was implemented through jumps to random locations that did not have any cells at rate  $k_s$ .

The evolution of the colony was implemented by counting the number of cells that could only grow ( $N_1$ ) and those that could divide and move ( $N_2$ ) and updating the system following a Gillespie algorithm [115]. The simulation was initiated by placing a single cell at the centre of the lattice ( $L/2, L/2, L/2$ ), and then the following steps were iterated:

1. Find the total number of cells in the system and count their available nearest neighbours. Cells with more than three empty neighbouring sites belong to population  $N_2$ ; otherwise, they belong to population  $N_1$ .
2. Find the expansion surface of the colony by defining an array that contains all the available growing positions (free neighbouring sites).
3. Find the total event rate  $T$  as the sum of all the possible events:  $T = N_1 \cdot k + N_2 \cdot (k + k_s)$ . Find the duration of the event as  $\tau = -\ln(r)/T$  where  $r$  is a random number from a uniform distribution ( $r = U \subseteq (0, 1)$ ). Increase the simulation time by  $\tau$ .
4. Draw a random number,  $a$ , from a uniform distribution between zero and one ( $a = U \subseteq (0, 1)$ ) and determine which event will happen as:
  - (a) If  $a > (N_1 + N_2) \cdot k/T$ , a growing event occurs. A random element of the surface of the colony is chosen, and a new cell is added to that position.
  - (b) Otherwise, a swimming event happens. A random cell from the  $N_2$  population is chosen. The new position of the cell is determined by choosing three random Gaussian numbers of zero mean and standard deviation  $\sigma$ . If the given numbers provide an empty position, the cell position is updated. If the new position is already occupied by another cell, three new random numbers are thrown until an empty position is found.
5. Return to (1).

As a result, the simulations gave a 3D lattice that could be visualised as a binary image. The resulting *in silico* colonies were analysed using an analogue procedure to the one previously described for the experimental colonies. The only difference was that the binarisation step was unnecessary, as the colonies were already in binary form. The simulations also generated a complete colony. To align better with the experimental results and account for the limitations encountered when imaging a thick sample, half of the colony was cropped, and the analysis was performed only in this portion of the aggregate.

## 2.3 Results

### 2.3.1 Satellite colonies form around three-dimensional colonies

*E. coli* MG1655 wild-type (wt) single cells were embedded in a semi-dense matrix composed of M63+glu and 0.3% agarose following the methodology previously described in section 2.2.1. Confined mono-clonal quasi-spherical colonies emerged after 15 h of incubation at 37 °C. The colonies were smaller than 200  $\mu\text{m}$  in diameter due to the physical constraints of the experimental system and the slower growth of the cells compared to batch systems. The isolated cell started growing exponentially, but as the dense colony began to form (within 3 hours), the growth of the community transitioned to a linear trend over time (Fig:2.6).

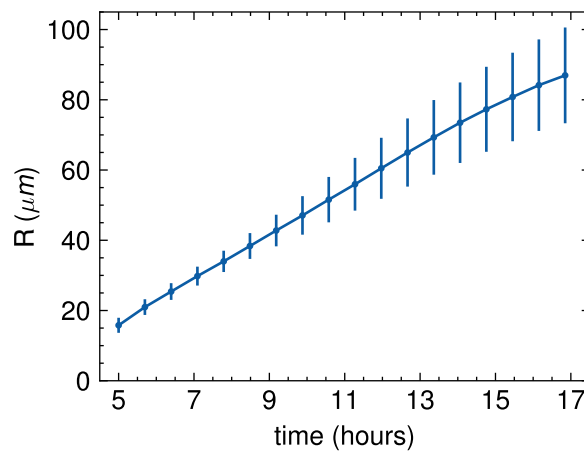


Fig. 2.6 Radial expansion for a 3D colony of the parental strain (wt). The colony radius (R) versus time is obtained by tracking the colonies in a minimal medium (M63+glu) at an intermediate agarose concentration (0.3%). The full line is the average of eight samples, and the error bars correspond to the standard deviation of the sample.

The wt cells were additionally embedded at the same agarose concentration (0.3%) in a rich nutritional medium, LB. The incubation time in LB was reduced to 13h to accommodate for variations in growth rates under different conditions (Fig: 2.3). After imaging, two distinct colony morphologies were observed: wt- and wt+. These morphologies emerged in the same wells across both low and high-nutritional media. The 3D colonies categorised as wt- grew as compact quasi-spherical aggregates with small protrusions, as illustrated in the first column of Fig.2.7. For most of the colonies (34/40 for M63+glu and 17/18 for LB), the small protrusions appeared to detach from the main colony and started to grow as small independent satellite colonies (Fig. 2.7). Colonies that exhibited satellites were referred to as wt+.

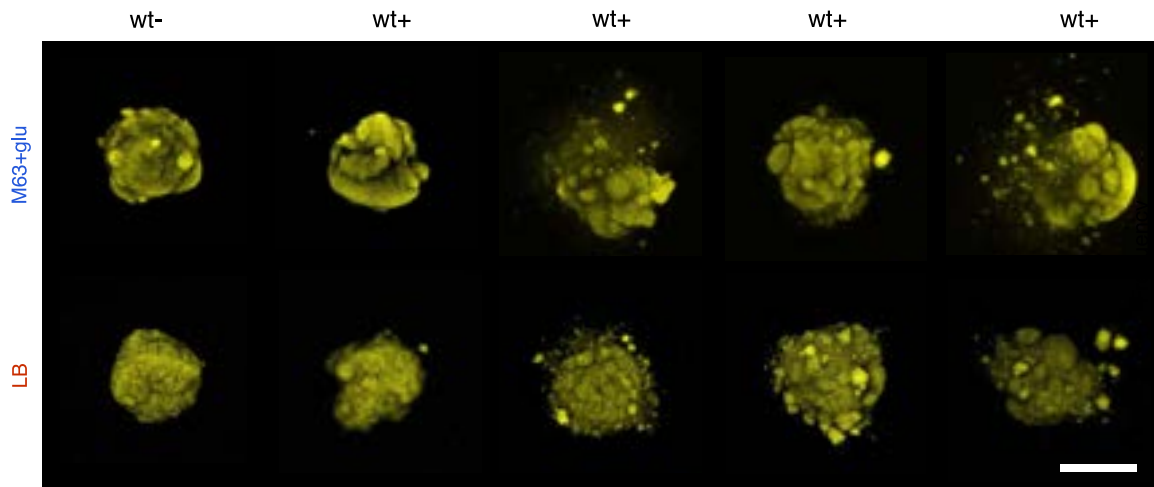


Fig. 2.7 Maximum intensity projections of three-dimensional colonies of wt in 0.3% agarose and minimal (M63+glu) or rich medium (LB). The image shows the two distinct observed morphologies: colonies that present satellites (wt+) and colonies that grow as single aggregates (wt-). The scale bar corresponds to 200  $\mu\text{m}$ .

To investigate whether the observed morphologies were exclusive to growth in an agarose matrix, the experiments were replicated for cells embedded in a minimal medium with 0.5% agar. Both morphologies were also observed at 0.5% agar (Fig.2.8). The wt+ (21/39) morphology showed a slightly higher prevalence compared to wt-.

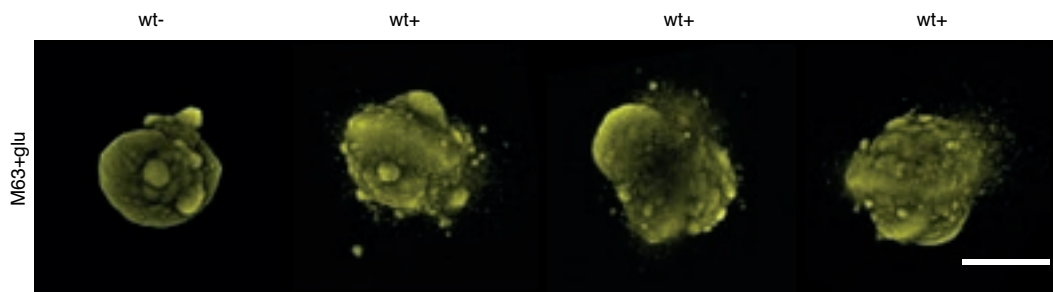


Fig. 2.8 Maximum intensity projections of three-dimensional colonies of wt in 0.3% agarose and minimal (M63+glu) medium. The image shows the two distinct observed morphologies: colonies that present satellites (wt+) and colonies that grow as single aggregates (wt-). The scale bar corresponds to 200  $\mu\text{m}$ .

From the colonies exhibiting the wt+ morphology imaged at 0.3% agarose, the following quantities were measured (see section 2.2.1): number of satellites, volume of satellites, distance satellite-main colony and main colony volume (Fig. 2.9). In both media, colonies with less than 10 satellites were more prevalent. The typical volume of satellites ( $<10^3 \mu\text{m}^3$ ) and the prevalence of smaller satellites were shared across both nutritional media.

However, the main aggregate volume was significantly different between media,  $(1.3 \pm 0.6) \cdot 10^6 \mu\text{m}^3$  for M63+glu and  $(4 \pm 1) \cdot 10^6 \mu\text{m}^3$  for LB. The distance between satellites and the main colony exhibited a longer tail in minimal medium, although the main values of the distributions were comparable for both media.

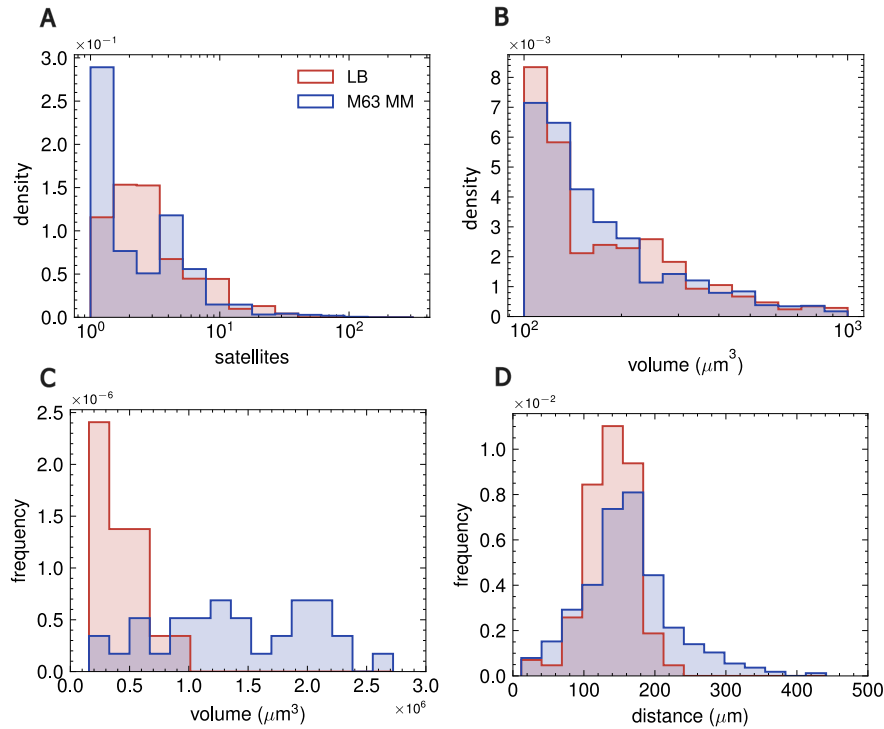


Fig. 2.9 Quantification of 3D wt+ colonies at 0.3% agarose. **A:** Distributions of the number of satellites pr. colony (log-scale) in either LB ( $N = 17$ ) and M63 + glu ( $N = 34$ ). **B:** Distributions of satellite volumes (log-scale) in either LB ( $N = 149$ ) or in M63 + glu ( $N = 574$ ). **C:** Distribution of volumes of the main colonies in either LB ( $N = 17$ ) and M63+glu ( $N = 34$ ). **D:** Distributions of distances from the centre-of-mass of satellites to the centre-of-mass of the main colony in either LB ( $N = 17$ ) and M63 + glu ( $N = 34$ ).

The analysis of the wt+ colonies showed that satellite emergence was a consistent phenomenon across both nutritional media. However, the mechanism behind their formation remained elusive. Satellites appeared far from the main aggregate, suggesting that their formation was not only a result of cell-cell interactions during growth but also involved cell motility. It appeared that a few cells could detach from the main colony and migrate to a different part of the matrix. As these cells began to grow in their new location, they formed a satellite colony, thereby colonising new space. If the hypothesis were correct, it would imply that when imaging the mature colonies, individual cells should be observed navigating the environment around the main aggregate before they begin to grow.

The resolution of the 20x objective was too small to resolve single cells, so some colonies were imaged with a 63x objective. Zooming in on the edge of the colony allowed us to test the previous hypothesis. When imaged with the 63x objective (Fig.2.10), single cells and small aggregates that were not resolved with the 20x were observed, indicating that cell detachment was more frequent than satellite formation.

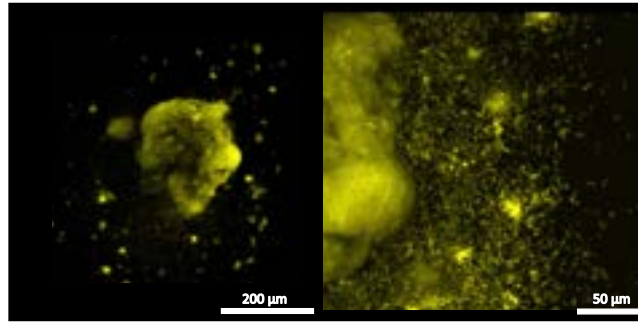


Fig. 2.10 Maximum intensity projection of a wt+ colony in minimal medium (M63+glu) and 0.3% agarose imaged at 20x and 63x. At 20x, it seems that the colony has a smooth edge and is surrounded by satellites. The 63x objective reveals that the transition is not that smooth and that the main aggregate is surrounded by individual cells that have left the main colony but haven't started to grow as satellites.

To understand satellite formation further, it was investigated how their emergence depends on the density of the substrate and different bacterial surface structures important for motility and adhesion processes.

### 2.3.2 Deletion of extracellular structures causes loss of satellite morphology

Cell envelope components are complex, and their interaction with the substrate-matrix is still not fully understood. However, this interplay cannot be overlooked [116, 117]. In surface-attached colonies, cell-adhesive structures like fimbria modulate the morphology of the colony [118]. A collection of six mutants lacking diverse structures, described in Tab.2.1, was investigated. The deleted structures were flagella, type I pili, colanic acid, curli fimbriae, and antigen 43 (Fig.2.11). Three-dimensional colonies of each mutant were obtained as they grew in M63+glu at 0.3% agarose. Flagella are helical filaments responsible for bacterial locomotion mechanisms such as swimming and swarming [88]. Additionally, flagella play a role in initial surface colonisation in biofilms and in cell-cell interactions [119, 120]. However, their role in more complex environments remains largely not yet understood [121]. The non-flagellated mutant,  $\Delta$ fliC, exhibited all (N=21) their 3D colonies without satellites.

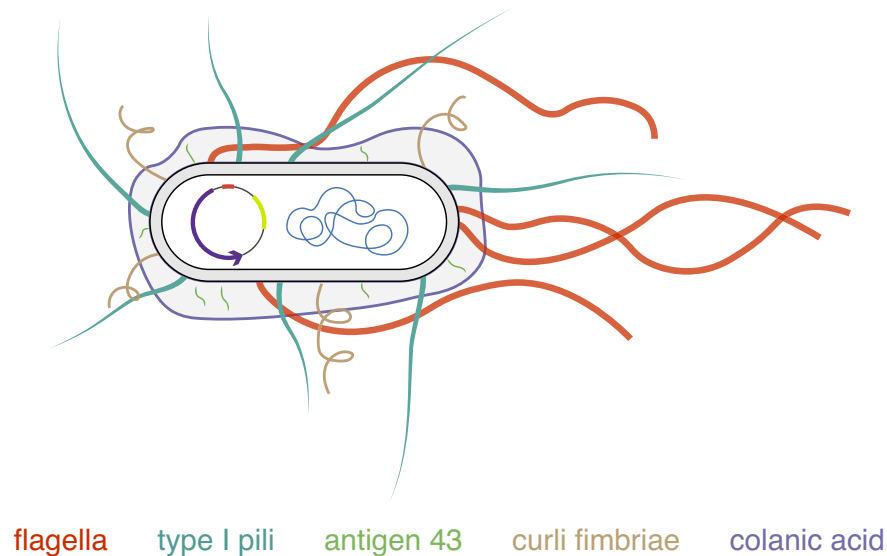


Fig. 2.11 Sketch of an *E. coli* cell and the structures deleted in the mutants used in the study. The sketched elements include (not to scale) the genome, the fluorescence-carrying plasmid and the extracellular structures: flagella (red), antigen 43 (beige), type I pili (dark green), curli fimbriae (light green), and colanic acid (purple).

Pilus (fimbria) are hair-like appendages involved in multiple processes, such as bacterial conjugation. In this study, a mutant,  $\Delta\text{fim}$ , that did not express type I pili was investigated. Type I pili are crucial for cell-cell adhesion and the maturation of biofilms [119]. Another structure important for cell-cell adhesion is antigen 43. Antigen 43 is an auto-transporter *handshake* protein found in high copy numbers in bacterial cells (up to 50.000 pr. cell [122]). A mutant,  $\Delta\text{flu}$ , with a deletion in the gene encoding this *handshake* protein, was used in the study. An inverse regulation between type I pili and antigen 43 has been reported. [123]. Therefore, a double-mutant,  $\Delta\text{flu}\Delta\text{fim}$ , was included in the study. None of the colonies of the mutants (N=21 for  $\Delta\text{flu}$  and  $\Delta\text{fim}$  and N=22 for  $\Delta\text{flu}\Delta\text{fim}$ ) presented satellites.

There are adhesion-related structures that are predominantly expressed at room temperature (25°C), such as EPS colanic acid and curli fimbriae [124, 125]. A mutant lacking colanic acid ( $\Delta\text{cps}$ ) and a mutant lacking curli fimbriae ( $\Delta\text{csgAB}$ ) were used in the study. All the colonies of both mutants (N=17 for  $\Delta\text{cps}$  and N=18 for  $\Delta\text{csgAB}$ ) had wt- morphology. As the 3D colonies were incubated at 37°C, it remains unclear whether the structures were being expressed at all. In summary, the wt+ morphology was lost for all the investigated mutants (Fig.2.12).

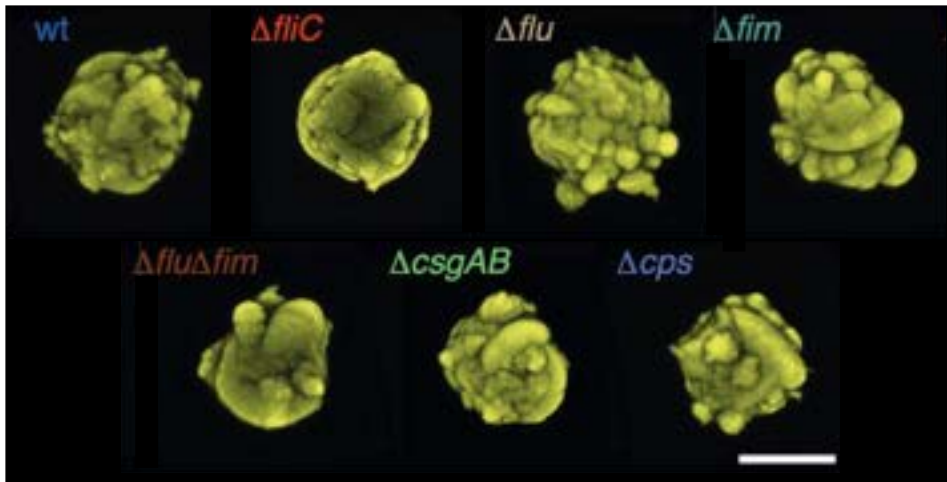


Fig. 2.12 Maximum intensity projection of the 3D colonies of the mutants in minimal media (M63+glu) and 0.3% agarose. None of them presented satellites. The scale bar corresponds to 200  $\mu\text{m}$ .

### 2.3.3 Motility is reduced when extracellular structures are deleted

The initial hypothesis behind satellite formation was that some cells were able to detach themselves from the main aggregate to navigate the environment. How motile a cell is must be a key parameter for satellite formation. Apart from the non-flagellated mutant, where the absence of satellites was anticipated, it was unexpected to find that none of the other five mutants exhibited satellite morphology either.

To understand why wt+ morphology was lost, motility assays were conducted at low agarose. The assays were repeated for three different agarose concentrations (0.2%, 0.3% and 0.4%) in both LB and M63+glu.

At the lowest agarose tested, 0.2%, the parental strain (wt) was the fastest in both media, Fig.2.13, and all the strains except  $\Delta\text{fliC}$  exhibited motility. It is important to note that there were significant differences in speed between strains, particularly in LB, where the wt strain covered a distance approximately three times greater than the second fastest strain,  $\Delta\text{cps}$ . At higher substrate stiffnesses (0.3% and 0.4% agarose), the average travelled distances were significantly reduced for all strains, with only the parental strain exhibiting movement.

The difference between the maximum distances reached by the wild-type strain (wt) in each medium ( $14.3 \pm 3.7$  in M63+glu and  $87.5 \pm 11.4$  in LB at 0.2% agarose) was consistent with findings from previous studies. Flagella production is linked with a high metabolic cost [126, 127]. Therefore, it was expected that lower nutritional media would result in reduced flagellar production and, consequently, less movement.

The motility assay showed that all the tested mutants presented reduced motility compared to the wt strain. This result aligns with the hypothesis that satellite colonies form as a consequence of how motile cells are when the environment imposes a mechanical limitation.

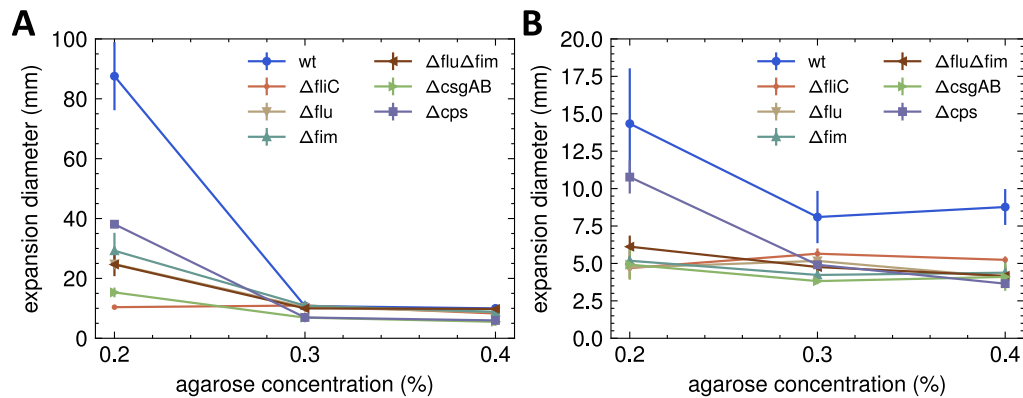


Fig. 2.13 Motility assay in low-density agarose. Expansion diameters (mm) after 24 h of incubation vs agarose concentrations in LB (A) and M63 + glu (B) for the six mutants and the parental strain.

### 2.3.4 Density of the substrate matrix controls satellite emergence

If satellite formation was indeed influenced by the motility of cells under different environmental conditions, it was worth studying how the emergence of satellites changed as the mechanical limitations of the substrate were altered. The investigation was only conducted with two strains: the one exhibiting the highest motility (wt) and the one expected to present reduced motility due to the deletion of flagella ( $\Delta$ fliC). The 3D colonies were grown in both nutritional media (LB and M63+glu), with the agarose concentration varying from 0.25% to 0.35%.

At 0.3% agarose, the previously reported morphologies were observed: high prevalence of wt+ morphology for the parental strain and no satellite morphology for the non-flagellated strain (Fig.2.14). When the agarose concentration was reduced to 0.25%, the parental strain satellite morphology was lost in both media. Instead, a general dispersion of cells within the matrix was observed. At a higher agarose concentration (0.35%), satellite morphology was also lost for wt, and all colonies appeared as single aggregates. In contrast, the non-flagellated strain consistently grew as a single compact aggregate. However, at lower agarose, it was noticeable that the force that the matrix generated over the cells was reduced, allowing them to grow with a more convoluted surface.

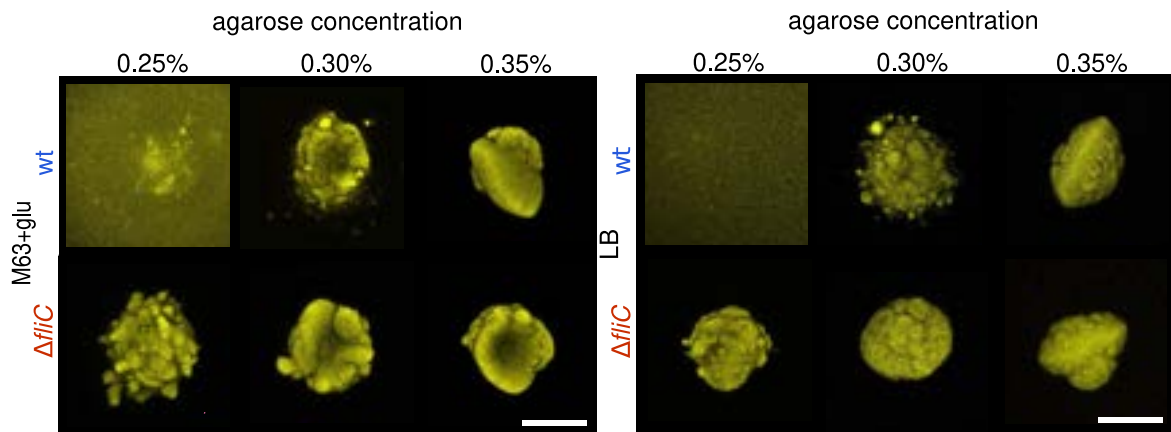


Fig. 2.14 Maximum intensity projections of 3D colonies of the parental (wt) and the flagella mutant ( $\Delta$ fliC) colonies. The colonies were grown in either minimal (M63+glu) or rich (LB) medium at three different but close values of agarose concentrations (0.25, 0.3 and 0.35 %). The scale bar corresponds to 200  $\mu$ m.

In both strains, a smoother colony surface was observed as the agarose concentration increased. At 0.35% agarose, it was possible to observe some oblate colony shapes. This colony shape was a direct consequence of the stiffness of the environment. In agreement with other studies [128], all the 3D colonies present an oblate shape when growing at agarose concentrations higher than 0.4% (Fig. 2.15). This oblate shape has been suggested to arise due to the stiffness contrast between the bacterial community and the environment, which generates a force that promotes internal cell ordering [95].

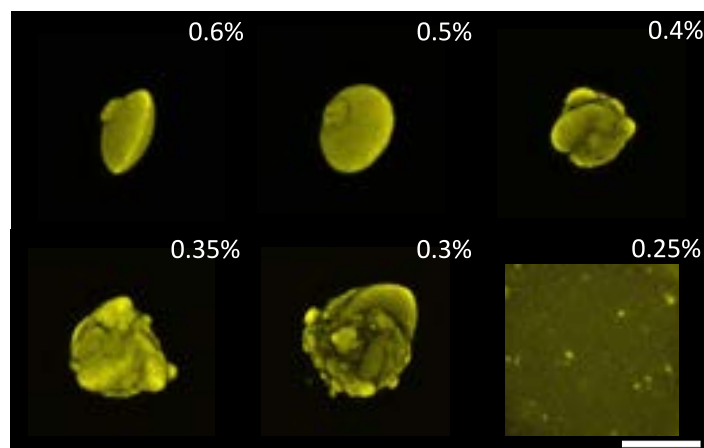


Fig. 2.15 Maximum intensity projections of wt colonies grown in M63+glu at six different agarose concentrations. At low agarose concentrations (0.25%), the cells spread in the medium without forming aggregates. As the agarose concentration increases, the surface of the colony becomes smoother, and the morphology of the aggregate transitions to an oblate shape (0.5-0.6%). The scale bar corresponds to 200 $\mu$ m.

Our findings suggest that satellite morphology represents a transitional state between two states: one in which cells are tightly confined by environmental forces and another in which cells can spread freely within the matrix.

### 2.3.5 Satellite formation speeds up colonisation

The experimental data pointed to satellite formation as a consequence of growth and events where cells move far from the initial colony. A simple mathematical model of colony growth was proposed to reproduce the satellite morphology of the 3D colonies. The model allowed further study of the experimental system and understanding of how this expansion mode can contribute to the colonisation of the environment.

The model was a modified version of the Eden growth model, where cells were not only allowed to grow but also swim if they were located on the surface of the colony. The model is described in detail in the methods section (chapter 2.2.2). The timescale of a swimming event was considered to be much shorter than the time between two cell divisions. Therefore, instead of simulating the whole swimming trajectory of the cells, the swimming event was implemented as a dispersal jump to a final position.

Two parameters essentially controlled the model. The first one was the rate of swimming  $k_s$  compared to the rate of dividing  $k$ , which was set to unity for simplicity. The second one was the standard deviation  $\sigma$  of the Gaussian distribution that the final cell positions followed. The simulations were run until a million division/swimming events were performed. Considering that one lattice site corresponded to one cell of  $\approx 1 \mu\text{m}^3$  in volume and that the colonies were compact, each simulation provided a colony of approximately  $100 \mu\text{m}$  in diameter.

The *in silico* colonies were obtained for  $k_s \in \{2, 5, 7, 10\}$  and  $\sigma \in \{0.001, 0.05, 0.1, 0.2\}$ . At low jump frequencies and short jump distances, the colonies looked like a compact aggregate with smooth surfaces (Fig. 2.16). As the swimming distances increased (higher  $\sigma$ ), small protrusions appeared on the surface, leading to satellite breakouts. The number of satellites also increased as the swimming frequency ( $k_s$ ) increased. When both parameters reached the highest value tested in the simulation ( $k_s=0.2$  and  $\sigma = 10$ ), the colonies no longer looked like a compact aggregate. The system presented many small colonies growing close to others, mimicking the spread of cells observed at low agarose concentrations (Fig. 2.15).

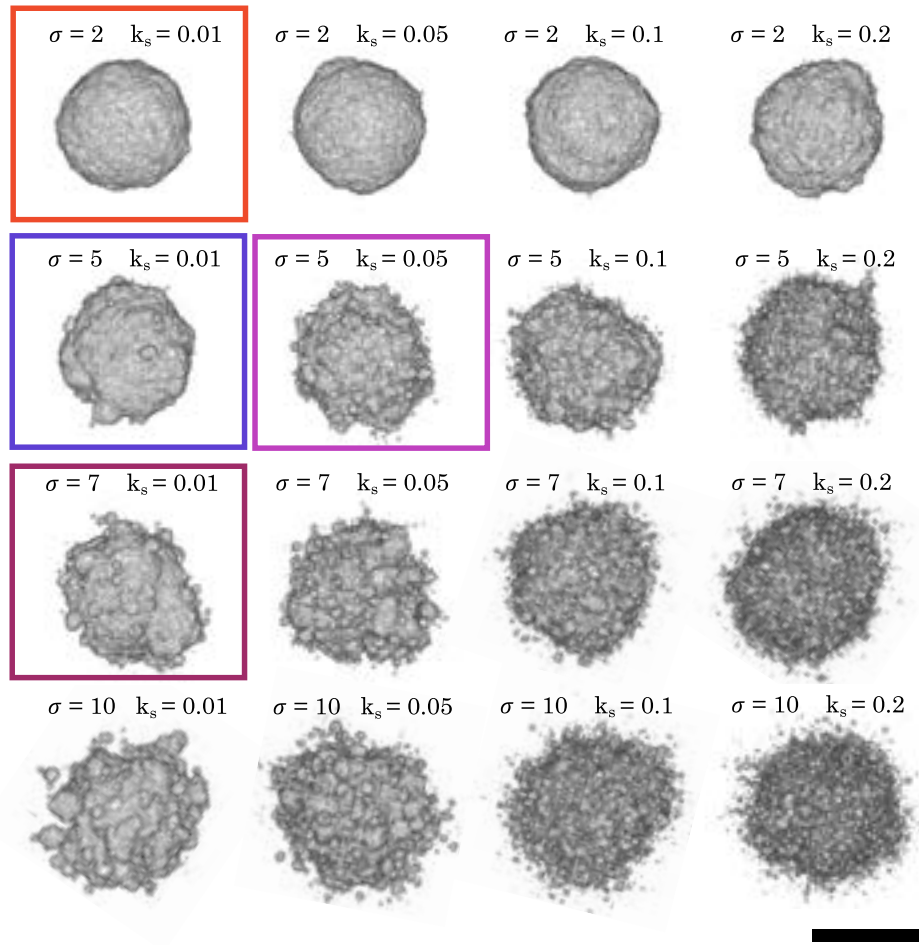


Fig. 2.16 Effect of frequency,  $k_s$ , and distance,  $\sigma$ , of jumps in the simulations of 3D colonies after  $10^6$  division/jump events. As both quantities increase, the number of satellites increases. At the maximum values tested, the structure no longer resembles a colony with satellites but rather numerous small colonies growing closely together. The scale bar corresponds to 100 pixels.

The marked colonies in Fig. 2.16 were analysed following the method previously described in section 2.2.2. The colonies obtained with  $\sigma = 2$  and  $k_s = 0.01$  were excluded as they did not present wt+ morphology. The analysis was performed for 30 repetitions per condition ( $N=30$  for  $\sigma = 5 - k_s = 0.01$ ,  $\sigma = 5 - k_s = 0.05$  and  $\sigma = 7 - k_s = 0.01$ ) considering that one lattice site corresponded to  $1 \mu\text{m}^3$ . The trends of the parameters (Fig. 2.17) followed those obtained for the *in vitro* colonies (Fig. 2.9). The number of satellites remained low, and those with higher prevalence were those smaller than  $10^3 \mu\text{m}^3$ . The main aggregate size did not reproduce the difference observed for both nutritional media; rather, they appeared the same for all the analysed conditions. Lastly, the distance from the satellite to the colony was smaller than the ones reported for the experiments.

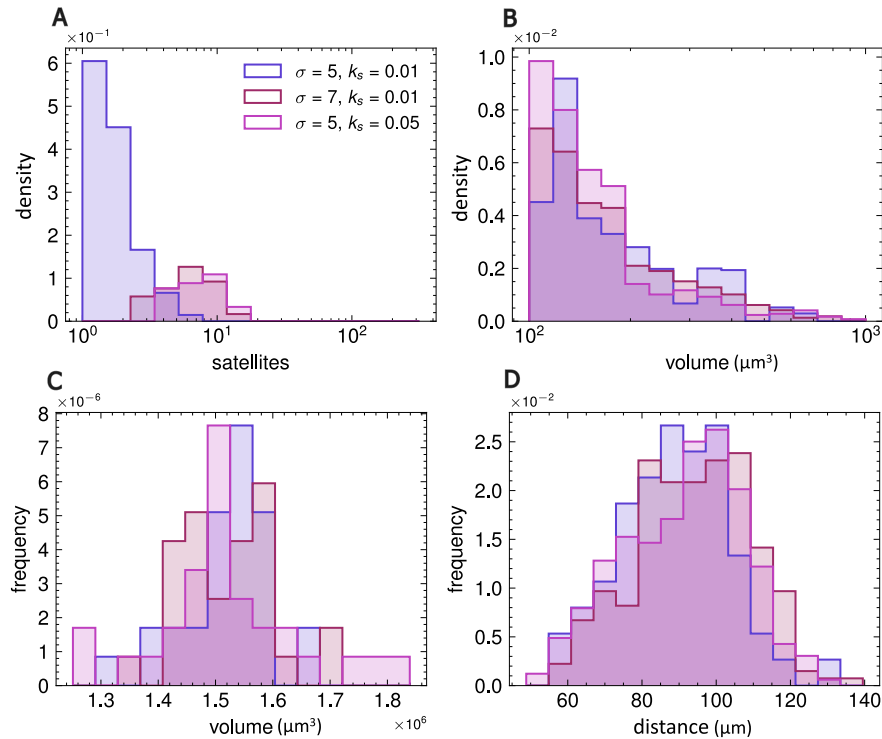


Fig. 2.17 Quantification of *in silico* colonies ( $N=30$ ) for 3 different sets of  $\sigma$  and  $k_s$ . Each lattice site corresponds to  $1 \mu\text{m}$ , and the colour-coding is the same as in Fig.2.16 **A**: Distributions of the number of satellites pr. colony (log-scale). **B**: Distributions of satellite volumes (log-scale) **C**: Distribution of volumes of the main colonies **D**: Distributions of distances from the centre-of-mass of satellites to the centre-of-mass of the main colony.

In the experimental setup, it was a challenge to obtain time-evolution of the 3D colonies. The model allowed the study of how the colonies changed over time. Keeping track of the number of cells over time for the *in silico* colonies, it became clear how the colonies with wt+ morphology grew faster than those without any satellites ( $\sigma = 2$  and  $k_s = 0.01$ ), Fig.2.18. Hence, these results predict that satellite outbreaks speed up the colonisation of the substrate. As previously described, bacterial populations under dimensional constraints exhibit initial exponential growth, followed by a linear expansion phase. During this phase, only the outer region of the colony has sufficient access to space and nutrients for reproduction. When a cell moves to a different location within the matrix and initiates growth, there is a brief period during which the population undergoes exponential growth. Therefore, having more satellites increases the rate at which a population originating from a single cell can expand.

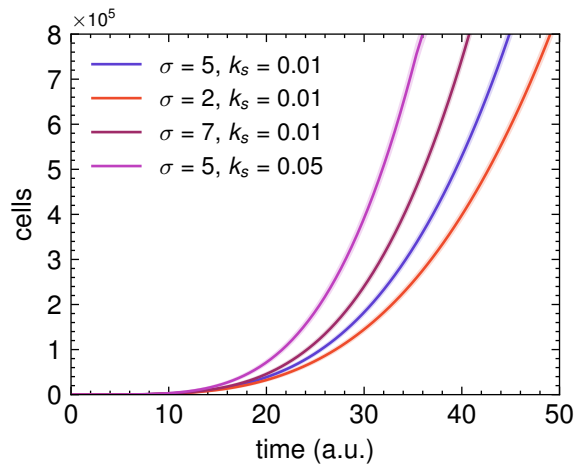


Fig. 2.18 Time-evolution of the *in silico* colonies coloured in Fig. 2.16. Each line corresponds to 25 samples, and the time is defined as in chapter 2.2.2. The shaded region corresponds to the standard deviation of the samples.

## 2.4 Discussion

In liquid media and at low viscosities, bacteria propel themselves using flagella, following the run-and-tumble model [85]. However, the mechanisms bacteria employ to navigate visco-elastic media remain largely unclear. A recent experimental study by T. Bhattacharjee et al. [94] tracked the trajectories of single cells migrating through a porous medium. The study found that bacterial velocity is highly dependent on the pore size of the environment. This result aligns with several theoretical studies [129–131] that showcase how the maximum speed of cells decreases as they collide with objects, which experimentally corresponds to a reduction in the pore size of the environment. When being inside a hydrogel, bacterial movement can be described as a combination of two processes. The cells will alternate movement and re-orientation events with stalling, where they become trapped within the structure of the substrate matrix. If the substrate contains agarose, the microstructure of the environment can exhibit a broad distribution of pore sizes. In our experimental study, satellites were observed at 0.3%, where the pore size of the hydrogel ranges between a few micrometres ( $\approx 10^{-6}$  m) and a few hundred nanometres ( $\approx 10^{-9}$  m). See Fig. 2.19 and reference [132] for a metastudy. The pore size of some structures being larger than  $1 \mu\text{m}$  allowed the *E. coli* cells to squeeze through them and navigate the environment, enabling them to invade new regions. As the agarose concentration increased, the pore size was reduced, restricting cell movement and thereby preventing the emergence of satellite colonies. We suggest that flagella are necessary for this type of movement, although the resulting motility mode is significantly different from the one observed in liquid media.

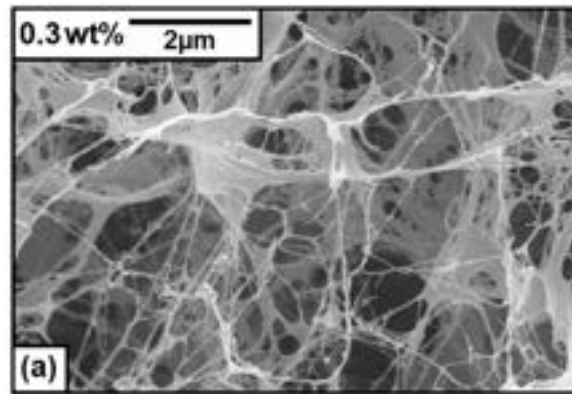


Fig. 2.19 Cryo-SEM micrograph of 0.3% agarose hydrogel. The pore size ranges between  $10^{-6}$  and  $10^{-9}$  m. It corresponds to Fig.2(a) from [132]. Reprinted under Copyright Clearance Center's RightsLink® license.

From our study, we conclude that the emergence of satellite colonies around three-dimensional wt isogenic colonies is a direct consequence of individual bacteria migrating away from the main population. Cell detachment will occur at the right experimental conditions, where there is enough stiffness to promote the growth of the cells as dense communities, and the pore size of the substrate is big enough so cells can squeeze through it. We propose that the emergence of satellites represents a distinct mechanism from those observed during the dispersal step of mature biofilms. (Fig. 2.1) [76, 78, 133]. The dispersal step is defined to occur upon nutrient depletion in the environment or in response to chemical signals that promote it. In our experimental setup, satellites emerge continuously throughout the development of the three-dimensional colony, as can be seen in the supplementary time-lapse videos of [97]. Therefore, it was assumed that the size of a satellite could be interpreted as a direct estimate of how long the founder cell had departed from the main colony. The time-lapse videos also show how some satellites were re-absorbed into the main colony. While the time-lapse videos offer new information about the dynamics of the 3D colonies, they do not present a complete picture of the growth dynamics of satellites, as they were captured using an inverse fluorescent microscope rather than an LSCM.

None of the 3D colonies from the mutant strains exhibited satellite morphology. A shared trait between mutant colonies (at 0.3% agarose) was a rough surface, except for the non-flagellated strain ( $\Delta$ fliC), which displayed colonies with smoother surfaces. As observed, in the time-lapse of wild-type colonies, satellites can be reabsorbed into the main colony if they are close to it. Given that the motility of the mutant strains was reduced compared to the parental strain (Fig.2.13), we hypothesise that some mutant cells were still capable of escaping the confinement of the main colony and navigating the environment. However, due to their limited motility, they were quickly reabsorbed into the main aggregate. Therefore, the

mountainous structures observed at the surface of the 3D colonies could be attributed to cells escaping with short dispersal distances. In favour of the hypothesis, there will be the fact that as the stiffness of the environment increases and the cells experience higher confinement, the colony transitions to a new morphology with a completely smooth surface (see Fig.2.15 ). Recently, it was suggested that the protrusions are a consequence of nutrient instabilities at the surface of growth [134, 135]. We expect such instabilities to be more relevant at later time points when the colony has reached a greater volume, as in our experimental system, we expect very nutrient depletion.

As bacteria transition from a planktonic lifestyle to forming aggregates, they undergo a phenotypic switch to express aggregation phenotypes rather than motility ones [136]. Therefore, it was expected that by deleting certain genotypes from the chromosome and thereby suppressing aggregation phenotypes, the cells would become more motile or at least exhibit motility phenotypes under more conditions. Multiple interdependencies between motility and adhesion genes have been reported. The constitutive expression of type I pili (*fim*) reduces flagellar expression, thereby compromising motility [137]. In a similar fashion, over-expression of antigen 43 (*flu*) prevents flagellar expression [138]. A down-regulation of motility is also present at regulatory networks that promote the expression of curli fimbriae (*csgAB*) and colanic acid (*cps*) [139, 140]. Despite these reports, we did not observe an increase in motility in any of the mutants used in the study; on the contrary, we observed a decrease in motility compared to their parental strain (Fig.2.13). The cause behind this decrease in motility remains unclear, but it showcases how complex the formation of three-dimensional colonies can be. Some of the extracellular structures deleted in our study not only decrease flagellar expression but also inhibit other important structures required for biofilm formation. Expression of type I pili and colanic acid physically block antigen 43 [123, 141], as it requires very close proximity between cells to bind to them. Furthermore, antigen 43 exhibits inverse regulation with type I pili [142].

The modified Eden-growth model reproduced the overall morphology of some of the wt+ colonies (see Fig.2.20. When analysing the *in silico* colonies that produced satellites, the distributions of the number and size of satellites reproduce the *in vitro* results (Fig. 2.17 A, B and Fig. 2.9 A, B). With only two parameters ( $\sigma$  and  $k_s$ ) to change the behaviour of the colonies, the model fails to reproduce the distance from the satellites to the main aggregate and its size.

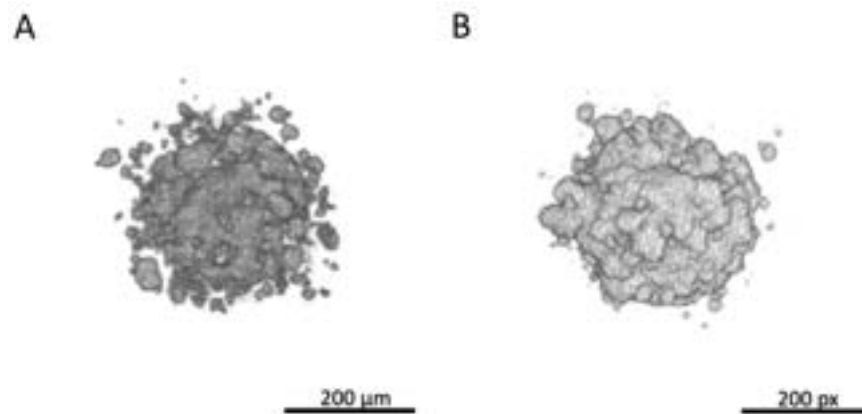


Fig. 2.20 Comparison between *in vitro* (A) and *in silico* (B) colonies. The simulations reproduce the main morphological features of some of the experimental colonies.

The simulations show how colonies that form satellites expand faster than linearly (Fig.2.18) yet slower than the exponential growth observed in liquid cultures (Fig.2.3). It has been proven theoretically by Hallatschek and co-workers that populations accelerate their spread not only based on fitness but also on the dispersion profile of the population. [143, 144]. Populations will expand more rapidly when the dispersal profiles exhibit a fat tail. In our model, we still observe faster-than-linear spread despite the dispersion profile (distances) following a Gaussian distribution. In the model, the movement of cells that leads to satellite emergence is an event restricted to the surface of the colony. As the colony grows, the number of active cells that can swim away from the main colony will increase. Consequently, the system will continue to evolve super-linearly over time. Since the model does not account for growth strategies over long time scales, it remains unclear whether persistent super-linear growth would also be observed in *in vitro* colonies once nutrient depletion begins.

In this chapter, we studied how three-dimensional colonies develop when embedded in an agarose matrix. The properties of the substrate were changed to mimic studies performed in two-dimensional range expansions [145]. We presented how 3D colony expansion of a motile strain leads to the formation of satellite colonies. Using a lattice model, we showed how satellite colonies accelerate population expansion into a super-linear regime over time. Satellites allow a faster spread of the community in complex environments while retaining the high structure of a 3D colony. This strategy can be advantageous in multiple environments. Spreading using a combination of growth and occasional migrations ensures both fast invasion and stable occupations of unknown horizons.



# Chapter 3

## Cell morphology shapes the self-organisation of bacterial communities

### 3.1 Introduction

Bacterial species exhibit a variety of shapes and sizes [146, 147]. Typically, their size ranges from 0.5 to 5  $\mu\text{m}$  in length. Bacterial shapes can be classified into three broad categories: rod-shaped, sphere-shaped and curved-shaped (Fig.3.1). Sphere-shaped bacteria, known as cocci, tend to be non-motile and to arrange themselves in different configurations [148]. Rod-shaped bacteria, or bacilli, are generally larger than cocci and are more likely to be motile [149]. Curved-shaped include various forms such as spirilla [150], vibrios [151] and spirochaetes [152].

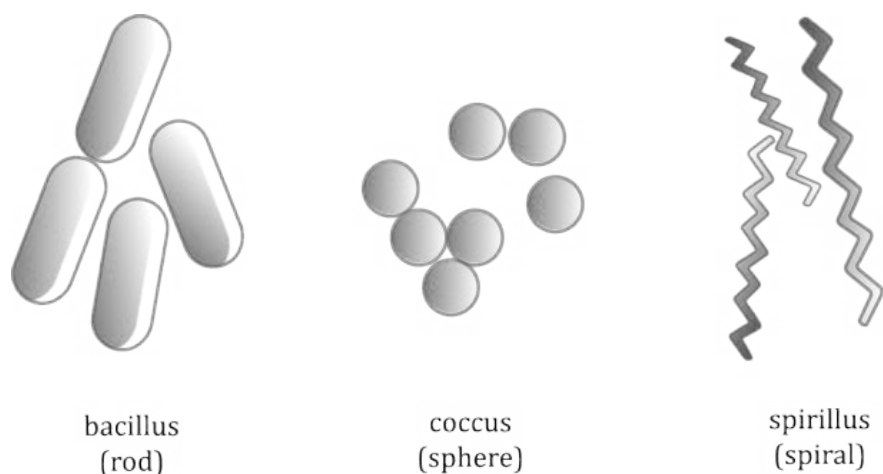


Fig. 3.1 Sketch the three main bacterial shape categories.

In isogenic bacterial populations, the cells will experience fluctuations in phenotypic traits, including cell shape, regardless of whether they are in batch cultures or surface-associated communities [153]. Some of these fluctuations are directly caused by stochastic variations during cell division [154]. Others are related to the stage of the growth cycle the cells are in [155], while some play a more significant role in functions within the community. One example of an isogenic population of cells exhibiting a functional change in shape is during biofilm formation. As bacteria form biofilms, the cells transition between states (Fig. 2.1) with distinct morphologies. For instance, *E. coli* cells are rod-shaped during exponential growth. As nutrient levels decrease, the cells transition to a shorter shape and start producing flagella. With further nutrient depletion, the cells become more spherical and start producing an extracellular matrix to form the biofilm. In mature biofilms, cells with different shapes self-organise within distinct regions of the community, with elongated cells in the growth areas and ovoid cells in non-dividing ones [156]. Morphology transitions are also observed during the evolution of bacterial infections. In the case of a uropathogenic *E. coli* infection, the cells switch from a non-motile spherical shape to motile rods and eventually grow into filaments that invade superficial bladder epithelial cells [157]. Cell shape also plays an important role in certain motility processes, such as swarming (Fig.2.2). For swarming to occur, cells must undergo a phenotypic transition that includes achieving an optimal aspect ratio, among other factors[158].

Fluctuations in cell shape lead to variations in cell size, which plays a crucial role in many processes, like chemical sensing [159]. The range of bacterial sizes is lower bounded by the smallest volume necessary to accommodate basic machinery to support cell growth, and upper bounded by the size that maintains efficient processing rates [160]. Smaller cells maximise their surface area to capture as many nutrients as possible [161], while larger bacteria are more prevalent in nutrient-rich environments where diffusion limitations are less significant [162].

Cell shape has been reported to play an important role in the self-organisation of *in vitro* surface-attached microbial communities. As a synthetic community composed of two isogenic subpopulations, each marked with a different colour, expands on a surface, it undergoes segregation. When the range expansions are performed with a rod-shaped bacterium (*E. coli*), the boundaries of the segregation pattern appear diffusive, particularly in contrast to the defined straight boundaries observed with rounder yeast cells (*S. cerevisiae*) [30]. The boundary between subpopulations created by segregation patterns plays a crucial role in processes requiring cell-to-cell contact, such as horizontal gene transfer (HGT) [54]. During HGT, bacteria acquire new genetic material from the environment or from other bacteria that are not part of their own lineage [163]. HGT can occur through three

mechanisms: transformation, transduction, or conjugation. Among these, only conjugation requires direct cell-to-cell contact. In conjugation, DNA, usually in the form of a plasmid, is transferred from a living donor bacterium to a living recipient bacterium via direct cell contact [147]. In gram-negative bacteria, this process often involves the expression of a conjugation pilus.

Competition experiments involving two *E. coli* subpopulations of distinct shapes have also been performed. During surface-attached range expansions, self-organisation of the subpopulations was observed along the z-axis of the colony. Rounder cells tended to rise to the upper part of the colony, while the elongated cells remained closer to the substrate and dominated the basal surface [60]. In range expansions, the expansion of the population by growth happens at the front of the colony, as the cells growing on the front will block the access to space and nutrients of the ones at the back. Consequently, a subpopulation is more likely to prevail by taking over the leading edge of the colony rather than by rising above the community. The way in which cell shape affects the horizontal expansion of the colony remains unknown.

### 3.1.1 Objectives

This chapter examines how cell shape affects the spatial organisation of bacterial communities. It aims to address two key research questions. The first one focuses on studying how cell shape, specifically its aspect ratio, impacts competition outcomes in spatially distributed communities. The second one explores how variations in cell shape lead to different diffusion boundaries and affect segregation patterns within isogenic populations.

Experimentally, the shape of *E. coli* can be modified via mutations of the *mreBCD* operon. This operon encodes for MreB, a filamentous protein homologous to actin found in eukaryotic cells [164]. The protein interacts with the cell membrane and maintains the rod shape of the cells by directing cell wall growth in areas of negative curvature. If MreB is depleted, the cells exhibit uniform cell wall growth, resulting in a spherical and enlarged shape [165, 166]. To investigate the impact of cell shape on competitive systems, three *E. coli* B-strains with mutations in the *mreB* gene were used. Experiments were designed to evaluate their competitive abilities in various settings. N. van den Berg and A. Sarlet performed 2D range expansions, whose main results were reproduced with an individual-based model (IBM) developed by K. Thijssen. T. Nguyen performed range expansions in three dimensions. From the experimental point of view, I contributed to the project by conducting control experiments and supervising students. This collaborative project led to the manuscript "Emergent collective alignment gives competitive advantage to longer cells during range

expansion" (Appendix: [A.2](#)), currently under review in Nature Physics. I contributed to the manuscript by writing, performing data analysis, and creating figures.

The effect of cell shape on segregation patterns was examined exclusively from a computational perspective. An individual-based model was modified to incorporate variations in cell shape, and simulations of isogenic colonies were conducted. These simulations allowed for the quantification of segregation patterns. To explore how boundaries influence cell-to-cell contact processes, horizontal gene transfer (HGT) via conjugation was simulated. Conjugation was modelled by simulating interactions between donor and recipient strains. When a donor cell and a recipient cell came into contact, a fixed probability was assigned for the recipient cell to become a transconjugant. The number of transconjugant cells was then used as a proxy to evaluate the efficiency of HGT for each cell shape. I performed all the simulations corresponding to this research question.

## 3.2 Materials and Methods

### 3.2.1 Experimental Methods

This section only includes the materials and methods of the experiments that I performed. Additional protocols can be found in the publication "Emergent collective alignment gives competitive advantage to longer cells during range expansion" [[45](#)], which is included in the supplementary material (Appendix: [A.2](#)).

**Bacterial strains** To perform the experimental study, derivatives of the REL606 *E. coli* B-strain [[19](#)] were used. Two strains, REL606*mreB*<sup>A53S</sup> (AS) and REL606*mreB*<sup>A53K</sup> (AK) with mutations in the *mreB* gene were compared to their parental strain REL606 (WT). The strain details can be found in [Tab.3.1](#) and references therein. The MreB protein controls the characteristic rod shape of *E. coli* cells. Therefore, depletions in the *mreBCD* operon lead to enlarged rounder cells. The three non-motile strains were available with two different plasmids, both of which offered kanamycin resistance. The plasmid pmaxGFP (pmaxCloning-Vector, Lonza) contains a green fluorophore (GFP) and pTurboRFP (pmaxCloning-Vector, Lonza), a red one (RFP).

Name	Strain	Relevant characteristics	Aspect Ratio (l/w)	Ref
WT	REL606	Ara(-), StrepR	$3.97 \pm 0.14$	[167]
AS	REL606 <i>mreB</i> <sup>A53S</sup>	WT with <i>mreB</i> <sup>A53S</sup> allele	$2.36 \pm 0.08$	[168]
AK	REL606 <i>mreB</i> <sup>A53K</sup>	WT with <i>mreB</i> <sup>A53K</sup> allele	$1.74 \pm 0.07$	[168]

Table 3.1 Description of *E. coli* strains used in the study. Modified from [45].

All the strains presented similar growth rates in liquid media, as can be seen in Fig.3.2, independently of their shape or expressed fluorophore. WT presented the higher aspect ratio with length =  $3.97 \pm 0.14 \mu\text{m}$  and width =  $0.68 \pm 0.09 \mu\text{m}$ . AS corresponded to the intermediate strain with length =  $2.34 \pm 0.34 \mu\text{m}$  and width =  $0.99 \pm 0.11 \mu\text{m}$ . AK corresponded to the rounder strain with length =  $1.82 \pm 0.30 \mu\text{m}$  and width =  $1.05 \pm 0.13 \mu\text{m}$ .

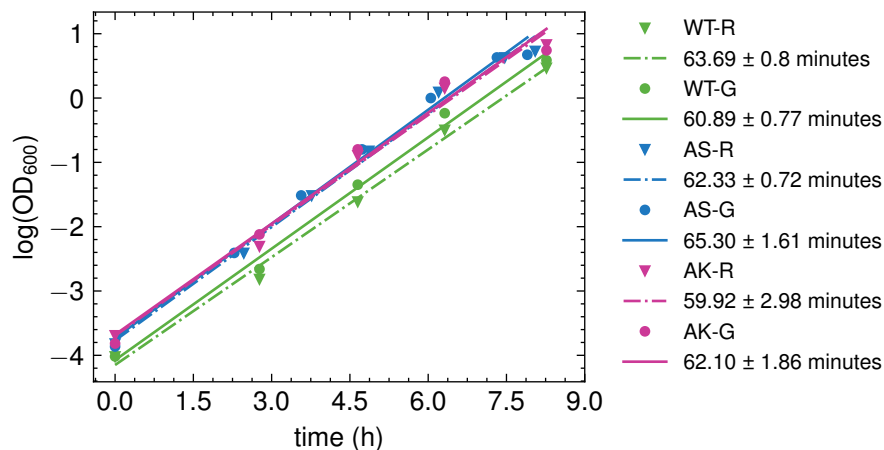


Fig. 3.2 Growth curves for all the strains used in this study, as they grew in M63+glu supplemented with kanamycin. The optical density,  $OD_{600}$ , versus time, (h), on a semi-logarithmic scale. The solid lines are linear fits to the data, and the legends state the corresponding doubling time. Modified from [45].

**Culture media** Experiments were performed in a minimal medium, supplemented with  $30 \mu\text{g}/\text{mL}$  kanamycin sulphate ( $\geq 95\%$ , K1377, Sigma-Aldrich) to maintain plasmid expression unless stated otherwise.

M63 supplemented with glucose (M63+glu) was used as a minimal medium. M63+glu was composed of 20% 5X M63 salt,  $1 \mu\text{g}/\text{ml}$  thiamine hydrochloride ( $\geq 99\%$ , T4625, Sigma-Aldrich),  $2 \text{ mM}$   $\text{MgSO}_4$  (63138, Sigma-Aldrich) and  $2 \text{ mg}/\text{ml}$  glucose ( $\geq 99.5\%$ , G7528, Sigma-Aldrich) dissolved in Millipore water.

The 5X M63 salt solution was composed of 15 g/l anhydrous  $\text{KH}_2\text{PO}_4$  ( $\geq 98.0\%$ , P9791, Sigma-Aldrich), 35 g/l 24 anhydrous  $\text{K}_2\text{HPO}_4$  ( $\geq 99.0\%$ , 60353, Sigma-Aldrich), 10 g/l  $(\text{NH}_4)_2\text{SO}_4$  ( $\geq 99.0\%$ , 09978, Sigma-Aldrich), 2.5 ml 20 mM  $\text{FeSO}_4$  ( $\geq 99.5\%$ , 44970, Sigma-Aldrich), 20mM Na-Citrate ( $\geq 99.5\%$ , 71402, Sigma-Aldrich).

**Competition in batch cultures** Overnight cultures of the three strains expressing each fluorophore were grown in M63+glu. The  $\text{OD}_{600}$  of the overnight cultures was measured, and all the possible strain combinations (AK/AS, WT/AK, WT/AS) were mixed pairwise (GFP+RFP) in equal proportions before diluting the sample a thousandfold into fresh medium. The new cultures were incubated at 37 °C. Cell counts (50000 per culture) were measured using a BD FACSJazz Cell Sorter (BD Biosciences, cat. no. 655490) before incubation and after 8 hours of incubation. The  $\text{OD}_{600}$  of each culture was measured every hour of incubation.

The fluorescence-activated cell sorting (FACS) data was processed using the Flowkit package [169] with a *logicle* transformation and clustered the counts with the *hdbscan* algorithm [170]. After clustering, the counts of the two main clusters (GFP and RFP) were extracted, and the frequencies of each population were defined as the ratio of cell counts of one subpopulation over the total number of cell counts. The results of the competitions were interpreted with the parameter relative fitness [167]. The relative fitness,  $W_{ij}$ , of strain  $i$  with respect to strain  $j$  is estimated as the ratio between the number of doublings of the subpopulations:

$$W_{ij} = \frac{\ln(N_i(t)/N_i(0))}{\ln(N_j(t)/N_j(0))}, \quad (3.1)$$

Where  $N_i(t)/N_i(0)$  and  $N_j(t)/N_j(0)$  are the ratios of the number of cells at time  $t$  compared to the starting point of strain  $i$  and  $j$ , respectively.

**Range expansions** Starting from overnight cultures of the strains of interest, a mix of final  $\text{OD}_{600} = 0.3$  was prepared. The proportion of each strain in the mixture was adjusted based on the measured  $\text{OD}_{600}$  of the overnight culture and the following equations 3.2, 3.3 and 3.4:

$$V_A = \frac{\text{OD}_{600}^{\text{final}}}{\text{OD}_{600}^A} \cdot \text{ratio}_A \cdot V_{\text{tot}} \quad (3.2)$$

$$V_B = \frac{\text{OD}_{600}^{\text{final}}}{\text{OD}_{600}^B} \cdot \text{ratio}_B \cdot V_{\text{tot}} \quad (3.3)$$

$$V_{\text{media}} = V_{\text{tot}} - V_A - V_B \quad (3.4)$$

Where  $V_{A,B}$  corresponds to the volume of each strain required for the final suspension of volume  $V_{tot}$ , and  $ratio_{A,B}$  is the desired fraction of each strain in the suspension. Then, 0.5  $\mu\text{l}$  of the final culture was placed on solid minimal media plates (M63+glu) with 1.5% agar. Various initial conditions were tested using this protocol. For isogenic competitions, the fraction of each strain in the initial droplet was always maintained at 1:1.

The incubation ( $37^\circ\text{C}$ ) period was set to 20 hours for isogenic two-dimensional range expansions. To obtain the expansion rate of isogenic colonies, after 15 hours of preliminary incubation ( $37^\circ\text{C}$ ), they were imaged with an inverted fluorescence microscope every 1.5 hours for 9 hours.

**Image acquisition** The 2D isogenic colonies were imaged with a laser-scanning confocal microscope (LSCM, Leica, SP5) using a 5x air objective (Nplan5 $\times$ 0.12PHO, Leica). The objective provides a (x,y)-resolution of 6.07  $\mu\text{m}$ . The green fluorescent protein (GFP) was excited with an argon laser at 488 nm, and its emission was collected around  $510 \pm 20$  nm. The red fluorescent protein (RFP) was excited with a Helium-neon laser at 543 nm, and its emission was collected around  $600 \pm 40$  nm. The z-resolution provided by the objective was 10  $\mu\text{m}$ . The colonies were imaged for a vertical range of 100  $\mu\text{m}$  (approximately 10 stacks).

An inverted microscope (Nikon Eclipse Ti fluorescent) was used to track the time evolution of the colonies. The microscope was paired with a camera (Andor, Belfast, UK), and a 4x air immersion objective was chosen (Nikon, Plan Fluor, 4x/0.13,  $\infty$ /1.2 WD 16.5). In this setup, the GFP was excited with a mercury-vapour lamp and filtered using the FITC (FITC Filter Cube Set, Olympus, York, UK). The RFP was also excited with a mercury-vapour lamp and filtered with Texas Red cubes (Texas Red<sup>TM</sup> Filter Cube Set, Nikon, Tokyo, Japan).

**Image processing** The isogenic colonies were quantified from their GFP channel. After manually thresholding the channel, the number of sectors and their straightness over the radial dimension were calculated with a custom-made Python script that uses the OpenCV library [171]. Both quantities were obtained after the end of the homeland, once the initial population started to segregate and generate sectors.

The number of sectors was obtained by counting the colour transitions at a specified radius. The colour transitions were found by masking the colony (`cv2.bitwise_xor`) within a ring of 2 pixels width. The mask was created by drawing two concentric circles (`cv2.circle`). The number of contours in the masked colony was then found (`cv2.findContours`). Each contour represented a transition between pixels belonging to the background (value = 0) and pixels corresponding to cells (value = 1). The concentric rings increased their radii (one pixel

at a time) to scan the whole colony and find the number of transitions as a function of the radial distance.

The boundary straightness was also found by masking the colony into concentric rings. In this case, the ring presented a 50 pixels width. For each ring, the edges of the masked colony were detected (`cv2.Canny`), and the contours of these edges were identified. Then, the contours were filtered to include only those that touched both ends of the ring. The length of each relevant contour was divided by the length of the straight line that connected both ends of the contour, providing the straightness of the boundary. The concentric rings increased their radii (one pixel at a time) to scan the whole colony and find the boundary straightness as a function of the radial distance. The boundary straightness at each radial distance was calculated as the average straightness of all relevant contours.

The 2D range expansion of the colonies was quantified by thresholding the colony manually at each time point. The area that each colony occupied was found with the measurement function in Fiji [111]. The effective radius of the colony was estimated from the area, assuming that the surface corresponded to a circle ( $r \approx \sqrt{A/\pi}$ ). Finally, the evolution of the radius of the colony was plotted over time.

### 3.2.2 Computational methods

**CellModeller** To investigate how cell morphology influenced the spatial self-organization of bacterial communities, an individual-based model capable of simulating different cell shapes was needed. In this chapter, simulations were performed with the open-source simulator CellModeller [172]. CellModeller is a Python-based framework designed for IBM of multicellular systems. It has previously been used to describe plant tissues [173], and recently, it has been widely used in the simulation of rod-shaped bacterial communities [25].

CellModeller enables the modelling of signalling processes, both intracellular and extracellular, and gene regulatory networks within a growing population. A biophysical model governs cell growth. In the simulations described in this chapter, bacteria are modelled as rod-shaped rigid bodies, each with a preferred growth mode and momentum. The system evolves by finding the change of momentum of each cell as they collide with their neighbours.

In CellModeller, each cell is characterised by its position ( $\vec{r}$ ), orientation ( $\vec{\phi}$ ) and length ( $L$ ):  $\vec{x}(t) = (x, y, z, \phi_x, \phi_y, \phi_z, L)^T$ . The cell will increase its length at a certain rate, which can be constant or dependent on other parameters. For example, to model exponential growth, the rate should be proportional to the length of the cell ( $\dot{L} \propto L$ ). Once the cells reach a user-defined division length, typically twice their initial length, the cell will split into two new cells, adding a new element to the system. As the cells grow in discrete steps, the system is updated. The general algorithm of the model is:

1. Initialise a population.
2. Call a function, *update*, that contains user-defined rules for the growth of cells.
3. Split the cells that have reached the division size.
4. Integrate the growth of cells over a time step ( $\Delta t$ ) and find new cell positions following a biophysical model:
  - (a) Find new cell positions after they have increased in size. Their positions are determined by solving the equations of motion for a solid capsule, which involves calculating the net force, rotational motion, torque, and interaction with the substrate.
  - (b) From the cell positions, identify overlaps between cells and construct an overlapping matrix, where each matrix entry represents the greatest overlap between two cells.
  - (c) Solve the least squares regularised matrix inversion problem and find new cell positions.
5. Update the variables of each cell and return to step 2.

The details of the biophysical model are provided in the supplementary material of the publication by Rudge et al. [172].

**Simulations** The CellModeller code allowed for the adjustment of cell length, but their radius was fixed at a constant value ( $0.5\mu\text{m}$ ). To study the effect of cell shape, it was necessary to modify the code to allow changes in cell radius as well. This update altered the cell radius and, consequently, the overlapping regions between cells. However, no changes were made to the biophysical model, which approximated many forces while neglecting the radius. Therefore, further updates are required to reproduce all the force contributions in experimental colonies accurately.

With the updated code, two types of simulations were performed. In the first type, isogenic colonies of two subpopulations labelled with different colours were simulated. The system started with a 1:1 ratio of 2.500 total cells and evolved until the total population reached 100.000 cells. Then, the segregation patterns of the colonies were analysed using two quantities: the number of transitions and boundary straightness.

In the second type, conjugation was modelled. The system began with two different strains with the same cell shape: a donor strain and a recipient strain. Each subpopulation was labelled with a different colour. When a donor cell was in contact with a recipient cell,

there was a fixed probability ( $p = 0.85$ )[\[54\]](#) that the recipient would become a transconjugant cell. Transconjugant cells, labelled with a third colour, had the same properties as donor cells and could also conjugate with recipient cells with the same fixed probability ( $p = 0.85$ ). Conjugation was only simulated for a neutral plasmid, meaning its presence did not affect the growth rate of the strain ( $g_{donor} = g_{transconjugant} = g_{recipient}$ ). The population also evolved from a 1:1 ratio of 2.500 total cells until the total population reached 100.000 cells.

To avoid cells overlapping in the initial population, the simulations began by positioning the cells at a distance  $L$ , where  $L$  was the length of the cell, from each other in random directions (Fig.3.3A). Each cell was then assigned a random cell type.

Both simulation types were performed to compare cell types with either the same cell volume or aspect ratio. The volume of cells was fixed, considering them cylinders with hemispherical ends:

$$V_{cell} = \frac{4}{3}\pi r^3 + \pi r^2(l - 2r) \quad (3.5)$$

The details of the parameters used can be seen in Fig.3.3B and Fig.3.3C.

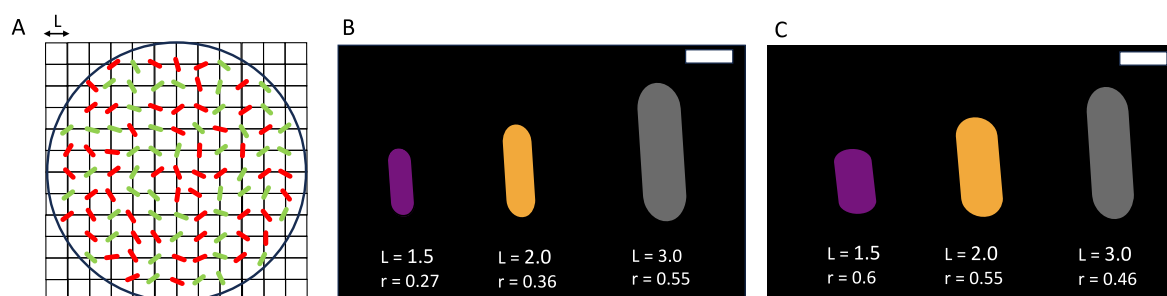


Fig. 3.3 Sketch of parameters used for CellModeller simulations. **A:** Sketch of the initial population from CellModeller simulations. The figure shows a lattice where each lattice site has size  $L$ , corresponding to the length of the cells. Each lattice site is randomly assigned a cell type and orientation. **B:** Cells simulated to study the effect of cell volume. All cells presented the same aspect ratio ( $L/2r = 3$ ). **C:** Cells simulated to study the effect of cell aspect ratio. All cells presented the same volume ( $1.25 \mu\text{m}^3$ ). The scale bar corresponds to  $1 \mu\text{m}$ .

**Data analysis** The data analysis of the simulated colonies was performed with custom-made Python scripts that extensively used the OpenCV library [\[171\]](#). While it was possible to analyse the data directly from the detailed positions and orientations of the cells provided by CellModeller, the analysis was instead performed on images created from these positions. This approach ensured consistency with the analysis of experimental colonies. The resulting colony images were split into different channels, as each cell type was labelled with a different colour.

The data analysis of the isogenic colonies was performed for one of the colour channels, as the other provides complementary information (Fig.3.4). The resulting patterns were quantified from binarised images by determining the number of colour transitions and measuring the straightness of the boundary sectors. Both quantities were obtained after the end of the homeland, once the initial population started to generate the sectors. The number of colour transitions was found with the same script described in the experimental image analysis. Fig.3.4B illustrates a simulated colony and the masked ring used to count the number of transitions. The boundary straightness was calculated using the same script described in the experimental section. Fig.3.4C shows the edges of the colony and the masks of the relevant contours within a 50  $\mu\text{m}$  ring.

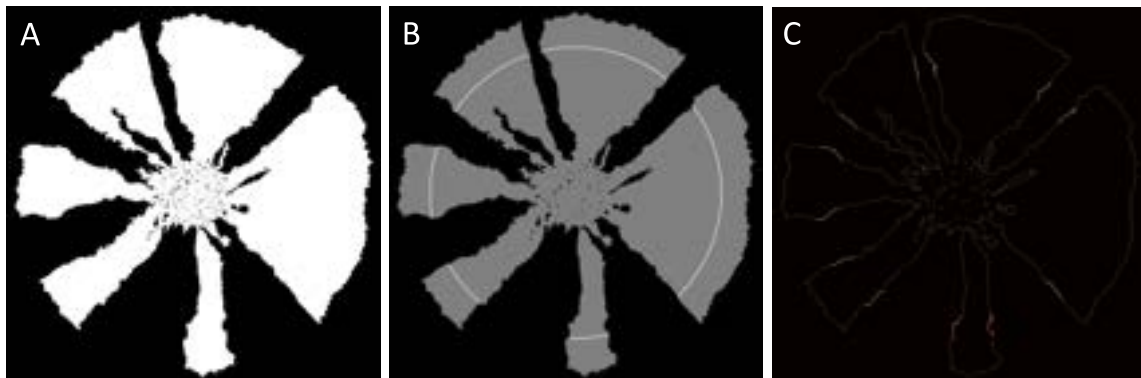


Fig. 3.4 Diagram showing the data analysis performed on isogenic colonies. **A:** Shows the visualisation of one of the colour channels. **B:** Shows one snapshot of the circle used to determine the intermixing index at a given radius. **C:** Shows the resulting edges and the masked contours from which the boundary straightness will be calculated.

For the conjugation simulations, the colonies were quantified with two parameters: the number of transconjugant regions and the total fraction of transconjugants. The number of transconjugant regions was determined by counting the transitions in the transconjugant channel, following the previously described protocol. The total fraction of transconjugant was calculated by dividing the number of transconjugant cells by the total population size.

## 3.3 Results

### 3.3.1 Batch cultures favour rounder cells

The three *E. coli* B-strains used in the study WT (REL606), AK (REL606*mreB*<sup>A53K</sup>) and (AS REL606*mreB*<sup>A53S</sup>) were isogenic except for their mutation in the *mreB* gene. The mutation gave each strain a different aspect ratio (see 3.1) while all maintained their rod-shaped morphologies. The variations in aspect ratio led to distinct cell volumes. In the exponential phase, the rounder strain (AK) presented a volume of  $1.27 \pm 0.56 \mu\text{m}^3$ , the intermediate strain (AS) was the largest with a volume of  $1.54 \pm 0.42 \mu\text{m}^3$ , and the WT strain (the longest one) had a volume of  $0.88 \pm 0.16 \mu\text{m}^3$ .

Regardless of their fluorophore (GFP or RFP), the three strains presented similar doubling times (Fig.3.2) when growing in minimal medium liquid cultures. However, the growth curve was obtained by measuring OD<sub>600</sub> values over time, which indicate the optical density at 600 nm of a sample via light scattering, and cells of distinct sizes and shapes can scatter light differently. Given that WT, AK, and AS cells had different volumes, the same OD<sub>600</sub> reading could correspond to different cell densities depending on the strain. The differences in cell densities were determined by plating liquid cultures and counting the number of colony-forming units, with one colony corresponding to one viable cell. It was found that the number of cells in solution for a certain OD<sub>600</sub> value increased as the cell volume decreased. The most significant difference was between WT and AK strains, where the same OD<sub>600</sub> reading corresponded to a 1.3-fold difference in cell count. Despite the density discrepancies, OD<sub>600</sub> was considered a reliable measure for preparing mixtures for the rest of the study.

To study the effect of cell shape on bacterial communities, control experiments were conducted to understand the behaviour of strains growing in batch culture, where spatial self-organisation is minimal. Following the protocol described in chapter 3.2.1, pairwise liquid cultures were prepared and incubated for 8 hours to assess the competition between the strains. The OD<sub>600</sub> of the cultures were measured every hour (Fig.3.5A). It was observed that all the mixed cultures presented comparable doubling times that matched those obtained for the cultures of single strain (Fig. 3.2). However, OD<sub>600</sub> alone did not reveal the outcome of the competition. Cell counts from the mixes were measured using fluorescence-activated cell sorting (FACS) to determine which strain grew better in batch cultures. The counts for each strain were used to calculate the relative fitness (detailed in chapter 3.2.1), which was derived from the ratio of counts between strains and is independent of the initial density fraction between strains. The resulting relative fitness ( $W$ ) is shown in Fig.3.5B. The closer  $W$  was to 1, the less growth advantage there was between strains. The experiments showed that shorter cells consistently had better growth in liquid cultures when co-cultured with longer ones.

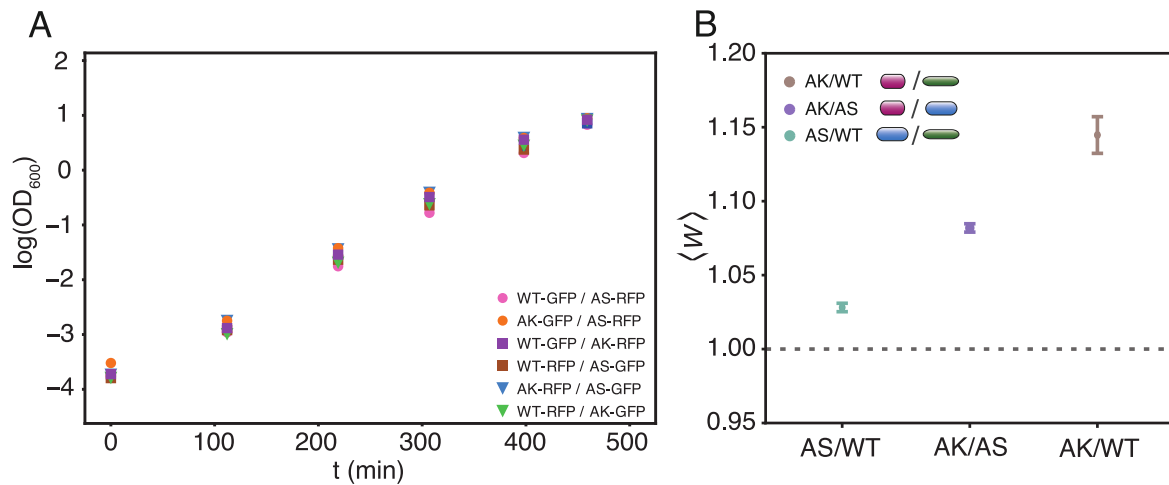


Fig. 3.5 Results of the batch competitions. **A:** Shows the  $OD_{600}$  over time for the competition mixes. **B:** Shows the relative fitness ( $W$ ) of the short strains over the long ones. Modified from [45].

### 3.3.2 Two-dimensional range expansions favour slender cells

Once the advantage of short cells was determined in liquid cultures, the competition experiments were conducted in two-dimensional settings. The experimental setup involved 2D range expansions, where the population grew from an inoculation droplet containing the two strains of interest in a 1:1 fraction. The colonies were grown on minimal medium plates (M63+glu) with 1.5% agar. After 3 days of incubation at 37°C, the resulting colonies were imaged with a confocal microscope. Although the colonies presented some thickness in the z-dimension, the analysis was performed on the projected communities on the x-y plane, focusing on the horizontal expansion of the populations.

When competing in pairs, the longer strain consistently ended up taking over the expansion front of the colony when mixed in equal fractions with a shorter strain. In the experimental setup, taking over the expansion front means that the cells will have better access to nutrients and enough place to divide. Thus, if one subpopulation completely covers the edge of the colony, it will out-compete the other. The takeover by the longer cells happened in less than 3 days, as can be seen from the area occupied by each cell type in Fig.3.6B. The short cells were out-competed in less than 20 hours of incubation (Fig.3.6C). The robustness of the phenomenon was tested by repeating the experiments, reducing the fraction of longer cells in the initial inoculum (see appendix A.2 [45] for detailed results).

The strength of the takeover by the long cells was quantified by measuring the surface fraction that they occupied over the radial distance of the community. In Fig.3.7A, the takeover curve is plotted for the three different strain combinations grown from initial 1:1 fractions. As the strains were isogenic, it was anticipated that the main factor determining the

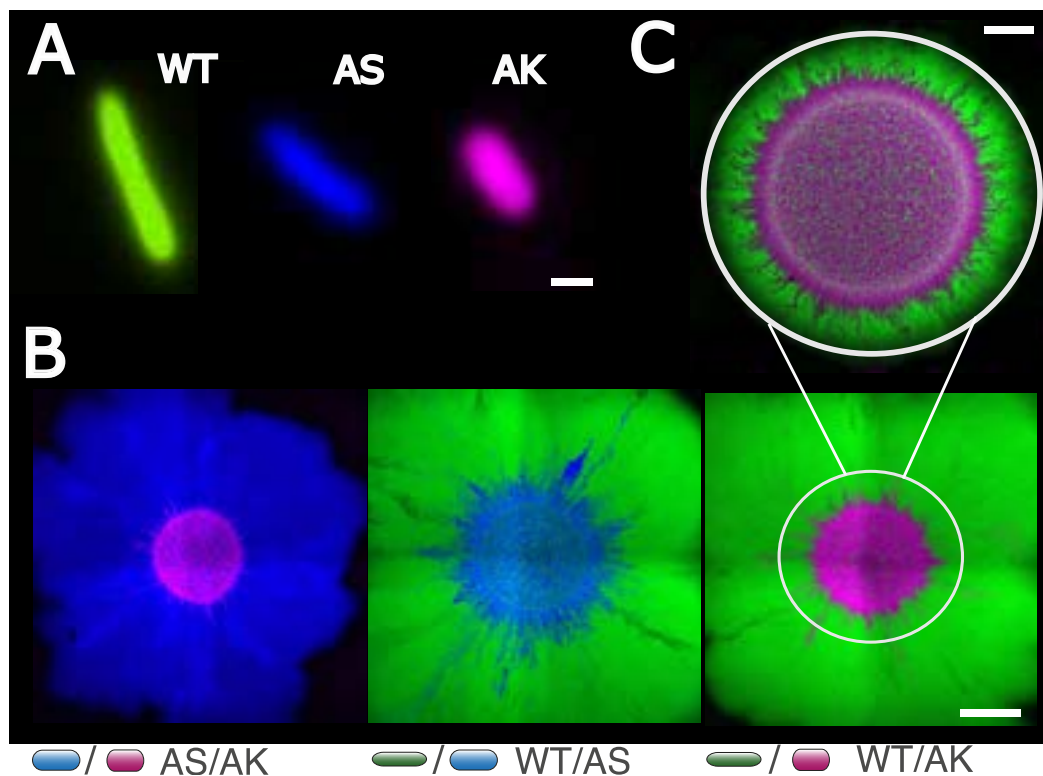


Fig. 3.6 Cells with a higher aspect ratio out-compete shorter ones in range expansions. **A:** Pseudo-coloured single cells of the strains used in the study, WT, AS and AK. The scale bar corresponds to  $1 \mu\text{m}$ . **B:** Maximum intensity z-projections of range expansions between AS/AK (blue/magenta), WT/AS (green/blue) and WT/AK (green/magenta). Images obtained after 3 days of incubation when the initial inoculum starts from a 1:1 ratio between strains. The longer cells of each pair take over the expansion front at the end of the competition. The scale bar corresponds to 1 mm. **C:** Range expansion of WT/AK (green/magenta) after 20h of incubation. The initial homeland and the band where the sectors start to merge can be observed. The scale bar corresponds to  $500 \mu\text{m}$ . Modified from [45].

colony self-organisation would be the relative aspect ratio between strains and that systems with the same relative aspect ratio would behave similarly. The AS/AK pair had a relative aspect ratio of 1.35; the WT/AS pair had a relative aspect ratio of 1.68, and the WT/AK pair had a relative aspect ratio of 2.28. Therefore, it was surprising to find a different takeover behaviour between the combinations with closer relative aspect ratios WT/AS and AS/AK. For the WT/AS mix, the longer strain needed more time (distance from inoculation) to conquer the expanding front, while for AS/AK, the takeover happens almost immediately. This difference in behaviour suggests that takeover cannot be solely attributed to relative aspect ratios but rather involves a more complex mechanism.

### 3.3.3 Mechanical interactions control edge takeover

A control experiment was performed to understand the mechanism behind the takeover by longer cells of the expansion front. The strains presented similar doubling times in liquid cultures, but their individual growth on top of surfaces was not characterised. The 2D growth of the strains was quantified by performing range expansions of isogenic colonies and measuring how their area increased over time for WT, AS and AK. The tracking of the colonies started after 20h of incubation at 37° C to ensure that the population entered the linear regime of growth. The obtained 2D expansion rates (Fig.3.7B) showed that longer cells spread faster on top of a substrate. This result was partially expected, as it has been reported that different cell shapes have distinct preferred growth modes in space. Rounder cells grow as cone-like colonies due to their tendency to grow towards the third dimension [60]. On the other hand, elongated cells grow with their surface close to the substrate. Despite the significant difference in expansion rates, the difference in the takeover strength still cannot be explained, as the relative difference in expansion rates remains constant for both the WT/AS and AS/AK pairs.

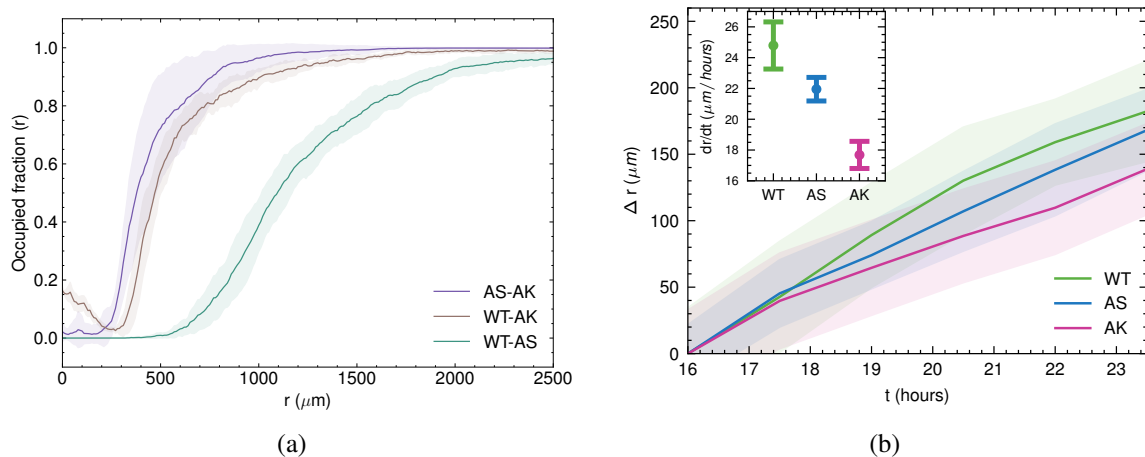


Fig. 3.7 **A**: Evaluation of range expansions via the occupation fraction of long cells along the radial length. The figure shows the takeover curves for the 2D competition experiments that initiate from a 1:1 ratio for AS/AK (purple, N=6), WT/AK (brown, N=5) and WT/AS (dark-green, N=9). The shaded regions show the standard error. **B**: Ensemble-averaged radial expansion, over time, of mono-strain colonies of WT (N= 4), AS (N = 6), and AK (N = 5) on agar (1.5%) substrate (M63+glu). The shaded regions correspond to the standard error of the mean. Inset: The ensemble-averaged expansion rates. Obtained from linear fits of the data. Modified from [45].

To elucidate the mechanism behind the takeover by longer cells, the edge of the colony was imaged starting from the initial inoculation droplet at the single-cell level. The single-cell experiments started from a 1:1 inoculation mixture of WT/AK strains. This strain

combination was chosen because it presented the highest relative aspect ratio between strains. The colony front was imaged every 30 minutes during the spawn of 12 hours (Fig.3.8). Initially, the cells of both strains WT and AK exhibited a random orientation. Over time, the longer cells (WT) start ordering themselves by aligning with their neighbours, while the rounder cells (AK) maintain their random orientations. As the longer cells aligned, they created channels that allowed them to squeeze between the shorter cells and eventually take over the expansion front. This phenomenon was quantified by thresholding the cells, determining their orientations and finding their nematic order parameter [174],  $q$ , which quantifies the relative alignment of a cell with its neighbours (see appendix A.2 [45] for detailed results).

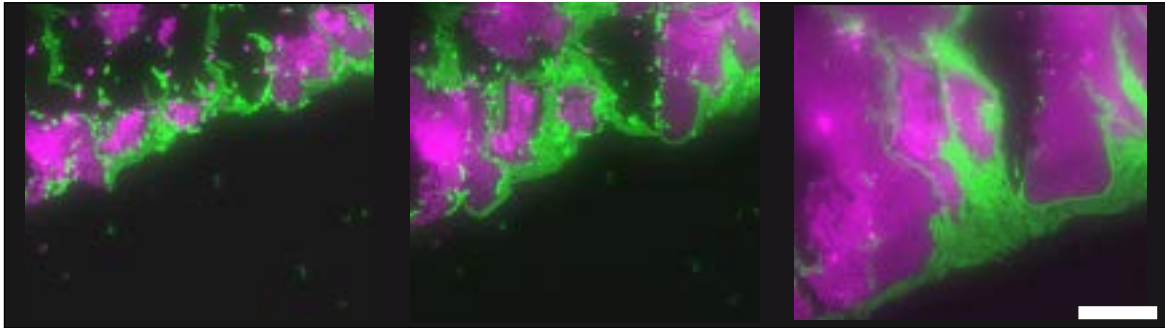


Fig. 3.8 Snapshots from single-cell fluorescence time-lapses of the competition edge between WT (green) and the *mreB* mutant AK (magenta). The first image was obtained after 3.5 hours, the middle one after 5 hours and the last one after 6.5 hours of growth. The scale bar corresponds to 20  $\mu\text{m}$ .

The experimental results on the single-cell level were reproduced using a minimal agent-based model [45]. The model considered cells as non-motile repulsive particles expanding on top of a surface. By fixing the width and the growth rate of the strains to the same value, the ratio between the aspect ratio of the strains was set to 2.28 (which matched the experimental value of the WT/AK mix). As the simulation progressed, the longer cells created channels aligned along the radial direction of growth. These long cells squeezed into the channels until they reached the colony front and aligned with it. It was then concluded that the takeover of the longest cells was due to the formation of the highly aligned domain of cells. The model also explained the differences in the takeover strength for the same relative aspect ratios. Even if the ratio of aspect ratios remained constant, a sufficiently slender shortest cell could start aligning and competing with the longest cells. In the experimental competition, both AS and WT presented nematic order; therefore, WT required more time to take over the expansion front. In the other mix (AS/AK), the short cells (AK) did not present alignment, facilitating the takeover of the long ones (AS).

### 3.3.4 Cell shape controls segregation patterns in isogenic two-dimensional colonies

The alignment of individual cells was proven crucial in 2D competition experiments, giving slender cells a mechanism to conquer the expanding front of the colony and out-compete shorter cells. However, whether said alignment presents any advantages outside a competitive setup remains unknown.

To further investigate the effect of cell shape, isogenic colonies were studied using 2D range expansions. The colonies were inoculated from a 1:1 ratio of the strain of interest (WT, AS and AK) labelled with both fluorophores (GFP and RFP) and incubated for 20 hours at 37°C. The colonies were then imaged with a confocal microscope. The resulting colonies presented different segregation patterns, which was a direct consequence of stochastic events at the expansion front, depending on their cell shape (Fig.3.9A). The longest cells (WT) generated sectors with a highly diffusive pattern. The strain with an intermediate aspect ratio (AS) also presented diffusive boundaries. For the rounder cells (AK), the boundary between sectors corresponded to almost straight lines. The difference in colony size observed in Fig.3.9A could be due to multiple factors, including stochastic variations in the inoculation droplet size and the preferred growth mode of each strain.

The segregation patterns observed in Fig.3.9A were quantified with two parameters: the number of colour transitions and the boundary straightness as a function of the radial distance starting from the end of the homeland. The number of colour transitions corresponded to the number of sectors and reflected the level of intermixing within the colony. The higher the intermixing, the higher the diversity of the community. From the curves Fig.3.9B, it was observed that the intermediate strain (AS) exhibited the highest maximum number of transitions, followed by the shorter strain (AK). The longest strain (WT) had the fewest sectors, indicating lower intermixing levels. The number of colour transitions remained approximately constant as a consequence of measuring the parameter from the edge of the homeland and stopping before the fluorescence of some sectors decreased. Consequently, the analysis in the experiments was limited to a relatively thin band of the colony. The mean number of colour transitions for each strain is reported in Table 3.2.

The boundary straightness (Fig.3.9C) over the radial distance corresponded with the visual observations shown in Fig.3.9A. The closer the boundary straightness was to one, the more linear the edge between sectors was. The boundary straightness remained almost constant for the entire measured radius. The mean boundary straightness for each strain is displayed in Table 3.2. As the aspect ratio of the cells increased, the boundaries became more diffusive, and the boundary straightness deviated from 1.

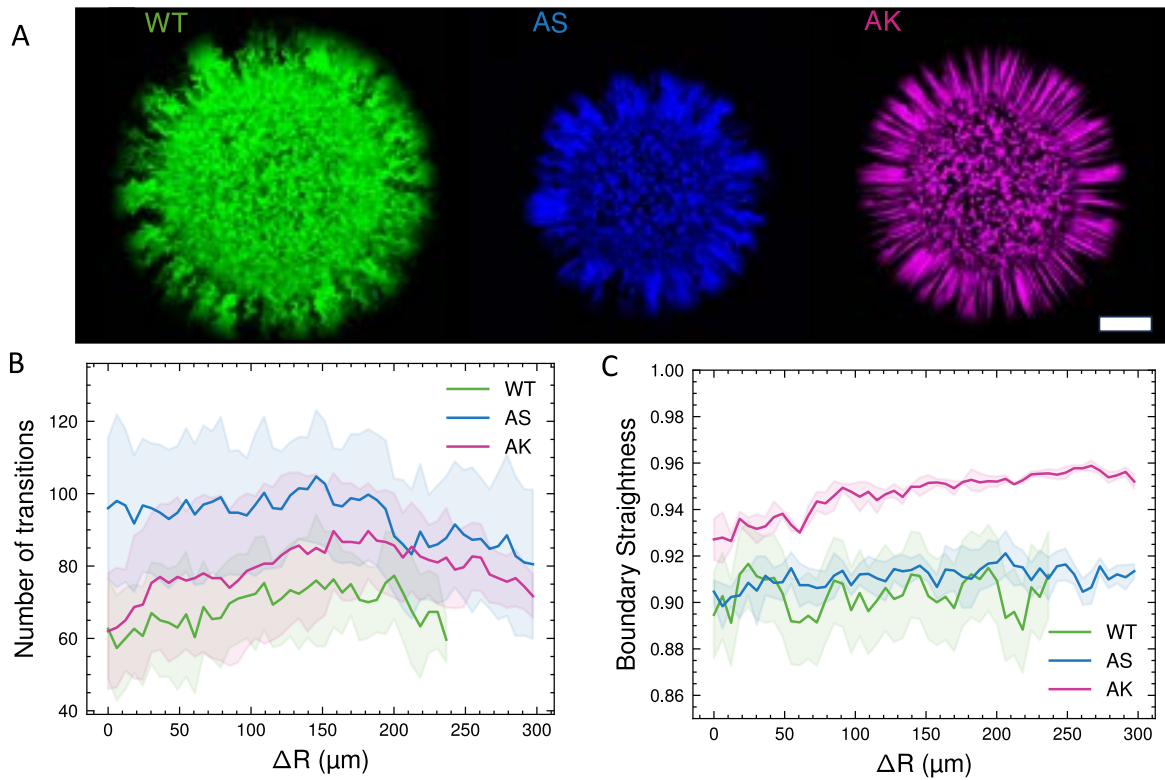


Fig. 3.9 Quantification of 2D range expansion of isogenic colonies **A**: The maximum intensity z-projections of isogenic colonies (WT/WT, AS/AS, and AK/AK) imaged by CLSM after 20 h of incubation. The WT and AS colonies presented coarse (highly diffusive) sector boundaries, while the rounder mutant (AK) had straighter (less diffusive) ones. The scale bar corresponds to 500  $\mu\text{m}$ . Modified from [45]. **B**: Number of transitions (N=3) over the radial distance from the end of the homeland. **C**: Boundary straightness (N=3) over the radial distance from the end of the homeland. As the cells become rounder, the straightness of the edges increases.

	Mean number of transitions	Mean boundary straightness
WT	$68.6 \pm 5.2$	$0.90 \pm 0.01$
AS	$93.5 \pm 6.0$	$0.91 \pm 0.01$
AK	$79.2 \pm 6.3$	$0.95 \pm 0.01$

Table 3.2 Mean number of colour transitions and boundary straightness for WT, AS and AK. The first column corresponds to the mean over the radius for the curves in Fig.3.9B. The second column corresponds to the averaged curves over the radial distance from the mean over the radius for the curves in Fig.3.9C. The error is the standard error of the measures.

Once the different segregation patterns were observed experimentally, the next step was to determine how they were controlled. However, since experimental strains presented both

different aspect ratios and total volumes, it was challenging to determine which parameter had a greater impact on the spatial self-organisation of the community.

To uncouple the effect of aspect ratio from the cell volume, simulations were conducted with the agent-based software CellModeller (chapter 3.2.2). Two subsets of simulations of 2D isogenic colonies, each starting from populations labelled with two different colours, were performed. In each subset, colonies from three different cell morphologies were compared, with either the aspect ratio ( $L/2r = 3$ ) or the volume ( $1.25 \mu\text{m}^3$ ) held constant across the simulations. The selected cell sizes are detailed in Tab.3.3 as well as Fig.3.3B,C. The lengths and radii chosen were specifically selected to replicate typical sizes of bacteria observed in natural environments. For each cell size, five different colonies were simulated, and their segregation pattern was quantified following chapter 3.2.2. The analysis provided the number of colour transitions and boundary straightness of the 2D *in silico* colonies.

	Aspect ratio ( $L/2r$ )	Volume ( $\mu\text{m}^3$ )
L = 1.5 r = 0.27	3.00	0.30
L = 2.0 r = 0.36	3.00	0.72
L = 3.0 r = 0.55	3.00	2.50
L = 1.5 r = 0.60	1.25	1.25
L = 2.0 r = 0.55	1.81	1.25
L = 3.0 r = 0.46	3.26	1.25

Table 3.3 Length (L) and radius (r) of single cells chosen for CellModeller simulations to radii populations with either the same volume ( $1.25 \mu\text{m}^3$ ) or the same aspect ratio ( $L/2r = 3$ ). The values of both the lengths and the radius are given in  $\mu\text{m}$ .

Figure 3.10A displays an example colony for each cell size tested when the aspect ratio was fixed ( $L/2r = 3$ ). Since the aspect ratio was kept constant across the simulations, the differences in patterns had an origin in variations of the cell volume. As cell volume increased, the total area of the colony increased. The number of colour transitions (Fig.3.10B) shows that all the colonies reached the highest number of transitions soon after the end of the homeland, followed by a decrease due to coalescence events. If the simulations had been run for longer times, the number of transitions was expected to reach a plateau, but in the displayed simulations, the system seemed to keep evolving as the number of sectors was not stabilised. The cells with smaller volumes, L = 1.5 and r = 0.27  $\mu\text{m}$  and L = 2.0 and r = 0.36  $\mu\text{m}$ , peaked around the same number of sectors (17 sectors), while the larger cells (L = 3.0 and r = 0.55  $\mu\text{m}$ ) had a smaller maximum number of transitions (13 sectors). The slope of the curves quantified the decrease in the number of transitions, shown in Table 3.4 together with the mean number of transitions. The smaller the cell volume, the faster the coalescence

of the colony sectors was. The boundary straightness (Fig.3.10C) of the colonies was not significantly different as the volume of the cell changed. The averaged boundary straightness is shown in Table 3.4.

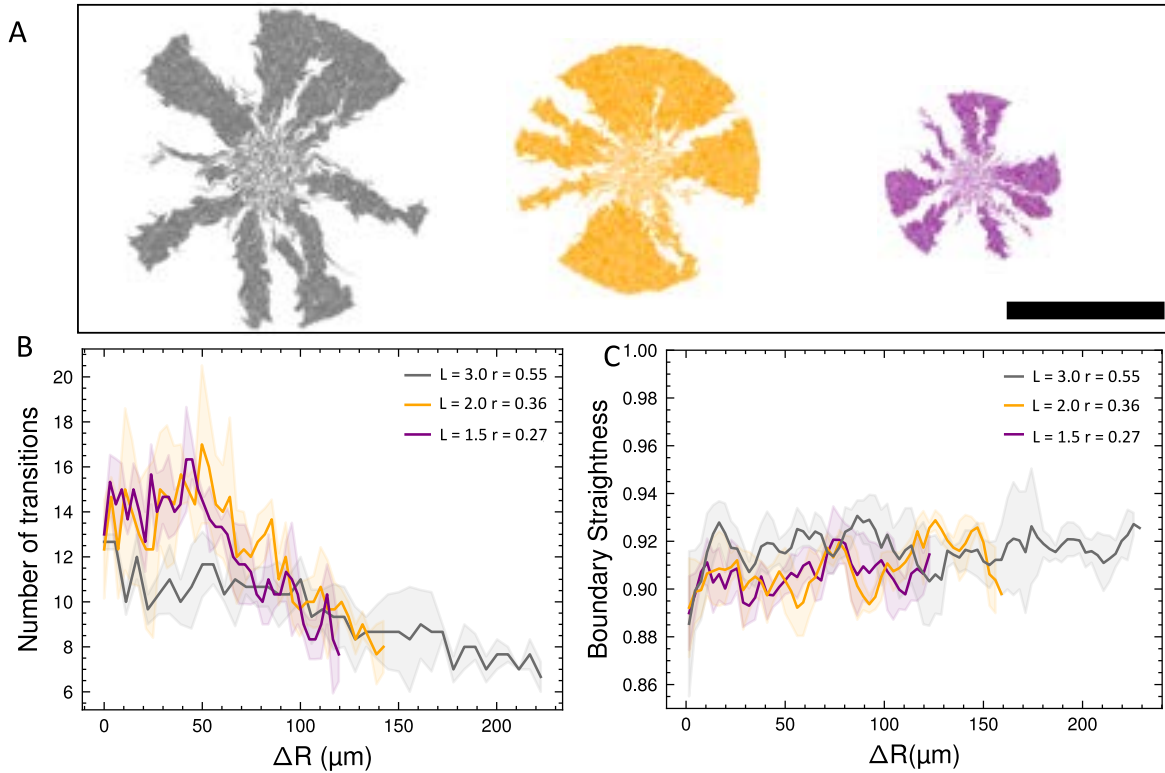


Fig. 3.10 Quantification of simulated colonies for cells with fixed aspect ratio. **A**: Resulting colonies for each cell type. The scale bar is  $200 \mu\text{m}$ . **B**: Number of transitions ( $N=5$ ) over the radial distance from the end of the homeland. The number of transitions peaked and fell at different rates for each cell volume. **C**: Boundary straightness ( $N=5$ ) over the radial distance from the end of the homeland. It remained similar for the three tested volumes.

Fixed aspect ratio	Mean number of transitions	Transition fall ( $10^{-2}$ transitions/ $\mu\text{m}$ )	Mean boundary straightness
$L = 1.5 \ r = 0.27$	$12.4 \pm 2.4$	$- 8.2 \pm 0.02$	$0.90 \pm 0.01$
$L = 2.0 \ r = 0.36$	$12.2 \pm 6.0$	$- 7.1 \pm 0.02$	$0.90 \pm 0.02$
$L = 3.0 \ r = 0.55$	$9.5 \pm 1.5$	$- 2.0 \pm 0.01$	$0.91 \pm 0.02$

Table 3.4 Quantification of *in silico* 2D colonies for cells with the same aspect ratio. The table displays the mean number of colour transitions and their decline, along with the mean boundary straightness. The values are obtained from the curves displayed in Fig.3.10B, C.

Figure 3.11A displays an example colony for each cell size tested when the volume was fixed ( $1.25 \mu\text{m}^3$ ). Since the cell volume was kept constant across the simulations, the differences in patterns had an origin in variations in the aspect ratio of cells. In this case,

all the colonies presented similar areas. The number of colour transitions (Fig.3.11B) was similar as the aspect ratio of the cell changed. The three types of cells peaked around the same value (12 sectors) and presented similar slopes in their decrease of colour transitions, as reported in Table 3.5. On the other hand, the boundary straightness profile changed with the aspect ratio of the cells. For the longer cells ( $L = 3$  and  $r = 0.46 \mu\text{m}$  and  $L = 2.0$  and  $r = 0.55 \mu\text{m}$ ), the boundaries were more diffusive than for the rounder cells ( $L = 1.5$  and  $r = 0.6 \mu\text{m}$ ), the mean value is displayed in Table 3.5.

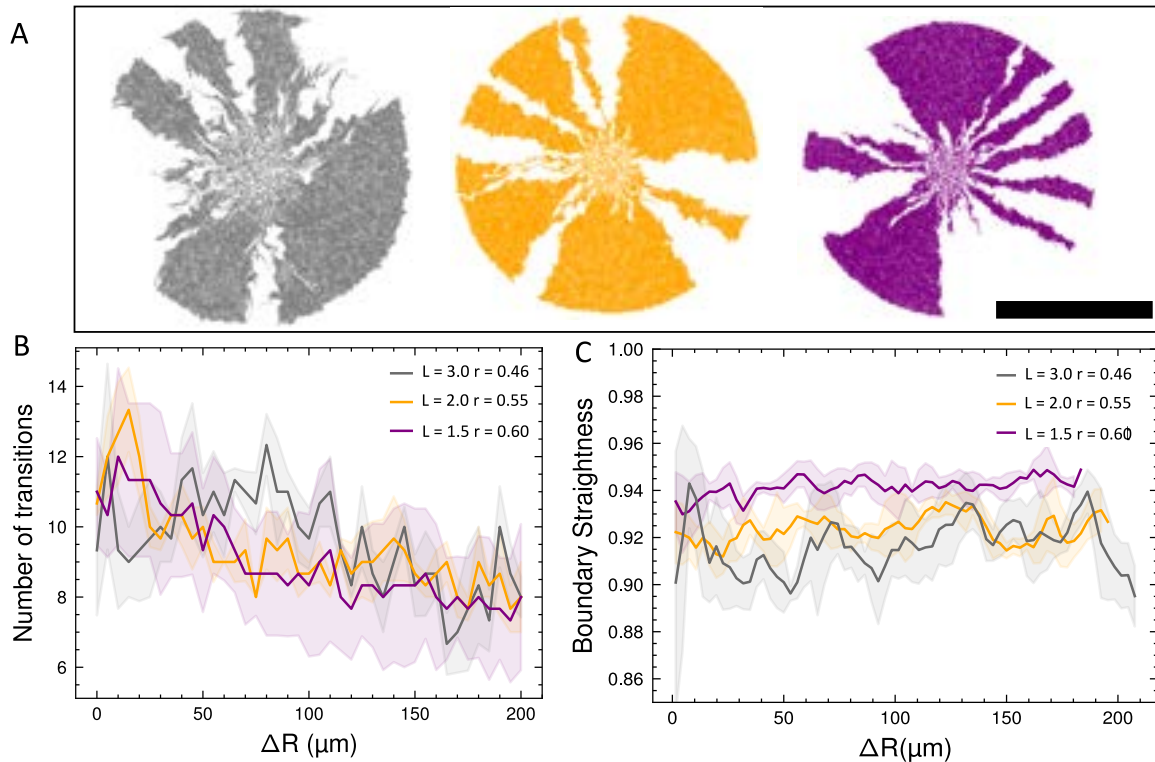


Fig. 3.11 Quantification of simulated colonies for cells with fixed volume. **A**: Resulting colonies for each cell type. The scale bar is  $200 \mu\text{m}$ . **B**: Number of colour transitions ( $N=5$ ) over the radial distance from the end of the homeland. The number of transitions follows the same trend for the three types of cells. **C**: Boundary straightness ( $N=5$ ) over the radial distance from the end of the homeland. The average boundary straightness increases as the aspect ratio of the cell decreases.

Fixed Volume	Mean number of transitions	Transition fall ( $10^{-2}$ transitions/ $\mu\text{m}$ )	Mean boundary straightness
$L = 1.5, r = 0.60$	$9.0 \pm 2.4$	$-1.9 \pm 0.02$	$0.94 \pm 0.02$
$L = 2.0, r = 0.55$	$9.4 \pm 1.2$	$-1.6 \pm 0.02$	$0.91 \pm 0.02$
$L = 3.0, r = 0.46$	$9.6 \pm 1.4$	$-1.7 \pm 0.03$	$0.91 \pm 0.02$

Table 3.5 Quantification of *in silico* 2D colonies for cells with the same volume. The table displays the mean number of colour transitions and their decline, along with the mean boundary straightness. The values are obtained from the curves displayed in Fig.3.11B, C.

The previous results suggest that the number of colour transitions, indicating the number of sectors, was dependent on the volume of the cells. In the experimental setup, the strain with the greater volume (AS) exhibited a higher number of colour transitions. For the simulations, we observe that cells with smaller volumes peak at higher values, but their values fall at a faster rate than those with bigger volumes. As the simulations did not reach the plateau, it is not possible to compare whether the number of sectors over there will reproduce the experimental trend. The simulations showed that the boundary straightness of the colonies was independent of cell volume but highly dependent on the aspect ratio of cells. In agreement with the experimental results, simulations of rounder cells led to straighter boundaries than slender ones.

### 3.3.5 Patterning of communities affects conjugation events

The previous section uncoupled the importance of cell volume and cell aspect ratio within segregation patterns, but it did not address the significance of these results. To navigate the relevance of self-organisation patterns, a system where cell-to-cell contact between subpopulations is important was simulated. The chosen system was the conjugation of a neutral plasmid. In said setup, both donor cells and recipient cells were considered. When recipient cells were in contact with donor cells, there was a fixed probability of plasmid transfer. If a recipient cell successfully incorporated the plasmid, it became a transconjugant cell, capable of spreading the plasmid to other recipient cells. Therefore, conjugation events require cell-to-cell contact. The greater the intermixing of a colony, the higher the number of contacts between different cell types, and more transconjugant cells were expected.

The simulations were also performed for the two previous sub-groups of cells (Tab.3.3). The resulting colonies were quantified by the number of transconjugant sectors across the radial distance, starting from the end of the homeland, and by the fraction of transconjugant cells over the total population. For the cells that presented a fixed aspect ratio ( $L/2r = 3$ ), the number of transconjugant sectors peaked for similar values (6 regions), Fig.3.12A. However, the number of transconjugant regions decreased with radial distance for all the volumes, indicating that transconjugant cells were left behind from the expansion front. When the volume of cells was kept constant ( $1.25 \mu\text{m}^3$ ), Fig.3.12B, the maximum number of transconjugant regions was highest for the slender cells. However, as the colony developed, the number of regions decreased rapidly. In contrast, for shorter cells, the number of transconjugant regions was kept constant as the radius increased, indicating that transconjugant cells remained active at the edge of the colony.

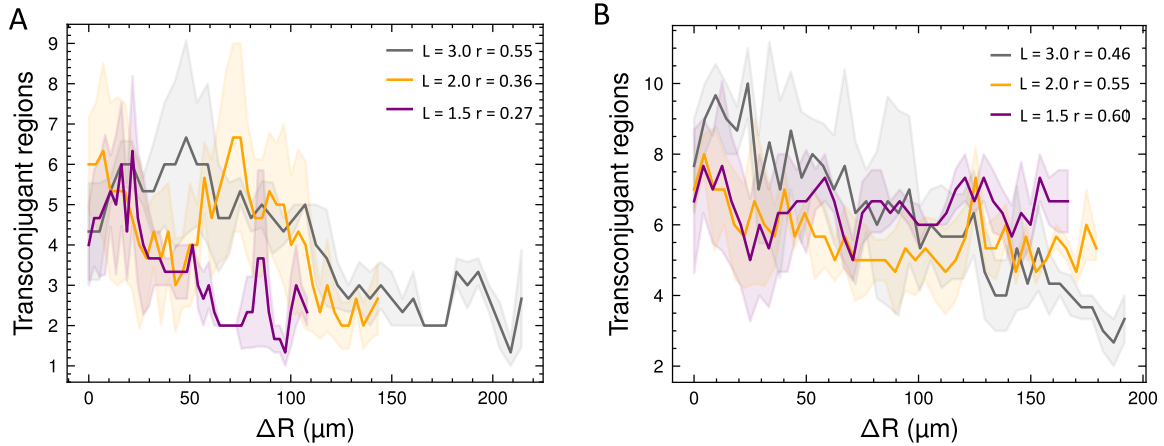


Fig. 3.12 Number of transconjugant regions for *in silico* colonies over the radial distance. **A**: For the subset of cells with a fixed aspect ratio ( $N=5$ ). **B**: For the subset of cells with a fixed volume ( $N=5$ ).

The total fraction of transconjugant cells was dependent on both cell volume and cell aspect ratio, as detailed in Table 3.6. Smaller cell volumes were associated with a lower fraction of transconjugant cells. Conversely, colonies from cells with a smaller aspect ratio had a higher prevalence of transconjugant cells.

Fixed aspect ratio	Transconjugants (%)	Fixed volume	Transconjugants (%)
$L = 1.5 \ r = 0.27$	$2.2 \pm 0.1$	$L = 1.5 \ r = 0.60$	$7.3 \pm 2.3$
$L = 2.0 \ r = 0.36$	$4.5 \pm 3.0$	$L = 2.0 \ r = 0.55$	$5.7 \pm 2.4$
$L = 3.0 \ r = 0.55$	$5.0 \pm 1.4$	$L = 3.0 \ r = 0.46$	$5.4 \pm 3.3$

Table 3.6 Fraction of transconjugants for *in silico* colonies. The values of both the lengths and the radius are in ( $\mu\text{m}$ ). **A**: For the subset of cells with a fixed aspect ratio ( $L/2r = 3$ ). **B**: For the subset of cells with a fixed cell volume ( $1.25 \mu\text{m}^3$ ).

Combining the results from Fig.3.12 and Table 3.6 to maximise the number of transconjugant cells (i.e., conjugation events), it is desirable to have a small aspect ratio combined with a large volume. Although slender cells may have more initial cell-to-cell contact, as the community develops, they will lose more regions due to coalescence events. Therefore, among the experimental colonies, the segregation pattern exhibited by AK (Fig.3.9A) is expected to present higher transconjugant regions and events.

### 3.4 Discussion

The experiments performed with three non-motile *E. coli* B-strains, a wild-type and two *mreB* mutants determined that rounder cells had a fitness advantage compared to longer cells when co-cultured in liquid media. This result did not invalidate Fig. 3.2, where similar doubling times were reported for WT, AS, and AK, as the fitness advantage had an origin in the lag time of each strain. Monds et al. [168] reported that the *mreB* mutants presented a shorter lag phase compared to their parental strain. Starting from 1:1 mixtures, the mutants initiated growth faster than WT, leading to an unbalanced number of cells that were maintained over the duration of the experiment, as the cells had similar doubling times. Therefore, the fitness difference was not directly related to the shape of cells but rather to their metabolism.

From the results in a liquid medium, it was initially expected that in 2D-dimensional range expansion, where reaching the edge of the colony is crucial to divide, the strains with shorter lag time would present an advantage. These strains would begin dividing earlier and thus have a better chance of dominating the expansion front. Starting from 1:1 fractions of a mix of the strains, the opposite behaviour was observed. The mutants, with a smaller aspect ratio, were quickly out-competed by the longer strain. When comparing the two mutants, the shorter one (AK) was out-competed by the mutant with a relatively higher aspect ratio (AS). Therefore, it was concluded that the key parameter controlling the takeover of the colony edge was the aspect ratio of the cells. The introduction of dimensionality changed the outcome of competition experiments. Additional experiments and computational simulations were required to explain the mechanism promoting such results. Time-lapse experiments at single-cell resolution revealed that longer cells exhibited alignment over time while shorter cells maintained random orientations. Said results were reproduced with an agent-based model. When cells that presented nematic ordering competed against cells that did not, they generated channels that allowed them to reach the edge of the colony. Once at the edge, they changed their orientation, conquered the expansion front and surrounded the whole colony. The model reproduces the takeover mechanism and predicts a threshold where short cells will start aligning and the competitive advantage of the long cells will be reduced. However, it is still an oversimplification of the system. It fails to explain why the takeover rate does not increase since the relative aspect ratio between strains increases, as observed experimentally.

The takeover of longer cells in 2D range expansions is not a trivial result. Previous studies have shown that different cell morphologies led to different growth modes on top of surfaces [60]. Usually, rounder cells are expected to grow in a "conical" colony as they grow more easily towards the third dimension. On the other hand, longer cells will grow with as much surface contact as possible. This result led to the speculation that rounder cells would take over longer ones [175] as they would stack on the z-direction. In range expansions, the

colony expands horizontally as a single-cell layer. Therefore, the effect of the z-structure was not relevant to determining the competitive advantage of the strains in our experimental system.

The quantification of 2D isogenic experimental colonies determined that cell shape is a determinant of the segregation patterns of the community. The cells with the smaller aspect ratio (AK) presented almost straight boundaries comparable to those observed in 2D expansions of round yeast cells [30]. On the other hand, as the cells became more elongated, the sector boundaries became more diffusive. Simultaneously, simulations with CellModeller were performed to determine whether the aspect ratio of the cells or their volume was responsible for said self-organisation. By keeping either the aspect ratio or the volume of cells constant, it was observed that the straightness of the sectors was highly dependent on the aspect ratio. In contrast, the number of sectors and coalescence events was more influenced by cell volume. Lower aspect ratios provided straighter boundaries. Conversely, big cell volumes reduced the number of sectors of the colony but maintained them for a longer time.

A conjugation system was simulated to understand the implications of the segregation patterns. For conjugation to occur, the cells need to be in direct contact. Therefore, increased intermixing within a colony leads to a higher frequency of conjugation events. Conjugation was increased for both bigger cell volumes and smaller aspect ratios. Bigger cell volumes maintained the colony intermixing for a longer time, therefore allowing more conjugation events to happen. Smaller aspect ratios provided the colony with more straight edges, meaning that subpopulations of cells were more in direct contact when the boundaries were not diffusive. Interestingly, a similar increase in conjugation events has been recently reported by Ruan et al. [54] when a system is under phage predation. Phage predation changes the self-organisation of the colony, making it transition from small intermixing with diffusive boundaries to high intermixing with straight boundaries (see Fig. 3.13).

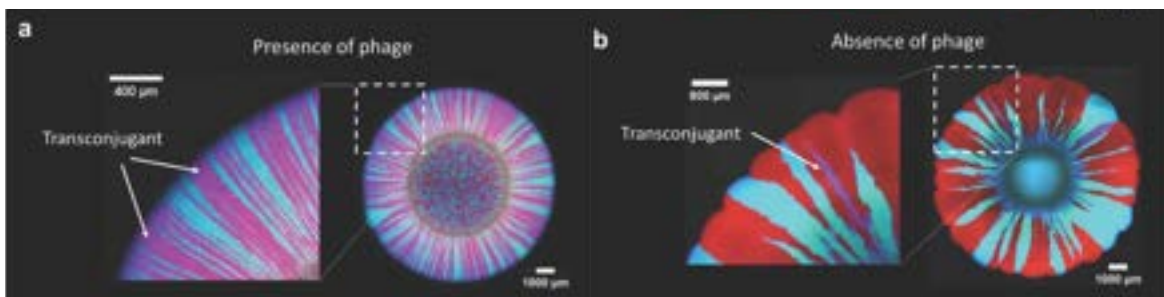


Fig. 3.13 Transconjugant regions in 2D range expansions. **A**: Under phage predation. **B**: Without phage predation. Fig.2 from [54]. Reprinted under Creative Commons BY 4.0 licence.

The results of the simulations performed with CellModeller suggest that cell shape is a parameter that alters the efficiency of HGT within spatially distributed communities. Further investigations are needed to determine whether the level of intermixing (cell volume) or the straightness of the boundary (cell aspect ratio) affects conjugation events more. The simulations were only performed in the case of a neutral plasmid, where the donor, recipient and transconjugant presented the same growth rate. But usually, the expression of plasmids comes with a metabolic cost. One of the following steps could be to perform the simulations with a detrimental plasmid (that reduces the growth of donor and transconjugant cells) or with an advantageous plasmid (that increases the growth of donor and transconjugant cells).

CellModeller provided a framework that enabled simulations with force interactions between bacteria. However, the simulations still fell short of capturing all the complex behaviours of the experimental colonies. The varying radius of cells was introduced in the system, so the cell dimensions were used to calculate the cell shapes and find the overlapping area between them. Despite this, further code modifications are required to comprehend the effect of cell shape in the self-organisation of colonies. For instance, in the current version, cells grow only by increasing in length, and it is the length the parameter that triggers cell division. A new version should include growth in volume and cell division controlled by it. Additionally, the biophysical model approximates many forces acting on slender rods of zero radius. Therefore, the equations need to be modified to account for the thickness of cells.

In long-term evolutionary experiments in liquid media, *E. coli* has been found to shorten and widen to increase its volume to uptake nutrients [176]. Still, as previously shown, the spatial organisation of the system can significantly change its outcome. In this chapter, the effect of cell shape in 2D range expansions has been extensively studied. From competition experiments, the cells with a higher aspect ratio presented a competitive advantage. When mixed with shorter cells, the long ones took over the expansion front of the colony, decreasing the intermixing of the short subpopulation to zero. On the other hand, simulations of 2D isogenic range expansions showed that small aspect ratios promoted HGT by conjugation events. Increased conjugative events might be advantageous, as cells that uptake DNA could acquire beneficial mutations, such as antibiotic resistance. Therefore, based on the results presented in this study, it is challenging to conclude about the role of cell shape from an evolutionary perspective.





# Chapter 4

## Indirect antibiotic resistance arises from local interactions

### 4.1 Introduction

Bacteria are involved in multiple key processes important for human health, yet they also cause serious infections. Antimicrobial agents can combat these infections, with antibiotics being the most effective ones. Antibiotics are drugs often derived from moulds that present different modes of action categorised as either bactericidal or bacteriostatic [177]. Bactericidal antibiotics kill the bacteria, whereas bacteriostatic antibiotics inhibit cell growth. Bactericidal antibiotics can kill bacteria through various mechanisms [178], with one of the most common being the disruption of the cell envelope. Bacteriostatic antibiotics typically inhibit protein synthesis pathways, but they can also interfere with other metabolic processes, such as DNA replication [177]. Classifying antibiotics as either bactericidal or bacteriostatic is often not a reliable metric in clinical settings. Bacteriostatic antibiotics can cause bacterial death for prolonged exposure times, while bactericidal antibiotics may not completely kill all the cells but rather impact their metabolism [179].

Antibiotic classes group antibiotics based on their chemical structures and provide a more relevant classification than their mode of action (Fig.4.1). The most common classes are  $\beta$ -lactams, macrolides and aminoglycosides.  $\beta$ -lactams are a class of bactericidal antibiotics that contain a beta-lactam ring in their chemical structure. In *E. coli*, they inhibit the cross-linking of the bacterial peptidoglycan by transpeptidases [180], leading to disruption of the bacterial cell wall. Aminoglycosides target aerobic gram-negative bacteria and inhibit protein synthesis by binding to the A-site on the 16S ribosomal RNA of the 30S ribosome [181].

Macrolides primarily target gram-positive bacteria and inhibit protein synthesis by binding to the 50S subunit of the ribosome [182].

In recent years, extensive exposure of bacteria to antibiotics has led to a significant increase in antimicrobial resistance. In 2019, there were 1.27 million deaths attributed to bacterial antimicrobial resistance [183]. Bacteria can develop resistance to antibiotics through diverse mechanisms, as represented in Fig.4.1 [184]. The most common resistance mechanisms include reduced permeability of the cell membrane, which limits the amount of drug that can enter the cell, and drug inactivation, where bacteria either degrade or transfer a chemical group to the antibiotic [185]. Antibiotic deactivation can occur both intracellularly and extracellularly.

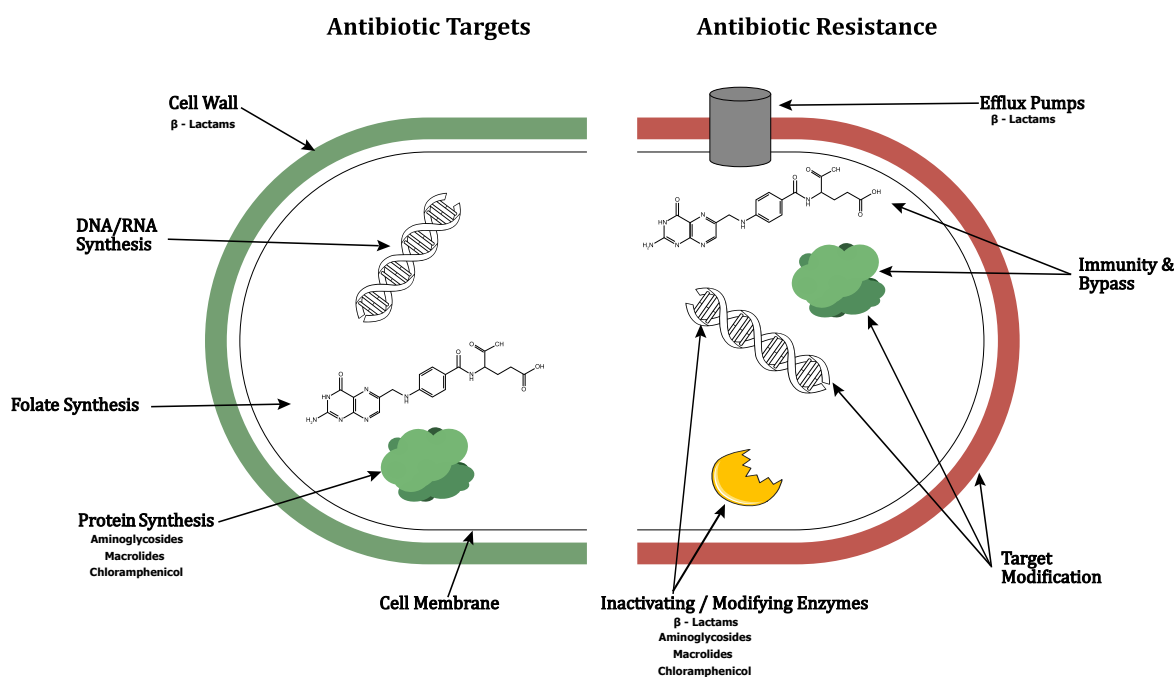


Fig. 4.1 Diagram with antibiotic targets and resistance mechanisms. The elements are not to scale. The diagram does not represent a Gram-positive or a Gram-negative cell wall.

From the clinical point of view, both acute and chronic infections that require treatment present cells that self-organise as biofilms. Bacteria growing as biofilms or complex bacterial communities exhibit a higher tolerance to antibiotic treatment [186–188]. It is important to differentiate between resistance mechanisms and tolerance. Resistant cells possess genetic traits that make them immune to antibiotics, whereas tolerant cells are sensitive to antibiotics but can survive prolonged treatment times [189]. As bacterial communities form complex three-dimensional communities, antibiotics must diffuse towards the centre of the colony. Complex spatial self-organisation of the community is enough to protect the cells compared

to their planktonic counterparts [190], as cells at the centre of the colony take longer to be affected by the drug. When the communities are protected by an extracellular matrix, as is in biofilms, the penetration of the antibiotic is reduced further [191], often leaving the centre of the biofilm unaffected by the drug. Additionally, as cells get confined at the centre of the biofilm, their metabolic activity is reduced [192], which further diminishes the efficacy of antibiotics targeting metabolic pathways, even if they reach the cells.

Due to the high prevalence of bacterial infections, understanding how antibiotic resistance and tolerance emerge within bacterial populations is important [61]. *In vitro* studies about antibiotic resistance are commonly conducted in liquid cultures. Recently, the studies have been extended to two-dimensional range expansions [25] and to biofilms grown in microfluidic chambers [193]. A common theme in these studies is the investigation of emergent cooperative behaviours within antibiotics under varying antibiotic stress [194].

An emergent behaviour observed in liquid cultures is indirect resistance. Indirect resistance (IR) refers to the ability of an antibiotic-resistant bacterial population to shield a sensitive population from antibiotic stress [195]. The emergence of IR depends significantly on the antibiotic class and the resistance mechanisms of the cells. IR occurs when the resistant population can detoxify the environment, reducing drug concentrations to levels that allow the growth of the sensitive subpopulation. In the study conducted by Nicoloff and Andersson [196], a direct relationship between the resistance mechanism and the emergence of IR was demonstrated. Indirect resistance was observed when antibiotic inactivation occurred extracellularly, as it happens for many  $\beta$ -lactams. In contrast, when antibiotic inactivation happened intracellularly, the emergence of IR depended on the rate of inactivation. IR emerged for fast intracellular inactivations, such as with macrolides or chloramphenicol. However, no IR emerged for slow inactivations, as happens with aminoglycosides. Indirect resistance has been reported for  $\beta$ -lactams not only in liquid cultures but also in range expansion experiments [197, 198]. However, indirect resistance has not yet been observed in spatially organised communities treated with antibiotics that are primarily inactivated intracellularly, such as macrolides or chloramphenicol.

Chloramphenicol (Cm) is a broad-range bacteriostatic antibiotic that targets bacterial ribosomes by binding the peptidyl transferase centre and inhibiting peptide chain elongation [199]. Chloramphenicol penetrates the bacterial membrane by diffusion. Once in the cytosol, Cm binds to the 50S ribosomal sub-unit at the peptidyltransferase site and prevents the binding of aminoacyl-tRNA to the A-site of the 50S sub-unit. As a result, bacterial growth is suppressed by inhibition of the peptide bond form. Resistance to chloramphenicol primarily results from intracellular antibiotic inactivation, but it can also occur due to reduced membrane permeability of the cells. The antibiotic inactivation happens via chloramphenicol

acetyltransferase (CAT). CAT neutralises the antibiotic by catalysing the addition of an acetyl group to Cm. Acetylation prevents the antibiotic from binding to its target. There are two distinct types of CAT. The *catA* gene can be found on transposons and plasmids. Gram-negative bacteria produce the CatB enzyme [200]. Chloramphenicol is no longer widely used to treat bacterial infections, but due to its interesting behaviour, it is frequently used to perform many *in vitro* studies. Its action shows a complex interplay with the physiology of *E. coli* cells [201] and can induce growth bi-stability in strains with moderate levels of resistance to the drug[202].

### 4.1.1 Objectives

This chapter delves into the emergence of indirect resistance in spatially distributed bacterial communities under chloramphenicol stress. While self-organised communities are reported to present higher tolerance to antibiotics, there is limited evidence that indirect resistance significantly contributes to this endurance. Understanding the role of indirect resistance and its connection to antibiotic tolerance could potentially explain the failure of antibiotic treatments in many clinical infections.

The study was conducted using *in vitro* and *in silico* systems. The investigation was designed to understand how the strength of indirect resistance changed as the communities self-organised into two-dimensional and three-dimensional conformations. Pairs of isogenic *E. coli* K-12 strains, differing only in their resistance to the antibiotic chloramphenicol, were chosen as the experimental system for this study. The experiments were conducted with antibiotic concentrations both above and below the minimum inhibitory concentration (MIC) of the sensitive strain. The MIC is defined as the lowest concentration of chloramphenicol that prevented visible growth of the sensitive cells under controlled *in vitro* conditions [203].

Chloramphenicol was the antibiotic chosen as it had been reported to lead to indirect resistance in batch cultures of *E. coli* [196]. In the strains of interest, chloramphenicol deactivation occurs intracellularly, meaning that resistant cells detoxify their environment locally. This makes the emergence of indirect resistance highly dependent on spatial organisation. If an antibiotic with extracellular degradation were used, the deactivating enzymes would diffuse further from the location of resistant cells, making the effect of spatial organisation more difficult to quantify, as sensitive bacteria not in direct contact with resistant cells could experience indirect resistance. Additionally, chloramphenicol is a bactericidal antibiotic at low concentrations, allowing experiments to be conducted above the MIC value of sensitive cells. When a sensitive population is treated with a bactericidal antibiotic above its MIC, the cells stay dormant rather than dying. This allows for their growth later in the system once the environment is detoxified by resistant cells.

I designed the original research question and performed the experiments and simulations to answer it. However, the project became highly collaborative. I performed the liquid and two-dimensional experiments together with A. Talliou. The collision of fluorescent 2D colonies was conducted by A. Talliou and A. Sarlet. I developed the agent-based model and the simulations presented in this chapter. Currently, B.H. Thomsen is working on an individual-based model that reproduces the experimental results of collision experiments. The results presented in this chapter are unpublished, and a manuscript containing them is under preparation at the time of submission with the preliminary title: "Indirect antibiotic resistance enhances colony tolerance in mixed bacterial communities" (see appendix A.3).

## 4.2 Materials and Methods

### 4.2.1 Experimental methods

**Bacterial Strains** The experimental study was performed with different pairs of one sensitive and one resistant strain to the antibiotic chloramphenicol (Cm). A detailed description of the strains can be found in 4.1 and references therein.

The first pair of strains, SLS4333 (SEN) and TSS290 (RES) were derivatives of *E. coli* K-12 MAS1081, a motile strain [204]. Cell motility did not play an important role in this study, as the experiments were either performed in well-mixed systems or in environments that hindered cell motility. The RES strain encoded the enzyme chloramphenicol acetyltransferase (CAT) in the *lac* operon. None of them contained any fluorescent markers. The strains could, however, be distinguished via blue-white screening when growing on appropriate substrates, as the resistance gene was encoded in the *lacZYA* operon. The blue-white screening was performed by adding the chromogenic substrate 5-bromo-4-chloro-3-indolyl- $\beta$ -D-galactopyranoside (X-gal) to the plates. If  $\beta$ -galactoside was produced, X-gal was hydrolysed, and consequently, an insoluble blue pigment was produced. Isopropyl  $\beta$ -D-1-thiogalactopyranoside (IPTG), a non-metabolizable analogue of galactose, was also added to the plates to induce the expression of the *lacZ* gene.

The second pair of strains, TB194 (RES-R) and TB204 (SEN-G) were derivatives of *E. coli* K-12 MG1655, also a motile strain [17]. Olga Schubert and Martin Ackermann kindly provided the strains from the Microbial Systems Ecology group (Eawag). The sensitive strain (SEN-G) had the Superfolder green-fluorescent protein (sfGFP) encoded in its chromosome. The resistant strain (RES-R) had a red fluorescent protein (mCherry) encoded in its chromosome. A flanked chloramphenicol resistance cassette provided the resistance to chloramphenicol. A complementary pair of strains was available where the

resistant strain TB193 (RES-G) contained the GFP in its genome, and the sensitive strain TB205 (SEN-R) the RFP.

Name	Strain	Relevant characteristics	Reference
SEN	SLS4223	K-12 MAS1081 (MG1655 $rph^+$ $gatC^+$ $glpR^+$ )	[205]
RES	TSS290	SLS4223: $lacZYA::cat$	[205]
RES-G	TB193	MG1655: $attP21-P_R-sfGFP-chlorR$	[206]
RES-R	TB194	MG1655: $attP21-P_R-mCherry-chlorR$	[206]
SEN-G	TB204	MG1655 $attP21::P_R-sfGFP$	[207]
SEN-R	TB205	MG1655 $attP21::P_R-mCherry$	[207]

Table 4.1 *E. coli* strains used in the study. Sine Lo Svenningsen kindly provided strains SLS4223 and TSS290. The strains TB193, TB194, TB204, and TB205 were kindly provided from the Olga Schubert and Martin Ackermann strain collection.

**Culture media** All experiments were performed using Luria-Bertani (LB) medium. The LB medium was composed of 10 g/l tryptone (16279751, Fisher Scientific), 5 g/l yeast extract (16279781, Fisher Scientific) and 5 g/l NaCl ( $\geq 99\%$ , S9888, Sigma-Aldrich) dissolved in Millipore water. The rich medium was supplemented with different chloramphenicol (C0378-5G, Sigma-Aldrich) concentrations varying from 1 to 9  $\mu\text{g}/\mu\text{l}$ . The antibiotic was stocked as a 10 mg/ml solution. To perform blue-white screening, the substrate was supplemented with 10  $\mu\text{l}$  X-gal (20 mg/ml) and 10  $\mu\text{l}$  IPTG (100 mM) per ml of media.

**MIC determination** The Minimum Inhibitory Concentration (MIC) of a bacteriostatic antibiotic corresponds to the lowest concentration (w/v) of the antibiotic, in our case Cm, that prevents visible cell growth under controlled *in vitro* conditions [203]. It can be determined in liquid cultures or on solid substrates, and its value can fluctuate depending on the experimental method used. Additionally, the MIC value for a bacteriostatic antibiotic is highly dependent on the nutritional media where it is determined [208]. The MIC value was determined via a susceptibility test conducted with E-TEST strips [209] on top of solid plates. Overnight cultures of the strains of interest were prepared. After diluting the culture to an  $OD_{600} \approx 0.2$ , 200  $\mu\text{l}$  of it was spread on top of a Petri dish (1.5% agar + LB). After 15 minutes, once the plate had dried, the antibiotic-infused strip was placed at the centre of the dish. The plates were then incubated (37°C) for 16 hours, and the results were visually read immediately after that. Following manufacturer instructions, the MIC value corresponded to the value on the strip where bacterial growth was inhibited by approximately 80%.

Susceptibility tests were conducted for all strains. As expected, the growth of the resistant strains was not hindered by the presence of chloramphenicol. Therefore, all the resistant strains had a MIC  $> 256 \mu\text{g/ml}$  Cm, which was the highest antibiotic concentration provided by the E-TEST strip. The MIC values of the sensitive strains can be found in Tab.4.2.

Name	Strain	MIC ( $\mu\text{g/ml}$ )
SEN	SLS4223	5
SEN-G	TB204	8
SEN-R	TB205	8

Table 4.2 The MIC values of the sensitive *E. coli* strains used in the study were obtained with an E-TEST strip placed on top of LB medium. The MIC values of TB204 and TB205 were the same since the strains were isogenic, with the only exception of their fluorescent protein.

The MIC values of the sensitive strains were used to design the experimental study. For each pair of strains, three distinct regions were explored: below MIC, at MIC, and above MIC.

**Growth curves** The strains were grown overnight at  $37^\circ\text{C}$  with shaking in LB medium without antibiotics. In the morning, the samples were 1000x diluted in fresh medium supplemented with the Cm concentration of interest. The initial optical density at 600 nm ( $\text{OD}_{600}$ ) was measured. Once incubation started (at  $37^\circ\text{C}$ ), the  $\text{OD}_{600}$  was measured every 45 minutes for 6 hours in total.

**Liquid competition** For competition in liquid experiments, overnight cultures of the strains ( $37^\circ\text{C}$ ) without antibiotics were diluted in a 1:1 suspension. The new suspension was set to start from an initial  $\text{OD}_{600}$  of 0.1. The ratio between each strain was adjusted based on the measured  $\text{OD}_{600}$  of the overnight cultures and the following equations 4.1, 4.2 and 4.3:

$$V_A = \frac{\text{OD}_{600}^{\text{final}}}{\text{OD}_{600}^A} \cdot \text{ratio}_A \cdot V_{\text{tot}} \quad (4.1)$$

$$V_B = \frac{\text{OD}_{600}^{\text{final}}}{\text{OD}_{600}^B} \cdot \text{ratio}_B \cdot V_{\text{tot}} \quad (4.2)$$

$$V_{\text{media}} = V_{\text{tot}} - V_A - V_B \quad (4.3)$$

Where  $V_{A,B}$  corresponds to the volume of each strain required to obtain a final culture of volume  $V_{\text{tot}}$ ,  $\text{ratio}_{A,B}$  corresponds to the desired fraction of each strain in the final mixture.

The samples were cultured for 6 hours at 37°C with shaking. After that time, the OD<sub>600</sub> of each solution was measured, and the number of cells of the culture was estimated (cells/ml  $\approx$  OD<sub>600</sub> · 5 · 10<sup>8</sup> cells/ml) [210]. With the cell number estimation, the culture was diluted to approximately 3 cells/ $\mu$ l. 100  $\mu$ l of the resulting suspension was plated on top of a Petri dish (1.5% agar + LB) without antibiotics but supplemented with IPTG and X-gal. After overnight incubation, the exact number of cells and the ratio between strains were estimated after counting the colony-forming units (CFUs) of each strain. The sensitive colonies appeared blue, while the resistant ones were colourless on top of the X-gal plates.

The experiment was repeated for medium supplemented with three different Cm concentrations (4,5 and 6  $\mu$ g/ml) and without antibiotics. For each condition, mixed cultures and individual resistant and sensitive strains were grown.

**Centre-Edge assay** Starting from overnight cultures of a resistant and a sensitive strain, non-supplemented with antibiotics, a mix of 1:1 fraction with a final OD<sub>600</sub> = 0.3 was prepared. The volume of each strain required was found with Eq.4.1, Eq.4.2 and Eq.4.3. Then, 0.5  $\mu$ l of the final culture was placed with a pipette on top of 1.5% agar + LB plates with different antibiotic concentrations.

After 48 hours of incubation (37°C), the colonies were sampled from two different points: the centre and the edge of the colony. Each sample was re-suspended in 0.9% saline (NaCl+H<sub>2</sub>O) and plated onto a 1.5% agar + LB plate supplemented with IPTG and X-gal. The sample from the centre of the colony was collected with a 10  $\mu$ l pipette. The edge of the colony was sampled after covering the centre of the colony with a glass tube and scrapping the rest. The plates were left to dry and were incubated for 16h. After incubation, the number of CFUs of each strain was counted to determine the ratio between subpopulations at the centre and at the edge of the colony. The sensitive colonies appeared blue, while the resistant ones were colourless on top of the X-gal plates.

The experiment was repeated for media supplemented with three different Cm concentrations (0.1, 1 and 4  $\mu$ g/ml) and without antibiotics.

**Relative Fitness** The relative fitness between two strains describes the reproductive success of one subpopulation over the other [167]. The relative fitness,  $W_{ij}$ , of strain  $i$  with respect to strain  $j$  is estimated as the ratio between the number of doublings of the subpopulations:

$$W_{ij} = \frac{\ln(N_i(t)/N_i(0))}{\ln(N_j(t)/N_j(0))}, \quad (4.4)$$

Where  $N_i(t)/N_i(0)$  and  $N_j(t)/N_j(0)$  are the ratios of a number of cells at time  $t$  compared to the starting point of strain  $i$  and  $j$ , respectively. The relative fitness was used to quantify liquid experiments, centre-edge assays and simulated populations. It was used to quantify either the fitness of the sensitive over the resistant strain or the fitness of the sensitive subpopulation growing under different conditions.

**Colony Collision** Starting from overnight cultures of the resistant and the sensitive strain, non-supplemented with antibiotics, each culture was diluted to reach an OD<sub>600</sub> of 0.3. From the diluted cultures, 1  $\mu$ l droplet of the sensitive strain was placed 1 mm away from a 1  $\mu$ l droplet of the resistant strain on top of solid agar plates (1.5% agar + LB) supplemented with different chloramphenicol concentrations. The plates were then incubated for 24 hours at 37°C until the colonies collided with each other.

The experiment was conducted for the non-fluorescent pair of strains (RES/SEN) by supplementing the plate with IPTG and X-gal. For the pair RES/SEN, the experiment was performed at 0, 4, 5, 5.5, 6, 7, 8 and 9  $\mu$ g/ml of chloramphenicol. The fluorescent strains (RES-R/SEN-G) were tested in this setup. After growing at either 0,3,4,5,6 or 7  $\mu$ g/ml, the collision edge of the colonies was imaged with an inverted fluorescent microscope.

**Image Acquisition** The collision of colonies was imaged with an inverted microscope (Nikon Eclipse Ti fluorescent) paired with a camera (Andor, Belfast, UK). A 4x air immersion objective was chosen (Nikon, Plan Fluor, 4x/0.13,  $\infty$ /1.2 WD 16.5). In this setup, the GFP was excited with a mercury-vapour lamp and filtered with the FITC cube (FITC Filter Cube Set, Olympus, York, UK). The RFP was also excited with a mercury-vapour lamp and filtered with the Texas Red cubes (Texas Red<sup>TM</sup> Filter Cube Set, Nikon, Tokyo, Japan).

**Image Analysis** The image analysis of the fluorescent colonies collision was performed with Fiji build-in functions [111]. The parameter characterised was the length of the collision border for the sensitive subpopulation, which expressed a GFP protein, as the antibiotic concentration increased. To do so, first, the GFP channel was manually thresholded. The border of the colony was found with Process→ Find Edges. Two parameters were obtained by quantifying the edge of the colony. The length of the resulting edge was measured with Analyse→ Measure. This function measures the distance between consecutive pixels and adds them up, providing the total length of the collision border,  $L_c$ :

$$L_c = \sum_{i=0}^{N-1} \sqrt{(x_{i+1} - x_i)^2 + (y_{i+1} - y_i)^2} \quad (4.5)$$

Where  $(x_i, y_i)$  represents the position of each pixel on the edge. The end-to-end distance ( $r_{ee}$ ) of the sensitive colony collision front was found by calculating the length of a straight line connecting the ends of the edge:

$$r_{ee} = \sqrt{(x_N - x_0)^2 + (y_N - y_0)^2} \quad (4.6)$$

Where  $(x_N, y_N)$  were the coordinates of the final pixel, and  $(x_0, y_0)$  were the coordinates of the initial pixel of the edge. By knowing the values of the length of the collision border ( $L_c$ ) and its end-to-end distance ( $r_{ee}$ ), a tortuosity parameter ( $T$ ) was defined as:

$$T = \frac{L_c}{r_{ee}} \quad (4.7)$$

The higher the tortuosity, the further the collision edge was from being a straight line.

## 4.2.2 Computational methods

**Lattice model** A study of the experimental system was conducted with a modified Eden growth model [114], incorporating the effects of a bacteriostatic antibiotic into the system. In the model, cells grew on a lattice, where each site could be occupied by at most one cell. The simulations were performed for cells growing in well-mixed, two-dimensional and three-dimensional communities.

The growth of communities in well-mixed and 2D conditions was simulated on a 2D squared lattice (of size  $L$ ), where each cell had four neighbouring sites. For the 3D simulations, cells grew in a cubic lattice (of size  $L$ ) with six neighbouring sites. Apart from the lattice dimension, the algorithm was the same for all three scenarios.

The system was initialised with an equal fraction of sensitive and resistant cells. Each subpopulation had distinct growth depending on the antibiotic concentration in the environment. The resistant cells had a constant growth rate ( $k_r$ ) across all antibiotic conditions. In contrast, the growth of the sensitive cells ( $k_s$ ) decreased as the antibiotic concentration increased.

To simulate the antibiotic field, a lattice representing the antibiotic concentrations was initialised with a constant value,  $A_{ini}$ . The antibiotic diffused through the lattice according to the diffusion equation ( $D = 1$ ) with Neumann boundary conditions.

$$\frac{\partial A}{\partial t} = D\nabla^2 A \quad (4.8)$$

The antibiotic concentration at lattice sites occupied by resistant cells decreased proportionally to the degradation rate of the resistant strain ( $\gamma$ ).

The evolution of the population was implemented by counting the number of resistant ( $N_r$ ) and sensitive ( $N_s$ ) cells that had available growing sites and updating the system following a Gillespie algorithm [115]. The following steps were iterated:

1. Find the total number of sensitive cells with available growth sites ( $N_s$ ) and evaluate their growth rate ( $k_s(A)$ ) using the antibiotic concentration at their lattice position.
2. Find the total number of resistant cells with available growth sites ( $N_r$ ). Resistant cells had a growth rate independent of antibiotic concentration ( $k_r$ ).
3. Find the total event rate  $T$  as the sum of all possible growth events:  $T = \sum^{N_s} k_s(A) + N_r \cdot k_r$ . Determine the duration of the event as  $\tau = -\ln(r)/T$  where  $r$  is a random number from a uniform distribution ( $r = U \subseteq (0, 1)$ ). Increase the simulation time and the integration time by  $\tau$ .
4. Draw a random number from a uniform distribution between zero and one ( $a = U \subseteq (0, 1)$ ) and determine which cell will grow. If  $a < \frac{\sum^{N_s} k_s(A)}{T}$ , a sensitive cell will divide. Otherwise, a resistant cell will grow.
5. Check if the integration time exceeds a user-defined time interval ( $dt$ ). If it does, set it back to zero and solve the diffusion equation for the antibiotic field, including a reduction of antibiotic concentration ( $-\gamma \cdot dt$ ) in the lattice sites occupied by resistant cells.
6. Return to (1). In a well-mixed system, shuffle the positions of the cells randomly before continuing.

The simulations were quantified with the relative fitness of the sensitive population compared to the resistant population. The parameter was introduced in Eq.4.4. All simulations were initialised with a droplet containing 70% cell occupancy and left to evolve until the cell count of the total population reached 20 times the initial cell number.

## 4.3 Results

### 4.3.1 Spatial organisation affects the outcome of indirect resistance

The impact of spatial organisation on the emergence of indirect resistance was investigated with agent-based simulations. The simulated systems contained two subpopulations of cells, resistant and sensitive, growing in the presence of a bacteriostatic antibiotic. The sensitive cells presented a growth rate dependent on antibiotic concentration, whereas the resistant cells had a constant growth rate. The growth rates as a function of antibiotic concentration are represented in Fig.4.2a. In the absence of antibiotics, sensitive cells grew faster than resistant ones. This difference in growth rates was chosen to reflect the metabolic cost associated with the expression of the resistance machinery. As the concentration of antibiotic increased, the growth rate of the sensitive cells decreased until reaching zero at approximately 5.5 (a.u.), which corresponded to the MIC value for the sensitive cells. The antibiotic diffused through the system following the diffusion equation and was locally degraded at rate  $\gamma$  by resistant cells. The system was simulated in well-mixed, two-dimensional and three-dimensional conditions, and the relative fitness of sensitive cells compared to resistant cells was measured ( $W_{SR}$ ). A relative fitness greater than one indicated preferential growth of sensitive cells, while values below one indicated preferential growth of resistant cells. Each spatial setting was simulated for eight initial antibiotic concentrations ( $A_{ini} \in (0, 7)$  a.u.) and four degradation rates by the resistant cells ( $\gamma = 0, 5, 50$  and  $500$ ).

The well-mixed conditions aimed to reproduce growth in liquid cultures with shaking. The system was initialised on a 2D lattice and evolved according to the algorithm described in section 4.2.2. At each time step, cell positions were updated randomly to mimic the zero-dimensional nature of liquid systems. The relative fitness of the sensitive strain in a well-mixed environment is shown in Fig.4.2b. At low antibiotic concentrations (from 0 to 2 a.u.), the sensitive strain was more fit than the resistant cells, even in the absence of antibiotic degradation ( $\gamma = 0$ , blue line). At intermediate values below MIC, if no degradation was present, the fitness of the sensitive cells declined sharply and reached zero above the MIC value (5.5 a.u.). A small antibiotic degradation ( $\gamma = 5$ , green line) allowed the sensitive cells to grow for values above their MIC. However, the sensitive strain was less fit than the resistant at high antibiotic concentrations. In contrast, with high levels of antibiotic degradation ( $\gamma = 50$  orange line and  $\gamma = 500$  red line), the sensitive cells not only grew above their MIC but also maintained their fitness advantage over the resistant cells.

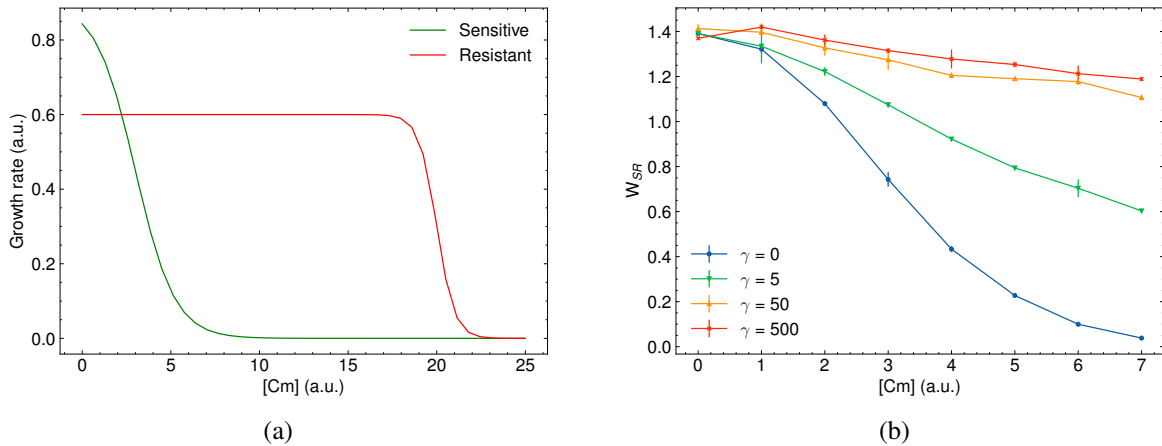


Fig. 4.2 **A**: Growth rate of the resistant and the sensitive simulated strains as a function of the antibiotic (a.u.). The resistant strain maintained its growth rate as the concentration increased, while the sensitive decreased at low antibiotic concentrations and stopped growing for concentrations above 5.5 (MIC). **B**: Relative fitness of the sensitive strain when co-cultured with a resistant strain in a well-mixed system at different antibiotic concentrations ( $N=5$ ). As the antibiotic degradation by the resistant strain increased ( $\gamma$ ), the sensitive strain maintained its fitness advantage even for values above its MIC.

The fitness of 2D communities is shown in Fig.4.3A. As reported for the well-mixed system at low antibiotic concentrations (from 0 to 2 a.u.), the sensitive strain was more fit than the resistant due to their differences in growth rates. In the absence of antibiotic degradation ( $\gamma = 0$ ), the fitness of the sensitive strains fell to zero for antibiotic concentrations below their theoretical MIC value. When degradation was present in the system, the fitness of the sensitive still fell as the antibiotic increased, but it did not reach zero. Similar trends were observed for the three degradation rates ( $\gamma = 5, 50$  and  $500$ ), suggesting that antibiotic degradation was not the key parameter controlling the outcome of the system. These results become easier to interpret when the spatial constraints of the communities are considered. As opposed to well-mixed conditions, in 2D communities, cells compete not only for nutrients but also for space. Once a subpopulation of cells was blocked from the expanding front, they could no longer grow because all their neighbouring sites were occupied. Consequently, regardless of the degradation rate, if resistant cells dominated the expansion front in the initial stages of the community, the sensitive population had limited opportunities to grow, even after the environment was detoxified by resistant cells. Fig.4.3B displays 2D communities when the initial antibiotic was set to 3 a.u. Without degradation ( $\gamma = 0$ , bottom colony), the resistant cells grew faster than the sensitive ones and took over the whole colony. For high levels of degradation ( $\gamma = 500$ , top colony), the sensitive cells experienced a decrease in antibiotic concentration early in the colony development, which increased their growth rate and led to the formation of sectors that persisted throughout the entire simulation.

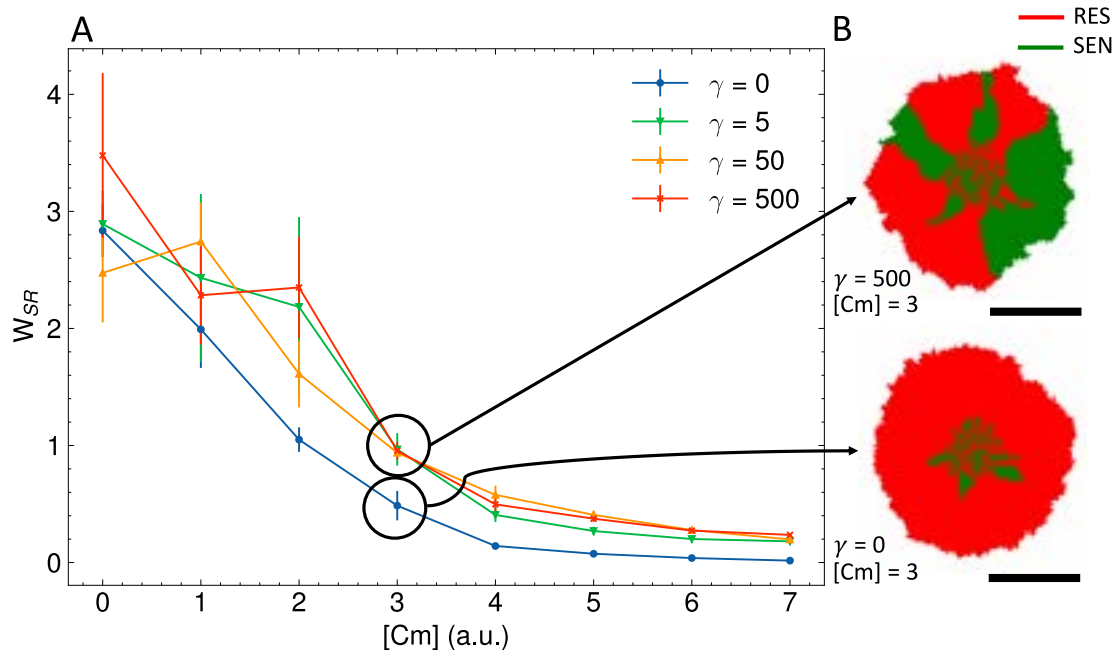


Fig. 4.3 **A**: Relative fitness of the sensitive strain over the resistant when they grow in 2D range expansions at different antibiotic concentrations ( $N=5$ ). In 2D systems, the degradation of antibiotic ( $\gamma$ ) did not stop the decrease of fitness of the sensitive strain as the antibiotic concentration increased. The fitness was obtained after the number of initial cells had been increased 20 times. **B**: Examples of the 2D simulated populations, with the sensitive cells represented as green pixels and the resistant cells as red. The top colony, where antibiotic degradation occurs, presents sectors of both the resistant and the sensitive strains. The bottom colony showcases how the sensitive strain loses the expansion front of the colony. The scale bar corresponds to 50 pixels (lattice sites).

The fitness of 3D communities is shown in Fig.4.4A. At low antibiotic concentrations (from 0 to 2 a.u.), the sensitive strain exhibited higher fitness compared to the resistant strain. In the absence of antibiotic degradation ( $\gamma = 0$ ), the fitness of the sensitive strain fell as the antibiotic concentration increased. The difference in the fall rate can be attributed to the spatial organisation of the community. In 3D, the cells still competed for space, but they had more possible growing sites compared to the 2D case. Therefore, longer times would be required for one population to block another subpopulation completely at the colony front. In 3D simulations, distinct fitness curves were observed for different degradation rates. Higher degradation rates ( $\gamma$ ) slowed the decrease in fitness as antibiotic concentration increased. Despite this, the fitness of the sensitive strain was never higher than one, but the sensitive cells managed to grow above their MIC for all the investigated degradation rates. Fig.4.4B displays 3D communities when the initial antibiotic was set to 3 a.u. Without degradation ( $\gamma = 0$ , bottom colony), the resistant cells grew faster than the sensitive ones and took most of the surface of the colony. However, regions of sensitive cells were still present. For high

levels of degradation ( $\gamma = 500$ , top colony), the sensitive cells experienced an increase in their growth rate and dominated the majority of the colony surface.

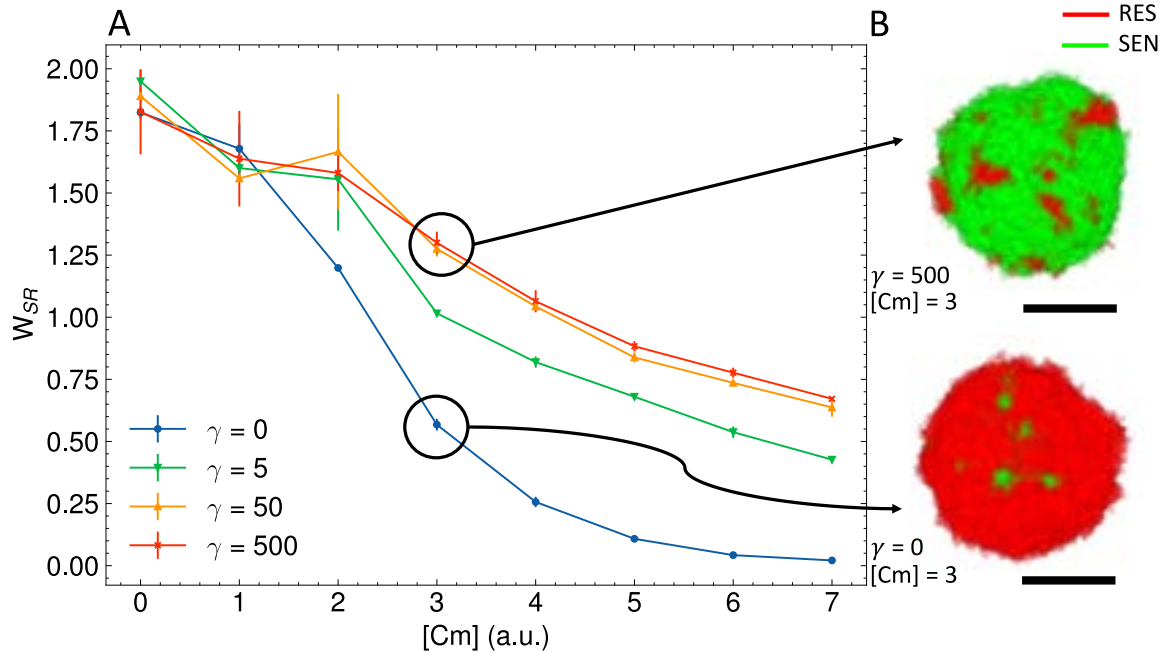


Fig. 4.4 **A**: Relative fitness of the sensitive strain over the resistant when they grow in 3D range expansions at different antibiotic concentrations ( $N=5$ ). In 3D systems, the degradation of antibiotic ( $\gamma$ ) increased the fitness of the sensitive strain compared to the case without degradation. The fitness was obtained after the number of initial cells had been increased 20 times. **B**: Examples of the 3D simulated populations, with the sensitive cells represented as green pixels and the resistant cells as red. The bottom colony, where there is no antibiotic degradation, showcases how the surface of the colony is almost fully occupied by resistant cells. The top colony, where antibiotic degradation occurs, presents the opposite behaviour, a surface dominated by sensitive cells. The scale bar corresponds to 50 pixels (lattice sites).

The simulations revealed qualitative differences as the communities grew across different spatial configurations. From the simulated systems, indirect resistance was expected in experimental studies performed in liquid cultures, as it was proven to be a robust phenomenon in the well-mixed simulations. In experimental 2D communities, indirect resistance was anticipated to be elusive and dependent on multiple variables. The emergence of indirect resistance was expected to be recovered in 3D communities, where the increased number of neighbouring cells provided more opportunities for interactions and complex competition.

### 4.3.2 Indirect resistance emerges in liquid cultures

The first part of the study aimed to show the emergence of indirect resistance when a resistant and a sensitive strain were treated with chloramphenicol in liquid cultures. The results were presented to be comparable to those reported by Frost et al. [198]. In that study, the cell divisions of the strains were plotted as a function of an antibiotic concentration. They observed indirect resistance for an extracellularly degraded antibiotic (carbenicillin) but not for an intracellularly degraded one (streptomycin). The results aligned well with the values reported by Nicoloff and Andersson [196].

The liquid experiments were performed using the sensitive strain SLS4223 (SEN) and the resistant strain TSS290 (RES) to the antibiotic chloramphenicol (Cm). The strains have been described in detail in section 4.2.1. The strains were grown both individually and co-cultured in rich liquid media at varying Cm concentrations. The experiments were conducted without antibiotics and at Cm concentrations below, above and at the MIC value ( $5 \mu\text{g/ml}$ ) of the sensitive strain. The results of the experiments were reported using the cell divisions parameter [198]. The cell divisions measured the number of times the initial number of cells of a subpopulation had doubled:

$$\text{Cell Divisions} = \log_2 \left( \frac{N_f}{N_i} \right) \quad (4.9)$$

Where  $N_i$  corresponds to the initial number of cells and  $N_f$  to the final number of cells of a subpopulation. In this study, the initial number of cells was estimated from the measured  $\text{OD}_{600}$  value of the initial culture using the conversion:  $\text{cells/ml} \approx \text{OD}_{600} \cdot 5 \cdot 10^8 \text{ cells/ml}$  [210]. The final number of cells was estimated from the  $\text{OD}_{600}$  value after 6 hours of incubation at  $37^\circ\text{C}$ . For the mixed cultures, the fraction of each subpopulation in said  $\text{OD}_{600}$  was obtained from CFU counting in blue-white screening plates (see section 4.2.1 for details).

The number of cell divisions as a function of the chloramphenicol concentration can be seen in Fig. 4.5a and Fig. 4.5b. In individual cultures, the resistant strain (RES) kept its number of cell divisions approximately constant as the antibiotic concentration increased. When co-cultured with the sensitive strain (SEN), in the absence of antibiotics, RES reduced its number of divisions. In the mixed system, as antibiotic concentration increased, the number of cell divisions of the resistant strain slightly increased (Fig.4.5a). The sensitive strain (SEN) decreased its number of cell divisions to less than one when growing by itself. It presented similar cell divisions for antibiotic concentrations below, above and at their MIC value ( $5 \mu\text{g/ml}$ )

When SEN was co-cultured with RES, it experienced an increase in cell divisions, not only in the absence of antibiotics but also when chloramphenicol was introduced into the system (Fig.4.5b). The number of cell divisions slightly decreased at the MIC value (5  $\mu\text{g/ml}$ ) but seemed to be maintained as the Cm concentration increased (6  $\mu\text{g/ml}$ ).

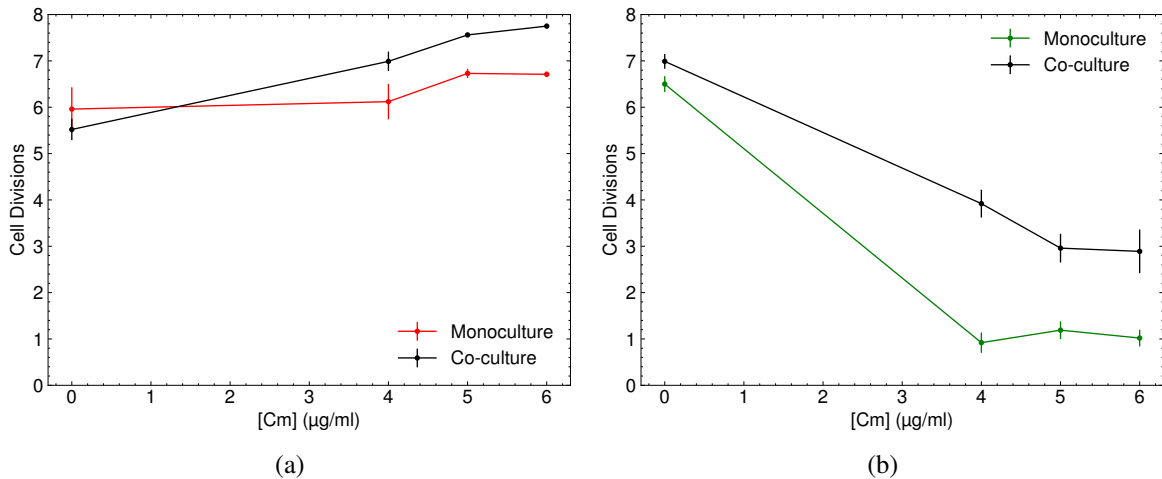


Fig. 4.5 **A**: Cell divisions of the resistant strain in monocultures (red) and co-cultured with a sensitive strain (black) at different chloramphenicol concentrations. **B**: Cell divisions of the sensitive strain in monocultures (green) and co-cultured with a resistant strain (black) at different chloramphenicol concentrations. The number of sensitive cell divisions increased in the co-culture, even for antibiotic values above its MIC.

The reported number of cell divisions indicated that the sensitive strain was able to grow in conditions where it could not do it alone when it was in the presence of resistant cells. Sensitive cells dividing above their MIC value indicated the emergence of indirect resistance in the experimental setup.

To be consistent with the results from the agent-based model simulations, the results of the liquid cultures were also represented as the relative fitness of the sensitive strain compared to the resistant strain ( $W_{SR}$ ). The relative fitness as a function of chloramphenicol for the liquid co-cultures can be seen in Fig.4.6. In the absence of antibiotics, the sensitive strain was more fit than the resistant strain ( $W_{SR} > 1$ ). However, this advantage fell in the presence of antibiotics. Comparing the behaviour of the fitness curve with the ones obtained from the simulation of the well-mixed systems, it can be concluded that the resistant strain degraded the antibiotic, but not at a particularly fast rate (Fig.4.2b).

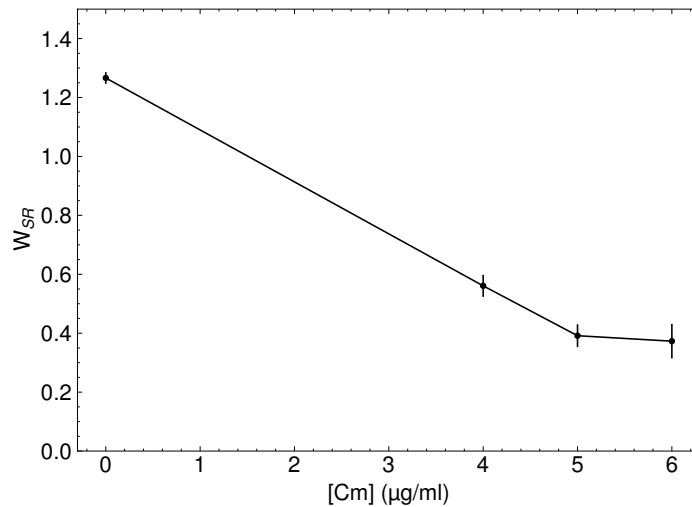


Fig. 4.6 Relative fitness of the sensitive strain compared to the resistant strain in liquid co-cultures. In the absence of antibiotics, the sensitive strain was more fit than the resistant, but the fitness fell with chloramphenicol concentration. The fitness was maintained above zero for antibiotic concentrations greater than the MIC value.

### 4.3.3 Resistant cells dominate two-dimensional range expansions

After demonstrating the emergence of indirect resistance in liquid cultures for the strains of interest, the next experiments aimed to find IR in two-dimensional configurations. The experiments performed were range expansions of mixed populations (1:1 fraction) on top of rich media agar plates at different chloramphenicol concentrations. Typically, range expansions use strains labelled with different fluorophores to quantify the occupancy of each subpopulation through fluorescent microscopy. Since RES and SEN were not fluorescent, the occupancy of each subpopulation was found with a different protocol, modified from Booth et al. [211]. After 48 hours of incubation, samples from the centre and the edge of the 2D colony were collected. The samples were re-suspended in saline (0.9% NaCl+H<sub>2</sub>O) to avoid cell divisions and plated on blue-white screening plates. The occupancy (%) of each cell type was defined as the fraction of cells obtained by counting CFUs in the resulting plates.

The 2D range expansions were repeated for the case without antibiotics as well as different Cm concentrations. The antibiotic concentrations chosen were lower than those used in the liquid system because the simulations anticipated that indirect resistance was more difficult to emerge in 2D systems at high antibiotic concentrations (Fig.4.3). Therefore, the study was conducted for three chloramphenicol concentrations below the MIC of the sensitive strain: 4 µg/ml, 1 µg/ml and 0.1 µg/ml.

Fig.4.7a and Fig.4.7b show the occupancy of the resistant and sensitive strains at the centre and edge of the colony, respectively. At the centre of the colony, in the absence of antibiotics, the sensitive strain had higher occupancy than the resistant one (Fig.4.7a). At antibiotic concentrations as low as  $0.1 \mu\text{g/ml}$ , the advantage of sensitive cells had already disappeared. The occupancy of the sensitive cells continued decreasing for  $1 \mu\text{g/ml}$  and reached values close to zero for  $4 \mu\text{g/ml}$ . A similar trend was reported at the edge of the colony (Fig.4.7b), where the sensitive strain did not occupy any fraction of the edge at  $4 \mu\text{g/ml}$ . These results indicated that in 2D conformations, the sensitive strain experienced compromised growth for values below its MIC when co-cultured with resistant cells.

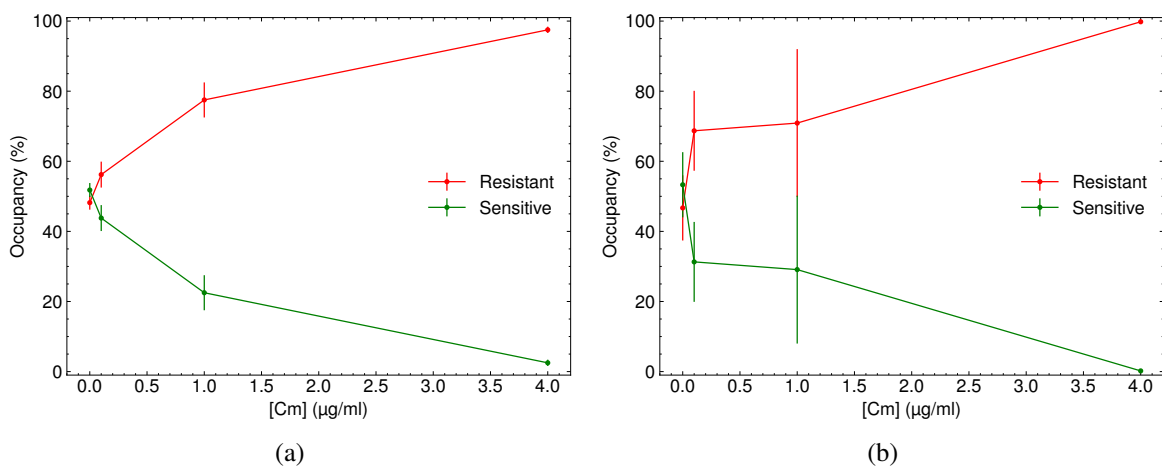


Fig. 4.7 **A**: Occupation of each strain (%) at the centre of a 2D colony at different chloramphenicol concentrations. The fraction of sensitive cells had already decreased at low antibiotic concentrations. **B**: Occupation of each strain (%) at the edge of a 2D colony at different chloramphenicol concentrations. The occupation at the edge of the colony followed the same pattern as the one at the centre. The resistant strain occupied most of the colony once an antibiotic was introduced into the system.

In this system, the relative fitness of the sensitive strain compared to the resistant was calculated from the samples at the centre of the colony, which provided the number of initial cells, and from the sample at the edge, which provided the final number of cells. Figure 4.8 shows the relative fitness as the chloramphenicol concentration increased. Without antibiotics, the sensitive strain was fitter than the resistant with a value really close to one, indicating that the advantage was minimal. The relative fitness decreased to 0.8 at  $0.1 \mu\text{g/ml}$  and remained constant until  $1 \mu\text{g/ml}$ . At  $4 \mu\text{g/ml}$ , the sensitive strain had a fitness close to zero, indicating that it did not benefit from coexisting with the resistant strain, and thus, no indirect resistance emerged. The fall in fitness was already predicted with the agent-based simulations. See Fig.4.3.

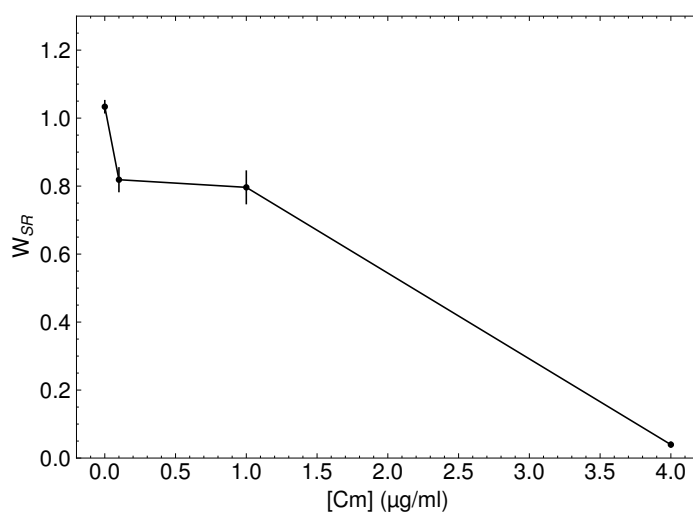


Fig. 4.8 The relative fitness of the sensitive strain compared to the resistant strain in 2D colonies was obtained from the samples at the centre (initial number of cells) and at the edge (final number of cells). In the absence of antibiotics, the sensitive strain was slightly more fit than the resistant, but the advantage quickly decreased, with chloramphenicol concentration falling to zero to values below its MIC.

The fitness advantage of the sensitive strain in the absence of antibiotics was expected to be higher than the one reported in Fig. 4.8 in order to observe indirect resistance in 2D configurations. For IR to emerge, the sensitive cells must grow relatively faster than the resistant ones without and at low antibiotic concentrations. The difference in growth rates would enable them to compete with the resistant cells once the environment is detoxified, preventing them from being left behind the expansion front. The experimental strains (RES and SEN) were characterised further by finding their growth rates at different chloramphenicol concentrations. Growth curve experiments were performed as detailed in section 4.2.1. The growth rates ( $\lambda$ ) obtained from fitting the curves are plotted in Fig.4.9 for the different antibiotic concentrations tested.

For media not supplemented with antibiotics, RES and SEN had no significant difference in growth rate. As anticipated, the resistant strain kept its growth rate constant despite the increase in the chloramphenicol concentration. Conversely, the growth rate of the sensitive strain began to decrease at  $0.1 \mu\text{g/ml}$  and at  $1 \mu\text{g/ml}$ , it was reduced to half its initial value. At  $4 \mu\text{g/ml}$  and  $5 \mu\text{g/ml}$ , no growth of the sensitive strain was detected, suggesting that the MIC value of SEN was actually below  $4 \mu\text{g/ml}$  when growing in liquid cultures for 6 hours. The MIC value of SEN obtained with the E-TEST was determined to be  $5 \mu\text{g/ml}$ . This discrepancy was not surprising, as MIC values are known to be highly sensitive to the testing protocol used [208].

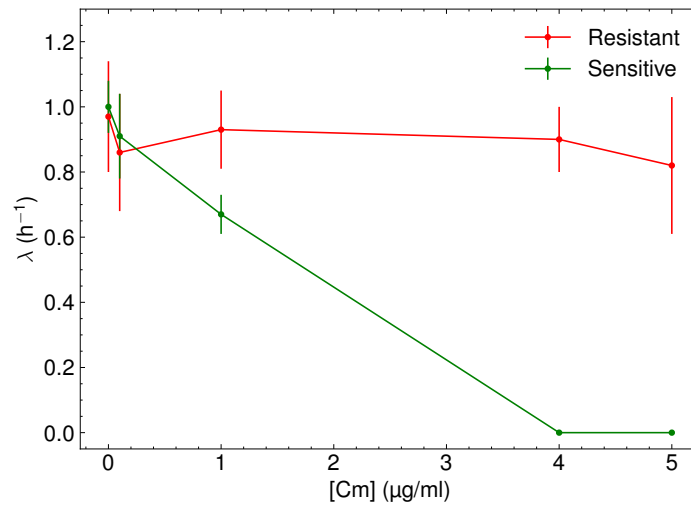


Fig. 4.9 Growth rate of RES and SEN in liquid cultures (LB) at different chloramphenicol concentrations. The resistant strain (TSS290) kept its growth rate constant over the investigated antibiotic concentrations. The sensitive strain (SLS4223) presented no growth for antibiotic concentrations below its reported MIC (5  $\mu\text{g/ml}$ ).

The growth rates of RES and SEN accounted for the lack of indirect resistance in 2D range expansions. The sensitive strain did not have a significant advantage over the resistant strain when no antibiotic was present, and its growth rate diminished as the antibiotic concentration increased. Therefore, when expanding in 2D, the resistant strain detoxified the environment but not quickly enough to allow the growth of sensitive cells at a fast rate. When the antibiotic was introduced into the system, resistant cells grew faster than sensitive ones. The resistant cells quickly reached the outer edge of the colony and continued to expand. This growth effectively blocked the sensitive cells, leaving them behind. Consequently, sensitive cells experienced a negative interaction from growing with resistant cells rather than benefiting from their protection against chloramphenicol.

#### 4.3.4 Indirect resistance arises in lower competitive settings

Indirect resistance was not observed in 2D range expansions where sensitive and resistant cells were co-cultured in equal proportions and competed for both nutrients and space. To observe IR in 2D settings, the experimental setup should be modified to reduce the competitive advantage of resistant cells, which arose from their difference in growth rates (Fig.4.9). The advantage of resistant cells could be reduced through diverse modifications, such as reducing their fraction in the initial inoculum of a 2D range expansion or studying the strains in a system where they would not directly compete for space. The latter was the option chosen as it was easy to implement by just placing droplets of each strain close

to the other on top of solid plates. As the droplets grew, each strain formed a colony, and these eventually collided. Thus, the sensitive and the resistant cells grew independently until collision, and all the interactions between cell types happened at the collision front. Such experimental setup was referred to as collision experiments.

During collision experiments, the focus was on how the resistant and sensitive strains interacted at the collision front to detect indirect resistance. Therefore, such a system was ideally studied via fluorescence to visualise cell interactions in detail. As previously stated, the resistant and sensitive strains used for the results presented in the previous sections did not express any fluorescent protein. Despite this limitation, preliminary collision experiments were performed with RES and SEN using blue-white screening plates to distinguish each strain. Blue-white screening plates were prepared at different chloramphenicol concentrations: 0, 4, 5, 5.5, 6, 7, 8 and 9  $\mu\text{g/ml}$ . Then, a 1  $\mu\text{l}$  droplet of SEN culture was inoculated 1 mm away from a previously deposited 1  $\mu\text{l}$  droplet of RES culture. The colonies were incubated at 37°C for 24 hours until they collided. The results of the study can be seen in Fig.4.10, where the sensitive cells correspond to the blue colonies as they hydrolysed X-gal.

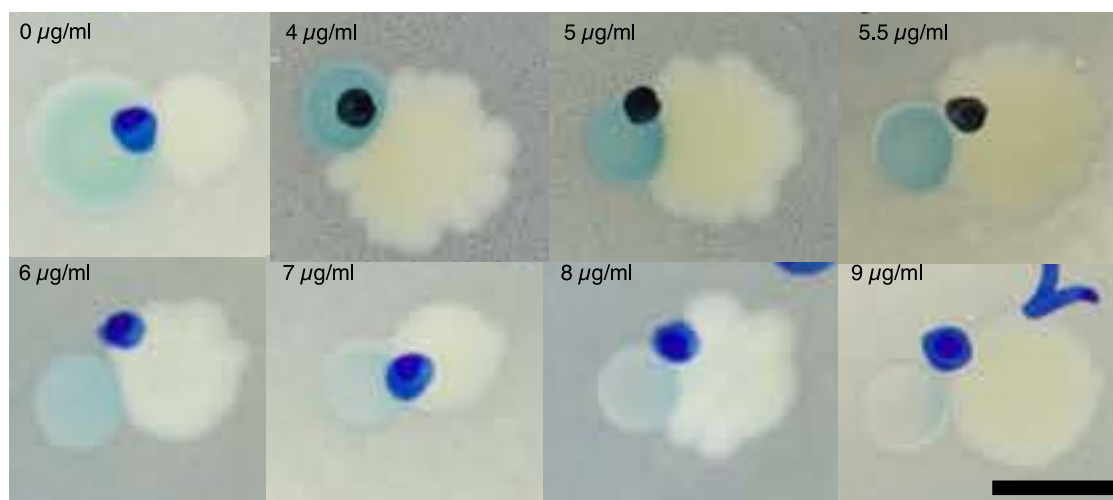


Fig. 4.10 Colony collision in blue-white screening plates (LB) at different chloramphenicol concentrations after 24h of incubation. The sensitive cells showcased a blue colour, while the resistant ones appeared colourless. The colony size was dependent on many stochastic parameters. However, increasing chloramphenicol concentration caused the sensitive colony to reduce its size consistently. The scale bar corresponds to 0.5 cm.

In the absence of antibiotics, resistant colonies appeared smaller in size compared to sensitive colonies, which displayed a uniform blue colour. When chloramphenicol concentration increased (4, 5, 5.5 and 6  $\mu\text{g/ml}$ ) but remained close to the MIC value of the sensitive strain, the size of the sensitive colony decreased compared to the resistant one and maintained a

uniform blue colour. As the antibiotic concentration went above the MIC of the sensitive cells (7, 8 and 9  $\mu\text{g/ml}$ ), the sensitive colony did not increase its size compared to the initial droplet, indicating that the antibiotic concentration was high enough to inhibit its growth. This growth reduction was also confirmed by the loss of uniform blue colour over the colonies. The emergence of regions with higher blue intensities indicated varying levels of metabolic activity within the population. At the highest antibiotic concentration, 9  $\mu\text{g/ml}$ , a gradient of colour towards the resistant colony was observed. This gradient indicated that the sensitive cells closer to the resistant ones were more metabolically active than those farther from them. When the colonies were incubated for an additional 48 hours, the resistant cells completely surrounded the sensitive colonies when growing at high antibiotic concentrations (7, 8 and 9  $\mu\text{g/ml}$ ). An example can be seen in Fig.4.11 for colonies grown at 9  $\mu\text{g/ml}$ . Interestingly, as the sensitive cells became surrounded by resistant cells, the colony regained a uniform blue colour, and some growth outside the inoculation droplet was visually observed.

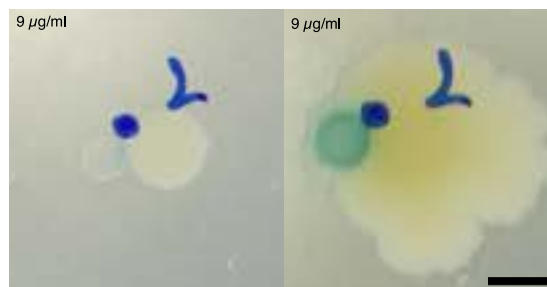


Fig. 4.11 Colony collision in blue-white screening plates (LB) at 9  $\mu\text{g/ml}$  chloramphenicol after 24 and 72 hours of incubation. The sensitive cells appeared blue, and the resistant ones remained colourless. After 48 additional incubation hours, the resistant cells started growing surrounding the sensitive ones, which made the latter increase its metabolic activity and appear more blue. The scale bar corresponds to 0.5 cm.

The change in metabolic activity of the sensitive cells, indicated by differences in blue intensity, was considered an indication of indirect resistance, as the sensitive cells closer to the resistant ones were more active. This setup proved to be a good experimental system for studying the emergence of indirect resistance in a two-dimensional system.

### 4.3.5 Intermixing between populations is induced by indirect resistance

A difference in the metabolic activity of the sensitive cells was observed in collision experiments via blue-white screening. However, fluorescence was required to understand which interactions happened at the collision front. The collision experiment was repeated for a different pair of sensitive (SEN-G) and resistant (RES-R) strains.

The sensitive strain TB204 (SEN) and the resistant strain TB194 (RES) to the antibiotic chloramphenicol (Cm) have been described in detail in section 4.2.1. The experiment was conducted by inoculating a  $1\ \mu\text{l}$  droplet of SEN-G culture 1 mm away from a previously deposited  $1\ \mu\text{l}$  droplet of RES-R culture in plates containing different Cm concentrations (0, 3, 4, 5, 6 or  $7\ \mu\text{g/ml}$ ). The plates were incubated for 24h at  $37^\circ$ . Once the colonies collided, the collision front was imaged with an inverted fluorescence microscope. Figure 4.12 shows the collision front at different antibiotic concentrations imaged with a 4x air objective. The sensitive cells appear green, and the resistant ones are red.

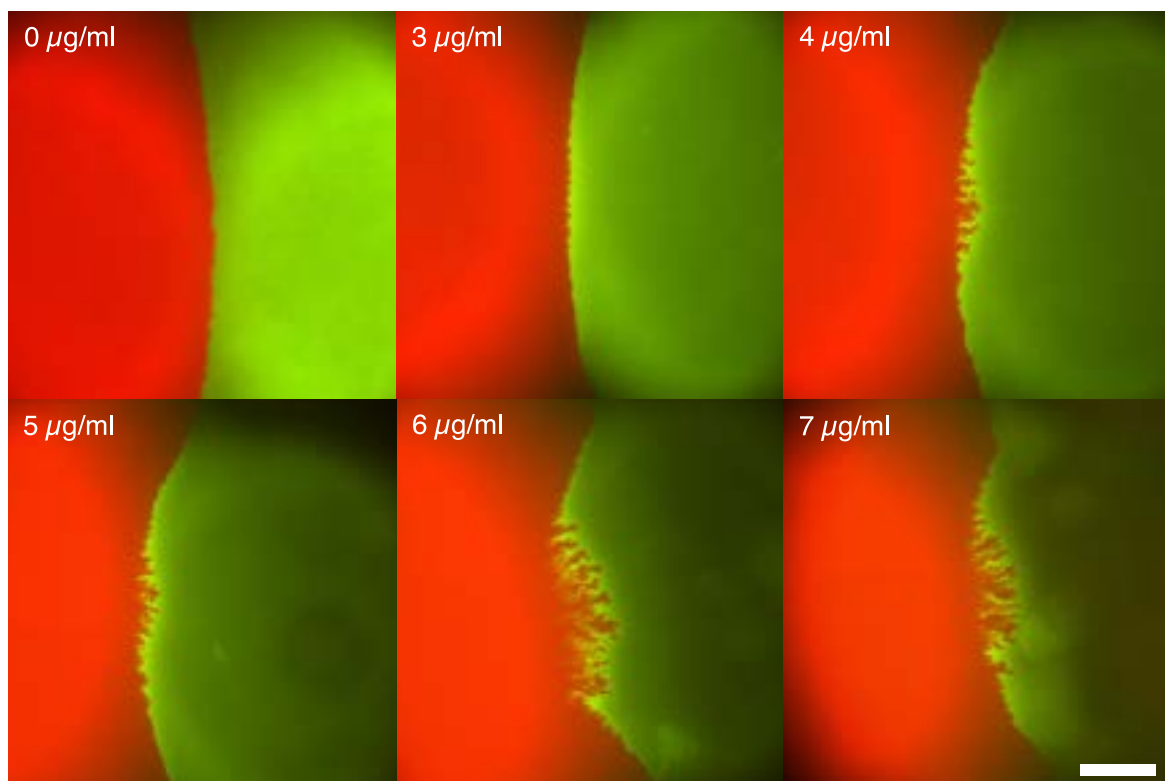


Fig. 4.12 Collision front of RES-R and SEN-G imaged with a 4x objective at different chloramphenicol concentrations. Without antibiotics, the collision front appeared as a straight line between the resistant (red) and sensitive (green) colonies. As the antibiotic concentration increased, the collision front appeared diffusive, and sectors of the sensitive colony emerged as the resistant colony grew towards it. The scale bar corresponds to  $500\ \mu\text{m}$ .

In the absence of antibiotics, the collision front between the sensitive and the resistant colony appeared as a straight line. At  $3\ \mu\text{g/ml}$ , the collision remained mostly straight, though some small perturbations were observed at its centre. These perturbations became more pronounced at  $4\ \mu\text{g/ml}$ , where the sensitive colony exhibited reduced growth evident from the curvature of the colony, which maintained the shape of the initial inoculation droplet. The deviations from a straight collision front were interpreted as sectors formed by the sensitive

cells as the resistant colony advanced towards them. As the chloramphenicol concentration increased further (5,6 and 7  $\mu\text{g/ml}$ ), both the number and the length of such sectors increased.

The behaviour observed in Fig.4.12 was quantified using the tortuosity parameter ( $T$ ), which measured how much the collision front deviated from a straight line. Higher tortuosities indicated intricated collision fronts, and tortuosities closer to ones corresponded to straight collision fronts. The tortuosity parameter as a function of chloramphenicol is plotted in Fig.4.13. The tortuosity increased with the antibiotic concentration.

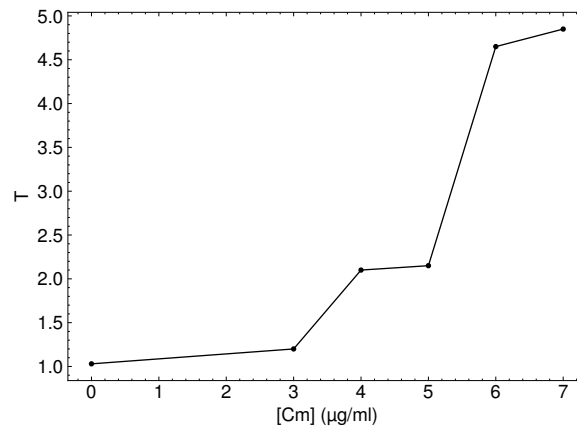


Fig. 4.13 Tortuosity of the colliding front at different antibiotic concentrations. The value was obtained after processing the fronts displayed in Fig4.12.

Collision experiments with fluorescent strains revealed an unknown phenomenon: as the antibiotic concentration increased, so did the tortuosity in the collision, leading to sensitive cells exhibiting greater contact with the resistant cells. The transition from a straight boundary to a convoluted one was interpreted as a result of indirect resistance, indicating that the sensitive cells benefited from their proximity to the resistant cells.

## 4.4 Discussion

A preliminary study conducted with an agent-based model examined how the relative fitness of a sensitive population compared to a resistant population varied as the spatial organisation of the system changed. Well-mixed simulations were performed to reproduce the conditions of experimental batch cultures. The relative fitness of the sensitive strain remained high even when high antibiotic concentrations and low drug degradation conditions were simulated. This indicated that indirect resistance was a robust phenomenon expected to emerge in a liquid medium, even with minimal drug degradation. When the simulations were extended to 2D range expansions, the fitness of the sensitive strain was rapidly decreased upon the

introduction of an antibiotic to the system. High levels of drug degradation were insufficient to increase the fitness of the sensitive strain. These results were a direct consequence of spatial competition among the cells. When growing in 2D range expansions, the strains competed for both nutrients and space, as the only growing cells were those located at the expansion front. Once one subpopulation dominated the expansion front, the other one was left behind, unable to continue expanding. In the 2D communities, once antibiotic was introduced, the sensitive cells exhibited a lower growth rate compared to resistant ones, which grew faster. When the antibiotic concentration was reduced enough for the sensitive cells to grow at fast rates, they were already physically blocked by a front of resistant cells. Consequently, indirect resistance in two-dimensional communities was challenging to observe because antibiotic degradation occurred locally, and cells had few neighbours. This limitation resulted in fewer interactions and rapid blockage of sensitive cells. When the simulations were extended to 3D range expansions, the fitness of the sensitive cells did not decrease as fast as in 2D, and high levels of antibiotic degradation facilitated a recovery in their fitness. That was due to the increased number of available neighbours in 3D. This recovery of indirect resistance was due to the increased number of available neighbours in 3D. A higher number of neighbours enhanced the interactions between strains and delayed the takeover of one subpopulation as it required a subpopulation to dominate an entire expansion surface, unlike in the 2D case where it was just an edge. The values of relative fitness also presented different maximums in the absence of antibiotics, depending on the spatial configuration. The relative fitness was highest in the 2D system, indicating that it was the setup that facilitated greater competition and led to a faster takeover by one population over the other. The relative fitness maximum was the lowest for the well-mixed system since the cells did not have to compete for space.

In liquid cultures, indirect resistance to chloramphenicol was reported when a resistant and a sensitive strain were co-cultured. The finding was in agreement with previously published reports [196]. In this experimental system, the presence of a resistant strain allowed the sensitive cells to divide even above their MIC value. When the same co-culture was inoculated onto plates, and the community evolved as a 2D range expansion, no evidence of indirect resistance was observed. The reduced indirect resistance was anticipated based on the agent-based simulation results. The determination of the growth rates for the strains at different chloramphenicol concentrations clarified why indirect resistance was not observed. Even at low antibiotic concentrations well below their MIC value, the sensitive cells divided slower than the resistant ones. This slower growth rate indicated that in a competitive setup like 2D expansions, the resistant cells had a significant advantage. Moreover, the growth of the sensitive strain was similar to that of the resistant strain in the absence of antibiotics. Therefore, even if the environment was completely detoxified, the sensitive cells had no

competitive advantage over the resistant ones. Consequently, their best chance was growing, occupying 50% of the space, as reported in Fig.4.7a and Fig.4.7b at zero chloramphenicol. The experimental results demonstrated the importance of spatial organisation influencing complex cell interactions. In liquid cultures, all the cells were in contact with each other, and the environment was uniform with small nutrient and drug gradients. When growing in two dimensions, the cells only interacted with their close neighbours, and strong gradients of nutrients and chemicals emerged. Although 3D range expansion experiments were not performed, the simulations suggested that as the number of contacts between cells and their neighbours increases, the observed indirect resistance may exhibit an intermediate behaviour between what was observed in liquid cultures and 2D experiments.

Collision experiments showed that complex interactions between sensitive and resistant cells happened in two dimensions when they were not in direct competition for nutrients and space. As antibiotic concentration increased, the sensitive cells exhibited more interactions with the resistant cells. At the collision border, the resistant cells locally degraded the antibiotic, creating regions where the sensitive cells could grow. Although the sensitive cells began to grow in these areas, they presented a lower growth rate compared to the resistant cells. The resistant cells then kept growing towards the sensitive cells, pushing them and creating sectors. A similar change in the pattern of range expansions has been considered a consequence of a shift in interactions between the constituents [46, 212]. The transition from a straight boundary to a complex pattern indicated a shift from a competitive setting to a more cooperative system. However, although the collision front suggests the emergence of cooperation between cells, further experiments need to be performed to quantify the benefit that the sensitive cells experience and determine if indirect resistance emerges.

The model presented in section 4.2.2 is insufficient to reproduce the behaviour observed in Fig.4.12. The emergence of sectors appears to have an origin in physical interactions, which were not considered in the previously described agent-based simulations. To better replicate the experimental results, the lattice model should include the physical cell interactions. Alternatively, force-based models could be used, but they are computationally expensive and can present challenges in coupling diffusing quantities, like antibiotics, to them.

The experiments performed with RES and SEN strains were designed based on the MIC value of the sensitive strain, which was determined with an E-TEST on LB media and found to be 5  $\mu\text{g/ml}$ . However, in both liquid and 2D systems, the sensitive cells stopped growing below such value, as indicated by the growth rates (Fig.4.9). The MIC is a value that can vary significantly depending on the method used to determine it. This does not necessarily indicate that the sensitive strain had a different tolerance to the antibiotic; it just had different growth modes depending on the conditions. The MIC of a bacteriostatic antibiotic is highly

dependent on the nutritional level of the environment, which is why all the experiments in the chapter were conducted with LB. Consequently, the results presented may not be extrapolated to other nutritional media.

The presented results are, at the date of submission, being supplemented with additional experiments and simulations. Specifically, the liquid experiments were repeated on the fluorescent strains using flow cytometry to determine the fitness between strains. Similar relative fitness has been observed in liquid conditions for the pair RES-R/SEN-G as for the pair RES/SEN presented in the thesis, indicating that indirect resistance also emerges between them. That RES-R cells protect SEN-G cells in liquid experiments confirms the nature of the transition front is a result of cooperative interactions between the cells. The new results are included in the preliminary manuscript in appendix A.3. Additionally, more collision experiments are being performed and quantified so simulations that include physical interaction between cells can reproduce the results.

This study described the emergence of indirect resistance exclusively for chloramphenicol. It is challenging to determine the extent to which these findings can be generalised to other antibiotics. It may be difficult to relate the results to antibiotics degraded extracellularly, as the deactivating enzymes diffuse through the system, diminishing the role of spatial organization. In systems with extracellular deactivation, indirect resistance is likely a result of global cooperation rather than the local cooperation between cells observed in intracellular deactivation. The behaviour of bactericidal antibiotics is also expected to differ significantly from that observed for chloramphenicol and may involve complex phenomena overlooked by our system. For example, when cells are under the effect of  $\beta$ -lactams, their cell wall is compromised and breaks. Under sub-lethal concentrations of  $\beta$ -lactams, the cell shape of sensitive cells changes, becoming more elongated [198]. As extensively described in chapter 3 the cellular shape has a significant impact on the outcome of bacterial competition. Thus, the outcome of the system may be influenced not only by the effects of the antibiotics but also by the phenotypical differences between strains.





# Chapter 5

## Discussion

This thesis presented three distinct systems that studied the spatial self-organisation of *E. coli* communities from a biophysical perspective. The resulting spatial distribution showed how interactions either with the environment or between constituents shaped their communities. In chapter 2, an isogenic population growing as three-dimensional conformation was studied, where the major driver of self-organisation were environmental factors, particularly the stiffness of the medium. Chapter 3 investigated how competitive interactions arising from cell shape controlled the self-assembly of the community. Lastly, chapter 4 delved into the effects of complex interactions that alter cell functionality, particularly their ability to grow under antibiotic stress as the population assembled into different configurations. Even though experiments coupled with agent-based simulations revealed many phenomena not previously reported, numerous questions remain open for each system.

The formation of satellite colonies, thoroughly described in chapter 2, was a consequence of complex bacterial motility modes as the cells navigated semi-solid media. All mutant strains exhibited reduced motility but grew as 3D colonies with intricated surfaces (Fig. 2.12). Mountainous surfaces were more pronounced in the mutants that maintained their flagella. Said structures are hypothesised to be satellites reabsorbed to the main colony, so their emergence in mutants could suggest that some cells managed to escape the main aggregate but moved only short distances before being quickly reabsorbed into the colony. Further studies could test whether mountainous surfaces were an actual consequence of motility by growing mutants in lower agarose concentrations. In a less stiff medium, wild-type cells spread completely, but the mutants might be able to increase the length of their movement and produce satellites.

To determine whether satellite formation promotes a super-linear spread of an experimental population, competition experiments between a motile and a non-motile strain could be conducted in 3D configurations. The expected outcome is that non-motile cells will grow

as compact aggregates close to their inoculation point, while motile cells at the surface of the colony will generate satellites. This would give the motile strain a competitive advantage by enabling its growth into unexplored regions and diminishing the effects of spatial competition. However, more complex phenomena could emerge, like bacterial hitchhiking or social spreading, which have been reported in 2D communities of motile and non-motile subpopulations [213, 214].

Further investigations could be performed with the experimental system described in chapter 3. When competing in pairs in 2D settings, the cells with the highest aspect ratio out-competed the shorter ones by aligning and dominating the expansion front. An agent-based model showed that the advantage due to alignment was correlated to the aspect ratio of the cells. There was a theoretical limit in the aspect ratio from which cells started to align. The competitive advantage of long cells was reduced when growing with other cells that could align, as experimentally observed in 2D range expansions. However, single-cell experiments focusing on two aligning strains could further validate this theoretical finding and potentially reveal new information about the system. What would be the outcome of three subpopulations with varying aspect ratios growing together remains unclear. It is possible that the shorter cells would be outpaced early in the development of the colony, allowing the intermediate and longer strains to compete for dominance of the expansion front. Alternatively, the introduction of a third strain could delay the takeover of one subpopulation, promoting genetic diversity.

In chapter 4, the importance of spatial organisation in processes that require cell-to-cell contact was highlighted. Less protection of a sensitive subpopulation was reported when the number of interactions with a resistant population was reduced. As of the submission date, the study presented on indirect resistance to chloramphenicol was still ongoing. Bacterial cheating, where subpopulations benefit from cooperation without paying the cost [215], was not observed experimentally. The sensitive cells benefited from the environmental detoxification provided by the resistant cells. Still, the cost of resistance to chloramphenicol was low, as both strains had similar growth rates in the absence of antibiotics. Consequently, the sensitive strain cells could not compete with the resistant ones once the environment was detoxified. If the growth rate of the resistant strain could be slowed down, more complex communities could emerge, potentially allowing sensitive cells to become cheaters.

One of the main points yet to be explored in chapter 4 is the experimental study of sensitive and resistant communities as they develop in three dimensions. From the results predicted from the simulations, higher protection of the sensitive cells is expected in such systems compared to the 2D case, though not as high as in the liquid systems. However, the experimental conditions to perform the investigation need to be carefully designed, as both

---

the resistant and the sensitive strains are motile derivatives of *E. coli* K-12. If the 3D range expansion is performed in an environment that allows cell motility, satellite colonies reported in chapter 2 could emerge. Interestingly, satellites should occur for both cell types. In the absence of antibiotics, a similar fraction of satellites should emerge for each strain. As the antibiotic concentration in the environment increases, the growth of the sensitive cells will be reduced, leading to a reduction in the expression of flagellum due to its high metabolic cost. Consequently, sensitive cells should be less motile, resulting in fewer satellites. On the other hand, the satellites of the resistant cells would detoxify the environment in regions farther from the main colony, potentially allowing single cells of the sensitive strain to grow. So, as the chloramphenicol concentration increases, the satellites of the sensitive cells could begin to develop near the resistant ones. The agent-based models of chapter 2 and chapter 4 could be coupled to investigate this intricate scenario.

The characterisation of indirect resistance for chloramphenicol cannot be extrapolated to antibiotics from different classes or with different deactivation modes. Since the antibiotic was intracellularly degraded, direct cell contact was required for other cells to benefit from the detoxification. However, if the antibiotic presented extracellular deactivation, as is the case for the bactericidal  $\beta$ -lactams, phenomena not addressed in this thesis would emerge.  $\beta$ -lactams compromise the bacterial cell wall, causing sensitive cells to become more elongated when growing under sub-lethal concentrations [198]. That means that in a 2D range expansion, the transition in cell shape will benefit the sensitive cells as they would align easier than the resistant cells, as described in chapter 3. Therefore, in the absence of antibiotics, sensitive and resistant cells will only differ in the growth rates associated with the resistance cost. However, when antibiotics are introduced at sub-lethal levels, sensitive cells will elongate and potentially take over the expansion front, as their growth is not impeded by the antibiotic, unlike with bacteriostatic agents. At the same time, the resistant cells will detoxify the environment, but once the takeover occurs, that is expected not to change the outcome of the system. The most interesting behaviour may occur at lethal antibiotic concentrations. In this scenario, the resistant cells could detoxify the environment to sub-lethal levels, allowing the elongated sensitive cells to advance to the expansion front. However, once these sensitive cells reach the expansion front, they might die due to lethal antibiotic concentration. This would maintain a dynamic system where, after the sensitive cells die at the expansion front, the resistant cells could continue to grow and detoxify the environment. This detoxification might facilitate another takeover by sensitive cells in the inner parts of the community, which, again, will die at the expansion front.

The thesis has identified parameters that influence the intermixing of bacterial populations, which allows the quantification of genetic diversity. Chapter 3 demonstrated how cell

morphology affects the intermixing of 2D populations, leading to an increase in cell-to-cell contacts that can enhance conjugation events. In chapter 4, the dimensionality of the system contributed to higher intermixing due to increased cell interactions. In chapter 2, the communities investigated originated from a single cell, making it challenging to assess how diversity might be influenced by satellite emergence. There are theoretical studies that demonstrate how the long-range dispersal of populations leads to a superlinear spread, which promotes higher genetic diversity [143, 144]. When colonies presented satellites, they spread super linearly, suggesting that satellite formation could be not only a favourable spreading technique but also a mechanism to promote diversity.

The changes in community diversity as colonies transition from two-dimensional to three-dimensional environments highlight that the results of two-dimensional range expansions should not always be generalised to natural systems where communities predominantly grow as three-dimensional configurations. The strength of competition can be overestimated in 2D systems. In 3D systems, the competitive strength of the communities is reduced, partly due to the increased fraction of the colony that can grow. Conversely, liquid systems often represent idealised conditions where competitive effects are neglected.

## 5.1 Closing remarks

To summarise and conclude, this thesis explored three experimental systems with their main properties reproduced and described through agent-based simulations.

When single *E. coli* cells were embedded into a semi-solid medium a novel motility-associated spreading strategy of the cells was reported. The formation of satellites allowed the cells to invade new territories while maintaining community protection.

As cells with different morphologies competed in two dimensions, longer cells interacted with shorter ones to align and reach the colony edge. Elongated bacteria presented a competitive advantage, as they obstructed the rounder cells from reaching the expansion front. Additionally, varying cell morphologies led to different self-organisation patterns. Rounder cells had more interactions, which promoted events requiring cell-to-cell contact, such as conjugation.

When resistant cells grew with sensitive ones, close cell-to-cell interactions were required to protect them from external stresses caused by a bacteriostatic antibiotic degraded intracellularly. The number of possible interactions and the resulting cooperation between subpopulations could be controlled by the dimensionality of the environment in which the cells grew.

Overall, this thesis underscores the importance of not overlooking the physical interactions between cells as they spatially self-organise since these can promote or demote behaviours not reported in liquid cultures.



# References

- <sup>1</sup>W. B. Whitman, D. C. Coleman, and W. J. Wiebe, “Prokaryotes: The unseen majority”, [Proceedings of the National Academy of Sciences](#) **95**, 6578–6583 (1998).
- <sup>2</sup>T. Venkova, C. C. Yeo, and M. Espinosa, “Editorial: The Good, The Bad, and The Ugly: Multiple Roles of Bacteria in Human Life”, [Frontiers in Microbiology](#) **9**, 1702 (2018).
- <sup>3</sup>H. Onyeaka and O. C. Ekwebelem, “A review of recent advances in engineering bacteria for enhanced CO<sub>2</sub> capture and utilization”, en, [International Journal of Environmental Science and Technology](#) **20**, 4635–4648 (2023).
- <sup>4</sup>E. R. Angert, “Alternatives to binary fission in bacteria”, en, [Nature Reviews Microbiology](#) **3**, 214–224 (2005).
- <sup>5</sup>R. M. Maier, “Chapter 3 - Bacterial Growth”, in [Environmental Microbiology \(Second Edition\)](#), edited by R. M. Maier, I. L. Pepper, and C. P. Gerba (Academic Press, San Diego, Jan. 2009), pp. 37–54.
- <sup>6</sup>J. Monod, “THE GROWTH OF BACTERIAL CULTURES”, en, [Annual Review of Microbiology](#) **3**, 371–394 (1949).
- <sup>7</sup>T. J. Silhavy, D. Kahne, and S. Walker, “The Bacterial Cell Envelope”, [Cold Spring Harbor Perspectives in Biology](#) **2**, a000414 (2010).
- <sup>8</sup>S. Garde, P. K. Chodiseti, and M. Reddy, “Peptidoglycan: Structure, Synthesis, and Regulation”, [EcoSal Plus](#) **9**, 10.1128/ecosalplus.ESP-0010-2020 (2021).
- <sup>9</sup>D. Claus, “A standardized Gram staining procedure”, en, [World Journal of Microbiology and Biotechnology](#) **8**, 451–452 (1992).
- <sup>10</sup>N. Saha, C. Monge, V. Dulong, C. Picart, and K. Glinel, “Influence of Polyelectrolyte Film Stiffness on Bacterial Growth”, [Biomacromolecules](#) **14**, 520–528 (2013).
- <sup>11</sup>C. Guégan, J. Garderes, G. Le Pennec, F. Gaillard, F. Fay, I. Linossier, J. -. Herry, M. -. B. Fontaine, and K. V. Réhel, “Alteration of bacterial adhesion induced by the substrate stiffness”, [Colloids and Surfaces B: Biointerfaces](#) **114**, 193–200 (2014).
- <sup>12</sup>A. Mai-Prochnow, M. Clauson, J. Hong, and A. B. Murphy, “Gram positive and Gram negative bacteria differ in their sensitivity to cold plasma”, [Scientific Reports](#) **6**, 38610 (2016).
- <sup>13</sup>K. Bush and P. A. Bradford, “-Lactams and -Lactamase Inhibitors: An Overview”, [Cold Spring Harbor Perspectives in Medicine](#) **6**, a025247 (2016).
- <sup>14</sup>J. Errington and L. T. van der Aart, “Microbe Profile: Bacillus subtilis: model organism for cellular development, and industrial workhorse”, [Microbiology](#) **166**, 425–427 (2020).

- <sup>15</sup>D. M. Gordon and A. Cowling, “The distribution and genetic structure of *Escherichia coli* in Australian vertebrates: host and geographic effects”, *Microbiology* **149**, 3575–3586 (2003).
- <sup>16</sup>J. B. Kaper, J. P. Nataro, and H. L. T. Mobley, “Pathogenic *Escherichia coli*”, en, *Nature Reviews Microbiology* **2**, 123–140 (2004).
- <sup>17</sup>B. Bj, “Derivations and genotypes of some mutant derivatives of *Escherichia coli* K-12”, *Escherichia coli and Salmonella typhimurium Cellular and Molecular Biology*, 2460 (1996).
- <sup>18</sup>F. R. Blattner, G. Plunkett, C. A. Bloch, N. T. Perna, V. Burland, M. Riley, J. Collado-Vides, J. D. Glasner, C. K. Rode, G. F. Mayhew, J. Gregor, N. W. Davis, H. A. Kirkpatrick, M. A. Goeden, D. J. Rose, B. Mau, and Y. Shao, “The complete genome sequence of *Escherichia coli* K-12”, eng, *Science (New York, N.Y.)* **277**, 1453–1462 (1997).
- <sup>19</sup>F. W. Studier, P. Daegelen, R. E. Lenski, S. Maslov, and J. F. Kim, “Understanding the Differences between Genome Sequences of *Escherichia coli* B Strains REL606 and BL21(DE3) and Comparison of the *E. coli* B and K-12 Genomes”, *Journal of Molecular Biology* **394**, 653–680 (2009).
- <sup>20</sup>R. M. Stubbendieck, C. Vargas-Bautista, and P. D. Straight, “Bacterial Communities: Interactions to Scale”, English, *Frontiers in Microbiology* **7**, 10.3389/fmicb.2016.01234 (2016).
- <sup>21</sup>A. Beavogui, A. Lacroix, N. Wiart, J. Poulain, T. O. Delmont, L. Paoli, P. Wincker, and P. H. Oliveira, “The defensome of complex bacterial communities”, en, *Nature Communications* **15**, 2146 (2024).
- <sup>22</sup>T. J. Rudge, F. Federici, P. J. Steiner, A. Kan, and J. Haseloff, “Cell Polarity-Driven Instability Generates Self-Organized, Fractal Patterning of Cell Layers”, *ACS Synthetic Biology* **2**, 705–714 (2013).
- <sup>23</sup>T. Hölscher and Á. T. Kovács, “Sliding on the surface: bacterial spreading without an active motor”, en, *Environmental Microbiology* **19**, 2537–2545 (2017).
- <sup>24</sup>L. Excoffier, M. Foll, and R. J. Petit, “Genetic Consequences of Range Expansions”, en, *Annual Review of Ecology, Evolution, and Systematics* **40**, 481–501 (2009).
- <sup>25</sup>Y. Ma, J. Ramoneda, and D. R. Johnson, “Timing of antibiotic administration determines the spread of plasmid-encoded antibiotic resistance during microbial range expansion”, en, *Nature Communications* **14**, 1–12 (2023).
- <sup>26</sup>B. E. Rittmann, “Microbial ecology to manage processes in environmental biotechnology”, *Trends in Biotechnology* **24**, 261–266 (2006).
- <sup>27</sup>A. Kouzuma and K. Watanabe, “Microbial Ecology Pushes Frontiers in Biotechnology”, *Microbes and Environments* **29**, 1–3 (2014).
- <sup>28</sup>K. N. Kragh, T. Tolker-Nielsen, and M. Lichtenberg, “The non-attached biofilm aggregate”, en, *Communications Biology* **6**, 1–13 (2023).
- <sup>29</sup>P.-T. Su, C.-T. Liao, J.-R. Roan, S.-H. Wang, A. Chiou, and W.-J. Syu, “Bacterial Colony from Two-Dimensional Division to Three-Dimensional Development”, en, *PLOS ONE* **7**, e48098 (2012).

- <sup>30</sup>O. Hallatschek, P. Hersen, S. Ramanathan, and D. R. Nelson, “Genetic drift at expanding frontiers promotes gene segregation”, *Proceedings of the National Academy of Sciences* **104**, 19926–19930 (2007).
- <sup>31</sup>O. Hallatschek and D. R. Nelson, “Life at the Front of an Expanding Population”, en, *Evolution* **64**, 193–206 (2010).
- <sup>32</sup>B. T. Weinstein, M. O. Lavrentovich, W. Möbius, A. W. Murray, and D. R. Nelson, “Genetic drift and selection in many-allele range expansions”, en, *PLOS Computational Biology* **13**, e1005866 (2017).
- <sup>33</sup>W. Liu, T. A. Tokuyasu, X. Fu, and C. Liu, “The spatial organization of microbial communities during range expansion”, *Current Opinion in Microbiology* **63**, 109–116 (2021).
- <sup>34</sup>C. D. Nadell, K. R. Foster, and J. B. Xavier, “Emergence of Spatial Structure in Cell Groups and the Evolution of Cooperation”, en, *PLOS Computational Biology* **6**, e1000716 (2010).
- <sup>35</sup>J. van Gestel, F. J. Weissing, O. P. Kuipers, and Á. T. Kovács, “Density of founder cells affects spatial pattern formation and cooperation in *Bacillus subtilis* biofilms”, *The ISME Journal* **8**, 2069–2079 (2014).
- <sup>36</sup>F. Goldschmidt, R. R. Regoes, and D. R. Johnson, “Metabolite toxicity slows local diversity loss during expansion of a microbial cross-feeding community”, *The ISME Journal* **12**, 136–144 (2018).
- <sup>37</sup>S. Mitri, E. Clarke, and K. R. Foster, “Resource limitation drives spatial organization in microbial groups”, en, *The ISME Journal* **10**, 1471–1482 (2016).
- <sup>38</sup>M. J. I. Müller, B. I. Neugeboren, D. R. Nelson, and A. W. Murray, “Genetic drift opposes mutualism during spatial population expansion”, *Proceedings of the National Academy of Sciences* **111**, 1037–1042 (2014).
- <sup>39</sup>F. Goldschmidt, L. Caduff, and D. R. Johnson, “Causes and consequences of pattern diversification in a spatially self-organizing microbial community”, en, *The ISME Journal* **15**, 2415–2426 (2021).
- <sup>40</sup>A. E. Blanchard and T. Lu, “Bacterial social interactions drive the emergence of differential spatial colony structures”, en, *BMC Systems Biology* **9**, 59 (2015).
- <sup>41</sup>N. W. Smith, P. R. Shorten, E. Altermann, N. C. Roy, and W. C. McNabb, “The Classification and Evolution of Bacterial Cross-Feeding”, English, *Frontiers in Ecology and Evolution* **7**, 10.3389/fevo.2019.00153 (2019).
- <sup>42</sup>G. D’Souza, S. Shitut, D. Preussger, G. Yousif, S. Waschina, and C. Kost, “Ecology and evolution of metabolic cross-feeding interactions in bacteria”, en, *Natural Product Reports* **35**, 455–488 (2018).
- <sup>43</sup>B. Momeni, K. A. Brileya, M. W. Fields, and W. Shou, “Strong inter-population cooperation leads to partner intermixing in microbial communities”, *eLife* **2**, edited by D. Tautz, e00230 (2013).
- <sup>44</sup>M. Gralka, F. Stiewe, F. Farrell, W. Möbius, B. Waclaw, and O. Hallatschek, “Allele surfing promotes microbial adaptation from standing variation”, en, *Ecology Letters* **19**, 889–898 (2016).

- <sup>45</sup>N. v. d. Berg, K. Thijssen, T. T. Nguyen, A. Sarlet, M. Cordero, A. G. Vázquez, N. Mitarai, A. Doostmohammadi, and L. Jauffred, *Emergent collective alignment gives competitive advantage to longer cells during range expansion*, en, Feb. 2024.
- <sup>46</sup>B. Borer, D. Ciccarese, D. Johnson, and D. Or, “Spatial organization in microbial range expansion emerges from trophic dependencies and successful lineages”, en, *Communications Biology* **3**, 1–10 (2020).
- <sup>47</sup>C. Liu, X. Fu, L. Liu, X. Ren, C. K. Chau, S. Li, L. Xiang, H. Zeng, G. Chen, L.-H. Tang, P. Lenz, X. Cui, W. Huang, T. Hwa, and J.-D. Huang, “Sequential Establishment of Stripe Patterns in an Expanding Cell Population”, *Science* **334**, 238–241 (2011).
- <sup>48</sup>E. O. Budrene and H. C. Berg, “Complex patterns formed by motile cells of *Escherichia coli*”, en, *Nature* **349**, 630–633 (1991).
- <sup>49</sup>A. I. Curatolo, N. Zhou, Y. Zhao, C. Liu, A. Daerr, J. Tailleur, and J. Huang, “Cooperative pattern formation in multi-component bacterial systems through reciprocal motility regulation”, en, *Nature Physics* **16**, 1152–1157 (2020).
- <sup>50</sup>R. Krishna Kumar, T. A. Meiller-Legrand, A. Alcinesio, D. Gonzalez, D. A. I. Mavridou, O. J. Meacock, W. P. J. Smith, L. Zhou, W. Kim, G. S. Pulcu, H. Bayley, and K. R. Foster, “Droplet printing reveals the importance of micron-scale structure for bacterial ecology”, en, *Nature Communications* **12**, 857 (2021).
- <sup>51</sup>W. Möbius, F. Tesser, K. M. J. Alards, R. Benzi, D. R. Nelson, and F. Toschi, “The collective effect of finite-sized inhomogeneities on the spatial spread of populations in two dimensions”, *Journal of The Royal Society Interface* **18**, 20210579 (2021).
- <sup>52</sup>C. Ruan, J. Ramoneda, G. Gogia, G. Wang, and D. R. Johnson, “Fungal hyphae regulate bacterial diversity and plasmid-mediated functional novelty during range expansion”, English, *Current Biology* **32**, 5285–5294.e4 (2022).
- <sup>53</sup>M. Pion, R. Bshary, S. Bindschedler, S. Filippidou, L. Y. Wick, D. Job, and P. Junier, “Gains of bacterial flagellar motility in a fungal world”, eng, *Applied and Environmental Microbiology* **79**, 6862–6867 (2013).
- <sup>54</sup>C. Ruan, J. Ramoneda, A. Kan, T. J. Rudge, G. Wang, and D. R. Johnson, “Phage predation accelerates the spread of plasmid-encoded antibiotic resistance”, en, *Nature Communications* **15**, 5397 (2024).
- <sup>55</sup>R. S. Eriksen, F. Larsen, S. L. Svenningsen, K. Sneppen, and N. Mitarai, “The dynamics of phage predation on a microcolony”, English, *Biophysical Journal* **123**, 147–156 (2024).
- <sup>56</sup>W. Möbius and L. Laan, “Physical and Mathematical Modeling in Experimental Papers”, English, *Cell* **163**, 1577–1583 (2015).
- <sup>57</sup>L. Eigentler, F. A. Davidson, and N. R. Stanley-Wall, “Mechanisms driving spatial distribution of residents in colony biofilms: an interdisciplinary perspective”, *Open Biology* **12**, 220194 (2022).
- <sup>58</sup>M. Gralka and O. Hallatschek, “Environmental heterogeneity can tip the population genetics of range expansions”, *eLife* **8**, edited by R. A. Neher, I. T. Baldwin, R. A. Neher, and M. Lavrentovich, e44359 (2019).
- <sup>59</sup>K. S. Korolev, J. B. Xavier, D. R. Nelson, and K. R. Foster, “A Quantitative Test of Population Genetics Using Spatiogenetic Patterns in Bacterial Colonies”, *The American Naturalist* **178**, 538–552 (2011).

- <sup>60</sup>W. P. J. Smith, Y. Davit, J. M. Osborne, W. Kim, K. R. Foster, and J. M. Pitt-Francis, “Cell morphology drives spatial patterning in microbial communities”, [Proceedings of the National Academy of Sciences](#) **114**, E280–E286 (2017).
- <sup>61</sup>M. J. Bottery, J. W. Pitchford, and V.-P. Friman, “Ecology and evolution of antimicrobial resistance in bacterial communities”, en, [The ISME Journal](#) **15**, 939–948 (2021).
- <sup>62</sup>S. Pande, F. Kaftan, S. Lang, A. Svatoš, S. Germerodt, and C. Kost, “Privatization of cooperative benefits stabilizes mutualistic cross-feeding interactions in spatially structured environments”, en, [The ISME Journal](#) **10**, 1413–1423 (2016).
- <sup>63</sup>M. Berlanga and R. Guerrero, “Living together in biofilms: the microbial cell factory and its biotechnological implications”, [Microbial Cell Factories](#) **15**, 165 (2016).
- <sup>64</sup>D. López, H. Vlamakis, and R. Kolter, “Biofilms”, en, [Cold Spring Harbor Perspectives in Biology](#) **2**, a000398 (2010).
- <sup>65</sup>R. S. Eriksen, S. L. Svenningsen, K. Sneppen, and N. Mitarai, “A growing microcolony can survive and support persistent propagation of virulent phages”, [Proceedings of the National Academy of Sciences](#) **115**, 337–342 (2018).
- <sup>66</sup>E. Hernández-Jiménez, R. del Campo, V. Toledano, M. T. Vallejo-Cremades, A. Muñoz, C. Largo, F. Arnalich, F. García-Rio, C. Cubillos-Zapata, and E. López-Collazo, “Biofilm vs. planktonic bacterial mode of growth: Which do human macrophages prefer?”, [Biochemical and Biophysical Research Communications](#) **441**, 947–952 (2013).
- <sup>67</sup>M. Kolpen, K. N. Kragh, J. B. Enciso, D. Faurholt-Jepsen, B. Lindegaard, G. B. Egelund, A. V. Jensen, P. Ravn, I. H. M. Mathiesen, A. G. Gheorge, F. B. Hertz, T. Qvist, M. Whiteley, P. Ø. Jensen, and T. Bjarnsholt, “Bacterial biofilms predominate in both acute and chronic human lung infections”, [Thorax](#) **77**, 1015–1022 (2022).
- <sup>68</sup>E. E. Mann and D. J. Wozniak, “Pseudomonas biofilm matrix composition and niche biology”, [FEMS Microbiology Reviews](#) **36**, 893–916 (2012).
- <sup>69</sup>A. Ghafoor, I. D. Hay, and B. H. A. Rehm, “Role of Exopolysaccharides in Pseudomonas aeruginosa Biofilm Formation and Architecture”, [Applied and Environmental Microbiology](#) **77**, 5238–5246 (2011).
- <sup>70</sup>R. Yin, J. Cheng, J. Wang, P. Li, and J. Lin, “Treatment of Pseudomonas aeruginosa infectious biofilms: Challenges and strategies”, [Frontiers in Microbiology](#) **13**, 955286 (2022).
- <sup>71</sup>C. Beloin, A. Roux, and J.-M. Ghigo, “Escherichia coli biofilms”, [Current Topics in Microbiology and Immunology](#) **322**, 249–289 (2008).
- <sup>72</sup>S. Arnaouteli, N. C. Bamford, N. R. Stanley-Wall, and Á. T. Kovács, “Bacillus subtilis biofilm formation and social interactions”, en, [Nature Reviews Microbiology](#) **19**, 600–614 (2021).
- <sup>73</sup>K. Schilcher and A. R. Horswill, “Staphylococcal Biofilm Development: Structure, Regulation, and Treatment Strategies”, [Microbiology and Molecular Biology Reviews](#) **84**, 10.1128/mnbr.00026–19 (2020).
- <sup>74</sup>O. E. Petrova and K. Sauer, “A Novel Signaling Network Essential for Regulating Pseudomonas aeruginosa Biofilm Development”, en, [PLOS Pathogens](#) **5**, e1000668 (2009).

- <sup>75</sup>G. Sharma, S. Sharma, P. Sharma, D. Chandola, S. Dang, S. Gupta, and R. Gabrani, “Escherichia coli biofilm: development and therapeutic strategies”, *Journal of Applied Microbiology* **121**, 309–319 (2016).
- <sup>76</sup>O. E. Petrova and K. Sauer, “Escaping the biofilm in more than one way: Desorption, detachment or dispersion”, *Current opinion in microbiology* **30**, 67–78 (2016).
- <sup>77</sup>K. P. Rumbaugh and K. Sauer, “Biofilm dispersion”, en, *Nature Reviews Microbiology* **18**, 571–586 (2020).
- <sup>78</sup>K. Sauer, P. Stoodley, D. M. Goeres, L. Hall-Stoodley, M. Burmølle, P. S. Stewart, and T. Bjarnsholt, “The biofilm life cycle: expanding the conceptual model of biofilm formation”, en, *Nature Reviews Microbiology* **20**, 608–620 (2022).
- <sup>79</sup>H. H. Tuson, G. K. Auer, L. D. Renner, M. Hasebe, C. Tropini, M. Salick, W. C. Crone, A. Gopinathan, K. C. Huang, and D. B. Weibel, “Measuring the stiffness of bacterial cells from growth rates in hydrogels of tunable elasticity”, en, *Molecular Microbiology* **84**, 874–891 (2012).
- <sup>80</sup>M. O. Lavrentovich, J. H. Koschwanetz, and D. R. Nelson, “Nutrient shielding in clusters of cells”, en, *Physical Review E* **87**, 062703 (2013).
- <sup>81</sup>M. O. Lavrentovich and D. R. Nelson, “Survival probabilities at spherical frontiers”, *Theoretical Population Biology* **102**, 26–39 (2015).
- <sup>82</sup>X. Shao, A. Mugler, J. Kim, H. J. Jeong, B. R. Levin, and I. Nemenman, “Growth of bacteria in 3-d colonies”, en, *PLOS Computational Biology* **13**, e1005679 (2017).
- <sup>83</sup>J. Adler, “Chemotaxis in Bacteria”, *Science* **153**, 708–716 (1966).
- <sup>84</sup>D. Lauffenburger, C. R. Kennedy, and R. Aris, “Traveling bands of chemotactic bacteria in the context of population growth”, *Bulletin of Mathematical Biology* **46**, 19–40 (1984).
- <sup>85</sup>K. F. Jarrell and M. J. McBride, “The surprisingly diverse ways that prokaryotes move”, en, *Nature Reviews Microbiology* **6**, 466–476 (2008).
- <sup>86</sup>N. Wadhwa and H. C. Berg, “Bacterial motility: machinery and mechanisms”, en, *Nature Reviews Microbiology* **20**, 161–173 (2022).
- <sup>87</sup>D. F. Blair, “HOW BACTERIA SENSE AND SWIM”, en, *Annual Review of Microbiology* **49**, 489–520 (1995).
- <sup>88</sup>J.-M. Swiecicki, O. Sliusarenko, and D. B. Weibel, “From swimming to swarming: Escherichia coli cell motility in two-dimensions”, *Integrative biology : quantitative biosciences from nano to macro* **5**, 1490–1494 (2013).
- <sup>89</sup>G. A. O’Toole and R. Kolter, “Flagellar and twitching motility are necessary for Pseudomonas aeruginosa biofilm development”, en, *Molecular Microbiology* **30**, 295–304 (1998).
- <sup>90</sup>J. Tchoufag, P. Ghosh, C. B. Pogue, B. Nan, and K. K. Mandadapu, “Mechanisms for bacterial gliding motility on soft substrates”, *Proceedings of the National Academy of Sciences* **116**, 25087–25096 (2019).
- <sup>91</sup>U. Alon, M. G. Surette, N. Barkai, and S. Leibler, “Robustness in bacterial chemotaxis”, en, *Nature* **397**, 168–171 (1999).

- <sup>92</sup>O. A. Croze, G. P. Ferguson, M. E. Cates, and W. C. K. Poon, “Migration of Chemotactic Bacteria in Soft Agar: Role of Gel Concentration”, *Biophysical Journal* **101**, 525–534 (2011).
- <sup>93</sup>J. Cremer, T. Honda, Y. Tang, J. Wong-Ng, M. Vergassola, and T. Hwa, “Chemotaxis as a navigation strategy to boost range expansion”, en, *Nature* **575**, 658–663 (2019).
- <sup>94</sup>T. Bhattacharjee and S. S. Datta, “Bacterial hopping and trapping in porous media”, en, *Nature Communications* **10**, 2075 (2019).
- <sup>95</sup>Q. Zhang, J. Li, J. Nijjer, H. Lu, M. Kothari, R. Alert, T. Cohen, and J. Yan, “Morphogenesis and cell ordering in confined bacterial biofilms”, *Proceedings of the National Academy of Sciences* **118**, e2107107118 (2021).
- <sup>96</sup>M. Burmølle, K. Johnsen, W. A. Al-Soud, L. H. Hansen, and S. J. Sørensen, “The presence of embedded bacterial pure cultures in agar plates stimulate the culturability of soil bacteria”, *Journal of Microbiological Methods* **79**, 166–173 (2009).
- <sup>97</sup>M. Cordero, N. Mitarai, and L. Jauffred, “Motility mediates satellite formation in confined biofilms”, en, *The ISME Journal* **17**, Publisher: Nature Publishing Group, 1819–1827 (2023).
- <sup>98</sup>L. Jauffred, R. Munk Vejborg, K. S. Korolev, S. Brown, and L. B. Oddershede, “Chirality in microbial biofilms is mediated by close interactions between the cell surface and the substratum”, en, *The ISME Journal* **11**, 1688–1701 (2017).
- <sup>99</sup>T. Baba, T. Ara, M. Hasegawa, Y. Takai, Y. Okumura, M. Baba, K. A. Datsenko, M. Tomita, B. L. Wanner, and H. Mori, “Construction of *Escherichia coli* K-12 in-frame, single-gene knockout mutants: the Keio collection”, *Molecular Systems Biology* **2**, 2006.0008 (2006).
- <sup>100</sup>J. F. Sambrook, “Experiments with Gene Fusions. Thomas J. Silhavy, Michael L. Berman, Lynn W. Enquist”, *The Quarterly Review of Biology* **61**, 96–97 (1986).
- <sup>101</sup>S. N. Cohen, A. C. Y. Chang, and L. Hsu, “Nonchromosomal Antibiotic Resistance in Bacteria: Genetic Transformation of *Escherichia coli* by R-Factor DNA\*”, *Proceedings of the National Academy of Sciences of the United States of America* **69**, 2110–2114 (1972).
- <sup>102</sup>A. Reisner, J. A. J. Haagensen, M. A. Schembri, E. L. Zechner, and S. Molin, “Development and maturation of *Escherichia coli* K-12 biofilms”, en, *Molecular Microbiology* **48**, 933–946 (2003).
- <sup>103</sup>C. Beloin, K. Michaelis, K. Lindner, P. Landini, J. Hacker, J.-M. Ghigo, and U. Dobrindt, “The Transcriptional Antiterminator RfaH Represses Biofilm Formation in *Escherichia coli*”, *Journal of Bacteriology* **188**, 1316–1331 (2006).
- <sup>104</sup>K. Kjærsgaard, M. A. Schembri, C. Ramos, S. Molin, and P. Klemm, “Antigen 43 facilitates formation of multispecies biofilms”, en, *Environmental Microbiology* **2**, 695–702 (2000).
- <sup>105</sup>G. Bertani, “STUDIES ON LYSOGENESIS I.”, *Journal of Bacteriology* **62**, 293–300 (1951).
- <sup>106</sup>B. Mao, A. Bentaleb, F. Louerat, T. Divoux, and P. Snabre, “Heat-induced aging of agar solutions: Impact on the structural and mechanical properties of agar gels”, *Food Hydrocolloids* **64**, 59–69 (2017).
- <sup>107</sup>M. Ghebremedhin, S. Seiffert, and T. A. Vilgis, “Physics of agarose fluid gels: Rheological properties and microstructure”, *Current Research in Food Science* **4**, 436–448 (2021).

- <sup>108</sup>L. Kvich, B. Fritz, S. Crone, K. N. Kragh, M. Kolpen, M. Sønderholm, M. Andersson, A. Koch, P. Ø. Jensen, and T. Bjarnsholt, “Oxygen Restriction Generates Difficult-to-Culture *P. aeruginosa*”, English, *Frontiers in Microbiology* **10**, 10.3389/fmicb.2019.01992 (2019).
- <sup>109</sup>N. Das, N. Triparthi, S. Basu, C. Bose, S. Maitra, and S. Khurana, “Progress in the development of gelling agents for improved culturability of microorganisms”, English, *Frontiers in Microbiology* **6**, 10.3389/fmicb.2015.00698 (2015).
- <sup>110</sup>B. W. Graf and S. A. Boppart, “Imaging and analysis of three-dimensional cell culture models”, eng, *Methods in Molecular Biology (Clifton, N.J.)* **591**, 211–227 (2010).
- <sup>111</sup>J. Schindelin, I. Arganda-Carreras, E. Frise, V. Kaynig, M. Longair, T. Pietzsch, S. Preibisch, C. Rueden, S. Saalfeld, B. Schmid, J.-Y. Tinevez, D. J. White, V. Hartenstein, K. Eliceiri, P. Tomancak, and A. Cardona, “Fiji: an open-source platform for biological-image analysis”, en, *Nature Methods* **9**, 676–682 (2012).
- <sup>112</sup>R. Hartmann, H. Jeckel, E. Jelli, P. K. Singh, S. Vaidya, M. Bayer, D. K. H. Rode, L. Vidakovic, F. Díaz-Pascual, J. C. N. Fong, A. Dragoš, O. Lamprecht, J. G. Thöming, N. Netter, S. Häussler, C. D. Nadell, V. Sourjik, Á. T. Kovács, F. H. Yildiz, and K. Drescher, “Quantitative image analysis of microbial communities with BiofilmQ”, en, *Nature Microbiology* **6**, 151–156 (2021).
- <sup>113</sup>N. Otsu, “A Threshold Selection Method from Gray-Level Histograms”, *IEEE Transactions on Systems, Man, and Cybernetics* **9**, 62–66 (1979).
- <sup>114</sup>M. Eden, “A Two-dimensional Growth Process”, in *Proceedings of the Fourth Berkeley Symposium on Mathematical Statistics and Probability, Volume 4: Contributions to Biology and Problems of Medicine*, Vol. 4.4 (University of California Press, Jan. 1961), pp. 223–240.
- <sup>115</sup>D. T. Gillespie, “Exact stochastic simulation of coupled chemical reactions”, *The Journal of Physical Chemistry* **81**, 2340–2361 (1977).
- <sup>116</sup>N. Kandemir, W. Vollmer, N. S. Jakubovics, and J. Chen, “Mechanical interactions between bacteria and hydrogels”, en, *Scientific Reports* **8**, 10893 (2018).
- <sup>117</sup>P. Serwer, B. Hunter, and E. T. Wright, “Cell–gel interactions of in-gel propagating bacteria”, *BMC Research Notes* **11**, 699 (2018).
- <sup>118</sup>H. Hasman, M. A. Schembri, and P. Klemm, “Antigen 43 and Type 1 Fimbriae Determine Colony Morphology of *Escherichia coli* K-12”, *Journal of Bacteriology* **182**, 1089–1095 (2000).
- <sup>119</sup>L. A. Pratt and R. Kolter, “Genetic analysis of *Escherichia coli* biofilm formation: roles of flagella, motility, chemotaxis and type I pili”, en, *Molecular Microbiology* **30**, 285–293 (1998).
- <sup>120</sup>G. O’Toole, H. B. Kaplan, and R. Kolter, “Biofilm formation as microbial development”, eng, *Annual Review of Microbiology* **54**, 49–79 (2000).
- <sup>121</sup>H. Du, W. Xu, Z. Zhang, and X. Han, “Bacterial Behavior in Confined Spaces”, English, *Frontiers in Cell and Developmental Biology* **9**, 10.3389/fcell.2021.629820 (2021).
- <sup>122</sup>P. Owen, P. Caffrey, and L. G. Josefsson, “Identification and partial characterization of a novel bipartite protein antigen associated with the outer membrane of *Escherichia coli*”, *Journal of Bacteriology* **169**, 3770–3777 (1987).

- <sup>123</sup>H. Hasman, T. Chakraborty, and P. Klemm, “Antigen-43-Mediated Autoaggregation of *Escherichia coli* Is Blocked by Fimbriation”, *Journal of Bacteriology* **181**, 4834–4841 (1999).
- <sup>124</sup>C. Prigent-Combaret, G. Prensier, T. T. Le Thi, O. Vidal, P. Lejeune, and C. Dorel, “Developmental pathway for biofilm formation in curli-producing *Escherichia coli* strains: role of flagella, curli and colanic acid”, en, *Environmental Microbiology* **2**, 450–464 (2000).
- <sup>125</sup>L. Gualdi, L. Tagliabue, S. Bertagnoli, T. Ieranò, C. De Castro, and P. Landini, “Cellulose modulates biofilm formation by counteracting curli-mediated colonization of solid surfaces in *Escherichia coli*”, eng, *Microbiology (Reading, England)* **154**, 2017–2024 (2008).
- <sup>126</sup>T. Bauchop and S. R. Elsdén, “The growth of micro-organisms in relation to their energy supply”, eng, *Journal of General Microbiology* **23**, 457–469 (1960).
- <sup>127</sup>T. E. Shehata and A. G. Marr, “Effect of Nutrient Concentration on the Growth of *Escherichia coli*”, *Journal of Bacteriology* **107**, 210–216 (1971).
- <sup>128</sup>A. J. Mitchell and J. W. Wimpenny, “The effects of agar concentration on the growth and morphology of submerged colonies of motile and non-motile bacteria”, eng, *Journal of Applied Microbiology* **83**, 76–84 (1997).
- <sup>129</sup>K. J. Duffy, P. T. Cummings, and R. M. Ford, “Random walk calculations for bacterial migration in porous media.”, *Biophysical Journal* **68**, 800–806 (1995).
- <sup>130</sup>G. Frangipane, G. Vizsnyiczai, C. Maggi, R. Savo, A. Sciortino, S. Gigan, and R. Di Leonardo, “Invariance properties of bacterial random walks in complex structures”, en, *Nature Communications* **10**, 2442 (2019).
- <sup>131</sup>N. A. Licata, B. Mohari, C. Fuqua, and S. Setayeshgar, “Diffusion of Bacterial Cells in Porous Media”, *Biophysical Journal* **110**, 247–257 (2016).
- <sup>132</sup>A. Ed-Daoui and P. Snabre, “Poroviscoelasticity and compression-softening of agarose hydrogels”, en, *Rheologica Acta* **60**, 327–351 (2021).
- <sup>133</sup>Y.-G. Jung, J. Choi, S.-K. Kim, J.-H. Lee, and S. Kwon, “Embedded Biofilm, a New Biofilm Model Based on the Embedded Growth of Bacteria”, *Applied and Environmental Microbiology* **81**, 211–219 (2015).
- <sup>134</sup>M. Matsushita, J. Wakita, H. Itoh, I. Ràfols, T. Matsuyama, H. Sakaguchi, and M. Mimura, “Interface growth and pattern formation in bacterial colonies”, *Physica A: Statistical Mechanics and its Applications* **249**, 517–524 (1998).
- <sup>135</sup>A. Martínez-Calvo, T. Bhattacharjee, R. K. Bay, H. N. Luu, A. M. Hancock, N. S. Wingreen, and S. S. Datta, “Morphological instability and roughening of growing 3D bacterial colonies”, *Proceedings of the National Academy of Sciences* **119**, e2208019119 (2022).
- <sup>136</sup>T. Trunk, H. S. Khalil, and J. C. Leo, “Bacterial autoaggregation”, *AIMS Microbiology* **4**, 140–164 (2018).
- <sup>137</sup>A. N. Simms and H. L. T. Mobley, “Multiple Genes Repress Motility in Uropathogenic *Escherichia coli* Constitutively Expressing Type 1 Fimbriae”, *Journal of Bacteriology* **190**, 3747–3756 (2008).

- <sup>138</sup>G. C. Ulett, R. I. Webb, and M. A. Schembri, “Antigen-43-mediated autoaggregation impairs motility in *Escherichia coli*”, eng, [Microbiology \(Reading, England\)](#) **152**, 2101–2110 (2006).
- <sup>139</sup>N. Sommerfeldt, A. Possling, G. Becker, C. Pesavento, N. Tschowri, and R. Hengge, “Gene expression patterns and differential input into curli fimbriae regulation of all GGDEF/EAL domain proteins in *Escherichia coli*”, eng, [Microbiology \(Reading, England\)](#) **155**, 1318–1331 (2009).
- <sup>140</sup>C. Pesavento, G. Becker, N. Sommerfeldt, A. Possling, N. Tschowri, A. Mehliis, and R. Hengge, “Inverse regulatory coordination of motility and curli-mediated adhesion in *Escherichia coli*”, [Genes & Development](#) **22**, 2434–2446 (2008).
- <sup>141</sup>M. A. Schembri, D. Dalsgaard, and P. Klemm, “Capsule Shields the Function of Short Bacterial Adhesins”, [Journal of Bacteriology](#) **186**, 1249–1257 (2004).
- <sup>142</sup>M. A. Schembri, D. W. Ussery, C. Workman, H. Hasman, and P. Klemm, “DNA microarray analysis of fim mutations in *Escherichia coli*”, eng, [Molecular genetics and genomics: MGG](#) **267**, 721–729 (2002).
- <sup>143</sup>O. Hallatschek and D. S. Fisher, “Acceleration of evolutionary spread by long-range dispersal”, [Proceedings of the National Academy of Sciences](#) **111**, E4911–E4919 (2014).
- <sup>144</sup>J. Paulose and O. Hallatschek, “The impact of long-range dispersal on gene surfing”, [Proceedings of the National Academy of Sciences](#) **117**, 7584–7593 (2020).
- <sup>145</sup>M. E. Asp, M.-T. Ho Thanh, D. A. Germann, R. J. Carroll, A. Franceski, R. D. Welch, A. Gopinath, and A. E. Patteson, “Spreading rates of bacterial colonies depend on substrate stiffness and permeability”, [PNAS Nexus](#) **1**, pgac025 (2022).
- <sup>146</sup>K. D. Young, “The Selective Value of Bacterial Shape”, en, [Microbiology and Molecular Biology Reviews](#) **70**, 660 (2006).
- <sup>147</sup>M. T. Cabeen and C. Jacobs-Wagner, “Bacterial cell shape”, en, [Nature Reviews Microbiology](#) **3**, 601–610 (2005).
- <sup>148</sup>A. Zapun, T. Vernet, and M. G. Pinho, “The different shapes of cocci”, [FEMS Microbiology Reviews](#) **32**, 345–360 (2008).
- <sup>149</sup>A. Amir and S. v. Teeffelen, “Getting into shape: How do rod-like bacteria control their geometry?”, en, [Systems and Synthetic Biology](#) **8**, 227 (2014).
- <sup>150</sup>M. E. Jacob, “Spirilla IV”, en, in [Veterinary Microbiology](#) (John Wiley & Sons, Ltd, 2022), pp. 219–224.
- <sup>151</sup>J. L. Jones, “VIBRIO | Introduction, Including *Vibrio parahaemolyticus*, *Vibrio vulnificus*, and Other *Vibrio* Species”, in [Encyclopedia of Food Microbiology \(Second Edition\)](#), edited by C. A. Batt and M. L. Tortorello (Academic Press, Oxford, Jan. 2014), pp. 691–698.
- <sup>152</sup>J. R. Cole, “5 - Spirochetes”, in [Diagnostic Procedure in Veterinary Bacteriology and Mycology \(Fifth Edition\)](#), edited by G. R. Carter and J. R. Cole (Academic Press, San Diego, Jan. 1990), pp. 41–60.
- <sup>153</sup>G. G. D’Souza, “Phenotypic variation in spatially structured microbial communities: ecological origins and consequences”, [Current Opinion in Biotechnology, Energy Biotechnology Environmental Biotechnology](#) **62**, 220–227 (2020).

- <sup>154</sup>J. M. Guberman, A. Fay, J. Dworkin, N. S. Wingreen, and Z. Gitai, “PSICIC: Noise and Asymmetry in Bacterial Division Revealed by Computational Image Analysis at Sub-Pixel Resolution”, en, *PLOS Computational Biology* **4**, e1000233 (2008).
- <sup>155</sup>M. C. F. van Teeseling, M. A. de Pedro, and F. Cava, “Determinants of Bacterial Morphology: From Fundamentals to Possibilities for Antimicrobial Targeting”, English, *Frontiers in Microbiology* **8**, 10.3389/fmicb.2017.01264 (2017).
- <sup>156</sup>D. O. Serra, A. M. Richter, G. Klauck, F. Mika, and R. Hengge, “Microanatomy at Cellular Resolution and Spatial Order of Physiological Differentiation in a Bacterial Biofilm”, *mBio* **4**, 10.1128/mbio.00103–13 (2013).
- <sup>157</sup>S. S. Justice, C. Hung, J. A. Theriot, D. A. Fletcher, G. G. Anderson, M. J. Footer, and S. J. Hultgren, “Differentiation and developmental pathways of uropathogenic *Escherichia coli* in urinary tract pathogenesis”, eng, *Proceedings of the National Academy of Sciences of the United States of America* **101**, 1333–1338 (2004).
- <sup>158</sup>B. Ilkanaiv, D. B. Kearns, G. Ariel, and A. Be’er, “Effect of Cell Aspect Ratio on Swarming Bacteria”, *Physical Review Letters* **118**, 158002 (2017).
- <sup>159</sup>A. Alonso and J. B. Kirkegaard, “Learning optimal integration of spatial and temporal information in noisy chemotaxis”, *PNAS Nexus*, pgae235 (2024).
- <sup>160</sup>A. L. Koch, “WHAT SIZE SHOULD A BACTERIUM BE? A Question of Scale”, en, *Annual Review of Microbiology* **50**, 317–348 (1996).
- <sup>161</sup>E. A. Martens, N. Wadhwa, N. S. Jacobsen, C. Lindemann, K. H. Andersen, and A. Visser, “Size structures sensory hierarchy in ocean life”, en, *Proceedings of the Royal Society B: Biological Sciences* **282**, 20151346 (2015).
- <sup>162</sup>P. A. Levin and E. R. Angert, “Small but Mighty: Cell Size and Bacteria”, *Cold Spring Harbor Perspectives in Biology* **7**, a019216 (2015).
- <sup>163</sup>B. J. Arnold, I.-T. Huang, and W. P. Hanage, “Horizontal gene transfer and adaptive evolution in bacteria”, en, *Nature Reviews Microbiology* **20**, 206–218 (2022).
- <sup>164</sup>H. P. Erickson, “Evolution in bacteria”, en, *Nature* **413**, 30–30 (2001).
- <sup>165</sup>T. Kruse, J. Bork-Jensen, and K. Gerdes, “The morphogenetic MreBCD proteins of *Escherichia coli* form an essential membrane-bound complex”, en, *Molecular Microbiology* **55**, 78–89 (2005).
- <sup>166</sup>T. S. Ursell, J. Nguyen, R. D. Monds, A. Colavin, G. Billings, N. Ouzounov, Z. Gitai, J. W. Shaevitz, and K. C. Huang, “Rod-like bacterial shape is maintained by feedback between cell curvature and cytoskeletal localization”, *Proceedings of the National Academy of Sciences* **111**, E1025–E1034 (2014).
- <sup>167</sup>R. E. Lenski, M. R. Rose, S. C. Simpson, and S. C. Tadler, “Long-Term Experimental Evolution in *Escherichia coli*. I. Adaptation and Divergence During 2,000 Generations”, *The American Naturalist* **138**, 1315–1341 (1991).
- <sup>168</sup>R. D. Monds, T. K. Lee, A. Colavin, T. Ursell, S. Quan, T. F. Cooper, and K. C. Huang, “Systematic Perturbation of Cytoskeletal Function Reveals a Linear Scaling Relationship between Cell Geometry and Fitness”, *Cell Reports* **9**, 1528–1537 (2014).

- <sup>169</sup>S. White, J. Quinn, J. Enzor, J. Staats, S. M. Mosier, J. Almarode, T. N. Denny, K. J. Weinhold, G. Ferrari, and C. Chan, “FlowKit: A Python Toolkit for Integrated Manual and Automated Cytometry Analysis Workflows”, English, *Frontiers in Immunology* **12**, 10.3389/fimmu.2021.768541 (2021).
- <sup>170</sup>L. McInnes, J. Healy, and S. Astels, “Hdbscan: Hierarchical density based clustering”, en, *Journal of Open Source Software* **2**, 205 (2017).
- <sup>171</sup>G. Bradski, “The OpenCV Library”,
- <sup>172</sup>T. J. Rudge, P. J. Steiner, A. Phillips, and J. Haseloff, “Computational Modeling of Synthetic Microbial Biofilms”, *ACS Synthetic Biology* **1**, 345–352 (2012).
- <sup>173</sup>T. Rudge and J. Haseloff, “A Computational Model of Cellular Morphogenesis in Plants”, en, in *Advances in Artificial Life*, edited by M. S. Capcarrère, A. A. Freitas, P. J. Bentley, C. G. Johnson, and J. Timmis (2005), pp. 78–87.
- <sup>174</sup>P. G. d. Gennes, J. Prost, P. G. d. Gennes, and J. Prost, *The Physics of Liquid Crystals*, Second Edition, Second Edition, International Series of Monographs on Physics (Oxford University Press, Oxford, New York, Apr. 1995).
- <sup>175</sup>B. Maier, “How Physical Interactions Shape Bacterial Biofilms”, eng, *Annual Review of Biophysics* **50**, 401–417 (2021).
- <sup>176</sup>D. J. Marshall, M. Malerba, T. Lines, A. L. Sezmis, C. M. Hasan, R. E. Lenski, and M. J. McDonald, “Long-term experimental evolution decouples size and production costs in *Escherichia coli*”, *Proceedings of the National Academy of Sciences* **119**, Publisher: Proceedings of the National Academy of Sciences, e2200713119 (2022).
- <sup>177</sup>G. A. Pankey and L. D. Sabath, “Clinical Relevance of Bacteriostatic versus Bactericidal Mechanisms of Action in the Treatment of Gram-Positive Bacterial Infections”, *Clinical Infectious Diseases* **38**, 864–870 (2004).
- <sup>178</sup>F. Baquero and B. R. Levin, “Proximate and ultimate causes of the bactericidal action of antibiotics”, en, *Nature Reviews Microbiology* **19**, 123–132 (2021).
- <sup>179</sup>N. Wald-Dickler, P. Holtom, and B. Spellberg, “Busting the Myth of “Static vs Cidal”: A Systemic Literature Review”, *Clinical Infectious Diseases* **66**, 1470–1474 (2018).
- <sup>180</sup>K. Kitano and A. Tomasz, “Triggering of autolytic cell wall degradation in *Escherichia coli* by beta-lactam antibiotics”, *Antimicrobial Agents and Chemotherapy* **16**, 838–848 (1979).
- <sup>181</sup>L. P. Kotra, J. Haddad, and S. Mobashery, “Aminoglycosides: Perspectives on Mechanisms of Action and Resistance and Strategies to Counter Resistance”, *Antimicrobial Agents and Chemotherapy* **44**, 3249–3256 (2000).
- <sup>182</sup>S. Lohsen and D. Stephens, “Current Macrolide Antibiotics and Their Mechanisms of Action”, en, in *Antibiotic Drug Resistance* (John Wiley & Sons, Ltd, 2019), pp. 97–117.

- <sup>183</sup>C. J. L. Murray, K. S. Ikuta, F. Sharara, L. Swetschinski, G. R. Aguilar, A. Gray, C. Han, C. Bisignano, P. Rao, E. Wool, S. C. Johnson, A. J. Browne, M. G. Chipeta, F. Fell, S. Hackett, G. Haines-Woodhouse, B. H. K. Hamadani, E. A. P. Kumaran, B. McManigal, S. Achalapong, R. Agarwal, S. Akech, S. Albertson, J. Amuasi, J. Andrews, A. Aravkin, E. Ashley, F.-X. Babin, F. Bailey, S. Baker, B. Basnyat, A. Bekker, R. Bender, J. A. Berkley, A. Bethou, J. Bielicki, S. Boonkasidecha, J. Bukosia, C. Carvalheiro, C. Castañeda-Orjuela, V. Chansamouth, S. Chaurasia, S. Chiurchiù, F. Chowdhury, R. C. Donatien, A. J. Cook, B. Cooper, T. R. Cressey, E. Criollo-Mora, M. Cunningham, S. Darboe, N. P. J. Day, M. D. Luca, K. Dokova, A. Dramowski, S. J. Dunachie, T. D. Bich, T. Eckmanns, D. Eibach, A. Emami, N. Feasey, N. Fisher-Pearson, K. Forrest, C. Garcia, D. Garrett, P. Gastmeier, A. Z. Giref, R. C. Greer, V. Gupta, S. Haller, A. Haselbeck, S. I. Hay, M. Holm, S. Hopkins, Y. Hsia, K. C. Iregbu, J. Jacobs, D. Jarovsky, F. Javanmardi, A. W. J. Jenney, M. Khorana, S. Khusuwan, N. Kissoon, E. Kobeissi, T. Kostyanev, F. Krapp, R. Krumkamp, A. Kumar, H. H. Kyu, C. Lim, K. Lim, D. Limmathurotsakul, M. J. Loftus, M. Lunn, J. Ma, A. Manoharan, F. Marks, J. May, M. Mayxay, N. Mturi, T. Munera-Huertas, P. Musicha, L. A. Musila, M. M. Mussi-Pinhata, R. N. Naidu, T. Nakamura, R. Nanavati, S. Nangia, P. Newton, C. Ngoun, A. Novotney, D. Nwakanma, C. W. Obiero, T. J. Ochoa, A. Olivas-Martinez, P. Olliaro, E. Ooko, E. Ortiz-Brizuela, P. Ounchanum, G. D. Pak, J. L. Paredes, A. Y. Peleg, C. Perrone, T. Phe, K. Phommasone, N. Plakkal, A. Ponce-de-Leon, M. Raad, T. Ramdin, S. Rattanavong, A. Riddell, T. Roberts, J. V. Robotham, A. Roca, V. D. Rosenthal, K. E. Rudd, N. Russell, H. S. Sader, W. Saengchan, J. Schnall, J. A. G. Scott, S. Seekaew, M. Sharland, M. Shivamallappa, J. Sifuentes-Osornio, A. J. Simpson, N. Steenkeste, A. J. Stewardson, T. Stoeva, N. Tasak, A. Thaiprakong, G. Thwaites, C. Tigoï, C. Turner, P. Turner, H. R. v. Doorn, S. Velaphi, A. Vongpradith, M. Vongsouvath, H. Vu, T. Walsh, J. L. Walson, S. Waner, T. Wangrangsimakul, P. Wannapinij, T. Wozniak, T. E. M. W. Y. Sharma, K. C. Yu, P. Zheng, B. Sartorius, A. D. Lopez, A. Stergachis, C. Moore, C. Dolecek, and M. Naghavi, “Global burden of bacterial antimicrobial resistance in 2019: a systematic analysis”, English, *The Lancet* **399**, 629–655 (2022).
- <sup>184</sup>M. A. Abushaheen, Muzaaheed, A. J. Fatani, M. Alosaimi, W. Mansy, M. George, S. Acharya, S. Rathod, D. D. Divakar, C. Jhugroo, S. Vellappally, A. A. Khan, J. Shaik, and P. Jhugroo, “Antimicrobial resistance, mechanisms and its clinical significance”, *Disease-a-Month, Antimicrobial resistance, mechanisms and its clinical significance* **66**, 100971 (2020).
- <sup>185</sup>E. M. Darby, E. Trampari, P. Siasat, M. S. Gaya, I. Alav, M. A. Webber, and J. M. A. Blair, “Molecular mechanisms of antibiotic resistance revisited”, en, *Nature Reviews Microbiology* **21**, 280–295 (2023).
- <sup>186</sup>K. Lewis, “Multidrug Tolerance of Biofilms and Persister Cells”, en, in *Bacterial Biofilms*, edited by T. Romeo (Springer, Berlin, Heidelberg, 2008), pp. 107–131.
- <sup>187</sup>U. Klümper, M. Recker, L. Zhang, X. Yin, T. Zhang, A. Buckling, and W. H. Gaze, “Selection for antimicrobial resistance is reduced when embedded in a natural microbial community”, eng, *The ISME journal* **13**, 2927–2937 (2019).
- <sup>188</sup>E. Amanatidou, A. C. Matthews, U. Kuhlicke, T. R. Neu, J. P. McEvoy, and B. Raymond, “Biofilms facilitate cheating and social exploitation of -lactam resistance in *Escherichia coli*”, en, *npj Biofilms and Microbiomes* **5**, 1–10 (2019).

- <sup>189</sup>A. Brauner, O. Fridman, O. Gefen, and N. Q. Balaban, “Distinguishing between resistance, tolerance and persistence to antibiotic treatment”, en, *Nature Reviews Microbiology* **14**, 320–330 (2016).
- <sup>190</sup>D. Lebeaux, J.-M. Ghigo, and C. Beloin, “Biofilm-Related Infections: Bridging the Gap between Clinical Management and Fundamental Aspects of Recalcitrance toward Antibiotics”, *Microbiology and Molecular Biology Reviews : MMBR* **78**, 510–543 (2014).
- <sup>191</sup>D. Davies, “Understanding biofilm resistance to antibacterial agents”, en, *Nature Reviews Drug Discovery* **2**, 114–122 (2003).
- <sup>192</sup>C. Sternberg, B. B. Christensen, T. Johansen, A. Toftgaard Nielsen, J. B. Andersen, M. Givskov, and S. Molin, “Distribution of Bacterial Growth Activity in Flow-Chamber Biofilms”, *Applied and Environmental Microbiology* **65**, 4108–4117 (1999).
- <sup>193</sup>F. Díaz-Pascual, R. Hartmann, M. Lempp, L. Vidakovic, B. Song, H. Jeckel, K. M. Thormann, F. H. Yildiz, J. Dunkel, H. Link, C. D. Nadell, and K. Drescher, “Breakdown of *Vibrio cholerae* biofilm architecture induced by antibiotics disrupts community barrier function”, en, *Nature Microbiology* **4**, 2136–2145 (2019).
- <sup>194</sup>R. A. Sorg, L. Lin, G. S. v. Doorn, M. Sorg, J. Olson, V. Nizet, and J.-W. Veening, “Collective Resistance in Microbial Communities by Intracellular Antibiotic Deactivation”, en, *PLOS Biology* **14**, e2000631 (2016).
- <sup>195</sup>J. L. Maddocks and J. R. May, “" INDIRECT PATHOGENICITY " OF PENICILLINASE-PRODUCING ENTEROBACTERIA IN CHRONIC BRONCHIAL INFECTIONS”, *The Lancet*, Originally published as Volume 1, Issue 7599 **293**, 793–795 (1969).
- <sup>196</sup>H. Nicoloff and D. I. Andersson, “Indirect resistance to several classes of antibiotics in cocultures with resistant bacteria expressing antibiotic-modifying or -degrading enzymes”, *Journal of Antimicrobial Chemotherapy* **71**, 100–110 (2016).
- <sup>197</sup>A. Sharma and K. B. Wood, “Spatial segregation and cooperation in radially expanding microbial colonies under antibiotic stress”, en, *The ISME Journal* **15**, 3019–3033 (2021).
- <sup>198</sup>I. Frost, W. P. J. Smith, S. Mitri, A. S. Millan, Y. Davit, J. M. Osborne, J. M. Pitt-Francis, R. C. MacLean, and K. R. Foster, “Cooperation, competition and antibiotic resistance in bacterial colonies”, *The ISME Journal* **12**, 1582–1593 (2018).
- <sup>199</sup>G. D’Achille and G. Morroni, “Chapter Six - Side effects of antibiotics and perturbations of mitochondria functions”, in *International Review of Cell and Molecular Biology*, Vol. 377, edited by S. Marchi and L. Galluzzi, Mitochondria and Bacterial Pathogens - Part B (Academic Press, Jan. 2023), pp. 121–139.
- <sup>200</sup>E. J. Rogers, M. S. Rahman, R. T. Hill, and P. S. Lovett, “The Chloramphenicol-Inducible *catB* Gene in *Agrobacterium tumefaciens* Is Regulated by Translation Attenuation”, *Journal of Bacteriology* **184**, 4296–4300 (2002).
- <sup>201</sup>P. Greulich, M. Scott, M. R. Evans, and R. J. Allen, “Growth-dependent bacterial susceptibility to ribosome-targeting antibiotics”, *Molecular Systems Biology* **11**, 0796 (2015).
- <sup>202</sup>J. B. Deris, M. Kim, Z. Zhang, H. Okano, R. Hermsen, A. Groisman, and T. Hwa, “The innate growth bistability and fitness landscapes of antibiotic-resistant bacteria”, en, *Science (New York, N.Y.)* **342**, 1237435 (2013).

- <sup>203</sup>I. Wiegand, K. Hilpert, and R. E. W. Hancock, “Agar and broth dilution methods to determine the minimal inhibitory concentration (MIC) of antimicrobial substances”, en, [Nature Protocols](#) **3**, 163–175 (2008).
- <sup>204</sup>T. S. Stenum, M. Kongstad, E. Holmqvist, B. Kallipolitis, S. L. Svenningsen, and M. A. Sørensen, “Three Ribosomal Operons of *Escherichia coli* Contain Genes Encoding Small RNAs That Interact With Hfq and CsrA in vitro”, English, [Frontiers in Microbiology](#) **12**, 10.3389/fmicb.2021.625585 (2021).
- <sup>205</sup>B. Gummesson, S. A. Shah, A. S. Borum, M. Fessler, N. Mitarai, M. A. Sørensen, and S. L. Svenningsen, “Valine-Induced Isoleucine Starvation in *Escherichia coli* K-12 Studied by Spike-In Normalized RNA Sequencing”, English, [Frontiers in Genetics](#) **11**, 10.3389/fgene.2020.00144 (2020).
- <sup>206</sup>M. S. Manna, Y. T. Tamer, I. Gaszek, N. Poulides, A. Ahmed, X. Wang, F. C. R. Toprak, D. R. Woodard, A. Y. Koh, N. S. Williams, D. Borek, A. R. Atilgan, J. D. Hulleman, C. Atilgan, U. Tambar, and E. Toprak, “A trimethoprim derivative impedes antibiotic resistance evolution”, en, [Nature Communications](#) **12**, 2949 (2021).
- <sup>207</sup>K. Tomasek, T. Bergmiller, and C. C. Guet, “Lack of cations in flow cytometry buffers affect fluorescence signals by reducing membrane stability and viability of *Escherichia coli* strains”, [Journal of Biotechnology](#) **268**, 40–52 (2018).
- <sup>208</sup>B. A. Berryhill, T. Gil-Gil, J. A. Manuel, A. P. Smith, E. Margollis, F. Baquero, and B. R. Levin, “What’s the Matter with MICs: Bacterial Nutrition, Limiting Resources, and Antibiotic Pharmacodynamics”, [Microbiology Spectrum](#) **11**, e04091–22 (2023).
- <sup>209</sup>A. Wanger and K. Mills, “Etest for susceptibility testing of *Mycobacterium tuberculosis* and *Mycobacterium avium-intracellulare*”, [Diagnostic Microbiology and Infectious Disease](#) **19**, 179–181 (1994).
- <sup>210</sup>J. A. Myers, B. S. Curtis, and W. R. Curtis, “Improving accuracy of cell and chromophore concentration measurements using optical density”, [BMC Biophysics](#) **6**, 4 (2013).
- <sup>211</sup>S. C. Booth, O. J. Meacock, and K. R. Foster, *Cell motility greatly empowers bacterial contact weapons*, en, Oct. 2023.
- <sup>212</sup>D. Ciccacese, A. Zuidema, V. Merlo, and D. R. Johnson, “Interaction-dependent effects of surface structure on microbial spatial self-organization”, [Philosophical Transactions of the Royal Society B: Biological Sciences](#) **375**, 20190246 (2020).
- <sup>213</sup>L. Xiong, Y. Cao, R. Cooper, W.-J. Rappel, J. Hasty, and L. Tsimring, “Flower-like patterns in multi-species bacterial colonies”, [eLife](#) **9**, edited by D. Weigel, A. M. Walczak, and A. Seminara, e48885 (2020).
- <sup>214</sup>L. M. McCully, A. S. Bitzer, S. C. Seaton, L. M. Smith, and M. W. Silby, “Interspecies Social Spreading: Interaction between Two Sessile Soil Bacteria Leads to Emergence of Surface Motility”, [mSphere](#) **4**, 10.1128/msphere.00696–18 (2019).
- <sup>215</sup>A. Leinweber, R. Fredrik Inglis, and R. Kümmerli, “Cheating fosters species co-existence in well-mixed bacterial communities”, en, [The ISME Journal](#) **11**, 1179–1188 (2017).



# Appendix A

## Manuscripts

### A.1 Motility mediates satellite formation in confined biofilms

**Authors:** [Mireia Cordero](#)<sup>1</sup>, Namiko Mitarai<sup>1</sup> and Liselotte Jauffred<sup>1</sup>

**Affiliations:** <sup>1</sup>Niels Bohr Institute, University of Copenhagen, Copenhagen 2100, Denmark

**Journal:** The ISME Journal, 17, 1819–1827 (2023)

**DOI:** 10.1038/s41396-023-01494-x

**My contributions:** I designed the study in collaboration with NM and LJ. I performed the experiments as well as the data analysis and computational simulations. I wrote the article and made the figures.

**Notes in relation to Master's Thesis:** The initial research project was conceived during my master's thesis. Therefore, the initial experimental methods and computational simulations have been described there. All the results except figures S3 and S4 were obtained during my PhD. The manuscript was fully written during my PhD.



# Motility mediates satellite formation in confined biofilms

Mireia Cordero <sup>1</sup>, Namiko Mitarai <sup>1</sup>✉ and Liselotte Jauffred <sup>1</sup>✉

© The Author(s) 2023

Bacteria have spectacular survival capabilities and can spread in many, vastly different environments. For instance, when pathogenic bacteria infect a host, they expand by proliferation and squeezing through narrow pores and elastic matrices. However, the exact role of surface structures—important for biofilm formation and motility—and matrix density in colony expansion and morphogenesis is still largely unknown. Using confocal laser-scanning microscopy, we show how *satellite* colonies emerge around *Escherichia coli* colonies embedded in semi-dense hydrogel in controlled in vitro assays. Using knock-out mutants, we tested how extra-cellular structures, (e.g., exo-polysaccharides, flagella, and fimbria) control this morphology. Moreover, we identify the extra-cellular matrix' density, where this morphology is possible. When paralleled with mathematical modelling, our results suggest that satellite formation allows bacterial communities to spread faster. We anticipate that this strategy is important to speed up expansion in various environments, while retaining the close interactions and protection provided by the community.

*The ISME Journal* (2023) 17:1819–1827; <https://doi.org/10.1038/s41396-023-01494-x>

## INTRODUCTION

While many bacterial species can grow as free-swimming cells in planktonic mode, they will often adhere to a substrate or small enclosure to form dense communities like biofilms [1]. The biofilm community offers protection from local threats. For instance, against the shear flow by attaching to a solid substrate or by protecting the inner cells from the immune system, toxins, or bacteriophages [2, 3]. Also, the local, high cell density helps bacteria share necessary chemicals within the community [4]. The importance of biofilm formation is also reflected in the fact that bacteria have many genes contributing to cell-adhesive structures, such as exo-polysaccharides (EPS), fimbriae, and flagella [5]. These biofilms often grow—as the name indicates—as quasi-two-dimensional (2D) colonies on substrates, but also as three-dimensional (3D) communities in habitats, such as gels, tissues (e.g., the human gut), and soils. Despite this high prevalence, we still lack a full understanding of how dynamic morphologies of 3D biofilms are controlled.

When a bacterial community grows as a dense colony, the surface expands outwards as cells are proliferating, with a doubling time close to what we know from well-mixed liquid cultures. Behind the fast-growing pioneering cells on the front, is a quiescent region, where proliferation is slowed down significantly, due to space constraints [6] and metabolite limitations [7, 8]. Thus, the resulting expansion of the colony surface makes the population grow linearly over time [8, 9], in contrast to the exponential growth in early colonies or liquid cultures. Therefore, the motility of cells is crucial to speed up colony expansion. It is well-established by swimming assays in low density hydrogel (~0.2% agar), that chemotaxis is enhanced by nutrient shortage [10–12] or attractant gradients [13]. Chemotaxis accelerates expansion dynamics of populations by allowing access to more nutrient [14]. In liquid media, the chemotaxis of the model bacterium *Escherichia coli* is driven by swimming, specifically

bundling and propelling of flagella, which gives rise to a run-and-tumble motion. In visco-elastic media, bacterial migration is restricted more and more as elasticity is raised and pore size diminished [15], and the chemotaxis has been reported to be reversely proportional to the elasticity of the medium [12]. Therefore, above a certain threshold of medium density, colony expansion is solely growth driven. Furthermore, in a dense hydrogel (>0.5% agarose), the stress at the interface (between colony and media) gives rise to internal ordering of cells [16]. But what happens in the intermediate regions, where the hydrogel is semi-dense? Is it possible that cells can both retain colony characteristics but still speed up the expansion to enhance colonization?

Here we use mono-clonal *E. coli* colonies embedded in an agarose matrix [2, 17] as simple models of 3D colony formation. We use a combination of experiments and mathematical modelling to show how 3D colonies can join growth and flagella-based motility to colonize their local environment. We investigate how the spreading depends on the expression of extra-cellular structures and hydrogel concentration. We demonstrate that indeed 3D colony expansion—driven by the combination of growth and motility—gives rise to satellite colony formation and acceleration of the population expansion to be super-linear over time.

## RESULTS

### Satellite colonies form around 3D colonies

To mimic 3D biofilm evolution in natural settings, *E. coli* MG1566 wild-type (wt) single cells were embedded in low concentration ( $\approx 10$  cells/ml) in a semi-dense agarose (0.3%) matrix and incubated for 15 h at 37°C in a minimal defined medium composed of M63 supplemented with 20  $\mu$ m/ml glucose (M63 + glu). This protocol (Materials and Methods) resulted in confined,

<sup>1</sup>The Niels Bohr Institute, University of Copenhagen, Blegdamsvej 17, DK-2100 Copenhagen O, Denmark. ✉email: mitarai@nbi.dk; jauffred@nbi.dk

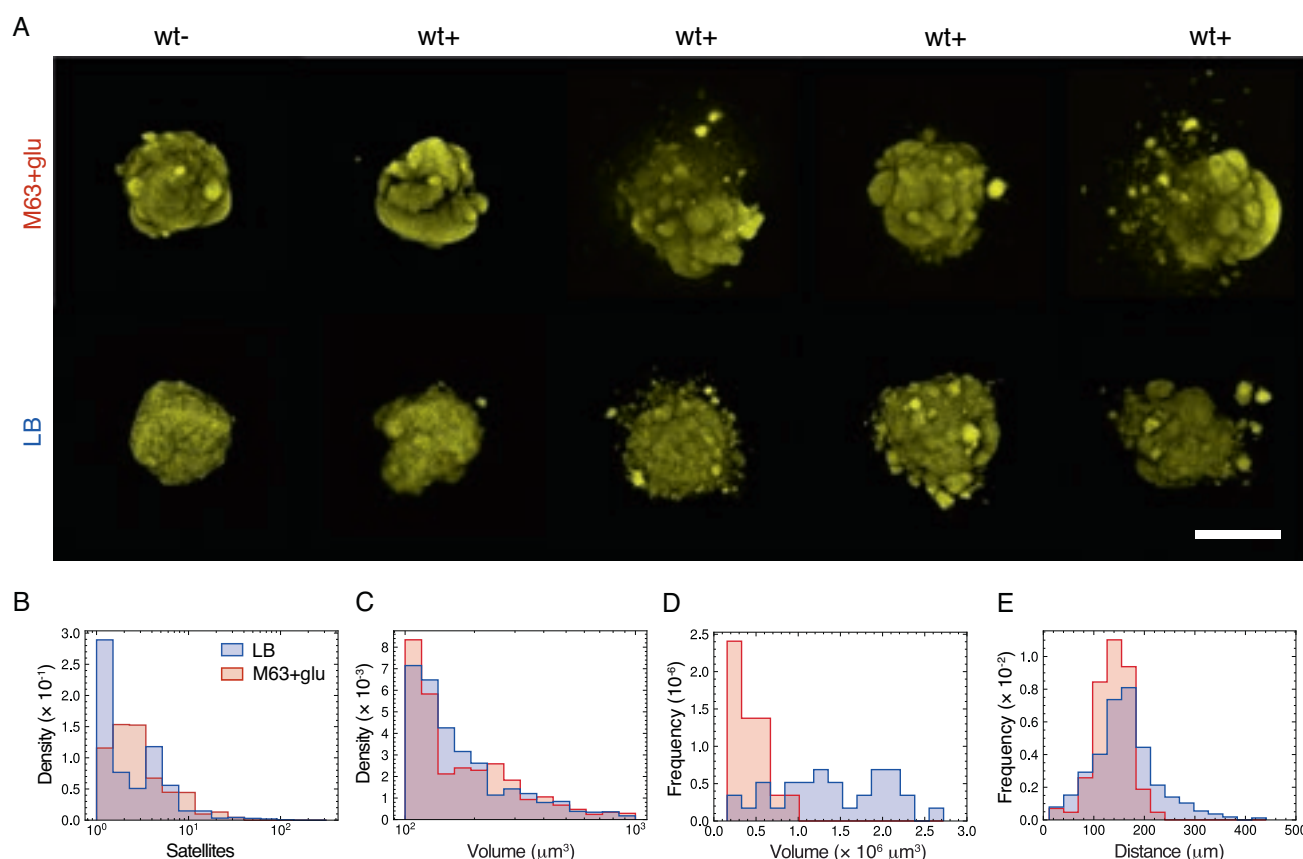


**Fig. 1** **Satellite morphology in mature 3D colonies.** **A** Examples of pseudo-colored 3D colonies (maximum intensity projections) in 0.3% agarose and minimal (M63+glu) or rich medium (LB). These examples show inhomogeneity of morphologies without satellites (wt-) or with satellites (wt+). The scale bar corresponds to 200  $\mu\text{m}$ . **B** Distributions of the number of satellites pr. colony (log-scale) in either LB ( $N = 17$ ) and M63 + glu ( $N = 34$ ). **C** Distributions of satellite volumes (log-scale) in either LB ( $N = 149$ ) or in M63 + glu ( $N = 574$ ). **D** Distribution of volumes of the main colonies in either LB ( $N = 17$ ) and M63+glu ( $N = 34$ ). **E** Distributions of distances from the center-of-mass of satellites to the center-of-mass of the main colony in either LB ( $N = 17$ ) and M63 + glu ( $N = 34$ ).

mono-clonal quasi-spherical colonies on the order of a few hundred  $\mu\text{m}$  in diameter. We also verified that the colony expansion after 15 h has slowed down from exponential to become linear over time (Supplementary Fig. S1). In parallel, we performed a similar experiment using a rich Luria-Bertani (LB) medium and a shorter incubation time of 13 h to account for differences in doubling time in the two media: 27.8 min (LB) vs. 68.4 min (M63 + glu) (Supplementary Fig. S2). In similar studies, these has been referred to as 3D biofilms [16, 18, 19], but here we use the term colony.

The resulting colonies grew as compact quasi-spherical colonies with a mountainous surface of multiple protrusions, denoted as wt- (Fig. 1A, first column). However, for the majority of 3D colonies, 34/40 (M63 + glu) and 17/18 (LB), these protrusions seem to have escaped the colony as small stationary satellite colonies, denoted as wt+ (Fig. 1A). Both morphology types occurred for colonies grown in both the minimal (M63+glu) and the rich media (LB). It is worth noticing that these two morphologies were not determined by any obvious variations between experiments, as we found wt- and wt+ side by side in the same culture wells. To evaluate whether this behavior was dependent on the specific hydrogel, we did a similar assay interchanging agarose with agar (0.5%) and found the majority of 3D colonies, 21/39 (M63 + glu) to be wt+ (examples in Supplementary Fig. S3).

From the subset of 3D colonies with satellite morphology (wt+), we measured the distributions of number of satellites, their volumes, distances to the main colony, as well as the main colony volumes, for both minimal (blue) and rich (red) medium

(Fig. 1B–E). The distribution of the number of satellites per 3D colony (Fig. 1B) shows that the majority had less than 10 satellites. Furthermore, from the distribution of satellite volumes, we found that satellites with smaller volumes had higher prevalence (Fig. 1C). The typical satellite size ( $<10^3 \mu\text{m}^3$ ) was about three orders of magnitude smaller than the average volumes of the main colonies, which were  $(1.3 \pm 0.6) \cdot 10^6 \mu\text{m}^3$  (M63 + glu) and  $(4 \pm 1) \cdot 10^5 \mu\text{m}^3$  (LB) (Fig. 1D). Finally, the distributions of distances between center-of-masses of the satellites and their respective main colony had average distances of  $161 \pm 64 \mu\text{m}$  and  $137 \pm 35 \mu\text{m}$  for minimal (M63 + glu) and rich (LB) medium, respectively (Fig. 1E). Our definition of a satellite is that it is completely detached from the main colony. It is, therefore, possible that we wrongly exclude some of the smaller ( $<100 \mu\text{m}$ ) distances between the center-of-masses (Fig. 1E), as the satellites have partly merged with the main colonies. From time-lapse imaging we found incidences of satellites forming and subsequently merging with the main colony (Supplementary movies 1–5).

A possible mechanism behind satellite formation is the combination of bacterial cell-cell interaction, motility, and the growth of the cells: A few cells can move away from the surface of the main colony escaping from their attachment to migrate to a different position in the gel, and each of them starts to grow into a new satellite colony. Therefore, in the following, we investigate how bacterial surface structures, as well as the density of the substrate, affect the emergence of satellite colonies. The first is achieved by studying mutants with deletions of structures

important for adhesion and motility, and the latter by modifying agarose concentration in the extracellular matrix.

### Deletion of extracellular structures causes loss of satellite morphology

One of the factors governing the morphology of 3D colonies and the appearance of satellites must be the complex interplay between cell envelope components and the extracellular matrix. So, bacterial cell-adhesive structures, such as exo-polysaccharides (EPS), fimbriae, and flagella are obvious components that can modulate the colony morphology. Therefore, we investigated a collection of mutants lacking diverse bacterial surface structures (Table 1). Figure 2A sketches the parental strain (wt) and the suppressed structures: flagella, type I pili, colanic acid, curli fimbriae and antigen 43.

To examine the influence of these surface components, we examined the 3D colony morphology after knock-out deletion and compared it with the wt colony morphology (Fig. 2B).

Flagella are helical filaments responsible for some of the locomotion mechanisms adopted by bacteria. By expressing flagella, cells can self-propel in liquids (swimming) and on surfaces (swarming) [20]. Furthermore, flagella have been shown to play a role in cell-substratum (e.g. initial colony formation [21]) and cell-cell interactions [5]. However, the role of these structures in

bacterial motility in confined environments remains largely unknown [22]. We tested a  $\Delta fliC$  mutant and did not find any satellite formation ( $N=21$ ). We also assessed a  $\Delta fim$  mutant without type I pili, which is a hair-like structures crucial for cell-cell adhesion [21]. The morphology of these mutants was also indistinguishable from that of wt- ( $N=21$ ).

The  $\Delta flu$  mutant has a deletion in the gene encoding the auto-transporter protein antigen 43, which comes in high copy numbers (up to 50,000 pr. cell [23]). Antigen 43 favors cell-cell interactions through chain-formation and is referred to as a *handshake* protein [24–26]. Given the inverse regulation of pili and antigen 43 [27], we tested both  $\Delta flu$  ( $N=21$ ) and the double mutant  $\Delta flu\Delta fim$  ( $N=22$ ) and found that both display a loss of satellite morphology; even when agarose was interchanged with 0.5% agar (Supplementary Fig. S4).

We also tested the EPS colonic acid mutant,  $\Delta cps$  ( $N=17$ ), as well as the  $\Delta csgAB$  ( $N=18$ ) with a deletion in the gene encoding a fibrous surface protein, curli fimbriae, important for both cell-cell and cell-substrate adhesion [28–32]. Even though *cps* and *csgAB* predominantly are expressed at ambient temperature [30, 33], the wt has in a prior been found to have capsules in contrast to the EPS colonic acid mutant ( $\Delta cps$ ), which had none [34]. In accordance with that we found wt+ morphology to be lost in both cases. In summary, we found that the satellite morphology (wt+) is lost in the confined colonies of all tested mutants.

### Deletion of extracellular structures reduces motility

Except for the flagella deletion that disables the most common mechanisms of bacterial motility (swimming/swarming), the effect of the other tested surface structures on bacterial confined motility is less apparent. To investigate this further, we performed classical motility assays in low density agarose for all strains used in this study. The assay was done using both rich (LB) and minimal media (M63 + glu) with varying agarose concentrations (0.2–0.4%).

The parental strain (wt) was the most motile in the low density (0.2% agarose) rich medium (LB), with an average distance reached of about three times the one of the second fastest,  $\Delta cps$  (Fig. 2C). All strains were found to be motile except the

**Table 1.** *Escherichia coli* strains used in the study.

Name	Strain	Relevant characteristics	Reference
wt	MS613	MG1655 K-12 reference (F-lambda- ilvG- rfb-50 rph-1) strain	[62]
$\Delta flu$	MS427	MG1655 $\Delta flu$	[68]
$\Delta fim$	MS428	MG1655 $\Delta fim$	[24]
$\Delta flu\Delta fim$	MS528	MG1655 $\Delta flu,\Delta fim$	[24]
$\Delta cps$	RMV340	MG1655 <i>cps</i> ::tet	[69]
$\Delta csgAB$	RMV612	MG1655 <i>csgAB</i> ::kan	[63]
$\Delta fliC$	NM109	MG1655 <i>fliC</i> ::kan	This study

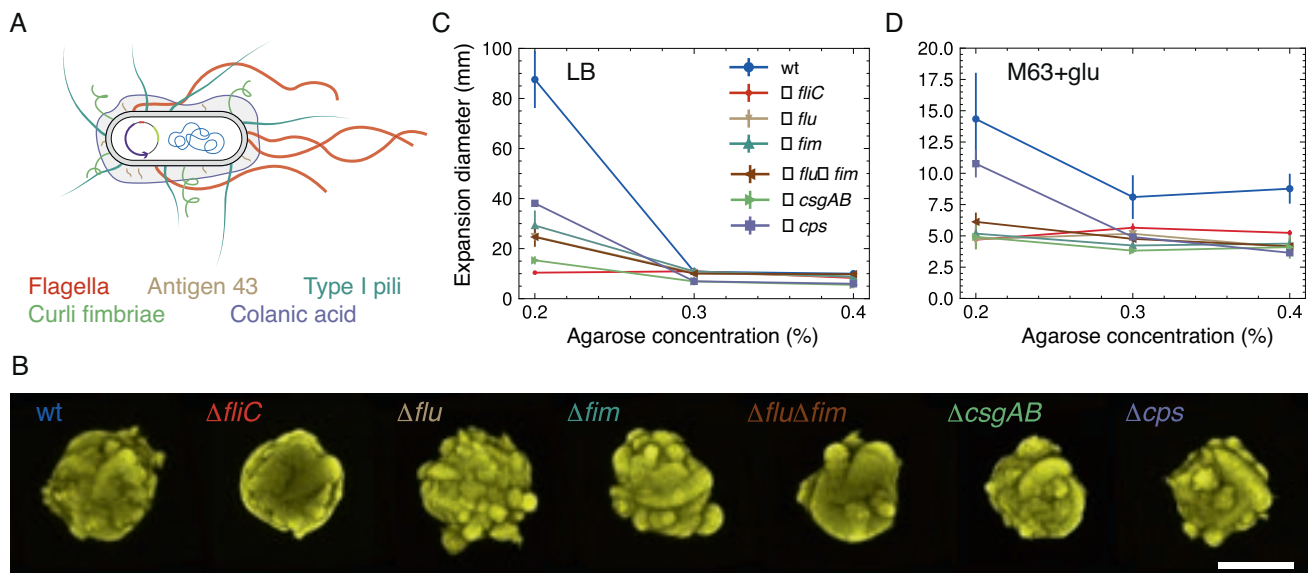


**Fig. 2** **3D morphology and motility of knock out mutants.** **A** Sketch of parental (wt) *E. coli* strain (not to scale). The sketched elements include the genome, the fluorescence-carrying plasmid and the extracellular structures: flagella (red), antigen 43 (beige), type I pili (dark green), curli fimbriae (light green), and colanic acid (purple). **B** Morphology of mutant 3D colonies. Examples of pseudo-colored fluorescent colonies (maximum intensity projections) grown in M63 + glu with 0.3% agarose. Scale bar corresponds to 200  $\mu$ m and color coding is the same as in (A). **C** Swimming assay in low density agarose. Diameters of expansion zones after 24 h of incubation vs. agarose concentrations in LB (C) and M63 + glu (D).

non-flagellated mutant,  $\Delta fliC$ , but with large variations in speed. This is in accordance with the fact that many of the bacterial surface structures display interdependent regulation [35]. At higher substrate stiffness (0.3–0.4% agarose), where swimming is no longer the main driver of motility, the average moving distances were considerably reduced for all strains.

We also tested all strains' behavior in a minimal medium (M63 + glu) (Fig. 2D). In the low density minimal agarose (0.2%) the motility of all strains was reduced, as can be seen by comparing the maximum distance reached by wt: ( $14.3 \pm 3.7$ ) cm vs. ( $87.5 \pm 11.4$ ) cm in rich medium (LB). The reduced motility in minimal media is consistent with previous studies: it has been attributed to the considerable metabolic cost of producing flagella [36, 37], while a recent study [13] has shown that the chemotaxis is strongly reduced when there is no supplement attractant, even if the primary carbon source is also an attractant. Again, at greater agarose concentrations (0.3–0.4% agarose) motility was reduced to a non-detectable level for all other than the wt.

Overall, the low density agarose assay suggested that all the mutant strains tested here have reduced motility compared to the wt strain. This is in line with the view that the satellite colonies form as a compromise between their inherent motility and the mechanical constraints imposed by the environment.

#### Density of extra-cellular matrix controls satellite emergence

Another factor that affects both bacterial motility and colony morphology is the density of the enclosing matrix. To explore the colony morphology dependence on this environmental factor, we limited our analysis to a comparison between the highly motile wt and the non-flagellated mutant ( $\Delta fliC$ ) that was non-motile in all tested experimental settings. We investigated mono-clonal colonies of both strains in varying agarose concentration (0.25–0.35%) in rich (LB) and minimal (M63 + glu) medium.

As already mentioned, we found satellite morphology (wt+) among the 3D colonies in 0.3% agarose with frequencies of 34/40 and 17/18 for the wt strain in minimal and rich medium, respectively (Fig. 3). Namely, the satellite morphology was conserved despite changes in nutrient composition and possible slight changes in elasticity between the experimental samples [38].

When reducing the agarose concentration (0.25%) the distinct satellite morphology was lost for wt, and general spreading of the cells inside the gel was observed (Fig. 3, 0.25%). On the other hand, when stiffness was increased (0.35%), 3D colonies grew under greater confinement, resulting in the loss of wt+ morphology. In contrast, the non-motile strain ( $\Delta fliC$ ) always grew as single compact colonies at all tested agarose concentrations. We still observed the agarose concentration dependence on the morphology, as at 0.25% agarose concentration the surface of  $\Delta fliC$  colonies appeared more loosely connected than at higher agarose concentrations.

Colony surfaces became smoother as matrix stiffness increased for both strains (Fig. 3, 0.35%). In some cases

(7/18 in M63-glu and 6/9 in LB), we even found slightly oblate colony shapes. This shape change depends on the density of the environment, such that for higher stiffness (>0.4% agarose) all tested 3D colonies grew as single oblate colonies (Supplementary fig. S5), in agreement with earlier reports [39]. Recently, this shape morphology has been suggested to originate from the stiffness contrast between the colonies and the environment [16]. These findings all together suggest that the emergence of satellites is a transitional state between the morphologies: i) where cells can swim—more or less freely—through the extra-cellular matrix, and ii) where cells are strictly confined.

#### Satellite formation possibly speeds up colonization

The overall experimental result suggests that the observed satellite morphology is due to a combination of local growth of confined colonies and rare excursions of motile cells. Therefore,

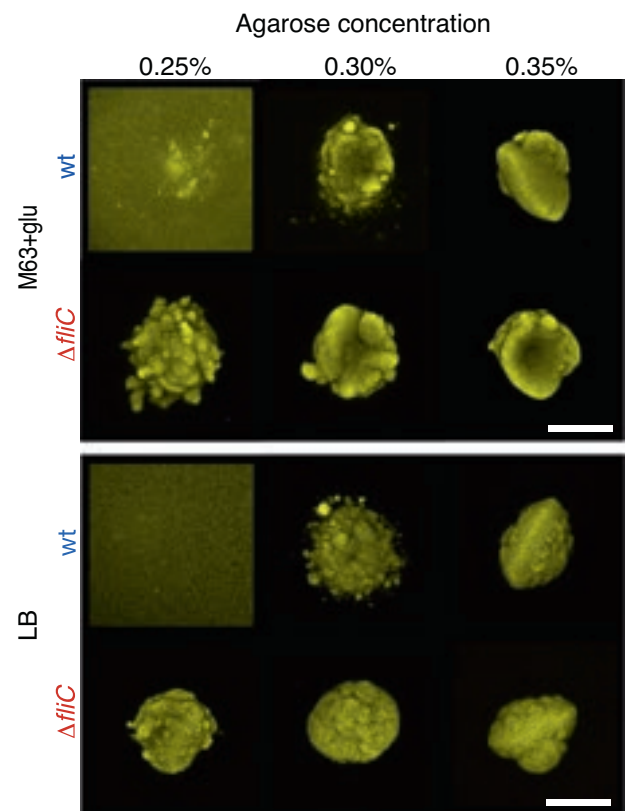


**Fig. 3 Effect on matrix density on 3D colony morphology.** Examples of pseudo-colored fluorescent parental (wt) or flagella mutant ( $\Delta fliC$ ) colonies (maximum intensity projections) grown in either minimal (M63+glu) or rich (LB) medium at various agarose concentrations. The scale bar corresponds to 200  $\mu\text{m}$ .

we propose a *simple* mathematical model of colony growth that has these two features and show that such a model indeed reproduces the 3D morphology of the confined bacterial colonies. We then used this model to further study how this mode of expansion can contribute to the overall colonization.

For this purpose, we modified the well-known Eden growth model, which is a lattice model, where the surface cells can divide to occupy empty nearest neighbor sites [40, 41]. Our modification allows for occasional escapes of single cells from the main colony. In other words, surface cells do not only grow but can also migrate to another empty site in the lattice. We assumed that the cells swim from site to site on timescales much faster than the time between two cell divisions (25–75 min, Supplementary Fig. S2). This assumption is based on the fact that cell divisions will decelerate swimming and experimental findings for *E. coli* in porous media [15]. So instead of simulating the cells' actual trajectory, we implemented the dispersal as a jump to a final position; chosen randomly by a radial Gaussian probability distribution centered around the starting site. Therefore, the model is essentially controlled by two parameters. The first is the rate of jumps,  $k_s$ , when the cell doubling rate,  $k$ , is set to unity. The second is the standard deviation,  $\sigma$ , of the Gaussian distribution of possible new sites to jump to. We ran the simulation until a million jump/division events. Thus, the resulting *in silico* colonies had widths of about 100  $\mu\text{m}$  assuming i) colonies are compact and ii) one occupied lattice site corresponds to one cell volume ( $\sim 1 \mu\text{m}^3$ ).

3D *in silico* colonies were obtained with  $\sigma \in \{2, 5, 7, 10\}$  and  $k_s \in \{0.001, 0.05, 0.1, 0.2\}$ . At low  $\sigma$  and  $k_s$ , the colonies were compact with smooth surfaces, as the distances ( $\sigma$ ) rise, small protrusions appear on the surface followed by satellite breakouts (Supplementary Fig. S6). As anticipated, the number of satellites also

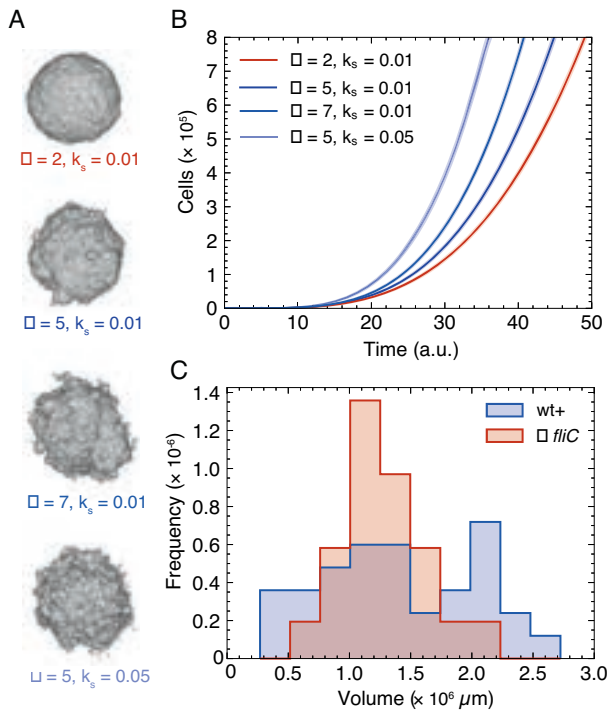


**Fig. 4 Population size and time evolution.** **A** Effect of frequency,  $k_s$ , and distance,  $\sigma$ , of jumps in the simulations of 3D colonies after  $10^6$  division/jump events; corresponding to motile (blue) and non-motile (red) colonies. **B** Time-evolution of each of the four examples ( $N = 25$ ) given in (A), where time is defined as detailed in Materials and methods. The shaded region corresponds to  $\pm$ SD. **C** Distribution of total colony volumes in minimal (M63+glu) medium of wt+ ( $N = 34$ ) and the flagella mutant  $\Delta flhC$  ( $N = 21$ ). The wt+ corresponds to the sum of volumes in Fig. 1C+D (M63 + glu).

increased as the jump frequency ( $k_s$ ) increased and ultimately ( $\sigma = 10$  and  $k_s = 0.2$ ) the simulated system was no longer confined. Instead, the cells spread mimicking the experimental results of wt in the low density agarose assay (Fig. 3, 0.25%).

In this system, the smooth and compact colonies (Fig. 4A, red) mimic the non-motile  $\Delta flhC$  colony (Fig. 2B) and the others (Fig. 4A, blue) different wt colonies (Fig. 1A). We analysed our *in silico* 3D colonies ( $N = 30$  of each) in the exact same way as in the experimental data (Fig. 1B–E) and found similar trends (Supplementary Fig. S7). With this we explored time evolution (Fig. 4B) and found that the colonies with wt+ morphology ( $\sigma = 5$  and  $k_s = 0.01$ ,  $\sigma = 7$  and  $k_s = 0.01$ , and  $\sigma = 7$  and  $k_s = 0.01$ ) clearly grew faster than the compact colonies ( $\sigma = 2$  and  $k_s = 0.01$ ). Hence, these results predict a view, where satellite outbreaks speed up the colonization of the extra-cellular matrix.

To test this prediction, we compared the experimental distributions of final total volumes of wt+ (blue) and  $\Delta flhC$  (red) (Fig. 4C). We found that the occurrence of satellites results in a more widespread distribution of volumes compared to the non-motile strain ( $\Delta flhC$ ). Surprisingly, there were also wt+ colonies with smaller volumes even though their doubling time may be slightly faster than that of  $\Delta flhC$ : 68.4 min vs. 72.9 min (Supplementary Fig. S2). While the wide distribution makes it hard to compare the average values in the current sample size, the wider distribution with more satellite colonies is in qualitative accordance with the distributions of the simulated 3D colonies (Supplementary Fig. S8).

## DISCUSSION

Even though the flagella-mediated motility of *E. coli* is well-described by the run-and-tumble model [42], we still lack the full

understanding of how bacteria migrate through porous or viscoelastic media. Several theoretical works concerning flagella-based motility describe how the migration can be slowed down when colliding with structures of various sizes [43–45]. Moreover, in a recent study, the individual trajectories of bacteria in a porous medium were imaged and the velocity was found to be highly dependent on pore size [15]. Furthermore, agarose gels have “spongy” microstructures with a broad distribution of pore sizes. Particularly, for the semi-dense agarose (0.3%) used in this study, the pores range from a few hundred nanometers to a few micrometers (see ref. [46] Fig. 16 for a metastudy). Relating this to our results, the porous hydrogel will barely allow the bacteria to squeeze through. Altogether, these reports indicate that *E. coli* moves through a porous medium constantly alternating between stalling (being trapped), re-orientation, and swimming. In accordance with this, we find that flagella are necessary for migration through the various semi-dense media used in this study (Fig. 3). However, the behavior we observed is still very different from swimming in agarose (Fig. 2C+D) as the main colonies (as well as the satellites) in 0.3% agarose had sharply defined surfaces, indicating that cell outbreak is a rare event. Also, we did not see any signs of the collective colony detachments, recently reported in mature colonies [19, 47, 48].

Given these observations, we propose that the satellite colonies are formed by the rare—but not too rare—detachment and migration of a single surface cell, followed by stalling, and subsequent growth. So, the volumes of satellites indicate when, in the colony’s history, the excursion occurred. Furthermore, the size also tells us that the dispersal of the founder cell was long enough to allow the sub-cluster to form before it is annexed to the main colony. We observed that larger satellites ( $>500 \mu\text{m}^3$ ) were much less common (Fig. 3 wt LB 0.3% for an example) than smaller ones (Fig. 1B), which is consistent with the proposed mechanism.

Our lattice model, which is based on an Eden growth model with rare jumping events added, successfully produced 3D colonies with satellite morphologies in a specific parameter range. The model predicted that the distribution of total colony volumes would be more widespread when the satellite formation is more frequent (e.g. compare  $\sigma = 5$  and  $k_s = 0.05$  vs.  $\sigma = 2$  and  $k_s = 0.01$  in Supplementary Fig. S8). This is consistent with our experimental findings, where we find the distribution of total volumes of the flagella mutant ( $\Delta flhC$ ) to be much narrower than for the parental (wt) strain (Fig. 4C).

Hallatschek and co-workers [49, 50] have theoretically demonstrated the impact of long-range dispersal in population expansion, especially when the dispersal distance distribution has a somewhat fat tail. In our model, the distribution of dispersion distances is Gaussian, but still the expansion dynamics of satellite-forming colonies is indeed faster than linear (Fig. 4B). On the other hand, it is also significantly slower than exponential growth (Supplementary Fig. S2). So, satellites form and then merge with the main colony and, thereby, limit the overall growth of the population. Nevertheless, our model suggests that in long term, the system will keep growing super-linearly, as the number of jumps (which is equivalent to the initialization of satellites) scales with the colony surface. In other words, as the growth of the main colony is linear (Supplementary Fig. S1) and the distribution of migration distances is unchanged over time, new satellites will keep forming and the main colony will never catch up with all the satellites. However, our model does not encompass spreading strategies on very long timescales, as the model ignores the effects of nutrient depletion and time-varying jumping distributions.

In our experiment, some of the main colonies of mutants produced very rough surfaces. Whilst the flagella knockout mutant’s surface ( $\Delta flhC$ ) was overall smooth, the other mutants had several small protrusions of their surfaces (Fig. 2B). There are a few factors that can possibly contribute to the roughness of the

surfaces. The first is that even for the mutants, which are less motile than wt (Fig. 1C+D), individual surface cells escape occasionally. However, they travel significantly shorter distances than wt cells do. If this is the case, the satellites will quickly be re-absorbed into the main colony (Supplementary videos 1–5). In other words, the mountainous surface could be explained by motility with short dispersals (small  $\sigma$ ). This is also in accordance with the fact that higher agarose concentrations (>0.3%) resulted in smoother surfaces (Fig. 3). Another possibility is the nutrient driven instability of the surface growth. Several studies have shown how surface roughening instabilities are reinforced by the resulting local nutrient depletion [51]. The nutrient-driven instability also explains the (pseudo-fractal) broccoli-like morphology recently reported for 3D *E. coli* colonies [52]. It is possible that such instabilities are relevant, especially in the later stage of colony development. However, this effect is not included in our model since it does not consider space limitations and nutrient depletion separately.

Whilst the model compares well with our experimental results with respect to the distributions of satellites, main colony volumes, and distances to satellites (Fig. 1C–E vs. Supplementary Fig. S7B–D), it fails to reproduce the distributions of the number of satellites (Fig. 1B vs. Supplementary Fig. S7A). We conclude that with only two parameters ( $\sigma$  and  $k_s$ ), we cannot cover the varieties of the natural system or the rare successful escapes. We speculate that this could be related to the variance in flagella abundance, even among cells with the same genotype. It is well-known that the expression of flagella is highly heterogeneous, particularly that there are large stochastic variations in number of flagella. This has been suggested to be an evolutionary favorable strategy, as the expression of flagella is very energy consuming [53], such that motility is retained on colony level even when motility is limited on a cellular level.

Except for the mutant that did not express flagella, the studied strains lacked structures related to adhesion and aggregation processes rather than to motility. Still, we do not fully understand why the antigen 43 mutant ( $\Delta flu$ ), is less motile than the wt and—maybe as a result—hindered in satellite formation (Fig. 2). Biofilm formation has been shown to be associated with the expression of antigen 43 [24] and type I pili [21]. So one might assume that antigen 43 repression would up-regulate motility. However, the picture is more complex, as both EPS colonic acid [34] and type I pili [27] block antigen 43 function. Moreover, both antigen 43 and type I pili expressions are phase variable [54] and they are inversely regulated [55]. Therefore, more studies must be done to unravel the role of the surface structures per se, without the inverse regulations, phase variability, and physical shielding.

In general, dominant aggregation phenotypes are expected to hinder motility. Hence, it is reasonable to expect that when these processes are suppressed, the motility will increase. However, in our experiments, all the mutants presented reduced motility compared to their parental strain. This demonstrates the complexity of the bacterial motility phenotype. Indeed, vast amount of literature indicate the complex interdependence of motility and surface structure genes. Over-expression of the *handshake* protein antigen 43 (*flu*) has been reported to impair motility, not because of increased aggregation but due to interfering with the expression of flagella [56]. Similarly, the constitutive expression of type I fimbriae (*fim*) compromises the motility of bacteria by reducing the expression of flagellin [57]. The expression of curli (*csgAB*) and colanic acid (*cps*) are promoted by regulatory networks that down-regulate motility [58–60], therefore they are normally expressed in a complementary manner. Similar motility has been reported between wt and  $\Delta flu$  [56], and between strains with and without type I fimbrial expression [61], while this was not the case in our system (Fig. 2).

Taking our results together, we suggest that satellite-formation allows bacteria to colonize unknown horizons faster (super-linear

over time), whilst still retaining the tight bindings of the biofilm. Such spreading behavior can be advantageous, when invading complex environments, such as competing microbial communities, soils, or mammalian tissues. While we observed the phenomenon in a rather narrow range of the agarose concentrations, in nature it is likely that there are large gradients in the restriction of motility by the complexity of the matrix. If so, spreading through a semi-dense matrix using a combination of growth and occasional migrations, is a strategy, which ensures both fast invasion and stable occupation.

While the flagella mutant's loss of satellites indicates the importance of flagella, more research is needed to explore how rare migratory events are enabled. For example, is it the inhomogeneity of gels that sometimes allows a cell to swim over long distances before being trapped? Or is it the cells that happen to express the relevant motility genes in high enough copy numbers to overcome the gel's resistance? Revealing the origin of the stochasticity behind rare excursions, may highlight unknown mechanisms of robust invasion of bacteria in complex environments.

## MATERIALS AND METHODS

### Bacterial strains and culture media

The *Escherichia coli* strains used in this study are derivatives of the wild-type MG1655 (K-12 F-lambda- ilvG- rfb-50 rph-1) [62] and are all listed in Table 1 and detailed in ref. [63] and references therein. However, the non-flagellated  $\Delta flhC$ , ( $\Delta flhC::kan$ ) mutant (NM109), was constructed specifically for this study through P1 transduction by moving  $\Delta flhC::kan$  from JW1908-1 (Keio collection [64]) to MS613 followed by selection on kanamycin [65]. All strains were transformed with the plasmid pVS132 carrying an Isopropyl  $\beta$ -D-1-thiogalactopyranoside (IPTG) induced yellow fluorescent protein (YFP) and ampicillin resistance for selection [66] following a previously published protocol [67–69].

**Culture media.** Experiments were done using either of the two growth media: The rich Luria-Bertani (LB) composed of 1% tryptone, 0.5% NaCl and 0.5% yeast extract or M63 minimal media consisting of 20% 5 × M63 salt [70], 1  $\mu$ g/ml B1, 2 × 10<sup>-3</sup> M MgSO<sub>4</sub>, and supplemented with 20  $\mu$ g/ml glucose (M63+glu). Both media were supplemented with 100  $\mu$ g/ml ampicillin, unless otherwise stated.

### Growth rate measurements

*E. coli* strains were grown overnight at 37 °C while shaking in either LB or M63+glu medium, before diluting 1000× in fresh medium without antibiotics. Initial OD<sub>600</sub> value (NanoPhotometer C40) was measured before incubation (37 °C) and repeated every hour.

### Swimming assay

Prior to experimentation, 96 mm dishes with 25 ml of either LB or M63+glu and various agarose concentrations: 0.2%, 0.3%, or 0.4% (w/v) were prepared and left to dry for 18 h on the bench. In parallel, strains were grown overnight while shaking (37 °C) in LB before inoculating 1  $\mu$ l in the middle of each dish. After 24 h of incubation (37 °C), the range diameters were measured.

### 3D bacterial colonies

*E. coli* strains were grown overnight at 37 °C while shaking in LB medium (OD<sub>600</sub> ≈ 4), before performing three consecutive thousand-fold dilutions until reaching a concentration of ≈ 10<sup>3</sup> cells/ml. Then cells were embedded in a transparent semi-dense matrix using the following procedure: First, media with 0.2–0.6% (w/v) agarose (SERVA cat. no. 11404) was melted (in a microwave) and shaken rigorously to ensure homogeneity. To minimize evaporation (and heat-induced aging [71]), we opened new 25 ml bottles of media and agarose each time, and made sure to avoid boiling. Secondly, media with agarose was aliquoted into 1 ml tubes and placed in a block-heater at 55 °C. After approximately 20 min, when the mixture had reached 55 °C, it was supplemented with ampicillin (100  $\mu$ g/ml) and 0.5 mM IPTG (for YFP induction). Then, 10  $\mu$ l of the diluted overnight culture was added and the mixture was immediately—to prevent untimely gelification and heat shocks—poured into a petri dish

(WillCo HBST-5040) with glass bottom. This results in a final concentration of  $\approx 10$  cells pr. well (i.e. 10 cells/ml). After a few minutes the mixture had solidified and the well was incubated upside-down ( $37^\circ\text{C}$ ) for 13 h (LB) or 15 h (M63 + glu) for all agarose concentrations: 0.2–0.6% (w/v). The different incubation times were chosen to balance different media-dependent growth rates (Supplementary Fig. S2). Using these small volumes, the matrix thickness was less than  $400\ \mu\text{m}$ , which ensures a minimum of oxygen depletion. To check this further, we compared the number of satellites pr. Colony with the position in the well (z-direction) and found no obvious correlation. However, the cost of this thin layer is a high risk of the colonies growing onto (and spreading fast over) the surface. Therefore, we discarded all wells, with colonies where this kind of growth had happened.

To parallel this assay, agarose was interchanged with 0.5% (w/v) agar (BD Difco Bacto Dehydrated Agar, Fischer Scientific) following the exact same procedure as described above. However, we found that the resulting agar gel is softer than the agarose gel, so, the density of agar 0.5% matches  $\approx 0.3\%$  agarose (Supplementary Fig. S9).

### Imaging of 3D bacterial colonies

3D colonies in microwell dishes were imaged with a laser-scanning confocal microscope (LSCM) (Leica, SP5) and a  $20\times$  air immersion objective (Nplan, L20x, 0.40corr $\infty$ ). YFP was excited by an argon laser with a wavelength of  $514\ \text{nm}$  and emission was collected around  $550 \pm 30\ \text{nm}$ .

To estimate how the colony radius changes with time, colonies were imaged with an inverted Nikon Eclipse Ti fluorescent microscope (Nikon, Tokyo, Japan) using a  $20\times$  air immersion objective (Splan flour, L20x, 0.45-corr $\infty$ ) paired with an Andor Neo camera (Andor, Belfast, UK). YFP was excited by a Hg lamp and the emission was collected at  $535 \pm 30\ \text{nm}$  upon excitation at  $500 \pm 20\ \text{nm}$  with a frame rate of one every 40 min.

The same approach was taken for the time-lapse movies of growing colonies (Supplementary Movie 1–5), however, the frame rate was one every 50 min. The reason we used wide-field fluorescence instead of LSCM for time-lapses was to reduce bleaching and photo-toxicity.

**Morphology measurements.** For snapshots of 3D colonies, we collected z-stacks that captured the entire colony with ( $x,y$ )-resolution of  $1.52\ \mu\text{m}/\text{pixels}$  and optimized z-resolution of  $1.33\ \mu\text{m}$ . The total imaging time of the colony was on the order of few minutes.

### Image processing

As the typical penetration depth of a LSCM is around  $100\ \mu\text{m}$  [72] and the dense colonies were of the order of  $200\ \mu\text{m}$ , the part of the colony furthest away in the scanning-laser direction (z-direction) suffers from strong distortions. Therefore, the following analysis was restricted to the half-colony closest to the LSCM objective by cropping the collected fluorescence z-stack using a custom-made Fiji [73] routine. 3D image segmentation was done with BiofilmQ [74] using the Otsu method for thresholding. Lastly, background noise was removed by eliminating outlier voxels of clusters smaller than  $11\ \mu\text{m}^3$ . The following BiofilmQ parameters were exported for subsequent analysis: Convexity, number of satellites, volumes, distances between center-of-masses, and nearest-neighbour objects. The same BiofilmQ parameters were exported for the in silico colonies, the thresholding step was skipped for them (as they are binary per se).

### Modified Eden growth model

To reproduce the features of the obtained experimental results a modified Eden growth model was implemented. In a three-dimensional cubic lattice of linear system size  $L$ , each lattice site can be occupied by at most one bacterial cell. Each cell can grow at a rate  $k$  if there is at least one empty site among their six next nearest-neighbour sites. On top of this, if three or more of the next nearest sites are empty, then in addition to the growth, the cell can jump to another location. This is implemented as a jump to a new randomly chosen location that happens at a rate  $k_s$ . This is implemented by counting the number of the cells that can only grow  $N_1$  and the number of cells that can both grow and swim  $N_2$  at each update and by applying a Gillespie algorithm. The initial condition is a single cell placed in the center of the system and then the following steps are iterated:

1. Find all the cells in the lattice and count the number of their empty nearest-neighbours. Among them, a cell that has less than four

available neighbouring sites belongs to the population  $N_1$ , otherwise, the cell belongs to the population  $N_2$ .

2. Define an array containing all empty neighbouring sites, corresponding to the surface of the colony.
3. Compute the total event rate  $T = N_1 \cdot k + N_2 \cdot (k + k_s)$ , and determine the duration to the next event as  $\tau = -\ln(r)/T$ , where  $r$  is a random number from a uniform distribution ( $r = U \subseteq (0,1)$ ). Proceed the time by  $\tau$ .
4. Draw a random uniform number,  $a$ , from a uniform distribution between zero and one ( $a = U \subseteq (0,1)$ ) and determine which event to happen by the following procedure:
  - a. If  $a > (N_1 + N_2) \cdot k / T$  a growing event happens. Choose a random surface site and add a new cell to it.
  - b. Otherwise, a swimming event happens. Choose a random cell of the sub-population  $N_2$ . Generate three random Gaussian distributed numbers of zero mean and standard deviation  $\sigma$ , to find the new position of the cell. If the new cell position is empty, update the cell position. If the new position is already occupied by another cell, draw a new position from the above-mentioned procedure until finding a new empty position.
5. Return to (1).

Pseudo-code is provided in the Supplementary text.

### Statistics

All mean values are given as (mean  $\pm$  SD) unless stated otherwise and only when data are tested against the null hypothesis that it is normally distributed.

### DATA AVAILABILITY

The code to generate the simulated data is available in Zenodo with <https://doi.org/10.5281/zenodo.7414919>.

### REFERENCES

1. Berlanga M, Guerrero R. Living together in biofilms: the microbial cell factory and its biotechnological implications. *Microb Cell Fact*. 2016;15:165.
2. Eriksen RS, Svenningsen SL, Sneppen K, Mitarai N. A growing microcolony can survive and support persistent propagation of virulent phages. *PNAS*. 2018;115:337–42.
3. Hernández-Jiménez E, Del Campo R, Toledano V, Vallejo-Cremades MT, Muñoz A, Largo C, et al. Biofilm vs. planktonic bacterial mode of growth: which do human macrophages prefer? *BBRC*. 2013;441:947–52.
4. Evans CR, Kempes CP, Price-Whelan A, Dietrich LE. Metabolic heterogeneity and cross-feeding in bacterial multicellular systems. *Trends Microbiol*. 2020;28:732–43.
5. O'Toole G, Kaplan HB, Kolter R. Biofilm formation as microbial development. *Annu Rev Microbiol*. 2000;54:49–79.
6. Tuson HH, Auer GK, Renner LD, Hasebe M, Tropini C, Salick M, et al. Measuring the stiffness of bacterial cells from growth rates in hydrogels of tunable elasticity. *Mol Microbiol*. 2012;84:874–91.
7. Lavrentovich MO, Koschwanetz JH, Nelson DR. Nutrient shielding in clusters of cells. *Phys Rev E*. 2013;87:062703.
8. Lavrentovich MO, Nelson DR. Survival probabilities at spherical frontiers. *Theor Popul Biol*. 2015;102:26–39.
9. Shao X, Mugler A, Kim J, Jeong HJ, Levin BR, Nemenman I. Growth of bacteria in 3-d colonies. *PLoS Comput Biol*. 2017;13:e1005679.
10. Alon U, Surette MG, Barkai N, Leibler S. Robustness in bacterial chemotaxis. *Nature*. 1999;397:168–71.
11. Sourjik V, Berg HC. Functional interactions between receptors in bacterial chemotaxis. *Nature*. 2004;428:437–41.
12. Croze OA, Ferguson GP, Cates ME, Poon WC. Migration of chemotactic bacteria in soft agar: role of gel concentration. *Biophys J*. 2011;101:525–34.
13. Cremer J, Honda T, Tang Y, Wong-Ng J, Vergassola M, Hwa T. Chemotaxis as a navigation strategy to boost range expansion. *Nature*. 2019;575:658–63.
14. Lauffenburger D, Kennedy CR, Aris R. Traveling bands of chemotactic bacteria in the context of population growth. *Bull Math Biol*. 1984;46:19–40.
15. Bhattacharjee T, Datta SS. Bacterial hopping and trapping in porous media. *Nat Commun*. 2019;10:2075.
16. Zhang Q, Li J, Nijjer J, Lu H, Kothari M, Alert R, et al. Morphogenesis and cell ordering in confined bacterial biofilms. *PNAS*. 2021;118:e2107107118.

17. Burmølle M, Johnsen K, Al-Soud WA, Hansen LH, Sørensen SJ. The presence of embedded bacterial pure cultures in agar plates stimulate the culturability of soil bacteria. *J Microbiol Methods*. 2009;79:166–73.
18. Strathmann M, Griebel T, Flemming HC. Artificial biofilm model—a useful tool for biofilm research. *Appl Microbiol Biotechnol*. 2000;54:231–7.
19. Jung YG, Choi J, Kim SK, Lee JH, Kwon S. Embedded biofilm, a new biofilm model based on the embedded growth of bacteria. *Appl Environ Microbiol*. 2015;81:211–9.
20. Swiecicki JM, Sliusarenko O, Weibel DB. From swimming to swarming: *Escherichia coli* cell motility in two-dimensions. *Integr Biol*. 2013;5:1490–4.
21. Pratt LA, Kolter R. Genetic analysis of *Escherichia coli* biofilm formation: roles of flagella, motility, chemotaxis and type I pili. *Mol Microbiol*. 1998;30:285–93.
22. Du H, Xu W, Zhang Z, Han X. Bacterial behavior in confined spaces. *Front Cell Dev Biol*. 2021;9:629820.
23. Owen P, Caffrey P, Josefsson LG. Identification and partial characterization of a novel bipartite protein antigen associated with the outer membrane of *Escherichia coli*. *J Bacteriol*. 1987;169:3770–7.
24. Kjærsgaard K, Schembri MA, Ramos C, Molin S, Klemm P. Antigen 43 facilitates formation of multispecies biofilms. *Environ Microbiol*. 2000;2:695–702.
25. Vejborg RM, Klemm P. Cellular chain formation in *Escherichia coli* biofilms. *Microbiology*. 2009;155:1407–17.
26. Diderichsen B. flu, a metastable gene controlling surface properties of *Escherichia coli*. *J Bacteriol*. 1980;141:858–67.
27. Hasman H, Chakraborty T, Klemm P. Antigen-43-mediated autoaggregation of *Escherichia coli* is blocked by fimbriation. *J Bacteriol*. 1999;181:4834–41.
28. Vidal O, Longin R, Prigent-Combaret C, Dorel C, Hooreman M, Lejeune P. Isolation of an *Escherichia coli* K-12 mutant strain able to form biofilms on inert surfaces: involvement of a new ompR allele that increases curli expression. *J Bacteriol*. 1998;180:2442–9.
29. Prigent-Combaret C, Vidal O, Dorel C, Lejeune P. Abiotic surface sensing and biofilm-dependent regulation of gene expression in *Escherichia coli*. *J Bacteriol*. 1999;181:5993–6002.
30. Prigent-Combaret C, Prensier G, Le Thi TT, Vidal O, Lejeune P, Dorel C. Developmental pathway for biofilm formation in curli-producing *Escherichia coli* strains: role of flagella, curli and colanic acid. *Environ Microbiol*. 2000;2:450–64.
31. Danese PN, Pratt LA, Dove SL, Kolter R. The outer membrane protein, antigen 43, mediates cell-to-cell interactions within *Escherichia coli* biofilms. *Mol Microbiol*. 2000;37:424–32.
32. Oh YJ, Hubauer-Brenner M, Gruber HJ, Cui Y, Traxler L, Siligan C, et al. Curli mediate bacterial adhesion to fibronectin via tensile multiple bonds. *Sci Rep*. 2016;6:33909.
33. Gualdi L, Tagliabue L, Bertagnoli S, Ierano T, De Castro C, Landini P. Cellulose modulates biofilm formation by counteracting curli-mediated colonization of solid surfaces in *Escherichia coli*. *Microbiology*. 2008;154:2017–24.
34. Schembri MA, Dalsgaard D, Klemm P. Capsule shields the function of short bacterial adhesins. *J Bacteriol*. 2004;186:1249–57.
35. Saldaña Z, Xicotencatl-Cortes J, Avelino F, Phillips AD, Kaper JB, Puente JL, et al. Synergistic role of curli and cellulose in cell adherence and biofilm formation of attaching and effacing *Escherichia coli* and identification of fis as a negative regulator of curli. *Environ Microbiol*. 2009;11:992–1006.
36. Bauchop T, Eldsen SR. The growth of micro-organisms in relation to their energy supply. *Microbiology*. 1960;23:457–69.
37. Shehata TE, Marr AG. Effect of nutrient concentration on the growth of *Escherichia coli*. *J Bacteriol*. 1971;107:210–6.
38. Kandemir N, Vollmer W, Jakubovics NS, Chen J. Mechanical interactions between bacteria and hydrogels. *Sci Rep*. 2018;8:10893.
39. Mitchell AJ, Wimpenny JW. The effects of agar concentration on the growth and morphology of submerged colonies of motile and non-motile bacteria. *J Appl Microbiol*. 1997;83:76–84.
40. Neyman J. Proceedings of the fourth Berkeley symposium on mathematical statistics and probability. University of California Press; Berkeley, California; 1961.
41. Jullien R, Botet R. Surface thickness in the Eden model. *Phys Rev Lett*. 1985;54:2055.
42. Jarrell KF, McBride MJ. The surprisingly diverse ways that prokaryotes move. *Nat Rev Microbiol*. 2008;6:466–76.
43. Duffy KJ, Cummings PT, Ford RM. Random walk calculations for bacterial migration in porous media. *Biophys J*. 1995;68:800–6.
44. Frangipane G, Vizsnyiczai G, Maggi C, Savo R, Sciortino A, Gigan S, et al. Invariance properties of bacterial random walks in complex structures. *Nat Commun*. 2019;10:2442.
45. Licata NA, Mohari B, Fuqua C, Setayeshgar S. Diffusion of bacterial cells in porous media. *Biophys J*. 2016;110:247–57.
46. Ed-Daoui A, Snaibre P. Poroviscoelasticity and compression-softening of agarose hydrogels. *Rheol Acta*. 2021;60:327–51.
47. Petrova OE, Sauer K. Escaping the biofilm in more than one way: desorption, detachment or dispersion. *Curr Opin Microbiol*. 2016;30:67–78.
48. Sauer K, Stoodley P, Goeres DM, Hall-Stoodley L, Burmølle M, Stewart PS, et al. The biofilm life cycle: expanding the conceptual model of biofilm formation. *Nat Rev Microbiol*. 2022;20:608–20.
49. Hallatschek O, Fisher DS. Acceleration of evolutionary spread by long-range dispersal. *PNAS*. 2014;111:4911–9.
50. Paulose J, Hallatschek O. The impact of long-range dispersal on gene surfing. *PNAS*. 2020;117:7584–93.
51. Matsushita M, Wakita J, Itoh H, Ràfols I, Matsuyama T, Sakaguchi H, et al. Interface growth and pattern formation in bacterial colonies. *Phys A Stat Mech*. 1998;249:517–24.
52. Martínez-Calvo A, Bhattacharjee T, Bay RK, Luu HN, Hancock AM, Wingreen NS, et al. Morphological instability and roughening of growing 3D bacterial colonies. *PNAS*. 2022;119:2208019119.
53. Klumpp S, Zhang Z, Hwa T. Growth rate-dependent global effects on gene expression in bacteria. *Cell*. 2009;139:1366–75.
54. Hasman H, Schembri MA, Klemm P. Antigen 43 and type 1 fimbriae determine colony morphology of *Escherichia coli* K-12. *J Bacteriol*. 2000;182:1089–95.
55. Schembri M, Ussey D, Workman C, Hasman H, Klemm P. DNA microarray analysis of fim mutations in *Escherichia coli*. *Mol Genet Genom*. 2002;267:721–9.
56. Ulett GC, Webb RI, Schembri MA. Antigen-43-mediated autoaggregation impairs motility in *Escherichia coli*. *Microbiology*. 2006;152:2101–10.
57. Simms AN, Mobley HL. Multiple genes repress motility in uropathogenic *Escherichia coli* constitutively expressing type 1 fimbriae. *J Bacteriol*. 2008;190:3747–56.
58. Sommerfeldt N, Possling A, Becker G, Pesavento C, Tschowri N, Hengge R. Gene expression patterns and differential input into curli fimbriae regulation of all GGDEF/EAL domain proteins in *Escherichia coli*. *Microbiology*. 2009;155:1318–31.
59. Wang Q, Zhao Y, McClelland M, Harshey RM. The RcsCDB signaling system and swarming motility in *Salmonella enterica* serovar Typhimurium: dual regulation of flagellar and SPI-2 virulence genes. *J Bacteriol*. 2007;189:8447–57.
60. Pesavento C, Becker G, Sommerfeldt N, Possling A, Tschowri N, Mehli A, et al. Inverse regulatory coordination of motility and curli-mediated adhesion in *Escherichia coli*. *Genes Dev*. 2008;22:2434–46.
61. Lane MC, Simms AN, Mobley HL. Complex interplay between type 1 fimbrial expression and flagellum-mediated motility of uropathogenic *Escherichia coli*. *J Bacteriol*. 2007;189:5523–33.
62. Bachmann B. *Escherichia coli* and *Salmonella*: Cellular and molecular biology. p 2460-2488; Editor: Neidhart F.C. ASM Press; Washington DC 1996.
63. Jauffred L, Munk Vejborg R, Korolev KS, Brown S, Oddershede LB. Chirality in microbial biofilms is mediated by close interactions between the cell surface and the substratum. *ISME J*. 2017;11:1688–701.
64. Baba T, Ara T, Hasegawa M, Takai Y, Okumura Y, Baba M, et al. Construction of *Escherichia coli* K-12 in-frame, single-gene knockout mutants: the Keio collection. *Mol Syst Biol*. 2006;2:2006.
65. Silhavy TJ, Berman ML, Enquist LW. Experiments with gene fusions. Cold Spring Harbor Laboratory; Cold Spring Harbor, New York; 1984.
66. Hallatschek O, Hersen P, Ramanathan S, Nelson DR. Genetic drift at expanding frontiers promotes gene segregation. *PNAS*. 2007;104:19926–30.
67. Cohen SN, Chang AC, Hsu L. Nonchromosomal antibiotic resistance in bacteria: genetic transformation of *Escherichia coli* by R-factor DNA. *PNAS*. 1972;69:2110–4.
68. Reisner A, Haagensen JA, Schembri MA, Zechner EL, Molin S. Development and maturation of *Escherichia coli* K-12 biofilms. *Mol Microbiol*. 2003;48:933–46.
69. Beloin C, Michaelis K, Lindner K, Landini P, Hacker J, Ghigo JM, et al. The transcriptional antiterminator RfaH represses biofilm formation in *Escherichia coli*. *J Bacteriol*. 2006;188:1316–31.
70. Elbing K, Brent R. Media preparation and bacteriological tools. *Curr Protoc Mol Biol*. 2002;59:1.1.1-1.1.7.
71. Mao B, Bentaleb A, Louerat F, Divoux T, Snaibre P. Heat-induced aging of agar solutions: Impact on the structural and mechanical properties of agar gels. *Food Hydrocoll*. 2017;64:59–69.
72. Graf BW, Boppart SA. Imaging and analysis of three-dimensional cell culture models. *Methods Mol Biol*. 2010;591:211–27.
73. Schindelin J, Arganda-Carreras I, Frise E, Kaynig V, Longair M, Pietzsch T, et al. Fiji: an open-source platform for biological-image analysis. *Nat Methods*. 2012;9:676–82.
74. Hartmann R, Jeckel H, Jelli E, Singh PK, Vaidya S, Bayer M, et al. Quantitative image analysis of microbial communities with biofilmQ. *Nat Microbiol*. 2021;6:151–6.

#### AUTHOR CONTRIBUTIONS

All authors developed the theory and MC performed the experiments and the computations. LJ and NM verified the analytical methods and supervised the findings of this work. All authors discussed the results and contributed to the final manuscript.

**FUNDING**

Open access funding provided by Royal Library, Copenhagen University Library.

**COMPETING INTERESTS**

The authors declare no competing interests.

**ADDITIONAL INFORMATION**

**Supplementary information** The online version contains supplementary material available at <https://doi.org/10.1038/s41396-023-01494-x>.

**Correspondence** and requests for materials should be addressed to Namiko Mitarai or Liselotte Jauffred.

**Reprints and permission information** is available at <http://www.nature.com/reprints>

**Publisher's note** Springer Nature remains neutral with regard to jurisdictional claims in published maps and institutional affiliations.



**Open Access** This article is licensed under a Creative Commons Attribution 4.0 International License, which permits use, sharing, adaptation, distribution and reproduction in any medium or format, as long as you give appropriate credit to the original author(s) and the source, provide a link to the Creative Commons licence, and indicate if changes were made. The images or other third party material in this article are included in the article's Creative Commons licence, unless indicated otherwise in a credit line to the material. If material is not included in the article's Creative Commons licence and your intended use is not permitted by statutory regulation or exceeds the permitted use, you will need to obtain permission directly from the copyright holder. To view a copy of this licence, visit <http://creativecommons.org/licenses/by/4.0/>.

© The Author(s) 2023

## Supplementary

# Motility mediates satellite formation in confined biofilms

Mireia Cordero<sup>1</sup>, Namiko Mitarai<sup>1,\*</sup>, and Liselotte Jauffred<sup>1,\*</sup>

<sup>1</sup>The Niels Bohr Institute, University of Copenhagen, Blegdamsvej 17, DK-2100 Copenhagen O, Denmark

\*Correspondence: mitarai@nbi.dk, jauffred@nbi.dk

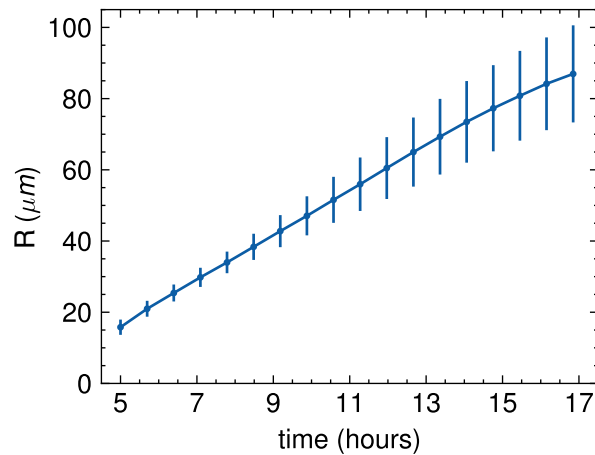


**Figure S1:** Colony growth dynamics for parental strain (wt). The colony radius (R) versus time in minimal medium (M63+glu) at intermediate agarose concentration (0.30%). The full line is the average development (N=8) and the error bars are  $\pm$ SD.

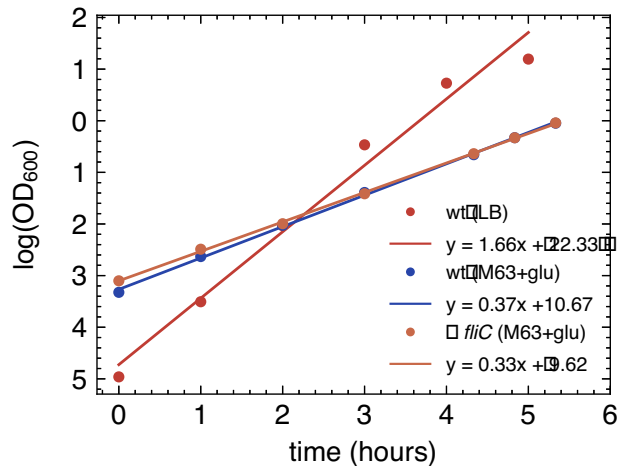


**Figure S2:** Growth curves for parental strain (wt) and flagella mutant ( $\Delta$ fliC). Plot shows the experimental data (circles) and the exponential fit (full lines). The doubling time is found as the  $\ln(2)$  divided by the slope of the growth curve (full lines). The resulting doubling times are 27.8 min (wt, LB), 68.4 min (wt, M63+glu), and 72.8 min ( $\Delta$ fliC, M63+glu).

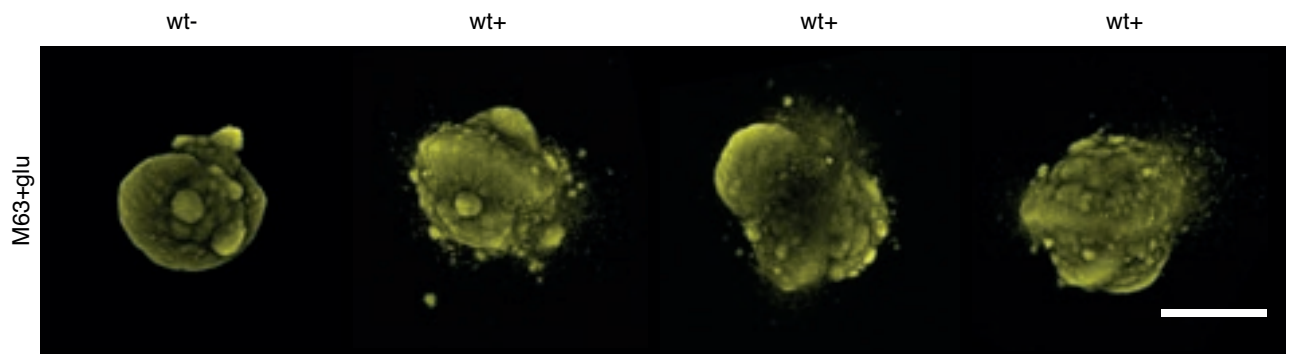


**Figure S3:** Satellite morphology in mature 3D colonies. Examples of pseudo-colored 3D colonies (maximum intensity projections) in 0.5% agar and minimal medium (M63+glu). These examples show inhomogeneity of morphologies without satellites (wt-) or with satellites (wt+). The scale bar corresponds to 200  $\mu\text{m}$ .

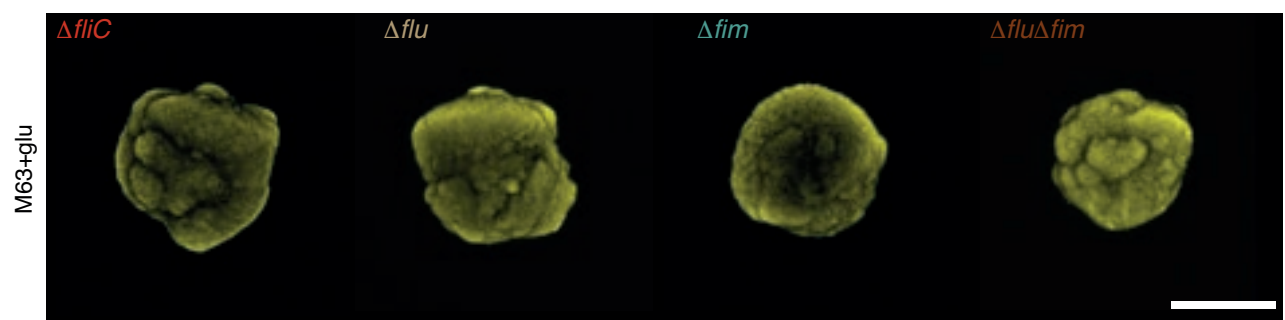


**Figure S4:** Morphology of mutant 3D colonies. Examples of pseudo-colored fluorescent colonies (maximum intensity projections) grown in M63+glu with 0.5% agar. The mutants lack either flagella ( $\Delta fliC$ ), antigen 43 ( $\Delta flu$ ), type I pili ( $\Delta fim$ ), and the double deletion ( $\Delta flu\Delta fim$ ). Scale bar corresponds to 200  $\mu\text{m}$  and color coding is the same as in figure 2A in the main article.

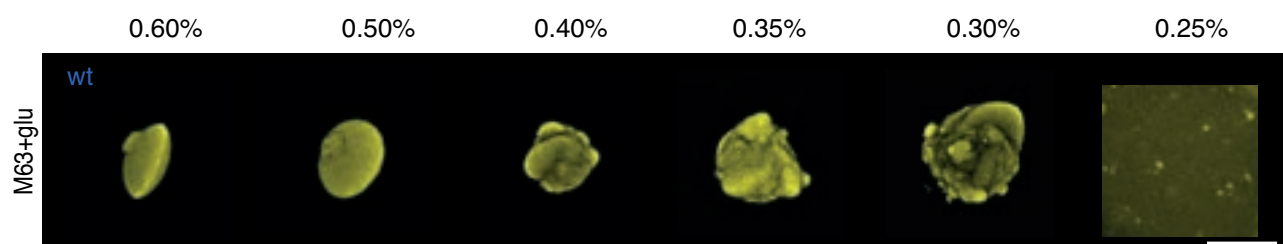


**Figure S5:** Effect of matrix elasticity on 3D biofilm morphology. Examples of pseudo-colored fluorescent wt biofilms (maximum intensity projections) grown in minimal medium (M63+glu) at various agarose concentrations. The scale bar corresponds to 200  $\mu\text{m}$ . At low agarose concentration (0.25%) cells swim through the media and at high concentrations ( $> 0.50\%$ ) biofilms' have an oblate shape and a smooth surface.

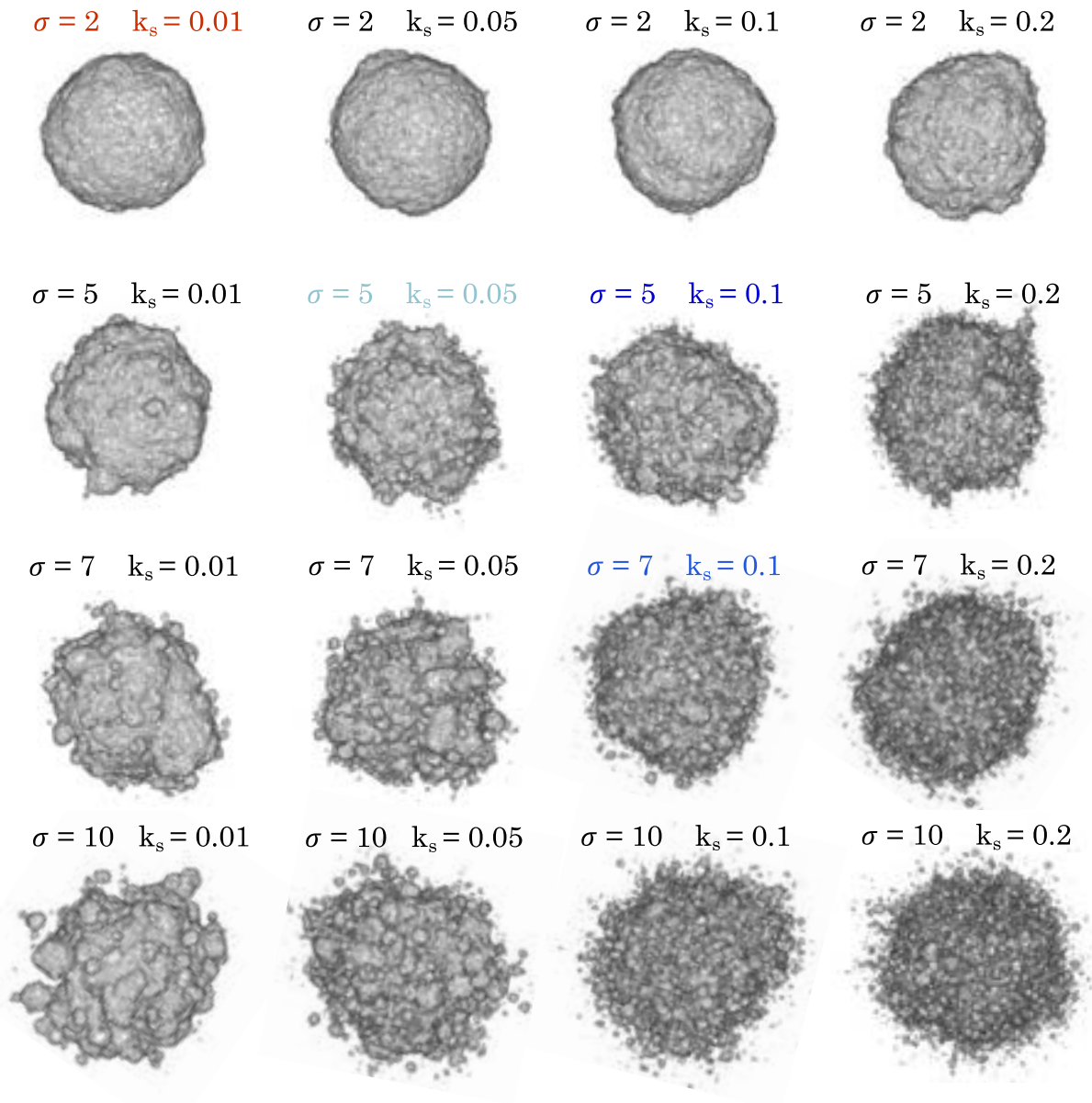


**Figure S6:** Effect of frequency,  $k_s$ , and distance,  $\sigma$ , of jumps in the simulations of 3D biofilms after  $10^6$  division/jump events. The color-coding is the same as in figure 4A in the main text.

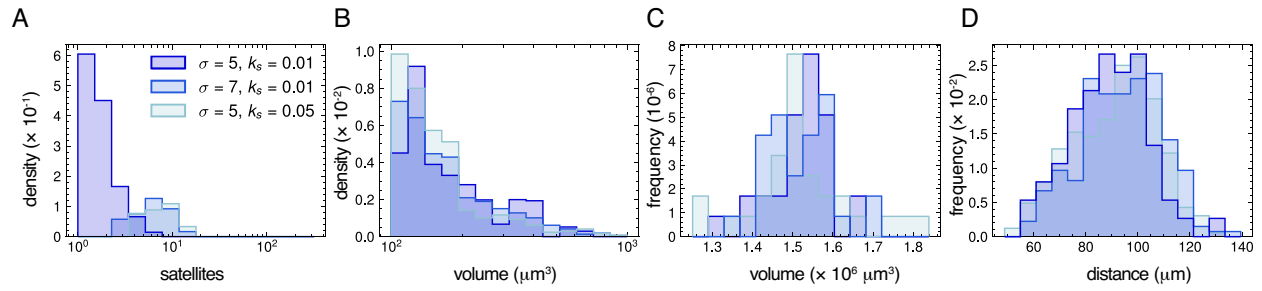


**Figure S7:** Satellite morphology in 3D biofilms. Simulated 3D biofilms ( $N=30$ ) for 3 different sets of  $\sigma$  and  $k_s$  ( $N=30$ ). Each lattice site corresponds to  $1 \mu\text{m}$  and the color-coding is the same as in figure 4A in the main text. **B:** Distribution of the number of satellites pr. biofilm (log-scale). **C:** Distributions of satellite volumes (log-scale) in either  $\sigma = 5$  and  $k_s = 0.01$  ( $N=61$ ),  $\sigma = 7$  and  $k_s = 0.01$  ( $N=223$ ), and for  $\sigma = 5$  and  $k_s = 0.05$  ( $N=271$ ). **D:** Distribution of volumes of the main colonies. **E:** Distributions of distances from the center-of-mass of satellites to the center-of-mass of the main colony.

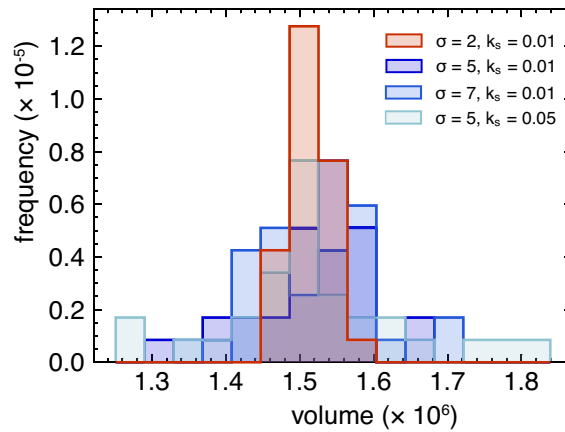


**Figure S8:** Total 3D biofilm volumes for simulated 3D colonies ( $N=30$ ), where each lattice site corresponds to  $1 \mu\text{m}$ . Color-coding is the same as in figure 4A in the main text.

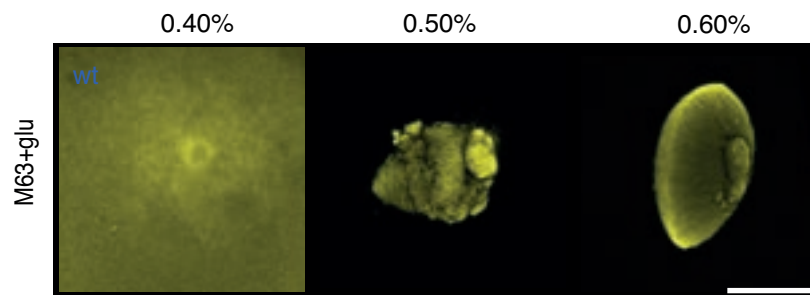


**Figure S9:** Effect of matrix elasticity on 3D biofilm morphology. Examples of pseudo-colored fluorescent wt biofilms (maximum intensity projections) grown in minimal medium (M63+glu) at various agar concentrations. The scale bar corresponds to  $200 \mu\text{m}$ . At low agar concentration (0.40%) cells swim through the media and at high concentrations ( $> 0.60\%$ ) biofilms have an oblate shape and a smooth surface.

## Computational Tools

# Motility mediates satellite formation in confined biofilms

Mireia Cordero<sup>1</sup>, Namiko Mitarai<sup>1,\*</sup>, and Liselotte Jauffred<sup>1,\*</sup>

<sup>1</sup>The Niels Bohr Institute, University of Copenhagen, Blegdamsvej 17, DK-2100 Copenhagen O, Denmark

\*Correspondence: mitarai@nbi.dk, jauffred@nbi.dk

**Input:** Lattice size  $L$ , growth rate  $k$ , swimming rate  $k_s$ , standard deviation  $std$  and an average  $\mu=0$  of a Gaussian distribution and the total number of events  $P$

**Result:** Aggregate of cells in a 3D lattice

- 1 Generate a 3D lattice of dimension  $L$  with empty sites  $Lat(i, j, k) = 0$  and occupied sites  $Lat(i, j, k) = 1$ ;
- 2 Place a single cell in the center of the lattice

$$Lat(L/2, L/2, L/2) = 1$$

```
for p ← 0 to P do
3  Define an empty colony surface, S;
4  Define an empty swimmers array, swim;
5  Set the number of each cell types, N1, N2 to zero;
6  foreach occupied site Lat(i, j, k) = 1 do
7  | Find and count the number of empty near neighbours β
      Lat(i ± 1, j, k) = 0 Lat(i, j ± 1, k) = 0 Lat(i, j, k ± 1) = 0
      Add the available sites position to the surface of the colony S.
8  | if β > 3 then
9  | | Add an element to N2 ;
10 | | Save the cell position in swim;
11 | else if 0 < β ≤ 3 then
12 | | Add an element to N1 ;
13 | end
14 | Find the total event rate T = N1 · k + N2 · (k + ks);
15 | Determine which event happens at time t = -ln(r)/T, with r = U ⊆ (0, 1), by throwing a random number from an
    uniform distribution a = U ⊆ (0, 1) ;
16 | if (N1 + N2) · k/T < a then
17 | | Chose a random surface site S(m, n, l) and update the colony by setting a cell in that position Lat(m, n, l) = 1;
18 | else
19 | | Throw three Gaussian numbers to determine the final position of the cell: xg = P(x) yg = P(y) zg = P(z);
20 | | Select an element of the swimmers array Lat(m', n', l');
21 | | if Lat(m' + xg, n' + yg, l' + zg) = 0 then
22 | | | Lat(m', n', l') = 0;
23 | | | Lat(m' + xg, n' + yg, l' + zg) = 1;
24 | | else
25 | | | Go to 19;
26 | | end
27 | end
28 end
```

**Algorithm 1:** 3D Eden Growth Model with swimmers

## **A.2 Emergent collective alignment gives competitive advantage to longer cells during range expansion**

**Authors:** Nathan van den Berg<sup>1</sup>, Kristian Thijssen<sup>1</sup>, Thu Trang Nguyen<sup>1</sup>, Adrien Sarlet<sup>1</sup>, Mireia Cordero<sup>1</sup>, Alba García Vázquez<sup>1</sup>, Namiko Mitarai<sup>1</sup>, Amin Doostmohammadi<sup>1</sup> and Liselotte Jauffred<sup>1</sup>

**Affiliations:** <sup>1</sup>Niels Bohr Institute, University of Copenhagen, Copenhagen 2100, Denmark

**Journal:** Under Review in Nature Physics

**DOI:** 10.1101/2024.01.26.577059

**My contributions:** I performed control experiments and co-supervised the students who were part of the project. I contributed to writing sections of the article, making figures, and revising the text.

## Article

# Emergent collective alignment gives competitive advantage to longer cells during range expansion

Nathan van den Berg<sup>1†</sup>, Kristian Thijssen<sup>1†</sup>, Thu Trang Nguyen<sup>1†</sup>, Adrien Sarlet<sup>1†</sup>, Mireia Cordero<sup>1</sup>, Alba García Vázquez<sup>1</sup>, Namiko Mitarai<sup>1</sup>, Amin Doostmohammadi<sup>1</sup>, and Liselotte Jauffred<sup>1</sup>

<sup>1</sup>The Niels Bohr Institute, University of Copenhagen, Blegdamsvej 17, DK-2100 Copenhagen O, Denmark

<sup>†</sup>These authors contributed equally

<sup>1</sup>Correspondence: mitarai@nbi.ku.dk, doostmohammadi@nbi.ku.dk, jauffred@nbi.ku.dk

**Keywords:** Biofilm, morphology, *Escherichia coli*, range expansion, spatio-genetic patterning, 3D growth

**ABSTRACT** Bacteria's competition for nutrients and territory drives biofilm evolution (1–4). The factors determining the outcome of competition among diverse bacterial species have a broad impact on a wide range of pathological (5), environmental (6), and microbiome interactions (7). While motility-related traits (8–11) and specific molecular mechanisms (12, 13) have been identified as potential winning attributes in bacteria, a shared and universally conserved feature determining competition remains elusive. Here, we demonstrate that a simple morphological feature of individual bacteria, cell aspect ratio, provides a winning trait for the population. Using growth-based range expansion experiments (14), we show that relatively longer bacteria robustly conquer the expanding front, even when initially in minority. Using an agent-based model of dividing bacteria, we reveal that the takeover mechanism is their emergent collective alignment: groups of locally aligned bacteria form "nematic arms" bridging the central region of the colony to the expanding front. Once at the front, bacteria align parallel to it and block the access of shorter bacteria to nutrients and space. We confirm this observation with single-cell experiments and further generalise our findings by introducing a generic continuum model of alignment-dominated competition, explaining both experimental and cell-based model observations. Moreover, we extend our predictions to spherical range expansions (15) and confirm the competitive advantage of being longer, even though the effect is less pronounced than in surface-attached colonies. Our results uncover a simple, yet hitherto overlooked, mechanical mechanism determining the outcome of bacterial competition, which is potentially ubiquitous among various bacteria. With the current advances in genetic engineering, varying aspect ratios can work as a simple tunable mechanism for the on-demand setting of the outcome of bacterial competitions with widespread implications for biofilm control.

## RESULTS

### Long bacteria win exclusively – even when outnumbered

We began by mixing two substrains of the non-motile *Escherichia coli* B: wild-type (WT) with a plasmid coding for green fluorescent protein (GFP) and an *mreB* mutant (AK) with a smaller aspect ratio (Table 1 and Supplementary Fig. S1) and with a plasmid coding for red fluorescent protein (RFP), see Fig. 1A. The mixture was inoculated on agar (1.5%) and resulted (after incubation) in a colony with three distinct regions from the centre and outwards (Fig. 1B): (i) the "homeland" where both strains were well mixed, (ii) a band thought to arise from the up-concentration of cells on the rim of the inoculation droplet (i.e., "coffee ring" (16, 17)), followed by (iii) a band where sectors merged. Strikingly, the WT (green) strain won over the shorter AK (magenta) during range expansion (outermost region of iii). We verified that these strains had similar growth rates (Supplementary Fig. S2A) and that takeover was independent of inoculation density (Supplementary Fig. S3). However, we found that the shorter strain had a growth advantage (in respect to the longer) in co-cultures (Supplementary Fig. S2B-C). Thus, WT wins in surface-attached colonies, even though this strain has a fitness disadvantage in liquid cultures.

To measure the strength of WT's advantage, we assessed the competition outcome for different strain ratios  $\zeta$ , which we defined as the inoculation density of the longer strain versus the shorter, quantified by optical density ( $OD_{600}$ ). We varied the ratio to identify the lower  $\zeta$ -limit for WT to outcompete AK. However, for all tested strain ratios  $\zeta$  (keeping combined inoculation density fixed), the longer strain (WT) consistently won over the shorter (AK) within the incubation time (20 h), see Fig. 1B. The takeover was noticeably slower in the  $\zeta = 0.001$  case, where WT sectors (green) spread azimuthally while curving around cone-shaped regions of shorter bacteria (magenta). Due to the difference in cell volume (Table 1), the number of cells in the stationary phase with same  $OD_{600}$  value is  $\sim 1.3$  times higher for WT than for AK (Materials and Methods). However,

van den Berg *et al.*

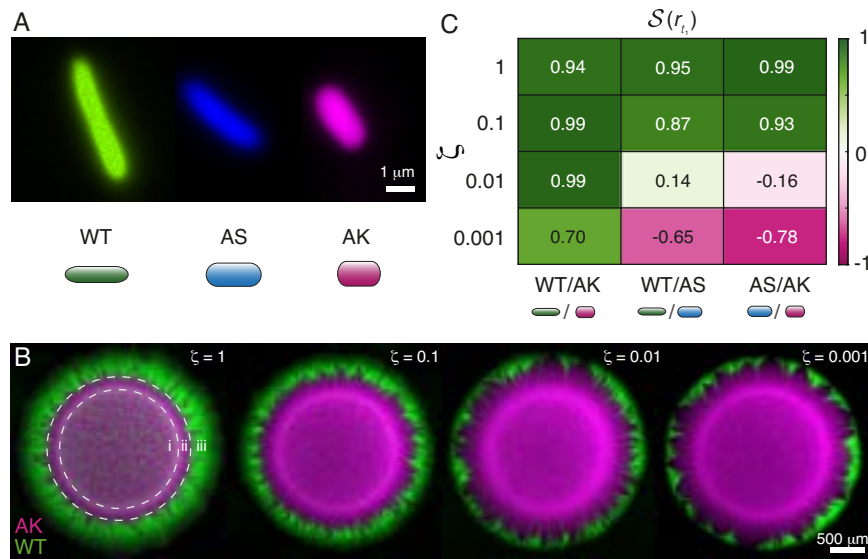


**Figure 1: Long bacteria win even when initially outnumbered.**

**A:** Single-cell (pseudo-coloured) fluorescence images of the wild type (WT) and the *mreB* mutants (AS and AK). The scale bar is 1  $\mu\text{m}$ . **B:** Maximum-intensity projected (pseudo-coloured) confocal scanning laser microscopy images of 20 h competition experiments between WT (green) and AK (magenta) at different initial (WT/AK) ratios:  $\zeta = \{1, 0.1, 0.01, 0.001\}$ . Three distinct regions: (i) homeland, (ii) coffee ring, and (iii) a band where sectors merged. The scale bar is 500  $\mu\text{m}$ . **C:** Heat map of strength,  $S(r_t)$ , at the specific radial distance  $r_t$  corresponding to the time:  $t_1 = 1.5$  days and averaged over several colonies (Supplementary Fig. S4).  $S = 1$  corresponds to the longer cells (WT or AS) winning,  $S = -1$  to the shorter (AS or AK), and  $S = 0$  to equal strength (i.e., neutral fitness). The heat map shows all three strain combinations AS/AK, WT/AS, and WT/AK versus  $\zeta$ . The cell graphics are to scale (Table 1).

because WT outcompetes AK even for the low strain ratios ( $\zeta \ll 1$ ), this slight advantage (in numbers) of WT is not enough to explain the competition outcome. Together, these results showed that the longer WT bacteria outcompete the shorter AK strain, even when initially outnumbered.

To explore the robustness of the impact of the aspect ratio, we introduced an additional *mreB* mutant (AS) with an intermediate aspect ratio (Fig. 1A and Supplementary Fig. S2) and set up competition experiments over 3 days (Supplementary Fig. S4). We kept the colour-coding, such that longer cells expressed GFP (WT or AS) and shorter RFP (AS or AK), and found no systematic dependence on the colour (Supplementary Fig. S5). While the intermediate AS strain lost against the longer WT bacteria, this previously losing AS outcompeted the shorter AK strain. This indicates that the aspect ratio of individual bacteria is the determining factor for the competition outcome in dividing *E. coli*. To quantify the competitive strength, we segmented and filtered the image stacks to obtain 2D masks reconstituting a connected colony surface, where all pixels were assigned one and only one colour. Behind the expanding colony front, additional cell-layers are formed, so we investigated the cross-sections (Supplementary Fig. S6) to rule out any dramatic changes in the composition of cells along the vertical direction. On this mask, we defined the radial distance  $r(t)$ , from the homeland boundary (i.e., the ring of high intensity of shorter cells). Then, we measured the strength  $S(r)$ , defined by the re-scaled occupancy of the longer cell, such that  $S = 1$  ( $S = -1$ ) signified that the longer (shorter) cells fully dominated. Fig. 1C is a heat map of how  $\zeta$  controls the strength,  $S(r_t)$ , at the radial distance corresponding to the time point  $t_1 = 1.5$  days of incubation (Materials and Methods). The quantitative analyses confirmed

Name	$l$ ( $\mu\text{m}$ )	$w$ ( $\mu\text{m}$ )	$l/w$	$V_{cell}$ ( $\mu\text{m}^3$ )	$V_{cell}$ ( $\mu\text{m}^3$ )*
WT	$2.68 \pm 0.45$	$0.68 \pm 0.09$	$3.97 \pm 0.14$	$0.88 \pm 0.16$	$0.40 \pm 0.06$
AS	$2.34 \pm 0.34$	$0.99 \pm 0.11$	$2.36 \pm 0.08$	$1.54 \pm 0.42$	$0.77 \pm 0.47$
AK	$1.82 \pm 0.30$	$1.05 \pm 0.13$	$1.74 \pm 0.07$	$1.27 \pm 0.56$	$0.51 \pm 0.26$

Table 1: Length ( $l$ ), width ( $w$ ), aspect ratio ( $l/w$ ), and cell volume ( $V_{cell}$ ), in logarithmic phase. \* denotes the average  $V_{cell}$  in stationary phase. All values are given as the mean  $\pm$ SD (Supplementary Fig. S1).

Emergent collective alignment gives competitive advantage to longer cells during range expansion

that WT always wins over AK, even when initially outnumbered by as much as  $\zeta = 0.001$  (i.e., one in thousands). For AS/AK and WT/AS combinations, we found few successful formations of sectors of the longer strain for  $\zeta \leq 0.01$ , indicating that the outcome is highly stochastic for small  $\zeta$  (Supplementary Fig. S4); averaging over several colonies resulted in  $\mathcal{S}(r_{t_i}) \lesssim 0$ . However, the sectors with longer bacteria tended to spread azimuthally with increasing  $r$ , indicating that they are likely to win the expanding front later on. In other words, the strain of longer aspect ratio could take over, if they succeeded in forming sectors early on (i.e., at small  $r$ ).

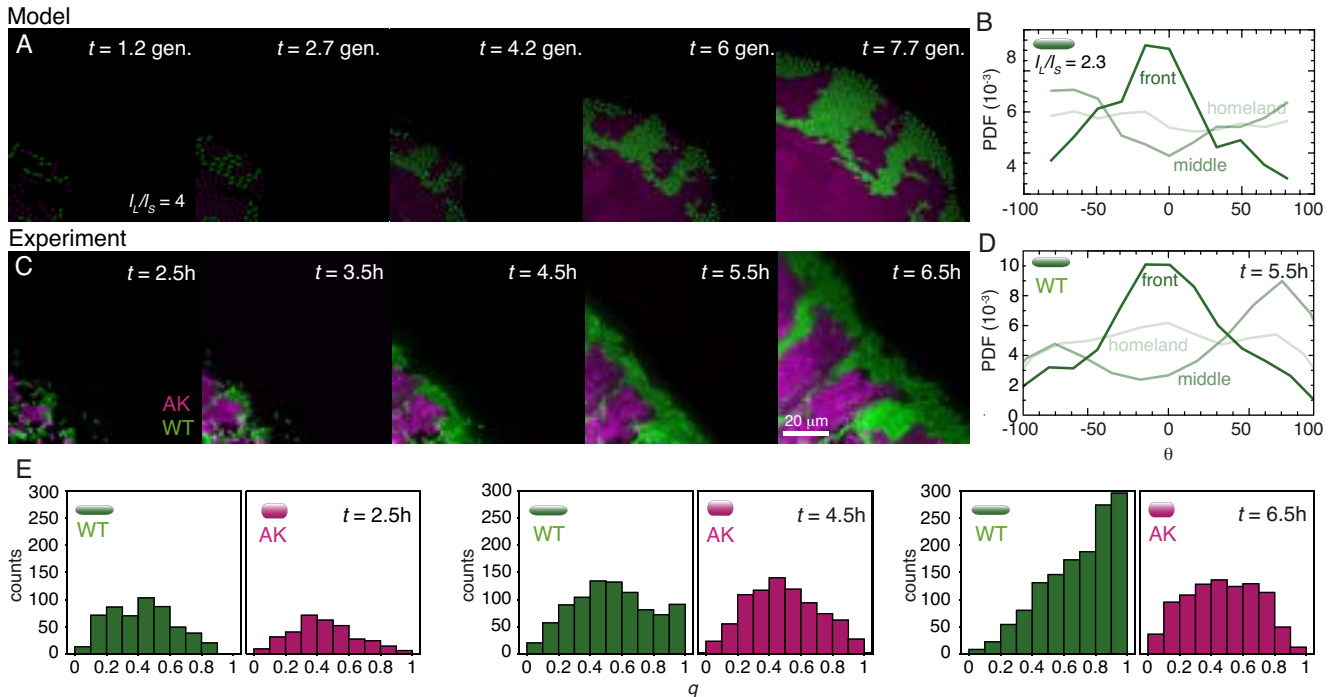


**Figure 2: Alignment-induced mechanism gives longer bacteria a mechanical winning advantage.**

**A:** Time series of particle-based simulations, where long bacteria (green) overtake the short bacteria (magenta) at the colony front by forming expanding regions along the front. The ratios between the aspect ratios were  $l_L/l_S = 2.3$  ( $\sim$  aspect ratio difference of WT and AK) and between the species:  $\zeta_i = 0.25$ . **B:** The probability distribution function, PDF, of the angle,  $\theta$ , to the expansion front at three equidistant regions of  $r$ : the region where particles originally was deposited (homeland), closest to the outer rim (front), and the region in between (middle) at time:  $t = 7.7$  gen. **C:** Snapshots from (pseudo-coloured) fluorescence time-lapses of competition between WT (green) and the *mreB* mutant AK (magenta) at time  $t$  after inoculation. The scale bar is  $20 \mu\text{m}$ . **D:** The probability distribution function, PDF, of the angle,  $\theta$ , to the expansion front at three equidistant regions of  $r$ : where the inoculation droplet originally was deposited (homeland), closest to the outer rim (front), and the region in between (middle). Data are from  $t = 5.5$  hours in (C). **E:** The nematic order parameter,  $q$ , of the experimental data in (C) for WT and AK individually corresponding to every second time frame in (A)  $t \in \{2.5, 4.5, 6.5\}$ h. The distributions did not differ significantly after 2.5 h ( $p > 0.1$ ) but they differed increasingly after 4.5 and 6.5 h ( $p < 0.001$ ).

### Alignment-induced mechanism gives longer bacteria a mechanical winning advantage

The experimental results suggested cell aspect ratio to be the determinant of the outcome of bacterial competition. In order to test if this is solely based on the mechanics of bacterial organisation, we simulated the range expansion in a minimal agent-based model (Materials and Methods). Bacteria were modelled as non-motile repulsive particles expanding on a 2D surface. The particles grew with the same fixed rate (with stochasticity). We distinguished longer from shorter species by setting the length at division as  $l_L$  and  $l_S$ , respectively. By using a constant width of  $w = 1$ , the aspect ratio ( $l/w$ ) of these particles were  $l_L$  and  $l_S$ . We used an inoculation ratio,  $\zeta_i = 0.25$  (ratio of number of long species over short), such that shorter bacteria were in majority, and placed individual particles (either  $l_L = 8$  or  $l_S = 3.5$ ) randomly in a small region. We then let the cells grow and interact to expand over the 2D surface, as seen in Fig. 2A.

As time evolved, the longer cells formed "channels" to the interface, in which they were aligned along the radial vector,  $\mathbf{r}$ .

van den Berg *et al.*

After the homeland had reached uniform density and the radial expansion began, longer cells squeezed through the channels to the colony front. As a result, the longer bacteria slowly began to dominate at the front, where they aligned with the interface. This channel-formation resulted in azimuthal spread of sectors of longer bacteria with increasing radial distance from the centre of the inoculation to the expanding front,  $r_f$ . Eventually, the sectors of longer bacteria curved around the sectors of shorter ones and took over the front. Thereby, the shorter cells lost their access to the front and, hence, nutrients and space. This suggests a purely mechanical mechanism. Longer bacteria locally form highly aligned domains (i.e., nematic arms), which connect the homeland to the outer rim of the colony and form a channel for longer bacteria to reach the front. Once at the front, the longer bacteria align parallel to it, as shown in Fig. 2B, and form a barrier, preventing further expansion of shorter bacteria (the case with short cell dividing faster is simulated for comparison (Supplementary Fig. S7)). Importantly, while the only difference between the competing bacteria in the model is their aspect ratio, this winning mechanism is an emergent collective property of bacteria that are longer than their neighbours.

To test the mechanism suggested by the cell-based model and investigate how populations compete at the individual cell scale, we ran time-lapse experiments with single-cell resolution. *E. coli* colonies were inoculated from a suspension of WT/AK in equal proportions ( $\zeta = 1$ ). We imaged the growth at the colony front over time  $t$ , as shown in Fig. 2C (Movie 1) and for an additional time-lapse (Supplementary Fig. S8, Movie 2). Individual bacteria were segmented and their orientation was determined and the angle,  $\theta$ , to the expanding colony front (i.e.,  $90^\circ$  to  $\mathbf{r}$ ) in three equidistant regions of  $r$  was measured (Fig. 2D). In agreement with the alignment-induced mechanical mechanism suggested by the agent-based model, we found that the winning WT bacteria align along  $\mathbf{r}$  (inside the colony) or along the expanding colony front. Furthermore, the nematic order parameter,  $q$ , which is a measurement of local orientation alignment (18), was calculated for every bacterium relative to its 8 closest neighbours, as extensively reported for bacterial mono-cultures (8, 19–23). The distribution of  $q$  was analysed at three different time points:  $t \in \{2.5, 4.5, 6.5\}$  h in Fig. 2E. The distributions of WT and AK strains did not differ significantly after 2.5 h ( $p > 0.1$ ), but they differed increasingly after 4.5 and 6.5 h ( $p < 0.001$ ). The distributions account for the visual observations in Fig. 2C that WT cells align with each other, while AK's alignment was weak. Together, model predictions and experimental quantifications show how the longer WT are squeezed by small clusters of growing AK cells and form channels of (radially) aligned bacteria. When they reach the colony front, they align with the expanding front and start dividing along the tangential direction. In this way, WT cut their shorter AK counterparts off from both nutrients and space.

To emphasise the generic mechanical nature of this takeover mechanism – set by aspect ratio and enhanced by stronger local alignment – we also employed a continuum model of a bi-phasic active nematic, where we took the two different bacteria types into account with an additional phase field order parameter  $\phi$ , where  $\phi > 0$  ( $\phi < 0$ ) corresponded to longer (shorter) bacteria regions modelled with a higher (lower) elastic constant and extensile activity (which mimics the dipolar force of division (24, 25)). It is well established that both orientational elasticity and extensile division activity are higher for higher aspect ratios (26, 27). We observed that even when the front is mostly populated by shorter bacteria, the phase corresponding to the more elongated bacteria eventually overtakes the shorter (Supplementary Fig. S9). Importantly, this phase segregation is solely driven by activity, stemming from cell divisions, and differences between aspect ratios, without any free-energy-driven phase separation. Remarkably, the longer bacteria take over the front by forming perpendicularly aligned nematic channels to the interface, in agreement with both the cell-based model and experimental observations (Fig. 2A and 2C). Consequently, the longer bacteria spread at the interface, as they aligned more strongly with it, due to their higher elastic constant.

## Takeover rate is set by differences in aspect ratios and the length of the shorter cell

Having established the competitive advantage of a large aspect ratio through experimental observations, cell-based and continuum models, we next turned to investigating the takeover rates. Fig. 3A shows the experimentally obtained strength  $\mathcal{S}(r)$  from the homeland ( $r = 0$ ) to the outer rim of the colonies for the strain combinations and  $\zeta$ -values that clearly switched within 3 days (i.e.,  $\mathcal{S}(r_{t_1}) > 0.85$  in Fig. 1C). We defined the takeover rates,  $\nu$ , as the slope of  $\mathcal{S}(r)$  and summarised them in Fig. 3B versus the length of the shorter strain (i.e.,  $l_S$ ). We paralleled this result with the agent-based simulations to measure the time-dependent strength,  $\mathcal{S}(r_f(t))$  (Fig. 3C) and the associated takeover rate,  $\nu_{\text{sim}}$ . This rate was also dependent on the aspect ratio difference  $l_L/l_S$ , as a more significant  $l_L/l_S$  resulted in a stronger alignment along the channels (Supplementary Fig. S10). Hence, the longer bacteria had enhanced access to the colony front. This is in agreement with the experimental observation that  $\nu$  is larger for WT/AK than WT/AS.

Surprisingly, we found that the takeover rates for the competition between longest and intermediate strains, WT/AS (grey), are significantly slower than for the two other strain combinations (longest versus shortest, WT/AK, and intermediate versus shortest, AS/AK), although the ratios of aspect ratios (Table 1) were similar for WT/AS and AS/AK ( $\sim 1.5$ ). Since our results established that the alignment-induced mechanism governs the competition between growing bacteria, we hypothesised that the difference in takeover rates were related to the relative ability of bacteria to form nematic domains. To explain the differences in the takeover rate  $\nu$  between WT/AS (longest versus intermediate) and AS/AK (intermediate versus shortest) (Fig. 3B),

Emergent collective alignment gives competitive advantage to longer cells during range expansion

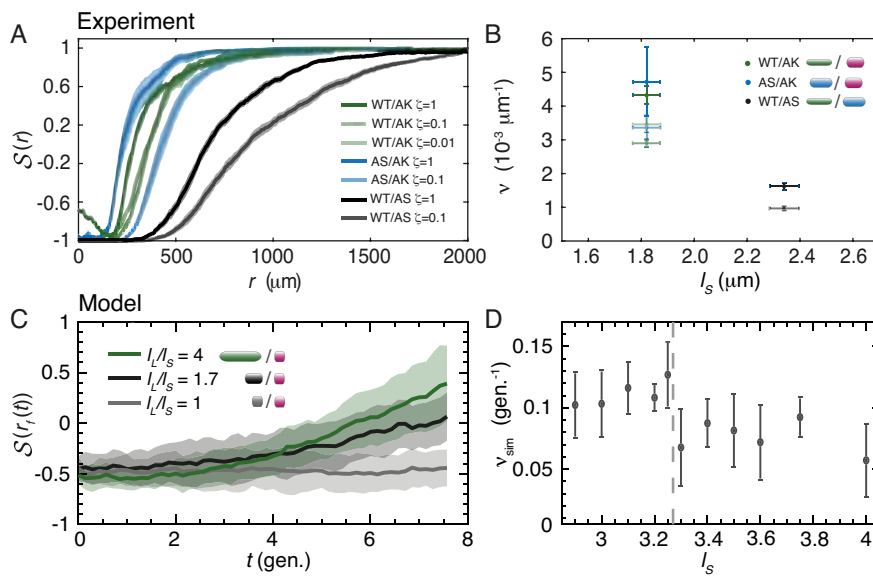


**Figure 3: Takeover rate is set by differences in aspect ratios and the length of the shorter cell.**

**A:** Competition is evaluated by the strength,  $S(r)$ , along the radial length,  $r$ , for the strain and ratios,  $\zeta$ , and strain combinations WT/AK (green), AS/AK (blue), and WT/AS (grey). We collected data from  $N \in \{5, 4, 5, 6, 8, 9, 9\}$  colonies (following order of legend) and ran the experiments for 3 days for all colonies to switch completely from  $-1$  to  $+1$ , which was the case for strain combinations and  $\zeta$ -values that fulfilled  $S(r_{t_1}) > 0.85$  in Fig. 1C. Notice how WT/AK mixed  $\zeta = 1$  drops from a higher  $S$ -level at the homeland boundary ( $r = 0$ ) before switching again. The shaded regions correspond to  $\pm$ SEM. **B:** Takeover rate,  $\nu$ , from (A) for WT/AK (green), AS/AK (blue), and WT/AS (grey) versus length of the shorter cell,  $l_s$ , for varying  $\zeta$  (opacity as legend in (A)). Slopes are found for the individual colonies by fitting the linear part around  $S \sim 0$  and  $\nu$  is the ensemble-average over  $N \in \{5, 4, 5, 6, 8, 9, 9\}$  colonies (following order of legend in (A)). The error bars correspond to  $\pm$ SEM.  $\nu$  of WT/AS ( $\zeta = 1$ ) is significantly different from AS/AK ( $p < 0.01$ ) and WT/AK ( $p < 0.001$ ). **C:** The time evolution of strength at the front,  $S(r_f(t))$ , where  $r_f(t)$  is the radial distance from the centre of the inoculation to the expanding front at time,  $t$ . The long bacteria cell aspect ratio is fixed to  $l/w = 4$ , the species ratio is set to  $\zeta_i = 0.25$ , and  $l_L/l_s = 4, 1.7$ , and  $1$  are shown. The shaded regions correspond to  $\pm$ SEM and  $N = 10$ . **D:** The simulation takeover rate,  $\nu_{\text{sim}}$ , (slope of (C) between  $t = 30$  gen. to  $t = 45$  gen.) for varying lengths of the shorter bacteria,  $l_s$ , with fixed ratio between long and short bacteria:  $l_L/l_s = 1.5$ . In simulations, bacteria with  $l_s \leq 3.25$  (dashed vertical line) are dominantly isotropic and bacteria with larger  $l_s$  are dominantly nematic. The error bars correspond to  $\pm$ SEM and  $N = 10$ .

we used the agent-based model to examine the takeover rate for fixed  $l_L/l_s$  ratio ( $\sim 1.5$ ), while varying  $l_s$  from no local alignment (isotropic) to local alignment (nematic). The transition between isotropic and nematic states is set by excluded volume interactions and is dictated by local density and particle length (28). Given our simulation doubling time, this transition occurred at around length  $l_s = 3.25$ . The agent-based model showed that the takeover rate dropped when both bacteria strains had local orientation ordering, see Fig. 3D. This explains why the switching speed was slower for WT/AS than for AS/AK: WT and AS both had nematic order, while in the AS/AK strain combination, only the longer AS were nematically aligning. This is also in accordance with the observation that the sector boundaries are more rugged for WT/AS (Supplementary Fig. S4), indicating that AS cells might be weakly aligning. Together, these results further highlight the emergent alignment as enhancing the takeover strength of the competing surface-attached bacteria and the importance of isotropic or nematic state of bacteria groups. The takeover rate is independent of the length of the individual bacteria, but only when the orientational packing of the mono-culture is the same (i.e. both species are within the isotropic or nematic phases). When, due to their individual lengths, the shortest bacteria species transition from isotropically packed to nematically ordered state, the takeover rate changes.

### Competition strength weakens in 3D

After establishing the significant advantage of elongation for surface-attached cells, we turned to 3D growth. The results so far have established that emergent nematic alignment is a competitive advantage. The local nematic order has been observed in 3D biofilms (29), though theoretically, it is expected that the nematic alignment weakens in 3D (30, 31) and as such we expected

van den Berg *et al.*

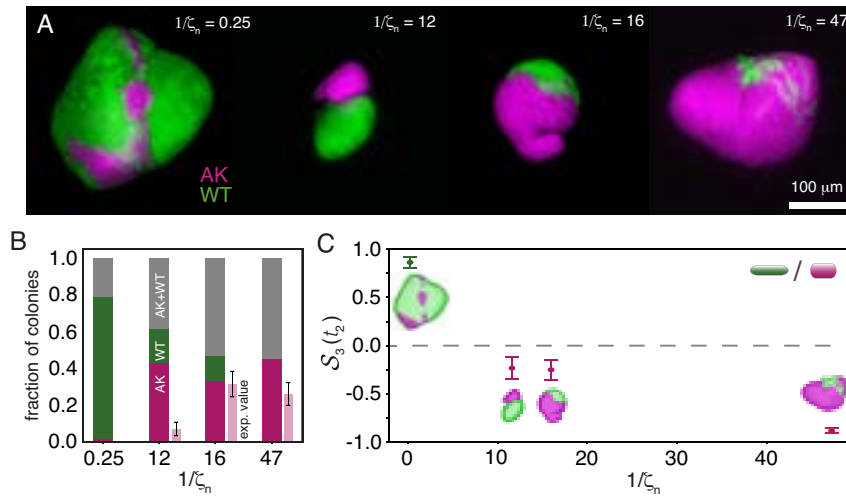


**Figure 4: Competition strength weakens in 3D colonies compared to surface-attached bacteria.**

**A:** Maximum-intensity projected (pseudo-coloured) fluorescence images of colonies formed from WT/AK inoculation beads of different ratios,  $\zeta_n$ . The scale bar corresponds to 100  $\mu\text{m}$ . **B:** Fraction of colonies with mono-coloured surfaces (WT or AK) or both (WT+AK). Predicted number of colonies (exp. value) originating from pure AK inoculation beads. Error bars correspond to  $\pm\text{SD}$ . **C:** Strength,  $\mathcal{S}_3(t_2)$ , of the ensemble of colonies versus  $1/\zeta_n$ , measured in (A). Here 1 (–1) corresponds to the longer (shorter) cells winning within the time,  $t_2 = 10\text{ h}$ , and 0 to equal strength (dashed grey line). The error bars correspond to  $\pm\text{SEM}$  and the number of colonies were  $N \in \{52, 49, 45, 53\}$  for  $1/\zeta_n \in \{0.25, 12, 16, 47\}$ , respectively.

that the takeover strength weakens, compared to surface-attached (2D) conditions. We tested our predictions in WT/AK colonies grown from inoculation beads of small volume (0.05 nl) in low-density (0.5%) agar (inset of Supplementary Fig. S11). We defined a strain ratio,  $\zeta_n$ , as the ratio of colony-forming units (CFU) of the longer strain versus the shorter (Supplementary Fig. S11), and imaged (with confocal-scanning laser microscopy) the resulting 3D colonies for various  $\zeta_n$ , as shown in Fig. 4A. We then sorted the ensemble of colonies into subgroups of either mono-coloured colonies (WT or AK) or colonies with both strains surviving at the surface (grey); distributions are given in Fig. 4B. For comparison, we also calculated (assuming a binomial distribution) the fraction of colonies that initially contained only AK or WT. The probability of a pure WT inoculation was negligibly small in all cases, in contrast to the probability of pure AK. It is, thus, unlikely that all mono-coloured WT colonies arose from pure WT inoculation beads. Instead, the longer strain (WT) had outcompeted the shorter (AK) during range expansion. We also found examples of the inverse, where AK had taken over the colony surface, even though the inoculum had both WT and AK.

To quantify the takeover strength, we segmented and filtered the image stacks to obtain 3D masks reconstituting a connected colony surface with the width of a single voxel, which were assigned one and only one colour (Supplementary Fig. S12 and Movie 3). In order to determine the strength,  $\mathcal{S}_3(t_2)$ , at a specific time,  $t_2$ , we quantified the proportion of the WT strain on the colony surface, as found in Fig. 4C. Interestingly, we found that when WT/AK are mixed four to one (i.e.,  $1/\zeta_n = 0.25$ ) WT occupies  $> 90\%$  of the surface and that  $\mathcal{S}_3(t_2)$  decreases, as  $1/\zeta_n$  increases. However, the longer (WT) still occupies a significant fraction despite a low initial ratio in the inoculation beads (Supplementary Fig. S12). For instance, when WT is only  $\sim 2\%$  of the inoculations ( $1/\zeta_n = 47$ ), it still occupies  $\sim 6\%$  of the final colonies' surfaces. Taken together, our results indicate that the longer cell still wins, but that its competitive strength is weakened.

## DISCUSSION

Using a set of three non-motile *E. coli* substrains, differing only in cell aspect ratios, we revealed that longer bacteria outcompete their shorter counterparts, even when initially outnumbered. By simulating the 2D colony growth, using the agent-based model of growing elongated particles with repulsive interactions, we showed that the advantage originates from local nematic ordering induced by mechanical interactions. The finding was experimentally confirmed by time-lapses of the takeover process at single-cell resolution: The longer WT cells aligned and formed nematic channels linking the homeland to the expanding front. After this, they aligned perpendicular to the front and eventually surrounded the whole colony, while the shorter AK cells were

cut off from nutrients and space. We further confirmed that this advantage is reproduced in 3D colonies, even though the effect was less prominent than in surface environments. We also found (from mono-strain colonies) that WT expands faster over a substrate surface than the shorter mutants (Supplementary Fig. S13), whose slower radial expansion is compensated by an increase in thickness (32–34). As the takeover happens in the monolayer at the expanding front, the expansion rate is not the determinant of the competition, instead it is the strain-strain interaction – enhanced by local alignment.

It has been long argued, based on phylogenetic studies, that the morphological development from rod-shaped to round-shaped bacteria (cocci) has happened independently several times and is associated with the loss of *mreB* (35–37). In long-term evolutionary experiments (in liquid medium), an *E. coli* B strain was found to enlarge its volume by shortening and widening (38, 39) in favour of enhanced metabolic efficiency (40). However, our results suggest that in other natural habitats such as on surfaces, in soils, and animal tissue, which are typically associated with spatial constraints and unpredictable supplies of nutrients, the advantageous morphology is the rod-shape, which conquers the habitat due to the enhanced ability of forming orientationally ordered domains extending from the homeland to the expansion front.

It is well-understood that morphology shapes colonies (e.g., tortuosity of sector boundaries (Supplementary Fig. S14–S15) (41, 42), swarming efficiency (43) and layering (44)). However, our results highlight an additional, yet so far overlooked, emergent property of bacteria in large communities caused by generic mechanical interactions rather than species-specific chemical cues. The simplicity of this morphological feature suggests a potential to be generalised over a wide range of bacteria species, confirmed by the reproduction of the results using minimal mechanical agent-based model and a generic continuum model. Our findings show how generic bacterial aspect ratios can influence bacterial advancements in growing colonies. Since biofilm-formation impacts various human activities (45, 46), a better understanding of their mechanical determinants can benefit numerous sectors, including ground remediation, biofouling of industrial installations, and changes in human microbiomes. The mechanical advantage of larger aspect ratios uncovered in this manuscript allows for a generic pathway to control biofilms by modifying the length of various bacteria, which is already achievable with existing technologies (47–49).

## AUTHOR CONTRIBUTIONS

NM and LJ conceived the original idea. NvdB, AS, and TTN conducted the experimental research including analysis. Specifically, NvdB did the surface-attached colony investigations, AS the single-cell resolved investigations, and TTN the 3D investigations. AD conceived the cell-based and continuum models. KT did the cell-based and continuum modelling. MC and AGV co-supervised the project and conducted substantial control experiments. NM, AD, and LJ supervised the project.

## FUNDING

This work was supported by the Danish National Research Foundation grant no. DFF 0165-00032B and grant no. DFF 0165-00103B (LJ), the Novo Nordisk Foundation grant no. NNF18SA0035142, NERD grant no. NNF21OC0068687 (AD) and grant no. NNF21OC0068775 (NM) and Synergy grant no. NNF23OC0086712 (LJ), the Villum Fonden Grant no. 29476 (AD), and the European Union via the ERC-Starting Grant PhysCoMeT (AD) and the Horizon 2020 research and innovation programme Marie Skłodowska-Curie grant no. 101029079-SIMMS (KT).

## ACKNOWLEDGEMENTS

The authors thank Dr. Michael Lisby for access to the FACS instrument and for generously sharing his expertise.

## REFERENCES

1. Flemming, H.-C., and S. Wuertz, 2019. Bacteria and archaea on Earth and their abundance in biofilms. *Nature Reviews Microbiology* 17:247–260. <https://www.nature.com/articles/s41579-019-0158-9>.
2. Ghoul, M., and S. Mitri, 2016. The Ecology and Evolution of Microbial Competition. *Trends in Microbiology* 24:833–845. <https://linkinghub.elsevier.com/retrieve/pii/S0966842X16300749>.
3. Nadell, C. D., K. Drescher, and K. R. Foster, 2016. Spatial structure, cooperation and competition in biofilms. *Nature Reviews Microbiology* 14:589–600. <https://doi.org/10.1038/nrmicro.2016.84>.
4. Persat, A., C. Nadell, M. Kim, F. Ingremeau, A. Siryaporn, K. Drescher, N. Wingreen, B. Bassler, Z. Gitai, and H. Stone, 2015. The Mechanical World of Bacteria. *Cell* 161:988–997. <https://linkinghub.elsevier.com/retrieve/pii/S0092867415005528>.

van den Berg *et al.*

5. Raffatellu, M., 2018. Learning from bacterial competition in the host to develop antimicrobials. *Nature Medicine* 24:1097–1103. <https://www.nature.com/articles/s41591-018-0145-0>.
6. Piccardi, P., B. Vessman, and S. Mitri, 2019. Toxicity drives facilitation between 4 bacterial species. *Proceedings of the National Academy of Sciences* 116:15979–15984. <https://pnas.org/doi/full/10.1073/pnas.1906172116>.
7. Rakoff-Nahoum, S., K. R. Foster, and L. E. Comstock, 2016. The evolution of cooperation within the gut microbiota. *Nature* 533:255–259. <http://www.nature.com/doifinder/10.1038/nature17626>.
8. Meacock, O. J., A. Doostmohammadi, K. R. Foster, J. M. Yeomans, and W. M. Durham, 2021. Bacteria solve the problem of crowding by moving slowly. *Nature Physics* 17:205–210. <http://dx.doi.org/10.1038/s41567-020-01070-6><https://www.nature.com/articles/s41567-020-01070-6>.
9. Lee, H., J. Gore, and K. S. Korolev, 2022. Slow expanders invade by forming dented fronts in microbial colonies. *Proceedings of the National Academy of Sciences* 119:e2108653119. <https://pnas.org/doi/full/10.1073/pnas.2108653119>.
10. Gude, S., E. Pinçe, K. M. Taute, A.-B. Seinen, T. S. Shimizu, and S. J. Tans, 2020. Bacterial coexistence driven by motility and spatial competition. *Nature* 578:588–592. <http://dx.doi.org/10.1038/s41586-020-2033-2><https://www.nature.com/articles/s41586-020-2033-2>.
11. Cordero, M., N. Mitarai, and L. Jauffred, 2023. Motility mediates satellite formation in confined biofilms. *The ISME Journal* 17:1819–1827. <https://www.nature.com/articles/s41396-023-01494-x>.
12. Booth, S. C., W. P. J. Smith, and K. R. Foster, 2022. Bows and swords : why bacteria carry short and long-range weapons. *bioRxiv* <https://www.biorxiv.org/content/10.1101/2022.10.13.512033v1>.
13. Borenstein, D. B., P. Ringel, M. Basler, and N. S. Wingreen, 2015. Established Microbial Colonies Can Survive Type VI Secretion Assault. *PLOS Computational Biology* 11:e1004520. <https://dx.plos.org/10.1371/journal.pcbi.1004520>.
14. Hallatschek, O., P. Hersen, S. Ramanathan, and D. R. Nelson, 2007. Genetic drift at expanding frontiers promotes gene segregation. *Proceedings of the National Academy of Sciences* 104:19926–19930. <https://pnas.org/doi/full/10.1073/pnas.0710150104>.
15. Vázquez, A. G., N. Mitarai, and L. Jauffred, 2024. Genetic mixing and demixing on expanding spherical frontiers. *ISME Communications* <https://academic.oup.com/ismecommun/advance-article/doi/10.1093/ismeco/ycae009/7585292>.
16. Deegan, R. D., O. Bakajin, T. F. Dupont, G. Huber, S. R. Nagel, and T. A. Witten, 1997. Capillary flow as the cause of ring stains from dried liquid drops. *Nature* 389:827–829. <https://www.nature.com/articles/39827><https://doi.org/10.1038/39827>.
17. Ruan, C., B. Borer, J. Ramoneda, G. Wang, and D. R. Johnson, 2023. Evaporation-induced hydrodynamics control plasmid transfer during surface-associated microbial growth. *Biofilms and Microbiomes* 9:58. <https://www.nature.com/articles/s41522-023-00428-x>.
18. De Gennes, P.-G., and J. Prost, 1993. *The physics of liquid crystals*. 83. Oxford university press.
19. Dhar, J., A. L. P. Thai, A. Ghoshal, L. Giomi, and A. Sengupta, 2022. Self-regulation of phenotypic noise synchronizes emergent organization and active transport in confluent microbial environments. *Nature Physics* 18:945–951. <https://www.nature.com/articles/s41567-022-01641-9>.
20. You, Z., D. J. Pearce, A. Sengupta, and L. Giomi, 2018. Geometry and Mechanics of Microdomains in Growing Bacterial Colonies. *Physical Review X* 8:031065. <https://link.aps.org/doi/10.1103/PhysRevX.8.031065>.
21. Nijjer, J., C. Li, M. Kothari, T. Henzel, Q. Zhang, J.-S. B. Tai, S. Zhou, T. Cohen, S. Zhang, and J. Yan, 2023. Biofilms as self-shaping growing nematics. *Nature Physics* 19:1936–1944. <https://www.nature.com/articles/s41567-023-02221-1>.

22. Hartmann, R., P. K. Singh, P. Pearce, R. Mok, B. Song, F. Díaz-Pascual, J. Dunkel, and K. Drescher, 2019. Emergence of three-dimensional order and structure in growing biofilms. *Nature Physics* 15:251–256. <https://www.nature.com/articles/s41567-018-0356-9>.
23. Copenhagen, K., R. Alert, N. S. Wingreen, and J. W. Shaevitz, 2021. Topological defects promote layer formation in *Myxococcus xanthus* colonies. *Nature Physics* 17:211–215. <https://www.nature.com/articles/s41567-020-01056-4>.
24. Allen, R. J., and B. Waclaw, 2019. Bacterial growth: a statistical physicist's guide. *Reports on Progress in Physics* 82:016601. <https://iopscience.iop.org/article/10.1088/1361-6633/aae546>.
25. Doostmohammadi, A., S. P. Thampi, and J. M. Yeomans, 2016. Defect-Mediated Morphologies in Growing Cell Colonies. *Physical Review Letters* 117:048102. <https://link.aps.org/doi/10.1103/PhysRevLett.117.048102>.
26. Wittmann, R., G. H. P. Nguyen, H. Löwen, F. J. Schwarzendahl, and A. Sengupta, 2023. Collective mechano-response dynamically tunes cell-size distributions in growing bacterial colonies. *Communications Physics* 6:331. <https://www.nature.com/articles/s42005-023-01449-w>.
27. Kröger, M., and P. Ilg, 2007. Derivation of Frank-Ericksen elastic coefficients for polydomain nematics from mean-field molecular theory for anisotropic particles. *The Journal of Chemical Physics* 127. <https://pubs.aip.org/jcp/article/127/3/034903/904677/Derivation-of-Frank-Ericksen-elastic-coefficients>.
28. Speranza, A., and P. Sollich, 2002. Simplified Onsager theory for isotropic-nematic phase equilibria of length polydisperse hard rods. *The Journal of Chemical Physics* 117:5421–5436. <https://pubs.aip.org/jcp/article/117/11/5421/184912/Simplified-Onsager-theory-for-isotropic-nematic>.
29. Drescher, K., J. Dunkel, C. D. Nadell, S. van Teeffelen, I. Grnja, N. S. Wingreen, H. A. Stone, and B. L. Bassler, 2016. Architectural transitions in *Vibrio cholerae* biofilms at single-cell resolution. *Proceedings of the National Academy of Sciences* 113. <https://pnas.org/doi/full/10.1073/pnas.1601702113>.
30. Tan, X., Y. Chen, H. Wang, Z. Zhang, and X. S. Ling, 2021. 2D isotropic-nematic transition in colloidal suspensions of ellipsoids. *Soft Matter* 17:6001–6005. <http://xlink.rsc.org/?DOI=D1SM00367D>.
31. Roller, J., J. D. Geiger, M. Voggenreiter, J.-M. Meijer, and A. Zumbusch, 2020. Formation of nematic order in 3D systems of hard colloidal ellipsoids. *Soft Matter* 16:1021–1028. <http://xlink.rsc.org/?DOI=C9SM01926J>.
32. Su, P.-T., C.-T. Liao, J.-R. Roan, S.-H. Wang, A. Chiou, and W.-J. Syu, 2012. Bacterial Colony from Two-Dimensional Division to Three-Dimensional Development. *PLoS ONE* 7:e48098. <https://dx.plos.org/10.1371/journal.pone.0048098>.
33. Duvernoy, M.-C., T. Mora, M. André, V. Croquette, D. Bensimon, C. Quilliet, J.-M. Ghigo, M. Baland, C. Belloin, S. Lecuyer, and N. Desprat, 2018. Asymmetric adhesion of rod-shaped bacteria controls microcolony morphogenesis. *Nature Communications* 9:1120. <https://www.nature.com/articles/s41467-018-03446-y>.
34. Steinberger, R., A. Allen, H. Hansma, and P. Holden, 2002. Elongation Correlates with Nutrient Deprivation in *Pseudomonas aeruginosa* Unsaturated Biofilms. *Microbial Ecology* 43:416–423. <http://link.springer.com/10.1007/s00248-001-1063-z>.
35. Yulo, P. R. J., and H. L. Hendrickson, 2019. The evolution of spherical cell shape; progress and perspective. *Biochemical Society Transactions* 47:1621–1634. <https://portlandpress.com/biochemsoctrans/article/47/6/1621/221467/The-evolution-of-spherical-cell-shape-progress-and>.
36. Errington, J., 2013. L-form bacteria, cell walls and the origins of life. *Open Biology* 3:120143. <https://royalsocietypublishing.org/doi/10.1098/rsob.120143>.
37. Siefert't, J. L., and G. E. Fox, 1998. Phylogenetic mapping of bacterial morphology. *Microbiology* 144:2803–2808. <https://www.microbiologyresearch.org/content/journal/micro/10.1099/00221287-144-10-2803>.
38. Lenski, R. E., M. R. Rose, S. C. Simpson, and S. C. Tadler, 1991. Long-Term Experimental Evolution in *Escherichia coli*. I. Adaptation and Divergence During 2,000 Generations. *The American Naturalist* 138:1315–1341. <https://www.jstor.org/stable/2462549>.

van den Berg *et al.*

39. Grant, N. A., A. Abdel Magid, J. Franklin, Y. Dufour, and R. E. Lenski, 2021. Changes in Cell Size and Shape during 50,000 Generations of Experimental Evolution with *Escherichia coli*. Journal of Bacteriology 203. <https://journals.asm.org/doi/10.1128/JB.00469-20>.
40. Marshall, D. J., M. Malerba, T. Lines, A. L. Sezmis, C. M. Hasan, R. E. Lenski, and M. J. McDonald, 2022. Long-term experimental evolution decouples size and production costs in *Escherichia coli*. Proceedings of the National Academy of Sciences 119. <https://pnas.org/doi/full/10.1073/pnas.2200713119>.
41. Müller, M. J. I., B. I. Neugeboren, D. R. Nelson, and A. W. Murray, 2014. Genetic drift opposes mutualism during spatial population expansion. Proceedings of the National Academy of Sciences 111:1037–1042. <https://pnas.org/doi/full/10.1073/pnas.1313285111>.
42. Hallatschek, O., and D. R. Nelson, 2010. Life at the front of an expanding population. Evolution 64:193–206. <https://academic.oup.com/evolut/article/64/1/193/6854125>.
43. Ilkanaiv, B., D. B. Kearns, G. Ariel, and A. BeáŽer, 2017. Effect of Cell Aspect Ratio on Swarming Bacteria. Physical Review Letters 118:158002. <http://link.aps.org/doi/10.1103/PhysRevLett.118.158002>.
44. Smith, W. P. J., Y. Davit, J. M. Osborne, W. D. Kim, K. R. Foster, and J. M. Pitt-Francis, 2017. Cell morphology drives spatial patterning in microbial communities. Proceedings of the National Academy of Sciences 114:E280–E286. <http://www.pnas.org/lookup/doi/10.1073/pnas.1613007114><https://doi.org/10.1073/pnas.1613007114>.
45. Shineh, G., M. Mobaraki, M. J. Perves Bappy, and D. K. Mills, 2023. Biofilm Formation, and Related Impacts on Healthcare, Food Processing and Packaging, Industrial Manufacturing, Marine Industries, and Sanitation-A Review. Applied Microbiology 3:629–665. <https://www.mdpi.com/2673-8007/3/3/44>.
46. Hayta, E. N., M. J. Ertelt, M. Kretschmer, and O. Lieleg, 2021. Bacterial Materials: Applications of Natural and Modified Biofilms. Advanced Materials Interfaces 8:2101024. <https://onlinelibrary.wiley.com/doi/10.1002/admi.202101024>.
47. Tanniche, I., and B. Behkam, 2023. Engineered live bacteria as disease detection and diagnosis tools. Journal of Biological Engineering 17:65. <https://jbioleng.biomedcentral.com/articles/10.1186/s13036-023-00379-z>.
48. Riglar, D. T., and P. A. Silver, 2018. Engineering bacteria for diagnostic and therapeutic applications. Nature Reviews Microbiology 16:214–225. <https://www.nature.com/articles/nrmicro.2017.172>.
49. Landry, B. P., and J. J. Tabor, 2017. Engineering Diagnostic and Therapeutic Gut Bacteria. Microbiology Spectrum 5. <https://journals.asm.org/doi/10.1128/microbiolspec.BAD-0020-2017>.

## Supplementary

# Emergent collective alignment gives competitive advantage to longer cells during range expansion

Nathan van den Berg<sup>1†</sup>, Kristian Thijssen<sup>1†</sup>, Thu Trang Nguyen<sup>1†</sup>, Adrien Sarlet<sup>1†</sup>, Mireia Cordero<sup>1</sup>, Alba García Vázquez<sup>1</sup>, Namiko Mitarai<sup>1</sup>, Amin Doostmohammadi<sup>1</sup>, and Liselotte Jauffred<sup>1</sup>

<sup>1</sup>The Niels Bohr Institute, University of Copenhagen, Blegdamsvej 17, DK-2100 Copenhagen O, Denmark

<sup>†</sup>These authors contributed equally

<sup>1</sup>Correspondence: mitarai@nbi.ku.dk, doostmohammadi@nbi.ku.dk, jauffred@nbi.ku.dk

## MATERIALS AND METHODS

### Bacterial strains

We used three subpopulations of the non-motile (1) *Escherichia coli* B strain REL606: the wild-type strain (WT) and the *mreB* mutants (2) REL606*mreB*<sup>A53S</sup> (AS) and REL606*mreB*<sup>A53K</sup> (AK) (3) (Table 1). The *mreB* gene in bacteria codes for the filament protein MreB, which is homologous to actin in eukaryotic cells (4). Depletion of the *mreBCD* operon in *E. coli* leads to spherical, enlarged, and eventually lysed cells (5). More specifically, MreB is responsible for maintaining the rod-like cell shape of *E. coli* cells by promoting cell wall growth in regions of negative cell wall curvature. Therefore, its depletion leads to homogeneous cell wall growth (6) by increasing the helical pitch of the filaments, causing shortening and widening of the bacteria's shape (7). All our strains carried a plasmid that constitutively expressed kanamycin resistance and either GFP, pmaxGFP (pmaxCloning-Vector, Lonza), with excitation/emission of 487/509 nm or RFP, pTurboRFP (pmaxCloning-Vector, Lonza), of 553/574 nm (8).

Name	Strain	Relevant characteristics	Reference
WT	REL606	Ancestral strain. Ara(-), StrepR	(9)
AS	REL606 <i>mreB</i> <sup>A53S</sup>	REL606 with <i>mreB</i> <sup>A53S</sup> allele	(3)
AK	REL606 <i>mreB</i> <sup>A53K</sup>	REL606 with <i>mreB</i> <sup>A53K</sup> allele	(3)

Table 1: *Escherichia coli* strains used in the study (kind gifts from the Kevin Foster Lab).

### Culture media

Throughout this study, we alternated between the following two media: rich Lysogenic broth (LB) and M63 minimal media (M63+glu) supplemented with 30 µg/ml kanamycin sulphate (≥ 95%, K1377, Sigma-Aldrich) to retain fluorescence, unless otherwise stated. For agar plates, we used either 0.5% or 1.5% BD Bacto™ agar (10455513, Fisher Scientific).

**M63+glu** The 5X M63 salt solution was composed of 15 g/l anhydrous KH<sub>2</sub>PO<sub>4</sub> (≥98.0%, P9791, Sigma-Aldrich), 35 g/l anhydrous K<sub>2</sub>HPO<sub>4</sub> (≥99.0%, 60353, Sigma-Aldrich), 10 g/l (NH<sub>4</sub>)<sub>2</sub>SO<sub>4</sub> (≥99.0%, 09978, Sigma-Aldrich), 2.5 ml 20 mM FeSO<sub>4</sub> (≥99.5%, 44970, Sigma-Aldrich), 20 mM Na-Citrate (≥99.5%, 71402, Sigma-Aldrich). The M63 minimal media was composed of 20% 5X M63 salt, 1 µg/ml thiamine hydrochloride (≥99%, T4625, Sigma-Aldrich), 2 mM MgSO<sub>4</sub> (≥99.5%, 63138, Sigma-Aldrich), 2 mg/ml glucose (≥99.5%, G7528, Sigma-Aldrich), dissolved in Millipore water.

**LB** The medium was composed of 10 g/l Gibco™ Bacto™ tryptone (16279751, Fisher Scientific), 5 g/l Gibco™ Bacto™ yeast extract (16279781, Fisher Scientific) and 5 g/l NaCl (≥99%, S9888, Sigma-Aldrich) dissolved in Millipore water.

### Cell culture

For starting the culture, bacteria from frozen glycerol stocks were streaked on LB or M63+glu agar (1.5%) plates to obtain microcolonies after overnight growth at 37 °C. A single colony from the streak plates was transferred into 2 ml LB and incubated

overnight at 37 °C under constant shaking to prevent biofilm formation. The OD<sub>600</sub> of the overnight cultures was measured after a 10-fold dilution (IMPLEN NanoPhotometer C40) to control the strain proportions in the resulting suspension.

## Imaging

**Confocal laser scanning microscopy (CLSM)** On a Leica DMI6000 CS SP5 (Leica, Wetzlar, Germany) we used the Ar (488 nm) and HeNe (543 nm) laser lines sequentially to excite GFP (detection: 498–536 nm) and RFP (detection: 568–641 nm), respectively. We alternated between the following magnification objectives: 5× air objective (Nplan5×0.12PHO, Leica), 20× air objective (NplA.20x0.40NA, Leica), and 100× oil immersion objective (100×0.17/D/HCX/PL/APO, Leica).

**Fluorescence microscopy** We used a Nikon ECLIPSE Ti microscope (Nikon, Tokyo, Japan) paired with an Andor Neo camera (Andor, Belfast, UK). GFP and RFP were excited by a Hg lamp using the FITC (FITC Filter Cube Set, Olympus, York, UK) and Texas Red cubes (Texas Red<sup>TM</sup> Filter Cube Set, Nikon, Tokyo, Japan), respectively. In combination with one of the following objectives: 4× air immersion objective (Nikon, Plan Fluor, 4x/0.13, ∞/1.2 WD 16.5), 20× air immersion objective (Nikon, Plan Fluor, 20x/0.50, ∞/0.17 WD 2.10) and 100× oil immersion objective (Nikon, Plan Apochromat λ, 100x/1.45 Oil, ∞/0.17 WD 0.13).

## Growth rate measurements

Starting from overnight cultures (WT+GFP, WT+RFP, AS+GFP, AS+RFP, AK+GFP, AK+RFP) in M63+glu liquid medium, we diluted 100× in M63+glu to final volumes of 5 ml. The cultures were incubated at 37 °C and the OD<sub>600</sub> was measured at regular intervals (1.25 h–1.75 h) for 5–6 h, while making sure to dilute appropriately to stay within the optimal range of the spectrometer. In parallel, we collected samples for CFU measurements. We diluted the sample to adjust the CFU count to ~100/plate, and 100 μl was plated on 3 LB agar (1.5%) plates and incubated overnight before CFU were counted.

## Cell aspect ratio and volume measurements

**Sample preparation and imaging** We collected samples (WT+GFP, AS+GFP, AK+GFP) in the stationary phase (i.e. immediately following overnight culture) and the log phase (3 h after dilution) for imaging. Single droplets of bacterial cultures were deposited on cover slides (#1.5) and imaged using fluorescence microscopy and the 100× objective.

**Image analysis** We measured the length,  $l$ , and width,  $w$ , of cells using the line tool in Fiji ImageJ to calculate the aspect ratio,  $l/w$ , and corresponding volumes:

$$V_{cell} = \frac{4}{3}\pi\left(\frac{w}{2}\right)^3 + \pi\left(\frac{w}{2}\right)^2(l-w), \quad (1)$$

where cell shapes were approximated to be cylinders with hemispherical ends. Using Eq. 1, we found the volume ratio between the WT and AK strains in the stationary phase to be ~ 1.3.

## Competition in liquid co-cultures

Overnight cultures (WT+GFP, WT+RFP, AS+GFP, AS+RFP, AK+GFP, AK+RFP) were grown in M63+glu liquid medium. The OD<sub>600</sub> of the overnight cultures was measured and the strains were mixed pairwise (GFP+RFP) in equal proportions ( $\zeta = 1$ ) and diluted 100× in M63+glu. Cultures were incubated at 37 °C and cell counts (50000 counts per sample) were measured right after mixing and again after 8 h of incubation, using a BD FACSJazz Cell Sorter (BD Biosciences, cat. no. 655490). In parallel, we measured the OD<sub>600</sub> to confirm that the overall growth rates of the co-cultures were the same as for the individual cultures. Data were processed using the Flowkit package (10) with a *logicle* transformation, and clustered with the *hdbscan* algorithm (11). After clustering, we extracted the counts of the two main clusters (GFP and RFP) and defined the frequencies of the two populations as the ratio of cell counts of one population (GFP or RFP) over the cell counts of both (GFP+RFP).

**Relative fitness** The relative fitness,  $W_{ij}$ , of strain  $i$  in respect to strain  $j$  is estimated here as the ratio of the number of doublings of the two competitors (i.e., identical to the ratio of their Malthusian parameters) (9):

$$W_{ij} = \frac{\ln(N_i(t)/N_i(0))}{\ln(N_j(t)/N_j(0))}, \quad (2)$$

where  $N_i(t)/N_i(0)$  and  $N_j(t)/N_j(0)$  are the ratios of number of cells at time  $t$  in respect to starting point of strain  $i$  and  $j$ , respectively. These ratios are obtained from multiplying the ratio of frequencies (i.e., at  $t = 8$  h in respect to  $t = 0$ ) with the dilution factor, which in our case was  $100\times$ .

## Cell density measurements

For each strain (WT+GFP, WT+RFP, AK+GFP, AK+RFP) we plated  $100\ \mu\text{l}$  of diluted overnight culture on LB plates with agar (1.5%), which were incubated overnight ( $37^\circ\text{C}$ ), before CFU were counted. We found similar results for the two colours and measured the (combined) conversion at  $\text{OD}_{600} = 1$  to be  $1.6 \cdot 10^9$  CFU and  $0.7 \cdot 10^9$  CFU, for WT and AK, respectively. Therefore, the cell number ratio between the WT and AK strains in stationary phase (same  $\text{OD}_{600}$ ) was measured to be  $\sim 2.2$ .

## 2D competition

**Sample preparation and imaging** Starting from overnight cultures, we adjusted the ratios (based on  $\text{OD}_{600}$ ) of the longer cells (WT or AS) versus the shorter (AS or AK) to  $\zeta \in \{1, 0.1, 0.01, 0.001\}$  and diluted to a final (and combined)  $\text{OD}_{600}$  of 0.3. The diluted cell culture was inoculated in  $0.5\ \mu\text{l}$  droplets on M63+glu plates with agar (1.5%). After either 20 h or 3 days of incubation ( $37^\circ\text{C}$ ), we imaged the colonies using the CLSM and the  $5\times$  objective. A vertical range of  $100\ \mu\text{m}$  was scanned and the resulting 3D images had voxel sizes of  $(x, y, z) = (6.07, 6.07, 10)\ \mu\text{m}$ .

**Cross-sections** The bacteria (WT and AK) were mixed in equal proportions, reaching a final  $\text{OD}_{600}$  of 0.3. The diluted cell culture was inoculated in  $0.5\ \mu\text{l}$  droplets on LB agar plates (1.5%). The plates were then incubated for 20 h ( $37^\circ\text{C}$ ). Fresh agar ( $55^\circ\text{C}$ ) was poured into the dishes to fully embed the bacterial colonies prior to sectioning. The agar was poured onto the original agar substrate, between the colonies, to avoid immediate direct contact with the colonies. Dishes were left to solidify at the bench (1 h). Approximately  $1\ \text{cm}^3$  was cut out around the colony, placed on a glass-bottomed dish and cut in half with a scalpel along the diameter of the colony. The halves were then rotated to image the cross-sections. These were imaged at  $4\times$  magnification using the fluorescence microscope, as well as  $20\times$  and  $100\times$  using the CLSM.

**Pre-processing** In many cases, colonies had outgrown the field of view ( $3.1\ \text{mm} \times 3.1\ \text{mm}$ ), so we stitched 4 images together using the Pairwise Stitching plugin in Fiji ImageJ (12). We made a maximum intensity pixel projection of each stack to get a flattened  $(x, y)$ -image of pixel size  $(x, y) = (6.07, 6.07)\ \mu\text{m}$ .

**Intensity adjustment of colour channels** To boost the contrast between the two channels, we divided channels (GFP and RFP) with each other to amplify the pixel value range of the two channels. Thus, for each pixel, we calculated a new intensity value,  $p(x, y)'$ , using a re-scaling value of 100 (8-bit image), such that:

$$p(x, y)' = \frac{p_{\text{GFP}}(x, y) + 100}{p_{\text{RFP}}(x, y) + 100}, \quad (3)$$

where  $p_{\text{GFP}}$  and  $p_{\text{RFP}}$  are the pixel values from the GFP and RFP channels, respectively. We found this method to be particularly useful in image areas with significant intensity variations (e.g., around the homeland) and for background removal (13).

**Pixel classification** For further analysis, we wanted all pixels to be classified as either GFP or RFP (never both). Therefore, we used the rescaled pixel intensities,  $p(x, y)'$ , distribution of the image and – consistently – found two peaks corresponding to GFP and RFP, and using Otsu's method, we estimated the threshold value to classify the pixels.

**Competition strength as a function of the radial vector in 2D** Colonies had clearly detectable regions and we defined the homeland as the well-mixed centre region, which roughly corresponded to where the original inoculation droplet was deposited. The boundary of this region was found by manual fitting of a circle and we identified the centre of this circle as the starting point of the radial vector  $\mathbf{r}(t)'$ , and the homeland boundary  $\mathbf{r}(t = 0)$  (after which clear sectors first appear). To account for variations in drop size, we defined the translated radial distance as

$$r(t) = |\mathbf{r}(t)'| - |\mathbf{r}(t = 0)|. \quad (4)$$

We defined the ensemble-averaged strength of  $N$  colonies to be the re-scaled occupancy of the GFP-expressing (and longer) bacteria at a given radial length  $r(t)$  as the sum over the following fraction:

$$S(r) = \frac{2}{N} \sum_{n=1}^N \frac{C_{\text{GFP}}^{(n)}(r(t))}{C^{(n)}(r(t))} - 1, \quad (5)$$

where  $C^{(n)}(r(t))$  is the total number of pixels of the circle of the  $n$ -th colony at radial distance  $r(t)$  and  $C_{\text{GFP}}^{(n)}(r(t))$  is the number of pixels occupied by GFP-expressing bacteria, such that  $C^{(n)}(r(t)) = C_{\text{GFP}}^{(n)}(r(t)) + C_{\text{RFP}}^{(n)}(r(t))$ . Defined like this,  $S$  had the value of 1 (-1) when the GFP-expressing (RFP-expressing) cells had taken over the complete perimeter at a specific radial distance. To compare the  $S$  at a specific time, we defined  $t_1 = 1.5$  days as halfway from the homeland border to the front of a colony after 3 days of incubation.

**Competition in isogenic bacteria** Starting from overnight cultures, we inoculated 1:1 ( $\zeta = 1$ ) two subpopulations (expressing GFP or RFP) of the same strain (WT/WT, AS/AS, or AK/AK) with the same fitness and shape at  $\text{OD}_{600} = 0.3$ . Plates were incubated for 20 h and CLSM imaged. We found patterns of spatially segregated lineages with a constant number of sectors (Supplementary Fig. S14A); well in accordance with earlier findings (8, 14).

**Zoom in on 2D competition isogenic boundaries** Plates were incubated (37 °C) for 3 days, before cutting out the colony and the according square of agar and placing it upside down in a glass-bottomed culture well (HBST-5040, WillCo Wells B.V.). The colonies were imaged with sequential z-stacks using CLSM in combination with the 100× objective and the resulting voxel size in  $(x, y, z) = (0.30, 0.30, 0.99) \mu\text{m}$ .

**Varying seeding density** We repeated the competition experiment (20 h) for WT/AK but for serial dilutions of seeding density. The co-culture of WT and AK mixed 1:1 and  $\text{OD}_{600} = 0.3$  was diluted 10-, 100-, and 1000-fold. We found the mixing of genotypes reduced in the homeland (i.e., patch sizes enlarged), but WT was still able to completely dominate the expansion front (Supplementary Fig. S3). So even though the seeding density regulates patch sizes (15, 16), the longer cell still wins.

**Rate of range expansion in 2D** Starting from overnight cultures (WT+GFP, AS+GFP, AK+GFP) in LB, we inoculated 0.5  $\mu\text{l}$  droplets of single-strain cultures ( $\text{OD}_{600} = 0.2$ ) on M63+glu agar (1.5%). After 15 h of incubation (37 °C), the plates were placed upside down on our inverted fluorescence microscope and imaged with a frame rate of  $1.5 \text{ h}^{-1}$  during 9 h using the 4× objective. We mapped the colony areas by (manual) thresholding and quantified the range expansion by calculating the effective colony radius,  $r$ , from the measured surface area using the Measurement function in Fiji.

## Single-cell resolution time-lapses

**Sample preparation** One colony of each WT and AK was transferred separately into 3 ml LB medium and incubated overnight (37 °C) under constant shaking. The  $\text{OD}_{600}$  of the overnight cultures were measured and they were mixed in equal proportions ( $\zeta = 1$ ), before 10-fold dilution and inoculation on M63+glu agar (1.5%) plates. Shortly following the inoculation, a rectangular piece of agar was cut out, flipped, and transferred upside down into glass-bottomed culture well (HBST-5040, WillCo Wells B.V.) and sealed with Parafilm®.

**Single-cell resolution time-lapses** The colonies were imaged in our inverted fluorescence microscope using the 100× objective. Fluorescence images were acquired with a frame rate of 2/h during 12 h. In addition, z-stacks were collected over a total range of 2  $\mu\text{m}$  (0.5  $\mu\text{m}$  spacing) for each time frame to cope with the relative roughness of the agar substrate surface at high magnification.

**Data analysis** The z-stacks were high-pass filtered and summed into a single image using a custom-made MATLAB procedure, thereby collapsing all the sharpest regions into a single plane. Bacteria were segmented by thresholding each time frame multiple times (twice for AK, thrice for WT) to consider variations in intensity and saturation within a single time frame. The binary images resulting from different thresholds (of the same time frame) were summed to collect as many bacteria as possible, despite non-uniform contrasts. Bacteria were detected using the Regionprops function in MATLAB (Image Processing Toolbox version 11.7). The function returned the  $(x,y)$ -coordinates and the orientation of each bacterium (major axis of the ellipse that has the same second-moments as the bacterium pixels region).

The local nematic order parameter  $q$  for a bacteria  $n$ , is calculated by locating the  $N_n = 8$  nearest neighbours  $n_i$  of the same strain and then using the definition:

$$q_n = \frac{1}{N_n} \sum_{n_i}^{N_n} \left( \frac{3}{2} \cos^2 \theta_i - \frac{1}{2} \right) \quad (6)$$

with  $\theta_i$  the orientation of the neighbouring bacteria orientation.

### 3D competition

**Encapsulating bacteria in inoculation beads** We produced four batches of 2.5% agarose inoculation beads containing different ratios of WT+GFP and AK+RFP following the procedure outlined in Ref. (17), excepting the following modifications: i) Cell densities in the beads were either  $OD_{600} = 0.65$  or  $OD_{600} = 1.45$  ( $OD_{600} = 4$  or  $OD_{600} = 8.6$  in the cell mix) for  $1/\zeta_n \in \{0.25, 12, 16\}$  and  $1/\zeta_n = 47$ , respectively. The latter was obtained by up-concentration through centrifugation of the overnight cultures. Varying the densities ensured reasonable numbers of (WT+GFP), despite low ratios (high  $1/\zeta_n$ ). We ii) filtered the PBS-bead suspensions through strainers with mesh sizes of 70, 50, and 40  $\mu\text{m}$  and let at least 10 ml additional PBS flow through the strainers to wash off the remaining silicone oil. We collected the beads in the 40  $\mu\text{m}$  strainer (diameters of 40–50  $\mu\text{m}$ ) by turning it upside down and flushing with 6–9 ml LB. More details can be found in the associated protocol (18).

**Mono-strain 3D colonies** As a control, we also prepared beads with two colours of the same strain. We followed the exact same procedure but with a different bacteria mixture: Overnight cultures were mixed 1:1 by adjusting the  $OD_{600}$  (WT+GFP/WT+RFP, AK+GFP/AK+RFP, AS+GFP/AS+RFP) and diluted in LB to a final (overall)  $OD_{600} = 0.07$  (0.4. in the cell mix).

**Bead concentration measurements** To measure the strain ratios and number of cells within the inoculation beads, we did serial dilutions ( $10^{-7} - 10^{-5}$ ) of the spare cell mixture from the encapsulation process. We plated 100  $\mu\text{l}$  of the dilution on LB agar (1.5%) plates and incubated overnight. From the number and colour of CFU, we deduced i) the ratio of WT to AK cells ( $1/\zeta_n$ ) and ii) the overall cell concentration of the mixture. Based on these results, we estimated the number of cells encapsulated within a bead by modelling the beads as perfect spheres with a radius of 45  $\mu\text{m}$ . The strain ratios were estimated from counting 1606, 2900, 3918, and 3472 CFU for  $1/\zeta_n \in \{0.25, 12, 16, 47\}$ , respectively.

As the small size limited the number of cells per bead and as the strains had different cell volumes (Table 1 in the main text), we defined a strain ratio,  $\zeta_n$ , as the ratio of CFU of the longer strain versus the shorter (measured before encapsulation in the beads). We found  $1/\zeta_n \in \{0.25, 12, 16\}$  with  $OD_{600} = 0.65$  and  $1/\zeta_n = 47$  with  $OD_{600} = 1.45$ ; the higher density for the latter ensured WT cells in most beads at this extreme ratio.

**Embedment of inoculation beads in 0.5% agar** To investigate competition in 3D, we embedded the inoculation beads within a 0.5% agar growth medium. We followed the protocol outlined in (17), excepting the following adaptations: i) Frozen bead stocks were diluted with LB (based on the measured concentration of beads per 1 ml frozen stock) aiming for 10 beads per well. Specifically, we diluted {650, 970, 130, 85}  $\mu\text{l}$  of frozen bead stock in 1 ml LB for  $1/\zeta_n \in \{0.25, 12, 16, 47\}$ , respectively. We counted on average  $10.9 \pm 3.3$  beads per well and ii) we incubated all colonies for 10 h.

**3D colony imaging** After incubation, wells were preserved at 4 °C until imaging (< 24 h) using the CLSM and the 20 $\times$  objective (discarding colonies that had reached the agar-glass or the agar-air interface). For bi-coloured colonies, we recorded two sequential (RFP then GFP) z-stacks with a resulting voxel volume of  $(x, y, z) = (1.51, 1.51, 1.33)$   $\mu\text{m}$ . For each strain ratio ( $1/\zeta_n$ ), we collected images from 4-5 different wells (> 40 colonies in total). As a control, we also mixed 1:1 (i.e.,  $\zeta_n = 1$ ) two subpopulations (expressing GFP or RFP) of the same strains and found that surface coverage was similar for both strains (Supplementary Fig. S12). In the case of WT/WT, this is well in accordance with earlier findings (17).

**Segmentation of 3D images** The 3D colony images were processed, segmented, and filtered for the surface using BiofilmQ (19) and Fiji/Image J (20). Only colonies expressing both strains were segmented, following the exact process described in Ref. (17).

**Competition strength as a function of time in 3D** We defined the ensemble-averaged strength of GFP-expressing bacteria (WT) on the colony surface as the re-scaled sum over the area fraction:

$$\mathcal{S}_3(t) = \frac{2}{N} \sum_{n=1}^N \frac{A_{\text{GFP}}^{(n)}(t)}{A^{(n)}(t)} - 1, \quad (7)$$

where  $A_{\text{GFP}}^{(n)}(t)$  is the area of GFP-expressing bacteria and  $A^{(n)}(t)$  is the total surface area of the  $n$ -th colony at time  $t$ , such that  $A^{(n)}(t) = A_{\text{GFP}}^{(n)}(t) + A_{\text{RFP}}^{(n)}(t)$ . In contrast to the 2D case,  $\mathcal{S}_3$  is a function of  $t$  (instead of  $r(t)$ ) as it refers to the surface at a given  $t$ , with varying  $r(t)$ . For colonies whose visible surface only expressed one of the two strains, we assigned  $A_{\text{GFP}}^{(n)} = 1$  (GFP-mono-coloured) or  $A_{\text{GFP}}^{(n)} = 0$  (RFP-mono-coloured). We also calculated the expectation value of the subset of  $N$  originating from pure RFP-expressing cells from estimated number of cells per bead ( $\text{CFU}/V_{\text{bead}}$ ), the total number of colonies ( $N$ ), and the WT/AK ratio ( $\zeta_n$ ); assuming a binomial distribution.

**Rate of range expansion in 3D** Starting from overnight cultures (WT+GFP, AS+GFP, AK+GFP) in LB, cells were embedded at low concentration ( $\sim 10/\text{well}$ ) in M63+glu agar (0.5%) matrix following the protocol described in (21). After 6 h of incubation ( $37^\circ\text{C}$ ) the mono-clonal colonies were imaged using our fluorescence microscope with a frame rate of 3/2 h during 16 h with a 20 $\times$  objective. Similar to the 2D case, we quantified the range expansion by manual thresholding and calculated the effective colony radius,  $r$ , from the (maximum-intensity) z-projected cross-sectional area using the Measurement function in Fiji.

**Statistics** All mean values are given as mean plus/minus the standard deviation (SD) or the standard error of the mean (SEM), when this is stated and only when data are tested against the null hypothesis that it is normally distributed. The normal distributions of  $\mathcal{S}$  were assessed with Shapiro-Wilk tests. Their distributions were compared between the WT and AK strains with Mann-Whitney U Tests. The significance of the differences in  $\nu$  were evaluated with a Students t-test.

## Computational models

**Particle model** The particle-based model is based on the SPR model presented and described in (22). A single bacteria is described as a rod,  $\alpha$ , consisting of a rigid chain of a number of Yukawa segments,  $n_\alpha$ , separated by length,  $l_\alpha$ , with segments of different rods repelling one another with a Coulomb-like point potential with potential strength,  $U_0 = 250$  (previous work has shown that results are independent on  $U_0$  provided it is large enough (23)), resulting in a total potential,  $U$ . The Yukawa screening length,  $\lambda$ , is taken as the width of the particle with the aspect ratio of the rod:  $L = n_\alpha l_\alpha / \lambda$ . Other particle potentials are used in the literature (Bsim 2.0 (24)), but our results are robust independently of this choice.

Bacterial growth is done stochastic. So, for every time step,  $\Delta t$ , we draw a random number **randn** (taken from the absolute value of a normal distribution with mean 0 and standard deviation 1). This random number is multiplied by the current particle length and the growth rate  $\gamma$  and then added to the particle length. The choice of distribution does not matter, because as long as an uncorrelated distribution is chosen, the method in the continuum limit gives the most basic ODE growth solver (Gro (25)):

$$\frac{\partial L}{\partial t} = \gamma L. \quad (8)$$

When the rod has reached the division length  $l$ , the particle is split into two. The timescales given in the manuscript are normalised by the generation time, which is purely set by  $\gamma$ .

We use overdamped equations of motion to then update the particle position and orientations (22):

$$f_t \frac{\partial \vec{r}_\alpha}{\partial t} = - \frac{\partial U}{\partial \vec{r}_\alpha} \quad (9)$$

$$f_r \frac{\partial \theta_\alpha}{\partial t} = - \frac{\partial U}{\partial \theta_\alpha}, \quad (10)$$

where  $\vec{r}_\alpha$  and  $\theta_\alpha$  are the centre and orientation of rod  $\alpha$ , respectively. This gives local force propagation even in the non-equilibrium state of an expanding colony, which retains the importance of mechanical interactions that are the highlight of our manuscript. This is in contrast to other bacterial solvers (e.g. Gro (25) and BSim 2.0 (24)) which use instantaneous global force minimisation to update the bacteria's positions and orientations.

At time zero ( $t = 0$ ), 40 rods are initialised in a small area with 10 rods having division aspect ratio,  $l_L$ , and random aspect ratios (uniform distribution) between  $l_L/2$  and  $l_L$  and 30 rods having division aspect ratio,  $l_S$ , and random aspect (uniform distribution) ratios between  $l_S/2$  and  $l_S$ , such that  $\zeta = 0.25$ .

**Competition strength in the particle model** To determine the competition strength  $S_f(t)$  at the interface at it evolves over time, we count all particles that exist in the front. We do this by dividing the colony into 10 slices (with centre at the centre of mass of the colony), determine the particle that is furthest from the centre of the colony and then take into account all particles that inhabit up to 5 decay lengths  $\lambda$  into the colony.

The takeover rate,  $\nu_{\text{sim}}$ , in the simulations is calculated from the  $S_f(t)$  curve of 10 different trajectories. The  $\nu_{\text{sim}}$  is the linear fit from generation time 5.5 to time 7.5.

**Continuum model** To describe the bacterial colony on a course-grained level, we study the evolution of the nematic order parameter  $\mathbf{Q} = 2q(\hat{n}\hat{n} - \frac{\mathbf{I}}{2})$ , where  $q$  and  $\hat{n}$  show the magnitude and orientation of the order, respectively, and  $\mathbf{I}$  represents the identity tensor (26).

In line with other dry active nematic studies (27), (28), we use the dynamics of the  $\mathbf{Q}$ -tensor is described by the Beris-Edwards equation

$$\frac{DQ_{ij}}{Dt} = \chi E_{ij} + \Gamma H_{ij}, \quad (11)$$

with respect to a symmetric gradients  $E_{ij}$  (shear tensor) and anti-symmetric  $\omega_{ij}$  (vorticity tensor) of a velocity field  $\vec{u}$ . We use the convected co-rotational time derivative  $DQ_{ij}/Dt = (\partial_t + u_k \partial_k) Q_{ij} - \omega_{ik} Q_{kj} + Q_{ik} \omega_{kj}$ .

In Eq. 11,  $\chi$  is the aligning parameter (taken as 0.8) and  $\Gamma = 0.1$  is the rotational diffusivity which along with  $H_{ij}$ , the molecular field, describes the relaxation of the  $\mathbf{Q}$ -tensor towards the minimum of a free energy described by:

$$\mathcal{F} = \frac{A}{2} (\mathbf{Q} : \mathbf{Q})^2 + \frac{K}{2} |\nabla \mathbf{Q}|^2. \quad (12)$$

The free energy includes the nematic alignment term (with coefficient  $A = 0.01$ ) and an elastic term  $K$  which penalises gradients in the  $\mathbf{Q}$  tensor.

Velocity is taken in the overdamped limit

$$f u_i = -\zeta \partial_j Q_{ij} + \eta \nabla^2 (\partial_j Q_{ij}) \quad (13)$$

where  $\zeta$  is the activity coefficient related to a force dipoles generated from division events (positive to correspond to the extensile limit), which is balanced by frictional dissipation into the surface  $f$  and a small viscous dissipation with viscosity  $\eta = 0.01$ . The outer edge of the colony is taken by assuming high friction  $f = 400$  outside a radius  $R_{\text{con}} > 30$ , while lower friction  $f = 4$  is used inside the radius  $R_{\text{con}} < 30$  (Supplementary Fig. S7). In addition, the incompressibility constraint is imposed on the total velocity field.

To distinguish the two bacterial concentrations, we introduce a phase-field binary order parameter  $\phi$ , which evolves according to a Cahn-Hilliard model

$$\partial_t \phi + \nabla \cdot (\vec{u} \phi) = \Gamma_\phi \nabla^2 \mu, \quad (14)$$

where  $\mu = \frac{\delta \mathcal{F}}{\delta \phi} - \nabla \cdot \left( \frac{\delta \mathcal{F}}{\delta \nabla \phi} \right)$  is the chemical potential with  $\Gamma_\phi = 0.3$  a mobility coefficient. We add to the free energy  $\mathcal{F}$  a single well potential  $f_{\text{DW}} = \frac{A_\phi}{2} \phi^2$  and an interfacial term  $f_1 = \frac{K_\phi}{2} (\nabla \phi)^2$  with  $A_\phi = 0.002$  and  $K_\phi = 0.02$  such that all bacterial phase-separation comes from activity dependence. We take  $\phi < 0$  as the shorter bacteria and  $\phi > 0$  as the longer bacteria. This is imposed by taking the phenomenological parameters  $\zeta$  and  $K$  to be dependent on the local  $\phi$  as:

$$\zeta = \begin{cases} 0.2 & \phi > 0 \\ 0.1 & \phi < 0 \end{cases} \quad (15)$$

$$K = \begin{cases} 0.09 & \phi > 0 \\ 0.05 & \phi < 0 \end{cases} \quad (16)$$

since it is well established that both orientational elasticity  $K$  and extensile activity due to division  $\zeta$  are higher for higher aspect ratios (29, 30). All equations are solved using a finite-difference method and we initialise our system by taking  $\phi = 0.01$  for radius  $R < 25$ , between  $R = 25$  and  $R = 30$   $\phi = -0.01$  and  $\phi = 0$  for  $R > 30$  in a system of size 80 by 80.

## SUPPLEMENTARY FIGURES

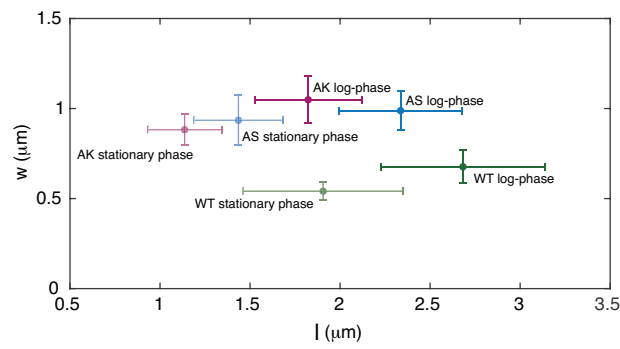


**Figure S1.** Aspect ratios for all strains used in this study. Width,  $w$ , versus length,  $l$ , of WT in both stationary phase ( $N = 32$ ) and log-phase ( $N = 39$ ), AS in both stationary phase ( $N = 47$ ) and log-phase ( $N = 38$ ), and AK in both stationary phase ( $N = 25$ ) and log-phase ( $N = 33$ ). Here stationary phase is measured directly in the overnight culture (0 h) and the log-phase 3 h after dilution (Fig. S2). The error bars are  $\pm\text{SD}$ .

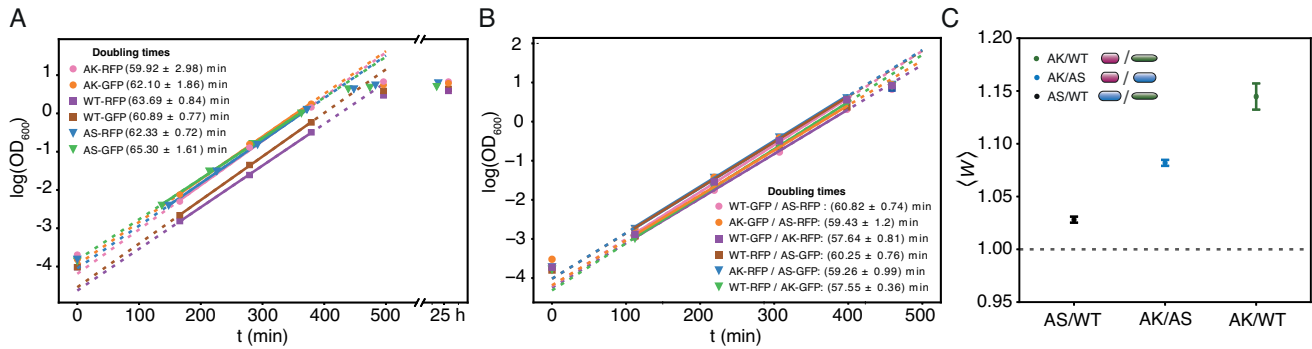


**Figure S2. A:** Growth rates for all strains used in this study. The optical density,  $OD_{600}$ , versus time,  $t$ , on a semi-logarithmic scale. The solid lines are linear fits to the data and the legends state the corresponding doubling times  $\pm$ SD. **B:** Growth rates for all strain combinations used in this study (same cultures as in (C)). The optical density,  $OD_{600}$ , versus time,  $t$ , on a semi-logarithmic scale. The solid lines are linear fits to the data and the legends state the corresponding averaged doubling times  $\pm$ SD. **C:** Pairwise competitions between all strain combinations in liquid medium (M63+glu) under constant shaking. The average fitness of the shorter strain relative to the longer,  $\langle W \rangle$ , is the ratio of doublings after 8 h averaged over the two independent cultures ( $N = 2$ ) with inverted fluorescence colouring. Error bars are  $\pm$ SD and the horizontal dashed line corresponds to equal fitness ( $\langle W \rangle = 1$ ). The trend is the same as earlier reported (3).

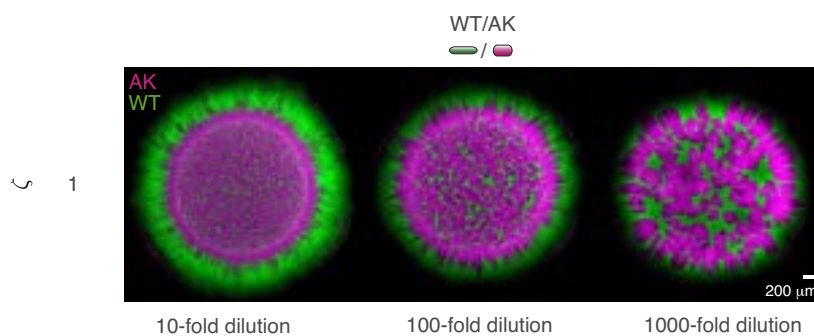


**Figure S3.** Seeding density regulates patch sizes but still the longer cell wins. Competition experiment (20 h) for serial dilutions of the optical density,  $OD_{600}$ , in a co-culture of WT and AK mixed 1:1 and diluted **A:**  $OD_{600}/10$ , **B:**  $OD_{600}/100$ , and **C:**  $OD_{600}/1000$ . For the latter, small channels of WT (green) are detectable between the patches of AK (magenta).

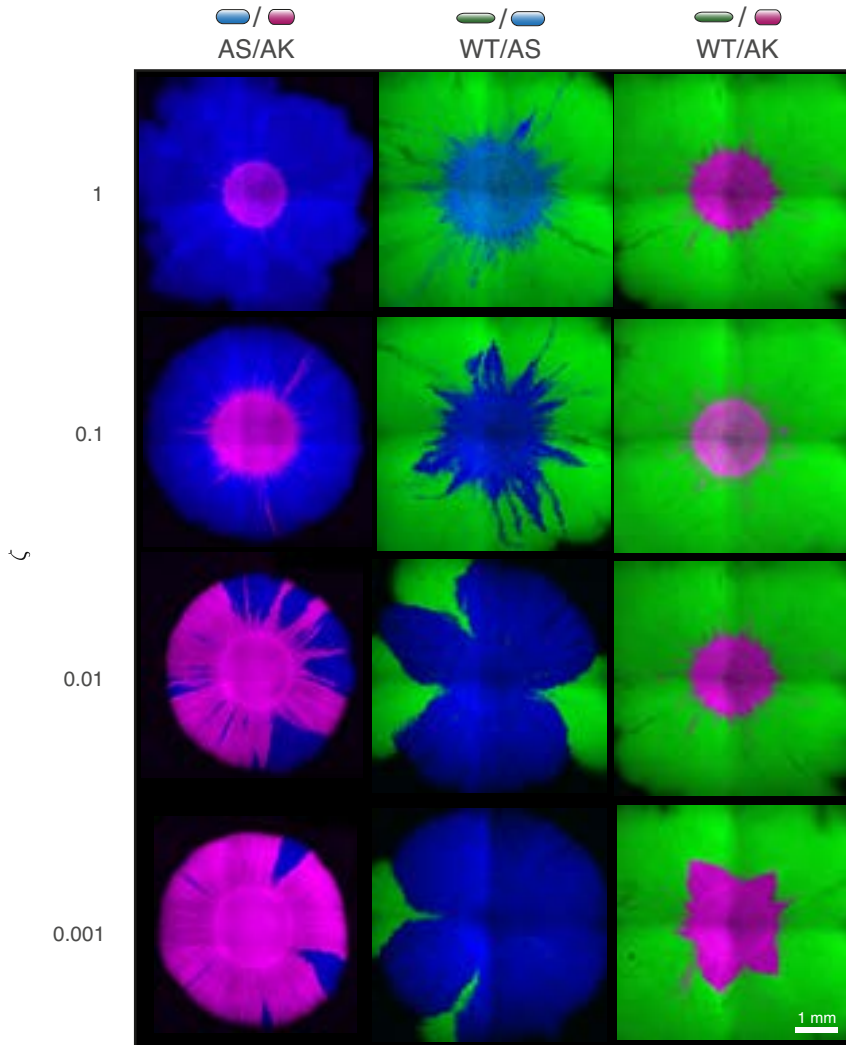


**Figure S4.** 3 days competition experiments. Fluorescence images (pseudo-coloured) example colonies (maximum intensity) z-projection from all strain combinations (AS/AK, WT/AS, WT/AK) imaged by CLSM. The scale bar corresponds to 1 mm. For WT/AK, with  $\zeta = 0.001$ , we only found 14 sectors surviving for 1.5 days (halfway from homeland to front) in 5 colonies, which closed off (i.e., sector was lost) rapidly hereafter. We note that even when the longer bacteria did not overtake the shorter within the explored time window, the sectors with longer bacteria tended to spread azimuthally with increasing  $r$ , indicating that they might eventually find their way to the expanding front.

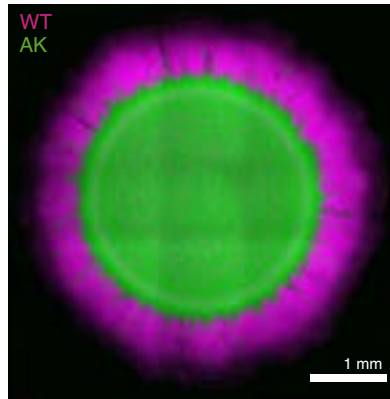


**Figure S5.** 20 h competition experiment with inverse colours. Example colonies (maximum intensity) z-projection from 1:1 ( $\zeta = 0.1$ ) WT/AK combination imaged by CLSM. The scale bar corresponds to 1 mm.

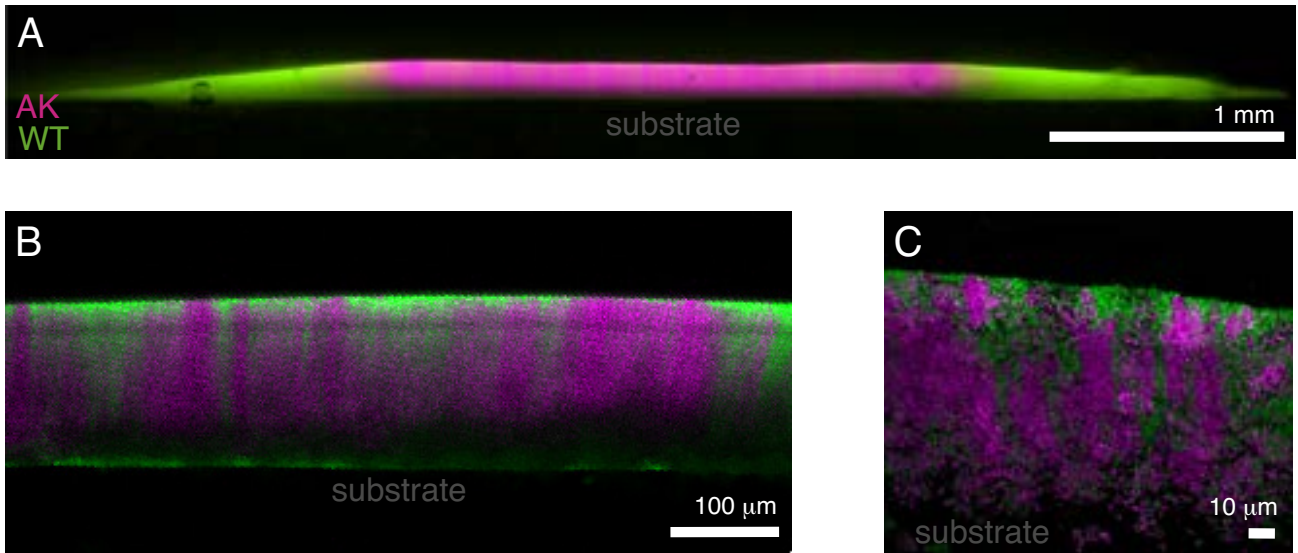


**Figure S6.** Cross-sections of 20 h competition experiments of WT (green) and AK (magenta) colonies. **A:** Example colony imaged with fluorescence microscopy and the 4× air objective. The scale bar corresponds to 1 mm. In the outer bands (i.e., outside of the homeland) the number of sectors are constant. **B-C:** Single layer of (pseudo-coloured) CLSM images from the centre of the colony using the 20× air objective and a scale bar of 100  $\mu\text{m}$  (B) and the 100× oil immersion objective and a scale bar of 10  $\mu\text{m}$  (C).

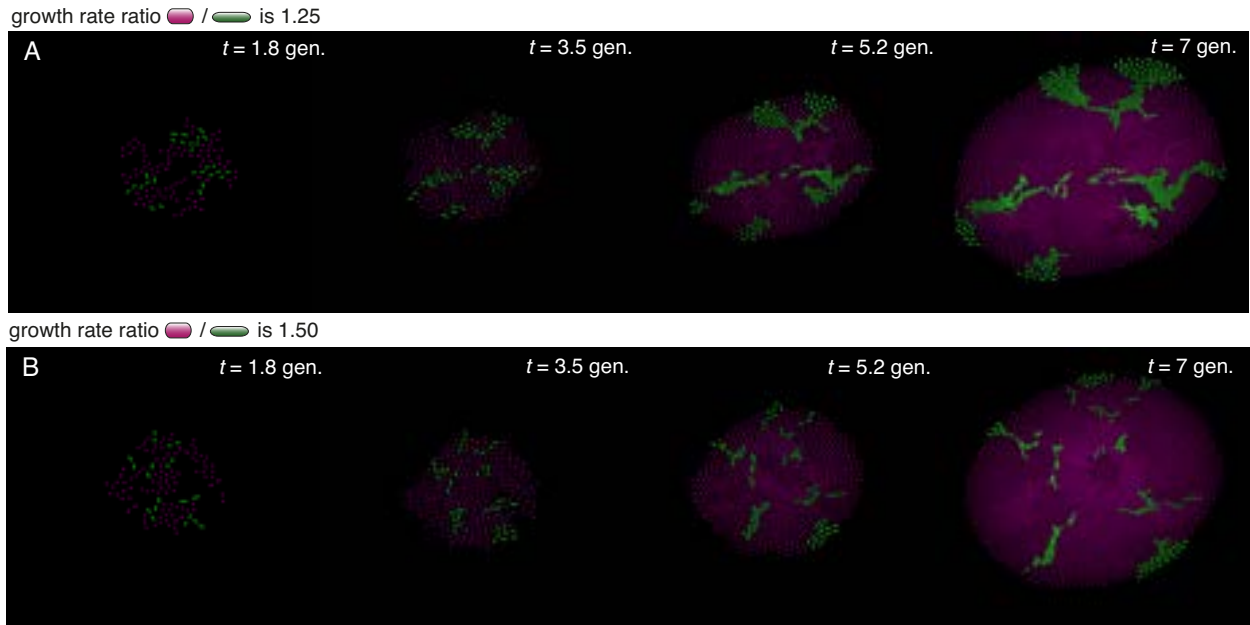


**Figure S7.** Representative snapshots of the simulation where the growth rate,  $\gamma$ , of the shorter bacteria (magenta) is faster than the longer (green). **A-B:** Representative snapshots from the simulation where shorter particles divide  $1.25\times$  (A) or  $1.5\times$  (B) faster than the longer bacteria and time is normalised with the generation time (gen) of the shorter. We remark that numbers start to dominate over mechanical interactions, such that even if the longer bacteria do overtake regions at the interface, the larger bacteria do not dominate the front, as the distance between long-dominated regions expand exponentially as smaller bacteria double (A). For even larger differences in growth rates (B), the number of shorter bacteria grows even more rapidly and the enlarged pressure in the smaller bacteria's sectors results in the longer bacteria being swapped away.

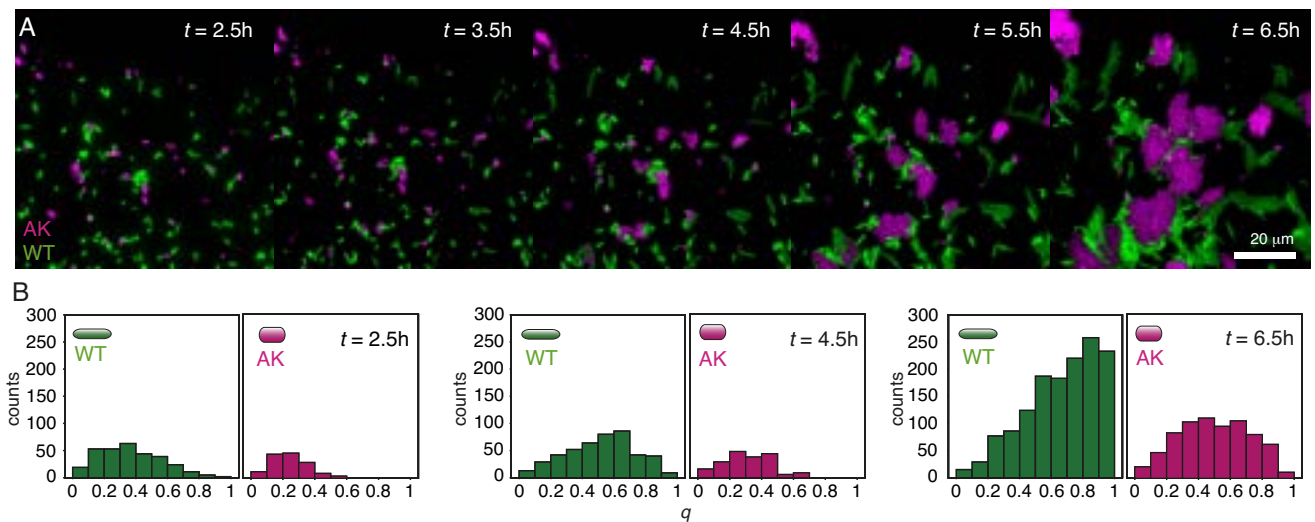


**Figure S8.** Long bacteria align more within clusters. **A:** Single cell (pseudo-coloured) time-lapses of competition between the two-colour wild-type (WT) and the *mreB* mutant (AK) at time points,  $t$ . Representative region of the larger images from which the data plotted in B was computed. The scale bar is  $20\ \mu\text{m}$ . **B:** The nematic order parameter,  $q$ , for WT and AK individually corresponding to every second time frame in (A)  $t \in \{2.5, 4.5, 6.5\}$ h.

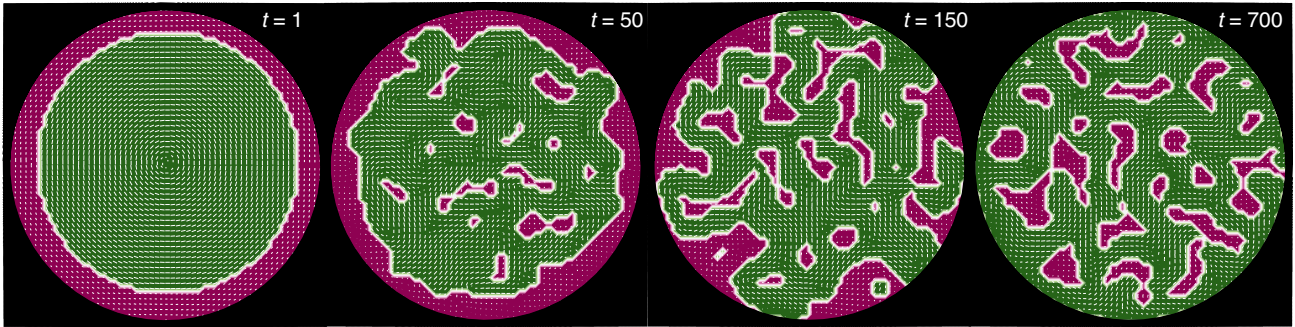


**Figure S9.** Time series of continuum dynamics where the phase representing short bacteria (magenta) starts at the edge while with time, the phase representing long bacteria (green) overtakes the short bacteria by forming pathways to the colony front.

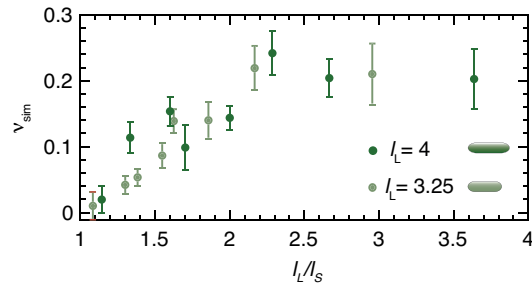


**Figure S10.** The takeover rate,  $v_{sim}$ , (slope between  $t = 30$  gen. to  $t = 45$  gen.) for varying length ratios,  $l_L/l_S$  bacteria ratios, where long bacteria still have  $w/l = 4$ .

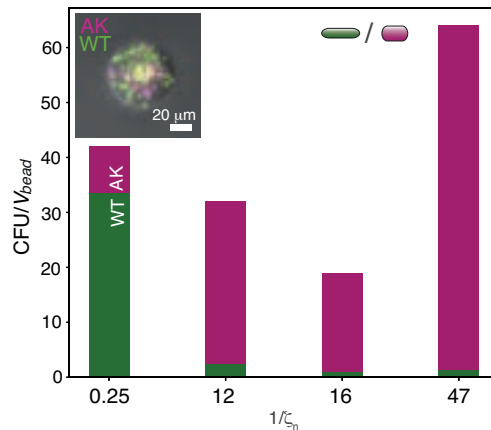


**Figure S11.** Cell concentrations in the various bead batches. The ratio of colony-forming units, CFU, versus the average bead volume,  $V_{bead}$ , for each strain ratio,  $1/\zeta_n$ . The colours indicate the fraction of WT (green) and AK (magenta). Inset: Merged image of the bright-field (grey), WT (green), and AK (magenta) of a bead with  $1/\zeta_n = 0.25$ . The scale bar corresponds to  $20 \mu\text{m}$ .

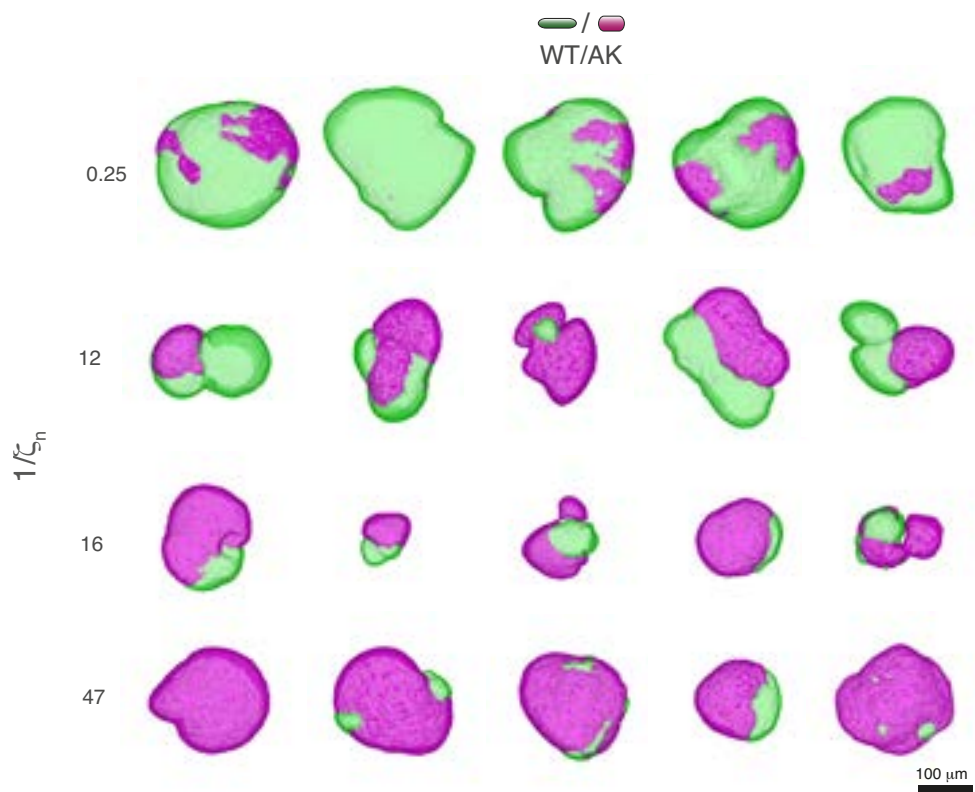


**Figure S12.** 10 h competition experiments. Example segmented masks of surfaces of two-coloured WT/AK colonies from all strain ratios imaged by CLSM. The scale bar corresponds to 100 μm.

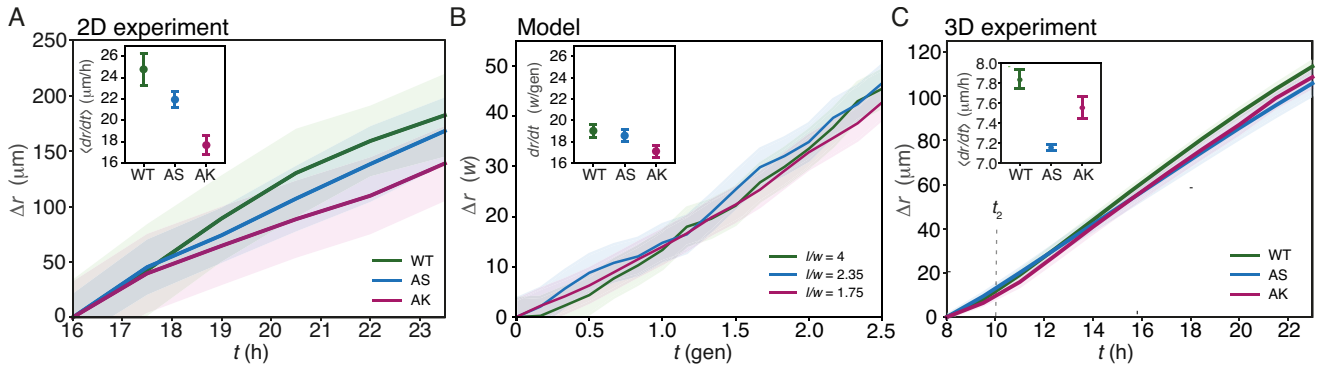


**Figure S13.** Long bacteria spread faster over substrates. **A:** Ensemble-averaged radial expansion,  $\Delta r = \langle r(t) - r(16\text{h}) \rangle$ , over time,  $t$ , of mono-strain colonies of WT ( $N = 4$ ), AS ( $N = 6$ ), and AK ( $N = 5$ ) on agar (1.5%) substrate (M63+glu). The shaded regions correspond to  $\pm$ SEM. Inset: The ensemble-averaged expansion rates,  $\langle dr/dt \rangle$ , are linear fits of the data and the error bars are  $\pm$ CI. **B:** Ensemble-averaged radial expansion,  $\Delta r = \langle r(t) - r(0) \rangle$ , of simulation data from mono-strain inoculations of cells with aspect ratios:  $l/w \in \{4, 2.35, 1.75\}$ .  $N = 10$  colonies for each  $l/w$ . The shaded regions correspond to  $\pm$ SEM. Inset: The ensemble-averaged expansion rates,  $\langle dr/dt \rangle$ , in number of cell widths,  $w$ , per generations (gen) are linear fits of the data and the error bars are  $\pm$ CI. To compare (A) and (B), 1 gen is approximately 1 h and  $w$  slightly less than 1  $\mu\text{m}$ . **C:** 3D radial growth of mono-clonal single strain colonies. Ensemble-averaged radial expansion,  $\Delta r = \langle r(t) - r(8\text{h}) \rangle$ , versus time,  $t$ , for WT ( $N = 5$ ), AS ( $N = 6$ ), and AK ( $N = 6$ ). The shaded regions correspond to  $\pm$ SEM and the vertical punctuated line to  $t_2 = 10$  h. The inset is the ensemble-averaged slopes of the linear fits,  $\langle dr/dt \rangle$ , and the error bars are  $\pm$ CI.

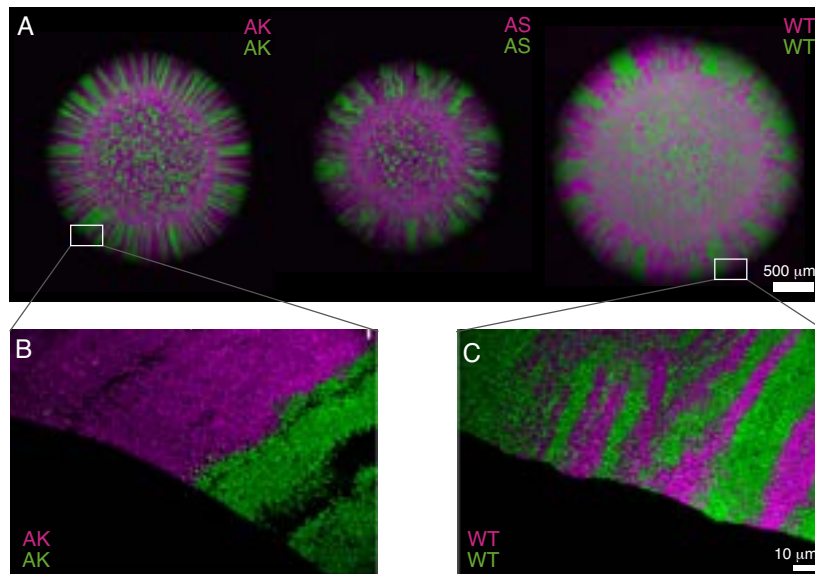


**Figure S14.** Segmentation patterns varies with genotype. **A:** The (maximum intensity) z-projections of example colonies (WT/WT, AS/AS, and AK/AK) imaged by CLSM after incubation (20 h). The scale bar corresponds to 500  $\mu\text{m}$ . In the outer bands (i.e., outside of the homeland) the number of sectors are constant. Despite the general features, qualitative differences among the strains are clear: WT's sector boundaries are coarse (highly diffusive) and the mutants have straighter (less diffusive) boundaries. **B-C:** Single layer (pseudo-coloured) images of competition between the two-colours at the front of the colony: The  *mreB* mutant (AK/AK) in (B) and wild-type (WT/WT) in (C). The scale bar is 10  $\mu\text{m}$ .

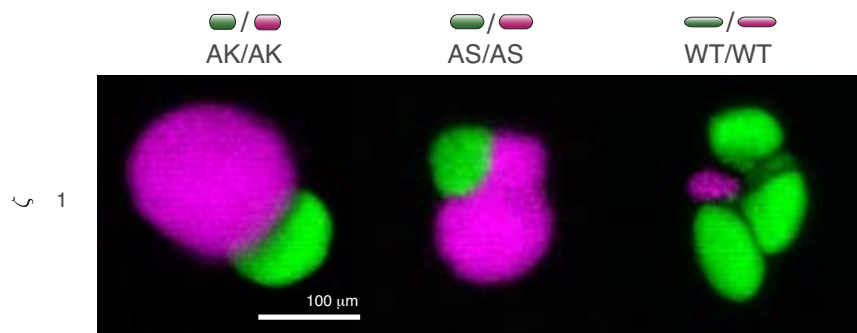


**Figure S15.** 10 h competition experiments. Example colonies (maximum intensity) z-projection from two-coloured strains colonies from all same strain ratios imaged by CLSM. The scale bar corresponds to 100 μm.

## MOVIE LEGENDS

### Movie 1

Long bacteria align over time with their neighbours and the expanding front. Time-lapse snapshots from (pseudo-coloured) fluorescence competition experiments between WT (green) and the *mreB* mutant AK (magenta), every 30 min, starting 1.5 h after inoculation.

### Movie 2

Another example of how long bacteria align over time with their neighbours and the expanding front. Time-lapse snapshots from (pseudo-coloured) fluorescence competition experiments between WT (green) and the *mreB* mutant AK (magenta), every 30 min, starting 1.5 h after inoculation.

### Movie 3

360° rotation view of a segmented mask of a 3D WT/AK colony surface. This mask is extracted from the first ( $1/\zeta_n = 0.25$ ) image in Figure 4B. The scale bar corresponds to 100  $\mu\text{m}$ .

## REFERENCES

1. Studier, F. W., P. Daegelen, R. E. Lenski, S. Maslov, and J. F. Kim, 2009. Understanding the Differences between Genome Sequences of Escherichia coli B Strains REL606 and BL21(DE3) and Comparison of the E. coli B and K-12 Genomes. *Journal of Molecular Biology* 394:653–680. <https://linkinghub.elsevier.com/retrieve/pii/S0022283609011383>.
2. Wachi, M., and M. Matsushashi, 1989. Negative control of cell division by *mreB*, a gene that functions in determining the rod shape of Escherichia coli cells. *Journal of Bacteriology* 171:3123–3127. <https://journals.asm.org/doi/10.1128/jb.171.6.3123-3127.1989>.
3. Monds, R. D., T. K. Lee, A. Colavin, T. Ursell, S. Quan, T. F. Cooper, and K. C. Huang, 2014. Systematic Perturbation of Cytoskeletal Function Reveals a Linear Scaling Relationship between Cell Geometry and Fitness. *Cell Reports* 9:1528–1537. <https://doi.org/10.1016/j.celrep.2014.10.040>.
4. Erickson, H. P., 2001. Evolution in bacteria. *Nature* 413:30–30. <https://www.nature.com/articles/35092655>.
5. Kruse, T., J. Bork-Jensen, and K. Gerdes, 2005. The morphogenetic MreBCD proteins of Escherichia coli form an essential membrane-bound complex. *Molecular Microbiology* 55:78–89. <https://onlinelibrary.wiley.com/doi/10.1111/j.1365-2958.2004.04367.x>.
6. Ursell, T. S., J. Nguyen, R. D. Monds, A. Colavin, G. Billings, N. Ouzounov, Z. Gitai, J. W. Shaevitz, and K. C. Huang, 2014. Rod-like bacterial shape is maintained by feedback between cell curvature and cytoskeletal localization. *Proceedings of the National Academy of Sciences* 111:E1025–E1034. <https://pnas.org/doi/full/10.1073/pnas.1317174111>.
7. Ouzounov, N., J. P. Nguyen, B. P. Bratton, D. Jacobowitz, Z. Gitai, and J. W. Shaevitz, 2016. MreB Orientation Correlates with Cell Diameter in Escherichia coli. *Biophysical Journal* 111:1035–1043. <https://linkinghub.elsevier.com/retrieve/pii/S000634951630580X>.
8. Smith, W. P. J., Y. Davit, J. M. Osborne, W. D. Kim, K. R. Foster, and J. M. Pitt-Francis, 2017. Cell morphology drives spatial patterning in microbial communities. *Proceedings of the National Academy of Sciences* 114:E280–E286. <http://www.pnas.org/lookup/doi/10.1073/pnas.1613007114https://doi.org/10.1073/pnas.1613007114>.
9. Lenski, R. E., M. R. Rose, S. C. Simpson, and S. C. Tadler, 1991. Long-Term Experimental Evolution in Escherichia coli. I. Adaptation and Divergence During 2,000 Generations. *The American Naturalist* 138:1315–1341. <https://www.jstor.org/stable/2462549>.
10. White, S., J. Quinn, J. Enzor, J. Staats, S. M. Mosier, J. Almarode, T. N. Denny, K. J. Weinhold, G. Ferrari, and C. Chan, 2021. FlowKit: A Python Toolkit for Integrated Manual and Automated Cytometry Analysis Workflows. *Frontiers in Immunology* 12. <https://www.frontiersin.org/articles/10.3389/fimmu.2021.768541/full>.
11. McInnes, L., J. Healy, and S. Astels, 2017. hdbSCAN: Hierarchical density based clustering. *The Journal of Open Source Software* 2:205. <http://joss.theoj.org/papers/10.21105/joss.00205>.

12. Preibisch, S., S. Saalfeld, and P. Tomancak, 2009. Globally optimal stitching of tiled 3D microscopic image acquisitions. Bioinformatics 25:1463–1465. <https://academic.oup.com/bioinformatics/article/25/11/1463/332497>.
13. van den Berg, N., 2023. Experimental study of bacterial cell shape's role in competition: elongated cells win in expanding mixed communities. Ph.D. thesis, University of Copenhagen, Copenhagen. [https://nbi.ku.dk/english/theses/masters-theses/nathanael-van-den-berg/Nath\\_na\\_1\\_van\\_den\\_Berg.pdf](https://nbi.ku.dk/english/theses/masters-theses/nathanael-van-den-berg/Nath_na_1_van_den_Berg.pdf).
14. Hallatschek, O., P. Hersen, S. Ramanathan, and D. R. Nelson, 2007. Genetic drift at expanding frontiers promotes gene segregation. Proceedings of the National Academy of Sciences 104:19926–19930. <https://pnas.org/doi/full/10.1073/pnas.0710150104>.
15. Eigentler, L., M. Kalamara, G. Ball, C. E. MacPhee, N. R. Stanley-Wall, and F. A. Davidson, 2022. Founder cell configuration drives competitive outcome within colony biofilms. The ISME Journal 16:1512–1522. <https://www.nature.com/articles/s41396-022-01198-8>.
16. van Gestel, J., F. J. Weissing, O. P. Kuipers, and Á. T. Kovács, 2014. Density of founder cells affects spatial pattern formation and cooperation in *Bacillus subtilis* biofilms. The ISME Journal 8:2069–2079. <https://www.nature.com/articles/ismej201452><https://academic.oup.com/ismej/article/8/10/2069-2079/7582470>.
17. Vázquez, A. G., N. Mitarai, and L. Jauffred, 2024. Genetic mixing and demixing on expanding spherical frontiers. ISME Communications <https://academic.oup.com/ismecommun/advance-article/doi/10.1093/ismeco/ycae009/7585292>.
18. García Vázquez, A., T. T. Nguyen, N. Mitarai, and L. Jauffred, 2024. Cell encapsulation in inoculation beads for 3D growth experiments. ProtocolExchange <https://protocolexchange.researchsquare.com/article/pex-2531/v1>.
19. Hartmann, R., H. Jeckel, E. Jelli, P. K. Singh, S. Vaidya, M. Bayer, D. K. H. Rode, L. Vidakovic, F. Díaz-Pascual, J. C. N. Fong, A. Dragoš, O. Lamprecht, J. G. Thöming, N. Netter, S. Häussler, C. D. Nadell, V. Sourjik, Á. T. Kovács, F. H. Yildiz, and K. Drescher, 2021. Quantitative image analysis of microbial communities with BiofilmQ. Nature Microbiology 6:151–156. <https://www.nature.com/articles/s41564-020-00817-4>.
20. Schindelin, J., I. Arganda-Carreras, E. Frise, V. Kaynig, M. Longair, T. Pietzsch, S. Preibisch, C. Rueden, S. Saalfeld, B. Schmid, J.-Y. Tinevez, D. J. White, V. Hartenstein, K. Eliceiri, P. Tomancak, and A. Cardona, 2012. Fiji: an open-source platform for biological-image analysis. Nature Methods 9:676–682. <https://www.nature.com/articles/nmeth.2019>.
21. Cordero, M., N. Mitarai, and L. Jauffred, 2023. Motility mediates satellite formation in confined biofilms. The ISME Journal 17:1819–1827. <https://www.nature.com/articles/s41396-023-01494-x>.
22. Meacock, O. J., A. Doostmohammadi, K. R. Foster, J. M. Yeomans, and W. M. Durham, 2021. Bacteria solve the problem of crowding by moving slowly. Nature Physics 17:205–210. <http://dx.doi.org/10.1038/s41567-020-01070-6><https://www.nature.com/articles/s41567-020-01070-6>.
23. Hamilton, W., 1971. Geometry for the selfish herd. Journal of Theoretical Biology 31:295–311. <https://linkinghub.elsevier.com/retrieve/pii/0022519371901895>.
24. Matyjaszkiewicz, A., G. Fiore, F. Annunziata, C. S. Grierson, N. J. Savery, L. Marucci, and M. di Bernardo, 2017. BSim 2.0: An Advanced Agent-Based Cell Simulator. ACS Synthetic Biology 6:1969–1972. <https://pubs.acs.org/doi/10.1021/acssynbio.7b00121>.
25. Gutiérrez, M., P. Gregorio-Godoy, G. Pérez del Pulgar, L. E. Muñoz, S. Sáez, and A. Rodríguez-Patón, 2017. A New Improved and Extended Version of the Multicell Bacterial Simulator gro. ACS Synthetic Biology 6:1496–1508. <https://pubs.acs.org/doi/10.1021/acssynbio.7b00003>.
26. De Gennes, P.-G., and J. Prost, 1993. The physics of liquid crystals. 83. Oxford university press.
27. Oza, A. U., and J. Dunkel, 2016. Antipolar ordering of topological defects in active liquid crystals. New Journal of Physics 18:093006. <https://iopscience.iop.org/article/10.1088/1367-2630/18/9/093006>.

28. Dell'Arciprete, D., M. L. Blow, A. T. Brown, F. D. C. Farrell, J. S. Lintuvuori, A. F. McVey, D. Marenduzzo, and W. C. K. Poon, 2018. A growing bacterial colony in two dimensions as an active nematic. *Nature Communications* 9:4190. <http://dx.doi.org/10.1038/s41467-018-06370-3><https://www.nature.com/articles/s41467-018-06370-3>.
29. Kröger, M., and P. Ilg, 2007. Derivation of Frank-Ericksen elastic coefficients for polydomain nematics from mean-field molecular theory for anisotropic particles. *The Journal of Chemical Physics* 127. <https://pubs.aip.org/jcp/article/127/3/034903/904677/Derivation-of-Frank-Ericksen-elastic-coefficients>.
30. Wittmann, R., G. H. P. Nguyen, H. Löwen, F. J. Schwarzendahl, and A. Sengupta, 2023. Collective mechano-response dynamically tunes cell-size distributions in growing bacterial colonies. *Communications Physics* 6:331. <https://www.nature.com/articles/s42005-023-01449-w>.

### **A.3 Indirect antibiotic resistance enhances colony tolerance in mixed bacterial communities**

**Authors:** Mireia Cordero<sup>1</sup>, Artemis Talliou<sup>1</sup>, Brage Haldor Thomsen<sup>1</sup>, Adrien Sarlet<sup>1</sup>, Namiko Mitarai<sup>1</sup> and Liselotte Jauffred<sup>1</sup>

**Affiliations:** <sup>1</sup>Niels Bohr Institute, University of Copenhagen, Copenhagen 2100, Denmark

**Status:** In preparation

**My contributions:** I conceived the original idea alongside NM and LJ. I also performed experiments and computational simulations. I am currently working on the article.

## Article

# Indirect antibiotic resistance enhances colony tolerance in mixed bacterial communities

Mireia Cordero<sup>1</sup>, Artemis Talliou<sup>1</sup>, Brage Haldor Thomsen<sup>1</sup>, Adrien Sarlet<sup>1</sup>, Namiko Mitarai<sup>1</sup>, and Liselotte Jauffred<sup>1</sup>

<sup>1</sup>The Niels Bohr Institute, University of Copenhagen, Blegdamsvej 17, DK-2100 Copenhagen O, Denmark

<sup>1</sup>Correspondence: mitarai@nbi.ku.dk, jauffred@nbi.ku.dk

**Keywords:** Biofilm, *Escherichia coli*, range expansion, spatio-genetic patterning, antibiotic resistance, antibiotic tolerance

## ABSTRACT

As cells in bacterial communities grow and divide, the community as a whole enlarges, a process referred to as *range expansion*. These communities are associated with strong mutualism and, even more often (1), competition for scarce nutrients and space. Competition is, therefore, an important driving force of evolution (2) and will result in strong segregation of sub-populations. Ultimately, only a few lineages from the initially well-mixed population will survive, and cell-cell mechanics govern the resulting pattern on the microscale and strong stochasticity. This has been investigated extensively in surface-attached colonies (e.g., (3, 4), but see Ref. (5) for a review). However, it is often difficult to identify the microscopic effects giving rise to emergent properties of bacterial communities.

Nonetheless, bacterial communities are not solely formed by competition but also through the interactions between cells, mediated through the degradation of a toxin, like antibiotics. Overall, there are two classes of antibiotics: bacteriocidal (i.e., kills) and bacteriostatic (i.e., pauses growth). Furthermore, the resistance against the antibiotics relies on a broad set of mechanisms but can roughly be either intra- or extracellular. Based on these different antibiotics and according to cell responses, cells can be classified as egoistic (i.e., only helping themselves) or altruistic (i.e., causing local depletion of antibiotics). Therefore, we can imagine all kinds of different resulting community compositions under varying antibiotic concentrations. But we need to control and manage these bacterial communities to address the escalating antibiotic crisis (6, 7). There is a variety of experiments suggesting cooperation among bacteria resistant to antibiotics and susceptible bacteria (e.g., Refs. (8) and (9)). These studies did not explicitly consider the spatial organisation and proximity of populations. Therefore, the stochastic nature of 'survival' in a spatially structured environment is, as yet, still overlooked.

Here, we investigate how spatial organisation controls the survival of bacteria susceptible to antibiotics in a hostile environment with otherwise lethal levels of antibiotics. We show cooperativity in well-mixed co-cultures of susceptible and resistant *E. coli* bacteria under varying antibiotic concentrations. Specifically, we show how bacteria resistant to a bacteriostatic antibiotic can deplete the environment enough to protect susceptible cells.

## MATERIALS AND METHODS

### Cell culture

**Bacterial strains** We used the strains of *E. coli* MG1655 listed in Table 1 with red (mCherry) and green fluorescent protein (GFP).

Name	Strain	Specifications	MIC ( $\mu\text{g}/\mu\text{l}$ )	Ref.
Res1	TSS290	SLS4223::lacZYA (no GFP, CAT)		This study
Sen1	SLS4223	MAS1081 (no GFP, no CAT)	1	This study
Sen4	SP427	MC4100: GFP	3	(10)
Res2	TB194	MG1655: mCherry, CAT	> 256	(11)
Res3	TB193	MG1655: sfGFP, CAT	> 256	(11)
Sen2	TB204	MG1655: sfGFP	8	(12)
Sen3	TB205	MG1655: mCherry	8	(12)

Table 1: List of *E. coli* K-12 strains used in this study and their measured MIC values in Cm ( $\mu\text{g}/\mu\text{l}$ ).

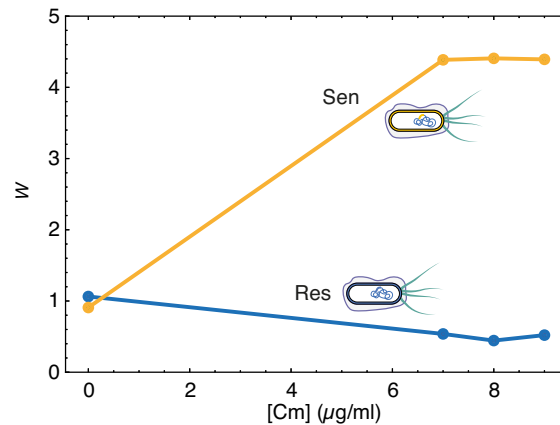


Figure 1: **Indirect resistance enhances the fitness of sensitive bacteria.** Pairwise competitions between all strain combinations in liquid medium (LB) under constant shaking. Relative fitness,  $W$ , of the Res (blue) and Sen (yellow) in co-culture with respect to the same strains in monocultures under different Cm concentrations is the ratio of doublings after 6 h.  $W = 1$  corresponds to equal fitness.

**Culture medium** We used rich Luria-Bertani (LB) composed of 10 g/l Gibco™ Bacto™ tryptone (16279751, Fisher Scientific), 5 g/l Gibco™ Bacto™ yeast extract (16279781, Fisher Scientific) and 5 g/l NaCl ( $\geq 99\%$ , S9888, Sigma-Aldrich) dissolved in Millipore water.

**Minimum Inhibitory Concentration** We found the Minimum Inhibitory Concentration (MIC) by spreading 200  $\mu$ l of cell culture ( $OD_{600} = 0.2$ ) on LB agar plates and carefully placing an E-TEST strip on top (Biomerieux, France). The plates were incubated for 20 hours ( $37^\circ\text{C}$ ) before reading off the value, at which growth was halted 1.

## Competition in liquid co-cultures

**OD characterisation** Overnight cultures (Res+Sen) were diluted to  $OD_{600}$  of 0.1 in fresh LB together with the co-culture mixed 1:1 (combined  $OD_{600} = 0.1$ ). These cultures were incubated under various Cm concentrations.

**OD and CFU characterization** Regularly ( $\sim 1/45 \text{ min}^{-1}$ ), we measured the  $OD_{600}$  (IMPLEN NanoPhotometer C40) was acquired every 45 minutes. In a parallel - but independent study - we estimated the number of doublings over the entire time range (6 h) by measuring the CFUs from cell culture right after dilution ( $t = 0$ ) and then again at  $t = 6$  h. The initial number of cells,  $N(0)$ , in all three samples, was  $\sim 5 \cdot 10^8/\text{ml}$ .

**Flow cytometry characterisation** Overnight cultures were grown in an LB liquid medium. The  $OD_{600}$  of the overnight cultures was measured, and the strains were mixed in equal proportions and diluted  $100\times$  in LB. Cultures were incubated at  $37^\circ\text{C}$  and cell counts (50000 counts per sample) were measured right after mixing and again after 6 h of incubation, using a BD FACSJazz Cell Sorter (BD Biosciences, cat. no. 655490). Data were processed using the Flowkit package (13) with a *hyper-log* transformation and clustered with the *hdbscan* algorithm (14). After clustering, we extracted the counts of the two main clusters and defined the frequencies of the two populations as the ratio of cell counts of one population over the cell counts of both.

**Doublings** The fitness of a strain under given environmental conditions can be quantified as the number of doublings,  $D$ , over a given period, which is:

$$D(t) = \log_2 \left( \frac{N(t)}{N(0)} \right), \quad (1)$$

where  $N(t)$  is the number of cells at time,  $t$ , and  $N(0)$  then is the initial number of cells.

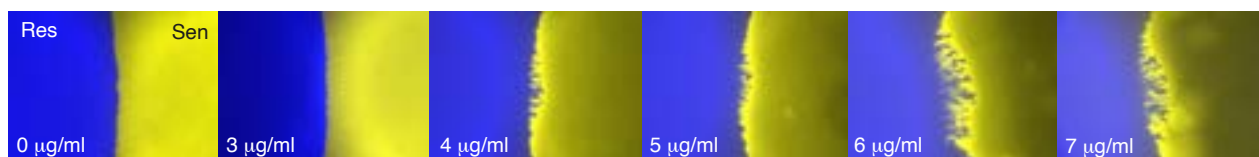


Figure 2: **Local de-toxification enhances the fitness of sensitive strains.** Images of the colliding front between two mono-culture colonies inoculated on an agar surface with varying concentrations of Cm (see legends) and incubated for 24 h.

**Relative fitness** The relative fitness,  $W_{ij}$ , of strain  $i$  with respect to strain  $j$  is estimated here as the ratio of the number of doublings of the two competitors (i.e., identical to the ratio of their Malthusian parameters) (15) and follows directly from Eq. 1:

$$W_{ij} = \frac{D_i}{D_j} = \frac{\ln(N_i(t)/N_i(0))}{\ln(N_j(t)/N_j(0))}, \quad (2)$$

where  $N_i(t)/N_i(0)$  and  $N_j(t)/N_j(0)$  are the ratios of the number of cells relative to the starting point of strains  $i$  and  $j$ , respectively. These ratios are obtained by multiplying the ratio of frequencies (i.e., at  $t = 6$  h relative to  $t = 0$ ) with the dilution factor, which in our case was  $100\times$ .

## Competition in surface-attached colonies

Overnight cultures were mixed in a 1:1 ratio to an  $OD_{600} = 0.3$ . We inoculated  $1 \mu\text{l}$  on agar plates with various Cm concentrations and incubated for 48 h ( $37^\circ\text{C}$ ). To measure the ratios of resistant to sensitive bacteria, we pipetted  $\sim 10 \mu\text{l}$ , from the centre of the colony, and resuspended in an isotonic buffer of 0.9% NaCl. Then, we removed the centre of the colony by poking a glass tube and sampled the edge by scraping the rest with an inoculation loop and resuspending in 0.9% NaCl. The cell solutions were plated, incubated, and sub-sequentially, CFUs were counted.

## Collision experiment

Overnight cultures (Res2 and Sen2) were diluted in LB to an  $OD_{600}$  of 0.3, and two droplets of  $0.5 \mu\text{l}$  were inoculated side by side with a distance of 100-500  $\mu\text{m}$  on LB agar plates with various Cm concentrations and incubated for 24 h.

**Imaging** Colliding colonies were imaged using an inverted fluorescent microscope (Nikon ECLIPSE Ti microscope) paired with a 4x air objective (Nikon, Plan Fluor, 4x/0.13,  $\infty/1.2$  WD 16.5). The fluorescent signals were sequentially excited and recorded using a Hg lamp, FITC (480/40 nm) and Texas Red (560/40 nm) cubes in combination with a camera (Andor Neo). Pre-processing and thresholding were done with Fiji ImageJ (16).

**Intensity gradient** Intensity profiles were obtained using the Plot Profile tool by taking the average intensity profiles over 5 lines (a single pixel wide and a length of 1000  $\mu\text{m}$ ) over the collision interface.

**Intermixing and straightness indices** Following the terminology of Johnson and co-workers (17).

## RESULTS

### Indirect resistance enhances the fitness of sensitive bacteria

For this, we used a set of strains of *E. coli*, the wild-type (Sen) and the otherwise heterogenic strain with the CAT gene, coding for resistance to chloramphenicol (Cm). In measuring the amount of exploitation of Res by Sen, we prepared a set of diluted, liquid mono-cultures of the Res and Sen strains as well as co-cultures mixed 1:1 in LB with various Cm concentrations (0-9  $\mu\text{g/ml}$ ). The numbers of cells in all these cultures at time  $t = 0$  and  $t = 6$  h were measured using flow cytometry, and the relative fitness,  $W$ , as defined in Eq. 2, was estimated by comparing a strain's (Res or Sen) abundance in the co-culture to the respective strain in the mono-culture. The results are shown in Fig 1 show similar fitness of Res and Sen ( $\sim 1$ ) in an environment with no antibiotics and that this changes considerably Sen when antibiotic levels rise. Here, Sen grows  $>300\%$  better when co-cultured with Res. In contrast, Res has a slight disadvantage from being exploited by Res. Thus, the relative

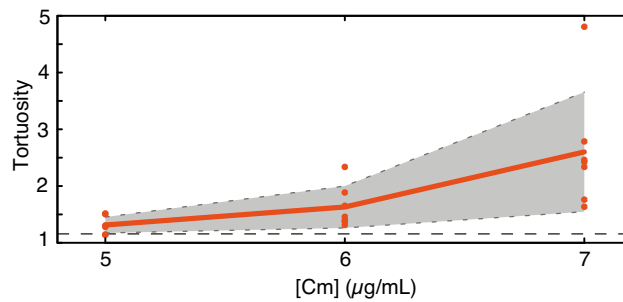


Figure 3: **The collision interface becomes more tortuous at higher antibiotic levels.** The tortuosity of interfaces between Sen and Res at varying Cm levels, where 1 is a straight line, and the dashed horizontal line corresponds to the tortuosity at [Cm]=0.

fitness of Sen is high in an environment where the detoxification of Cm is global, in the sense that diffusion is fast and the environment is homogeneous. Therefore, we next set out to investigate this indirect resistance in a structured environment.

### Local de-toxification enhances the fitness of sensitive bacteria

In order to investigate the dependence of Sen (yellow) to Res (blue) in a structured environment, we let Res and Sen mono-clonal colonies collide through range expansion on an agar surface under varying concentrations of Cm. Res and Sen collided frontally and mixed, and the resulting interfaces are shown in Fig. 2, and we find that the populations of Res and Sen become more and more intertwined along the interface. To quantify this, we measured the tortuosity (i.e., the inverse straightness) at varying Cm levels, as shown in Fig. 3, and found that the collision front becomes longer when antibiotic levels are raised.

## DISCUSSION

The spatial patterning emerging in surface-associated microbial colonies depends on the dominant interactions within the system. Therefore, we argue that general expectations regarding how the patterning regulates the colonies' antibiotic tolerance may not be reliable. Instead, the determinants have to be identified one by one.

Thus, an important outcome of our study is the establishment of a causal pathway between local antibiotic degradation, spatial organisation, and colony tolerance.

## AUTHOR CONTRIBUTIONS

MC, NM, and LJ conceived the original idea. MC, AT, and LJ performed liquid culture experiments. AS and AT performed surface-attached colony experiments. BHT and MC performed IBM and array-based models. NM and LJ supervised the project.

## FUNDING

This work was supported by the Danish National Research Foundation grant no. DFF 0165-00032B and grant no. DFF 0165-00103B (LJ), the Novo Nordisk Foundation NERD grant no. NNF21OC0068775 (NM) and Synergy grant no. NNF23OC0086712 (LJ).

## REFERENCES

- Palmer, J. D., and K. R. Foster, 2022. Bacterial species rarely work together. *Science* 376:581–582. <https://www.science.org/doi/10.1126/science.abn5093>.
- Ghoul, M., and S. Mitri, 2016. The Ecology and Evolution of Microbial Competition. *Trends in Microbiology* 24:833–845. <https://linkinghub.elsevier.com/retrieve/pii/S0966842X16300749>.
- Hallatschek, O., P. Hersen, S. Ramanathan, and D. R. Nelson, 2007. Genetic drift at expanding frontiers promotes gene segregation. *Proceedings of the National Academy of Sciences* 104:19926–19930. <https://pnas.org/doi/full/10.1073/pnas.0710150104>.
- Lee, H., J. Gore, and K. S. Korolev, 2022. Slow expanders invade by forming dented fronts in microbial colonies. *Proceedings of the National Academy of Sciences* 119:e2108653119. <https://pnas.org/doi/full/10.1073/pnas.2108653119>.

5. Eigentler, L., F. A. Davidson, and N. R. Stanley-Wall, 2022. Mechanisms driving spatial distribution of residents in colony biofilms: an interdisciplinary perspective. *Open Biology* 12:220194. <https://royalsocietypublishing.org/doi/10.1098/rsob.220194>.
6. Castañeda-Barba, S., E. M. Top, and T. Stalder, 2024. Plasmids, a molecular cornerstone of antimicrobial resistance in the One Health era. *Nature Reviews Microbiology* 22:18–32. <https://www.nature.com/articles/s41579-023-00926-x>.
7. Ciofu, O., C. Moser, P. Á. Jensen, and N. Højby, 2022. Tolerance and resistance of microbial biofilms. *Nature Reviews Microbiology* 20:621–635. <https://www.nature.com/articles/s41579-022-00682-4>.
8. Frost, I., W. P. J. Smith, S. Mitri, A. S. Millan, Y. Davit, J. M. Osborne, J. M. Pitt-Francis, R. C. MacLean, and K. R. Foster, 2018. Cooperation, competition and antibiotic resistance in bacterial colonies. *The ISME Journal* 12:1582–1593. <https://academic.oup.com/ismej/article/12/6/1582/7475455>.
9. Sharma, A., and K. B. Wood, 2021. Spatial segregation and cooperation in radially expanding microbial colonies under antibiotic stress. *The ISME Journal* 15:3019–3033. <https://academic.oup.com/ismej/article/15/10/3019/7474415>.
10. Bahl, M. L., S. J. Sørensen, and L. Hestbjerg Hansen, 2004. Quantification of plasmid loss in *Escherichia coli* cells by use of flow cytometry. *FEMS Microbiology Letters* 232:45–49. [https://academic.oup.com/femsle/article-lookup/doi/10.1016/S0378-1097\(04\)00015-1](https://academic.oup.com/femsle/article-lookup/doi/10.1016/S0378-1097(04)00015-1).
11. Manna, M. S., Y. T. Tamer, I. Gaszek, N. Poulides, A. Ahmed, X. Wang, F. C. R. Toprak, D. R. Woodard, A. Y. Koh, N. S. Williams, D. Borek, A. R. Atilgan, J. D. Hulleman, C. Atilgan, U. Tambar, and E. Toprak, 2021. A trimethoprim derivative impedes antibiotic resistance evolution. *Nature Communications* 12:2949. <https://www.nature.com/articles/s41467-021-23191-z>.
12. Tomasek, K., T. Bergmiller, and C. C. Guet, 2018. Lack of cations in flow cytometry buffers affect fluorescence signals by reducing membrane stability and viability of *Escherichia coli* strains. *Journal of Biotechnology* 268:40–52. <https://linkinghub.elsevier.com/retrieve/pii/S0168165618300166>.
13. White, S., J. Quinn, J. Enzor, J. Staats, S. M. Mosier, J. Almarode, T. N. Denny, K. J. Weinhold, G. Ferrari, and C. Chan, 2021. FlowKit: A Python Toolkit for Integrated Manual and Automated Cytometry Analysis Workflows. *Frontiers in Immunology* 12. <https://www.frontiersin.org/articles/10.3389/fimmu.2021.768541/full>.
14. McInnes, L., J. Healy, and S. Astels, 2017. hdbSCAN: Hierarchical density based clustering. *The Journal of Open Source Software* 2:205. <http://joss.theoj.org/papers/10.21105/joss.00205>.
15. Lenski, R. E., M. R. Rose, S. C. Simpson, and S. C. Tadler, 1991. Long-Term Experimental Evolution in *Escherichia coli*. I. Adaptation and Divergence During 2,000 Generations. *The American Naturalist* 138:1315–1341. <https://www.jstor.org/stable/2462549>.
16. Schindelin, J., I. Arganda-Carreras, E. Frise, V. Kaynig, M. Longair, T. Pietzsch, S. Preibisch, C. Rueden, S. Saalfeld, B. Schmid, J.-Y. Tinevez, D. J. White, V. Hartenstein, K. Eliceiri, P. Tomancak, and A. Cardona, 2012. Fiji: an open-source platform for biological-image analysis. *Nature Methods* 9:676–682. <https://www.nature.com/articles/nmeth.2019>.
17. Ramoneda, J., J. Schmidt, M. Manhart, D. C. Angst, D. R. Johnson, J. Ramoneda, and D. R. Johnson, 2023. Physical contacts between sparse biofilms promote plasmid transfer and generate functional novelty. *bioRxiv* <https://doi.org/10.1101/2023.02.01.526699>.

